Data Bank
NEA/DB/DOC(2014)1
www.oecd-nea.org

General Description of Fission Observables

JEFF Report 24
GEF Model

OECD
BETTER POLICIES FOR BETTER LIVES

NEA
NUCLEAR ENERGY AGENCY

Data Bank NEA/DB/DOC(2014)1

General Description of Fission Observables

GEF Model

Karl-Heinz Schmidt
Beatriz Jurado
CENBG, CNRS/IN2P3, Gradignan, France

Charlotte Amouroux
CEA, DSM-Saclay, France

June 2014

NUCLEAR ENERGY AGENCY
ORGANISATION FOR ECONOMIC CO-OPERATION AND DEVELOPMENT

ORGANISATION FOR ECONOMIC CO-OPERATION AND DEVELOPMENT

The OECD is a unique forum where the governments of 34 democracies work together to address the economic, social and environmental challenges of globalisation. The OECD is also at the forefront of efforts to understand and to help governments respond to new developments and concerns, such as corporate governance, the information economy and the challenges of an ageing population. The Organisation provides a setting where governments can compare policy experiences, seek answers to common problems, identify good practice and work to co-ordinate domestic and international policies.

The OECD member countries are: Australia, Austria, Belgium, Canada, Chile, the Czech Republic, Denmark, Estonia, Finland, France, Germany, Greece, Hungary, Iceland, Ireland, Israel, Italy, Japan, Luxembourg, Mexico, the Netherlands, New Zealand, Norway, Poland, Portugal, the Republic of Korea, the Slovak Republic, Slovenia, Spain, Sweden, Switzerland, Turkey, the United Kingdom and the United States. The European Commission takes part in the work of the OECD.

OECD Publishing disseminates widely the results of the Organisation's statistics gathering and research on economic, social and environmental issues, as well as the conventions, guidelines and standards agreed by its members.

NUCLEAR ENERGY AGENCY

The OECD Nuclear Energy Agency (NEA) was established on 1 February 1958. Current NEA membership consists of 31 countries: Australia, Austria, Belgium, Canada, the Czech Republic, Denmark, Finland, France, Germany, Greece, Hungary, Iceland, Ireland, Italy, Japan, Luxembourg, Mexico, the Netherlands, Norway, Poland, Portugal, the Republic of Korea, the Russian Federation, the Slovak Republic, Slovenia, Spain, Sweden, Switzerland, Turkey, the United Kingdom and the United States. The European Commission also takes part in the work of the Agency.

The mission of the NEA is:

- to assist its member countries in maintaining and further developing, through international co-operation, the scientific, technological and legal bases required for a safe, environmentally friendly and economical use of nuclear energy for peaceful purposes;
- to provide authoritative assessments and to forge common understandings on key issues, as input to government decisions on nuclear energy policy and to broader OECD policy analyses in areas such as energy and sustainable development.

Specific areas of competence of the NEA include the safety and regulation of nuclear activities, radioactive waste management, radiological protection, nuclear science, economic and technical analyses of the nuclear fuel cycle, nuclear law and liability, and public information.

The NEA Data Bank provides nuclear data and computer program services for participating countries. In these and related tasks, the NEA works in close collaboration with the International Atomic Energy Agency in Vienna, with which it has a Co-operation Agreement, as well as with other international organisations in the nuclear field.

Foreword

The Joint Evaluated Fission and Fusion (JEFF) Project is a collaborative effort among the member countries of the OECD Nuclear Energy Agency (NEA) Data Bank to develop a reference nuclear data library. The JEFF library contains sets of evaluated nuclear data, mainly for fission and fusion applications; it contains a number of different data types, including neutron and proton interaction data, radioactive decay data, fission yield data and thermal scattering law data.

The General fission (GEF) model is based on novel theoretical concepts and ideas developed to model low energy nuclear fission. The GEF code calculates fission-fragment yields and associated quantities (e.g. prompt neutron and gamma) for a large range of nuclei and excitation energy. This opens up the possibility of a qualitative step forward to improve further the JEFF fission yields sub-library.

This report describes the GEF model which explains the complex appearance of fission observables by universal principles of theoretical models and considerations on the basis of fundamental laws of physics and mathematics. The approach reveals a high degree of regularity and provides a considerable insight into the physics of the fission process. Fission observables can be calculated with a precision that comply with the needs for applications in nuclear technology. The relevance of the approach for examining the consistency of experimental results and for evaluating nuclear data is demonstrated.

Acknowledgements

Developments for the GEF code have been supported by the European Commission within the Sixth Framework Programme through EFNUDAT (project No. 036434) and within the Seventh Framework Programme through Fission-2010-ERINDA (project No. 269499), and by the OECD Nuclear Energy Agency. We thank Mr R. Capote for drawing our attention to recent data on prompt-neutron spectra from fission induced by energetic neutrons. Special thanks go to Mr E. Dupont who incited the work on this report and followed it with much interest and many helpful remarks.

Table of contents

List of Figures

List of Tables

1 Introduction

1.1 Core of the model

The phenomena related to nuclear fission result from many different processes. For many of these, there exist very elaborate models, for example for the capture of an incoming particle in a target nucleus and for the emission of neutrons and gamma radiation from an excited nucleus. However, the modelling of the re-ordering of the nucleons from an excited mono-nucleus into two (or eventually more) fragments is still a challenge for nuclear theory. Estimating the properties of the fission fragments with the high quality required for applications in nuclear technology still relies on empirical models [1]. The composition of the fragments in A and Z determines the starting points of the radioactive decay chains and defines the decay-heat production, their excitation energies determine the characteristics of prompt-neutron and prompt-gamma emission. The major problem is that a fissioning nucleus is an open system that evolves from a quasi-bound configuration to a continuum of possible configurations on the fission path, finally forming hundreds of different fragments with continuous distributions of different shapes, kinetic energies, excitation energies and angular momenta. One of the most advanced approaches for modelling low-energy nuclear fission describes the fission process by a numerical solution of the Langevin equations [2, 3] with eventually further approximations e.g. neglecting the influence of inertia on the dynamics [4]. A subspace of collective variables that is restricted by the limited available computing power is explicitly considered, while the coupling to most internal degrees of freedom is replaced by a heat bath. It is a draw-back that quantum-mechanical features are not properly considered in this classical approach. Another one follows the evolution of the fissioning system with quantum-mechanical tools [5]. However, the inclusion of dissipative processes and phenomena of statistical mechanics within quantum-mechanical algorithms is still not sufficiently developed [6, 7]. Also these calculations require very large computer resources.

The general description of fission observables (GEF model) presented in this work makes use of many theoretical ideas of mostly rather general character, avoiding microscopic calculations with their inherent approximations, e.g. the parameterisation of the nuclear force, and limitations, e.g. by the high computational needs. The large body of empirical information is used for developing a general description of the fission process, which is in good agreement with the empirical data. The theoretical frame assures that this model is able to provide quantitative predictions of the manifold fission observables for a wide range of fissioning systems.

The empirical input to the model requires adjusting a number of parameters by performing a large number of calculations for many systems. For this purpose, it is important that the calculation is relatively fast, allowing for applying fit procedures in order to find the optimum parameter values.

1.2 Additional ingredients

For the calculation of fission observables it is not enough to master the dynamics of the fission process, starting from an excited compound nucleus and ending with the formation of two separated nuclei at scission. Also the initial reaction that induced the fission process, for example the capture of a neutron, must be described, eventually including pre-compound processes. Furthermore, the competition of particle emission, gamma emission and fission must be considered, because it determines the relative contributions of different fissioning systems with different excitation-energy distributions, if the initial excitation energy is high enough for multi-chance fission to occur. After scission, the fragments may be highly excited, and, thus, they emit a number of particles, mostly neutrons and gamma radiation. Also, these processes should be considered in a complete model.

The GEF code aims to provide a complete description including the entrance channel and the de-excitation of the fragments. This is particularly important for the determination of the optimum parameters of the model, because all available observables should be included in the fit procedure. For this purpose, the algorithms should be very efficient in order to assure a short computing time. Therefore, whenever possible, approximations and analytical descriptions were preferred if they are precise enough not to alter the results beyond the inherent uncertainties of the model. More elaborate models that have been developed in many cases may easily be implemented in the code, once it will be fully developed.

1.3 Understanding of the fission process

The general character of the model makes it necessary to establish the systematics of the variation of the fission observables for different systems and as a function of excitation energy and to interpret the origin of these features. It will be shown that the basic ideas of the model are astonishingly powerful. Therefore, the links between the observations and the ingredients of the model enable extracting valuable information on the physics of the nuclear-fission process, much better than the inspection of isolated systems or the direct study of the measurements. An essential advantage provided by the model is the consistent description of essentially all degrees of freedom, due to the efficient computational technique of the code.

1.4 Further developments

The GEF model is unique in the sense that it treats the complete fission process with explicit consideration of a large number of degrees of freedom in a coherent way on physics ground. Thus it provides the links between the different processes and mechanisms and the fission observables. Even more, it preserves the correlations between the different degrees of freedom. It might be very useful for a better understanding of the fission process to carefully study any discrepancies between the model results and available experimental data. Moreover, the systematic trends and global features revealed or predicted by the

model may stimulate dedicated experiments and calculations on specific problems with microscopic models in order to better understand certain aspects of the fission process.

In the application for nuclear data, the GEF code may replace purely parametric descriptions for many quantities and serve as a realistic, consistent and complete event generator for transport calculations with dedicated codes like MCNP [8] or FLUKA [9].

1.5 Complementing, estimating and evaluating nuclear data

Since the empirical data are an important input of the model, it is suggestive that it can be useful for the evaluation of nuclear data. First, the predictions of the model may directly be used for estimating some fission observables, if no experimental data are available. The code can also be useful in order to check whether certain experimental results are in line with or in contradiction with observed trends and systematics. This may lead to an enhanced or diminished confidence level of these data or eventually stimulate dedicated experiments for verification. A very useful application may be the exploitation of the code results for complementing missing data. For this purpose, a special algorithm has been developed that "fine-tunes" the calculated values in a way that they fit to the available experimental data. This algorithm is implemented in the computer code MATCH [10].

2 Concept of the model

2.1 Completeness and generality

During almost seven decades of research, a rather clear, at least qualitative, comprehension of the different stages of the nuclear-fission process has emerged. These ideas guided us to establish the following concept of the general fission model, which is the subject of the present report.

At first, the nucleus needs to leave the first minimum at its ground-state shape, by passing the fission barrier, which in the actinides consists of two or may be even three consecutive barriers with a minimum in between. Since tunneling proceeds with a very low probability, as can be deduced from the long spontaneous-fission half lives, an excited nucleus has enough time to re-arrange its available energy. The probability for the passage of the fission barrier increases considerably, if the nucleus concentrates enough of its energy on the relevant shape degrees of freedom for avoiding tunneling as much as the available energy allows. The remaining energy, however, can be randomly distributed between the different states above the barrier without any further restriction, such that the barrier is passed with maximum possible entropy on the average [11]. For this reason, the fissioning system has no memory on the configurations before the barrier, except the quantities that are preserved due to general conservation laws: total energy, angular momentum and parity. Thus, the starting point of the model is the configuration above the outer fission barrier.

Beyond the outer barrier, one can define an optimum fission path, consisting of a sequence of configurations in deformation space with minimum potential energy for a certain elongation. Although the quantitative determination of this path depends on the shape parameterisation, this picture is helpful for revealing that the fissioning system is unbound only with respect to one degree of freedom, the motion in direction of the fission path. The system is bound with respect to motion in any other direction in deformation space. The distribution of the collective coordinate is given by the occupation probability of the states in the respective potential pockets, which eventually may have more than one minimum. Some of these degrees of freedom which are confined by a restoring force towards the potential minimum are directly linked to fission observables, e.g. the mass asymmetry $A_1/(A_1+A_2)$ or the charge polarisation $< Z_1 > -Z_{UCD}$ [1] with $Z_{UCD} = A_1 \times Z_{CN}/A_{CN}$. A_{CN}, Z_{CN}, A_i and Z_i are mass and atomic number of the fissioning system and of one fragment, respectively. The fission-fragment distribution in Z and A is given by the evolution of the respective collective variables, until the system reaches the scission configuration. Under the influence of dissipation and inertial forces, the value of the respective collective variable is the integral result of the forces acting on the whole fission path.

[1] For a continuous tracking of these degrees of freedom, suitable prescriptions must be defined that generalise these values that are defined for the separated fragments to the respective deformation parameters of the system on the fission path before scission.

From a theoretical model, one requires that the evolution of the fissioning system is fully described, considering all degrees of freedom, their dependencies and their correlations. Current microscopic models, either classical or quantum-mechanical ones, do not meet this requirement, because they only consider a restricted number of degrees of freedom. Statistical models applied at the saddle or at the scission point are not suited neither, because they neglect the dynamical aspects of the fission process.

The general fission model is a compromise that does not eliminate any of the complex features of the fission process by far-reaching approximations or restrictions from the beginning on. Instead, it makes use of a number of generally valid physics laws and characteristics that allow reducing the computing expenses to an affordable level.

2.2 General features of quantum mechanics

The observables from low-energy fission show strong manifestations of quantum-mechanical effects like the contributions of the different fission modes to the fission-fragment mass and total-kinetic-energy distributions that are related to nuclear shell effects and the considerable enhancement of even-Z fission fragments that are related to pairing correlations. These quantum-mechanical features are responsible for great part of the complexity of nuclear fission, and, thus, they considerably complicate the theoretical description of the fission process. The GEF model exploits a long-known general property of quantum mechanical wave functions in a strongly deformed potential in order to simplify this problem considerably.

When the two-centre shell model became available, it was possible to study the single-particle structure in a di-nuclear potential with a necked-in shape. Investigations of Mosel and Schmitt [12] revealed that the single-particle structure in the vicinity of the outer fission barrier already resembles very much the coherent superposition of the single-particle levels in the two separated fragments after fission. They explained this result by the general quantum-mechanical feature that wave functions in a slightly necked-in potential are already essentially localized in the two parts of the system. This feature is a direct consequence of the necking, independent from the specific shape parameterisation. This finding immediately leads to the expectation that the shells on the fission path that are responsible for the complex structure of fission modes are essentially given by the fragment shells. Potential-energy surfaces of fissioning systems calculated with the macroscopic-microscopic approach (e.g. ref. [13]) support this assumption.

As a consequence, the shell effects on the fission path can be approximately considered as the sum of the shell effects in the proton- and neutron-subsystems of the light and the heavy fission fragment. Thus, these shells do not primarily depend on the fissioning system but on the number of neutrons and protons in the two fission fragments. However, these shells may be substantially different from the shell effects of the fragments in their ground state, because the nascent fragments in the fissioning dinuclear system might be strongly deformed due to the interaction with the complementary fragment.

Other quantum-mechanical features to be considered are tunneling in spontaneous

fission and the uncertainty principle that induces fluctuations in the nuclide distributions of the fission fragments and that is assumed to generate their angular momenta.

2.3 General features of stochastic processes

Stochastic calculations revealed that, depending on the nature of the collective degree of freedom considered, dynamical effects induce a kind of memory on the fission trajectory due to the influence of dissipation and inertial forces [14]. The corresponding characteristic memory time determines, after which time a specific coordinate value is forgotten and how long it takes for this coordinate to adjust to modified conditions. This means that the distribution of a specific observable is essentially determined by the properties of the system, for example the potential-energy surface, at an earlier stage. According to experimental observations [15] and theoretical studies [16], the mass distribution is essentially determined already way before reaching scission. The memory of the charge-polarisation degree of freedom has been found to be much shorter [17, 18].

As a practical consequence, it is assumed in the GEF model that the measured distribution of a specific fission observable essentially maps a kind of effective potential, the system was exposed to by the characteristic memory time before reaching scission. In other words, the effective potential that is extracted from the measured distribution of a fission observable, implicitly includes the influence of dynamical effects.

2.4 General features of statistical mechanics

The transformation of energy between potential energy, intrinsic and collective excitations as well as kinetic energy is another very important aspect of the nuclear-fission process. It determines the partition of the fission Q value (plus eventually the initial excitation energy of the fissioning system) between kinetic and excitation energy of the final fragments. Moreover, the division of the total excitation energy between the fragments is of considerable interest, because it induces a shift of the isotopic distributions from the primary fragments by neutron evaporation towards less neutron-rich isotopes. It has also been noticed that the shape of the mass-dependent prompt-neutron yields strongly affects the mass values of the fission products deduced from kinematical double-energy measurements [19].

The GEF model takes advantage of the general laws of statistical mechanics, which govern the energetics of any object, independently of its size. In particular, statistical mechanics requires that the available energy tends to be distributed among the accessible degrees of freedom in equal share during the dynamical evolution of the system. This general law provides an invaluable estimation of the evolution of the intrinsic excitation energies and the population of the available states in the nascent fragments during the fission process with little computational expense.

2.5 Topological properties of the nuclear potential in multi-dimensional space

The shape-dependent nuclear potential of the fissioning system possesses a few regions which have special importance for the fission process. These are the nuclear ground state and the saddle points at the inner and the outer fission barrier. The topological property of the ground state is solely defined by the condition that the ground state is the nuclear state with the largest binding energy. No other condition is imposed on the surrounding of this state. It is trivial that increasing the binding energy in this state directly translates in lowering the mass of the nucleus in its ground state. This is different for a saddle point, which is the lowest threshold that must be passed when moving from the region around the ground state to the region around the second minimum or from the region around the second minimum towards scission. In this case, the height of the saddle has to be searched on a whole path in comparison to all other possible paths across the barrier. In addition, a local modification of the potential by a bump or a dip, for example by shell effects, does not have a big effect on the height of the saddle, because the fissioning nucleus will go around the bump, and it cannot profit from the depth of the dip, because the potential at its border has changed only little. Myers and Swiatecki expressed these ideas by the topographical theorem [20]. The topographical theorem is exploited in the GEF model for deriving a semi-empirical systematics of fission barriers.

2.6 Exploiting empirical knowledge

Many of the ideas outlined in the previous sections establish a link between measured observables and specific properties of the fissioning system. It is an essential part of the GEF concept that this empirical information is exploited to assure that the quantitative results of the model are in best possible agreement with the available experimental data. For this purpose, the ingredients of the model and its parameter values are adjusted in a global fit procedure that minimises the deviations from a large set of experimental data of different kind. Note that the GEF model, in contrast to current empirical models, is not a direct parameterisation of the observables. Instead, as was mentioned above, it describes the physics of the fission process, making use of several approximations based on general physics laws. The quality with which the GEF code is able to reproduce a large body of data with a moderate number of parameters will give an indication about the validity of these approximations.

2.7 Monte-Carlo method: Correlations and dependencies

Nuclear fission provides a large number of observables. The correlations between different kind of observables represent a valuable information on the fission process. Therefore, the GEF code is designed as a Monte-Carlo code that follows all quantities of the fissioning systems with their correlations and dependencies. Finally, all observables can be listed

event by event, which allows the investigation of all kind of correlations. Moreover, complex experimental filters can easily be implemented.

2.8 Range of validity

According to the concept of the GEF model, the range of validity is not strictly defined. Technically, the code runs for any heavy nucleus. However, the results of the model are more reliable for nuclei which are not too far from the region where experimental data exist. It is recommended not to use the code outside the range depicted in Figure 1 on the chart of the nuclides.

Figure 1: Validity range of the GEF model

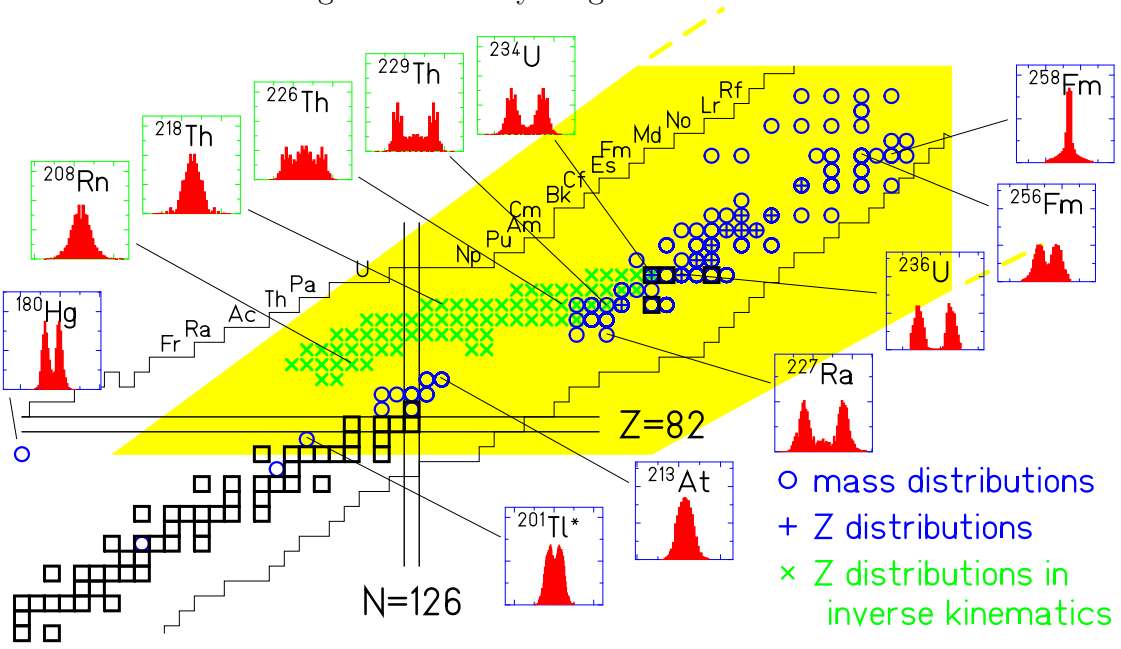

Note: The validity range of the GEF model is marked in yellow. For a detailed description of the figure see Figure 6.

3 Special developments

3.1 Systematics of fission barriers

One of the most critical input parameters of the GEF model is the height of the fission barrier. That is the energy a nucleus has to invest in order to proceed to fission without tunneling. Since experimental fission barriers are available for a rather restricted number of nuclei, only, a model description is needed in order to meet the requirement of the GEF model for generality.

An elaborate analysis [21] of available experimental data revealed that different theoretical models differ appreciably in their predictions for the average trend of the fission-barrier height along isotopic chains. Also self-consistent models deviate drastically from each other.

During the last years, the efforts for developing improved models for the calculation of fission barriers were intensified, using the macroscopic-microscopic approach [22, 23, 13, 24, 25, 26, 27], the density-functional theory [28, 29] and varieties of Hartree-Fock methods [30-33]. Still, the results from the different models, in particular in regions, where no experimental data exist, differ appreciably. Since the fission-barrier height is the difference of the mass at the saddle-point which defines the fission barrier and the ground-state mass, it is obvious that the fission-barrier values from these models cannot be more precise than the values of the ground-state masses, which show typical root-mean square deviations of at least several 100 keV from the experimental values.

An alternative approach that avoids this problem was used in ref. [34], by estimating the fission barrier as the sum of the macroscopic fission barrier and the ground-state shell correction, making use of the topographical theorem [20, 35]. In the GEF model, we follow this idea, however, we explicitly consider the pairing condensation energies in the ground state and at the barrier, because they are systematically different. For the macroscopic part of the fission barrier, we chose the Thomas-Fermi barriers of Myers and Swiatecki [36] and combined them with the Thomas-Fermi masses of the same authors [20] for determining the contributions of shells and pairing to the ground-state binding energy, because these models were found [21] to follow best the isotopic trends of the experimental masses and fission barriers.

In detail, the macroscopic fission-barrier height for the nucleus with mass number A and atomic number Z is calculated with the following relations, adapted from ref. [36]:

$$N = A - Z \tag{1}$$

$$I = (N - Z)/A \tag{2}$$

$$\kappa = 1.9 + (Z - 80)/75 \tag{3}$$

$$S = A^{2/3}(1 - \kappa I^2) \tag{4}$$

$$X = \frac{Z^2}{A(1 - \kappa I^2)} \tag{5}$$

For $30 \leq X < X_1$:

$$F = 0.595553 - 0.124136(X - X_1) \tag{6}$$

For $X \geq X_1$ and $X \leq X_0$:

$$F = 0.000199749(X_0 - X)^3 \tag{7}$$

with $X_0 = 48.5428$ and $X_1 = 34.15$. Finally, the Thomas-Fermi macroscopic fission barrier is given by:

$$B_f^{TF} = F \cdot S. \tag{8}$$

The higher one of the inner (E_A) and the outer (E_B) fission barrier ($B_f = \max(E_A, E_B)$) is given by the sum of the macroscopic fission barrier and the negative value of the microscopic contribution to the ground-state mass δE_{gs}^{mic} plus the microscopic contribution δE_f^{mic} to the binding energy at the respective barrier.

$$B_f = B_f^{TF} - \delta E_{gs}^{mic} + \delta E_f^{mic}. \tag{9}$$

The microscopic contribution to the ground-state mass is the difference of the actual ground-state mass and the macroscopic mass obtained with the Thomas-Fermi approach $\delta E_{gs}^{mic} = m_{gs} - m_{TF}$. It represents the structural variation of the ground-state mass due to shell correction δU_{gs} and pairing condensation energy δP_{gs}. The topographical theorem claims that the shell effect at the barrier can be neglected. Therefore, only the contribution from pairing must be considered: $\delta E_f^{mic} = \delta P_f$. Best agreement with the data is obtained by including the even-odd staggering of the binding energy at the barrier with $\delta P_f = -n \cdot 14/\sqrt{A}$, $n = 0, 1, 2$ for odd-odd, odd-mass and even-even nuclei, respectively.

The available measured fission barriers were used to deduce the following empirical function, which describes the difference between the inner and the outer barrier height:

$$E_A - E_B = 5.40101 - 0.00666175 \cdot Z^3/A + 1.52531 \cdot 10^{-6} \cdot (Z^3/A)^2. \tag{10}$$

The result of this procedure was not yet fully satisfactory, because the barriers around thorium were somewhat overestimated. This discrepancy decreases for lighter and for heavier elements. Figure 2 illustrates a possible reason for this deviation in a schematic way: The lower part shows the macroscopic potential, essentially given by the asymmetry-dependent surface energy and Coulomb interaction potential, for a lighter (dashed line), for a medium-heavy (full line) and for a heavier (dot-dashed line) nucleus. The upper part shows the schematic variation of the shell correction as a function of deformation, which is assumed to be the same for all nuclei in the region of the heavy nuclei concerned. The full potential can be assumed as the sum of the macroscopic and the microscopic potential. The first minimum of the nuclear ground state is deformed in the actinides considered. The full line in the lower part corresponds to the situation around thorium: The inner and the outer barriers have about the same height. This situation is realised when the second minimum is localised near the maximum of the macroscopic potential. In this situation, the inner and the outer barrier are localised at a deformation, where the

Figure 2: Microscopic and macroscopic potential in fission direction

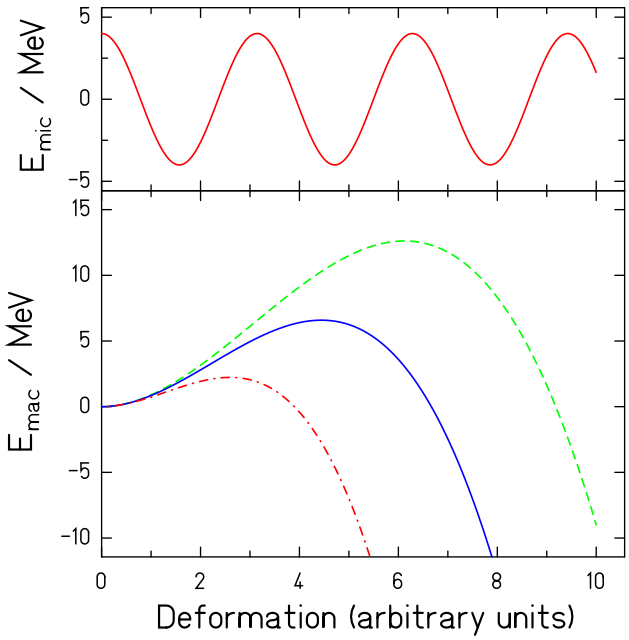

Note: Schematic drawing of the microscopic and the macroscopic potential in fission direction. See text for details.

macroscopic potential is far from its maximum value. For lighter nuclei, the maximum of the macroscopic potential moves to larger deformations, closer to the outer barrier, which becomes the higher one. For heavier nuclei, the maximum of the macroscopic potential moves to smaller deformations, closer to the inner barrier, which becomes the higher one. This consideration makes it understandable that the barriers of nuclei around thorium deviate systematically from the smooth trend expected from the topographical theorem: They are systematically smaller. This deviation was parametrised by the following correction term:
For $86.5 < Z < 90$:

$$\Delta B_f = -0.15(Z - 86.5) \tag{11}$$

For $90 \leq Z < 93$:

$$\Delta B_f = -0.15(Z - 86.5) + 0.35(Z - 90) \tag{12}$$

For $93 \leq Z < 95$:

$$\Delta B_f = -0.15(Z - 86.5) + 0.35(Z - 90) + 0.15(Z - 93) \tag{13}$$

For $Z \geq 95$:

$$\Delta B_f = -0.15(Z - 86.5) + 0.35(Z - 90) + 0.15(Z - 93) - 0.25(Z - 95) \tag{14}$$

Figure 3: Empirical correction to the fission barrier

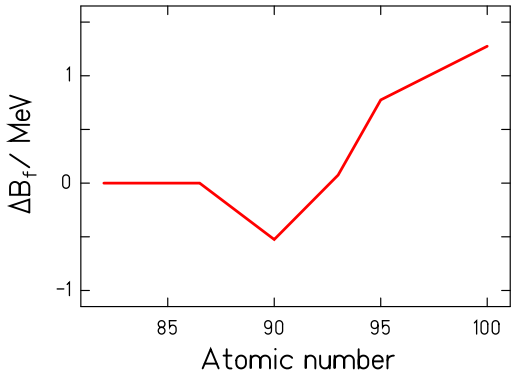

Note: Empirical correction applied to the fission barrier height obtained with the topographical theorem as a function of the atomic number of the fissioning nucleus.

The resulting function is depicted in Figure 3. In addition to the dip around $Z = 90$, which can be considered as a refinement of the topographical theorem, the barrier heights had to be further increased for the heavier elements in order to better reproduce the measured values. This latter effect, which is the only violation of the topographical theorem in our description, may be caused by shell effects at the barrier or by a shortcoming of the Thomas-Fermi barriers for the heaviest elements.

The fission barriers from the description used in the GEF code are compared in Figures 4 and 5 with different empirical and theoretical values. The theoretical values of Goriely et al. [33] are quite close to the empirical data, whereas the values of P. Möller et al. [13] [2] deviate strongly in their absolute values and in the isotopic trends. Obviously, the description used in the GEF code agrees rather well with the empirical data. In particular, this description can be extrapolated far away from the beta-stable region without any new assumptions. In several cases, the symbols are even hardly visible because they are covered by the experimental points.

The even-odd staggering of the fission barrier height is well reproduced by the model assuming a pairing-gap parameter $\Delta = 14/\sqrt{A}$, compared to an averge value of $\Delta = 12/\sqrt{A}$ in the nuclear ground state. This may eventually be an evidence for the deformation dependence of the pairing strength [37]. But a stronger pairing at the barrier is also expected by the systematically higher single-particle level density at the barrier compared to the ground state due to topological reasons: while the barrier is practically not lowered by shell effects compared to the macroscopic barrier, the nuclear ground state is almost generally more bound than the macroscopic ground state, because it is the state with the

[2] It is the benefit of ref. [13], compared to most theoretical work, that it presents extensive tables of calculated barrier parameters of the actinides, which makes the quantitative comparison with this theory feasible.

absolute lowest energy in deformation space. Generally, more binding by shell effects is related to a lower single-particle level density at the Fermi level. This kind of even-odd staggering is also present in the theoretical values [13] and [33], although the amplitude is not large enough.

Figure 4: Overview on fission barriers, part 1

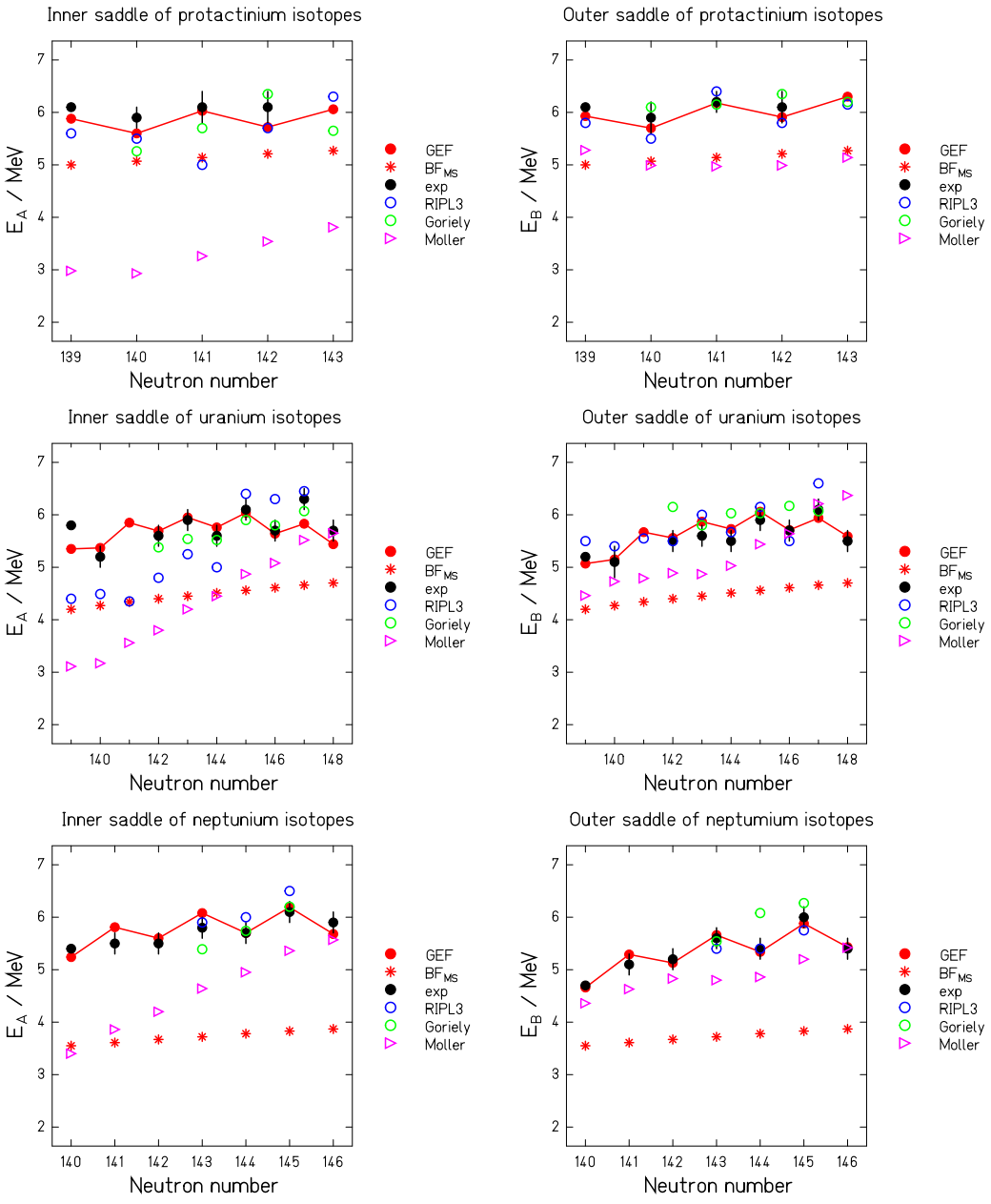

Note: Height of the inner and the outer fission barrier above the nuclear ground state for isotopes of protactinium, uranium and neptunium. The description used in the GEF model is compared with the experimental barriers determined in ref. [38] (marked by "exp"), with the empirical barriers given in RIPL3 [39], with the self-consistent theoretical barriers [33] given in RIPL3 (marked by "Goriely"), and with the macroscopic-microscopic barriers of P. Möller et al. [13]. In addition, the macroscopic fission barriers (BF_{MS}) from ref. [36] are shown.

Figure 5: Overview on fission barriers, part 2

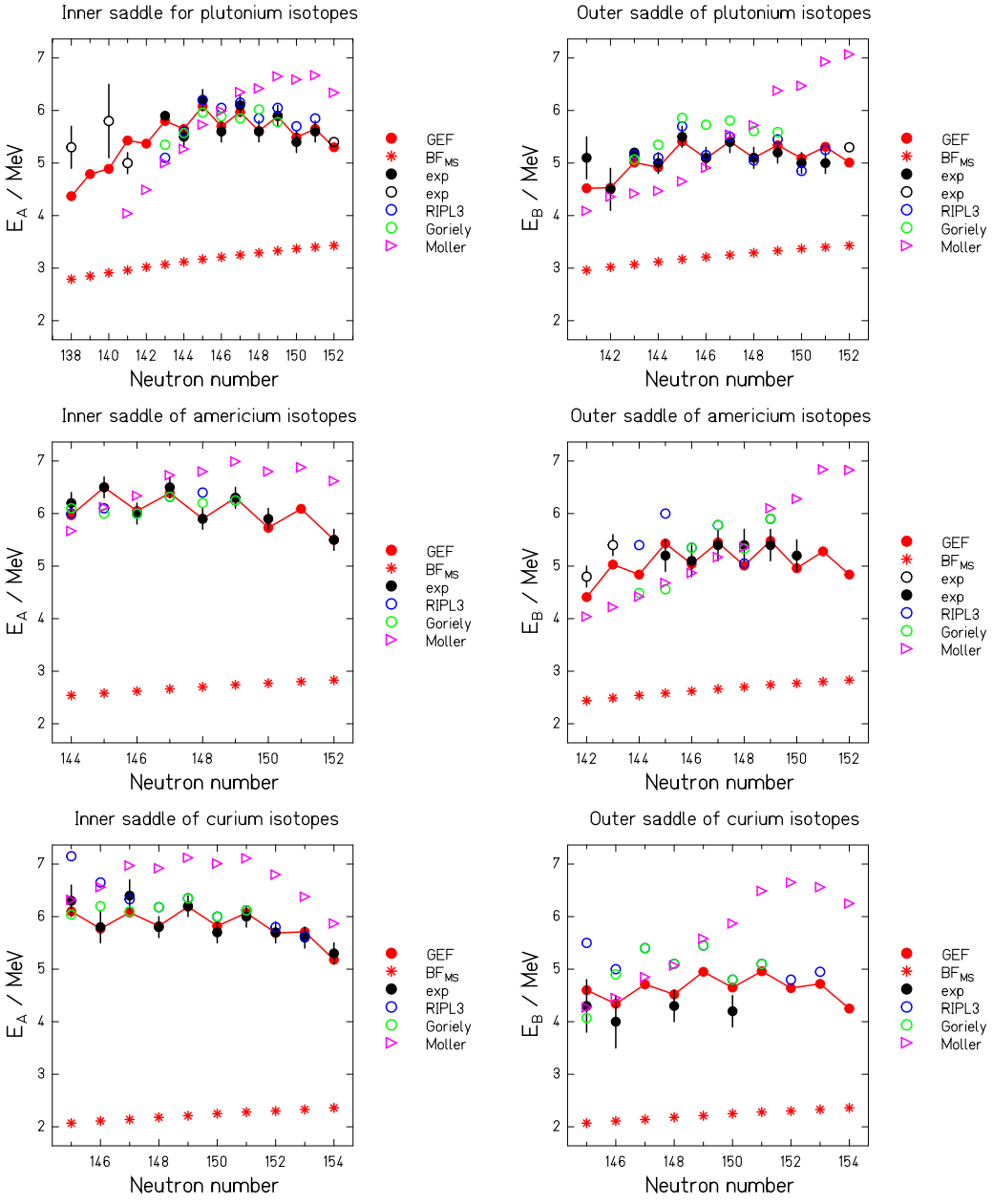

Note: Height of the inner and the outer fission barrier above the nuclear ground state for isotopes of plutonium, americium and curium. The description used in the GEF model is compared with the experimental barriers (marked by "exp") determined in ref. [38] (full symbols) and other papers cited in ref. [40] (open symbols), with the empirical barriers given in RIPL3 [39], with the self-consistent theoretical barriers [33] given in RIPL3 (marked by "Goriely"), and with the macroscopic-microscopic barriers of P. Möller et al. [13]. In addition, the macroscopic fission barriers (BF_{MS}) from ref. [36] are shown.

The rms deviations between the different sets of fission barriers shown in Figures 4 and 5 are listed in Table 1. There is a remarkably large deviation between the experimental data from Bjornholm and Lynn [38] and the recommended values of RIPL 3 [39]. The best agreement exists between the GEF parameterisation and the experimental values determined by Bjornholm and Lynn [38]. The rms deviation of 0.2 MeV does not exceed the estimated uncertainties of the experimental values [38] and is appreciably smaller than the rms deviations with which the best atomic mass models reproduce the experimental values.[3] Also, the self-consistent barriers of Goriely et al. [33] agree better with the experimental values of Bjornholm and Lynn than with the recommended values of RIPL 3 [39]. From the figures, one can deduce that the data from ref. [38] and the GEF parameterisation, which is deduced from the topographical theorem, agree best in the isotopic trend, while the theoretical values of ref. [33] and the RIPL 3 values show increasingly discrepant local deviations. The theoretical values of Möller et al. deviate most strongly from any other set. Considering that the only adjustment of the proposed description is the application of the simple and well justified global Z-dependent function shown in Figure 3, experiment and calculation are fully independent in their structural features and in their global dependency on neutron excess. The good agreement thus evidences that the barriers obtained with the present approach represent the experimental values better than the two theoretical models considered or the RIPL-3 recommended values.

Finally, the fission-barrier values of several heavy nuclei that are used in the GEF code are listed in Tables 2 and 3.

Table 1: RMS deviation between different sets of fission barriers

	exp	RIPL 3	GEF	Goriely	Möller
exp	—	0.43	0.20	0.37	1.1
RIPL 3	0.43	—	0.46	0.46	1.0
GEF	0.20	0.46	—	0.38	1.1
Goriely	0.37	0.46	0.38	—	1.0
Möller	1.1	1.0	1.1	1.0	—

Note: The table lists the RMS deviations in MeV between the different sets of fission barriers shown in Figures 4 and 5. References are given in the Figure captions. The typical uncertainty of the experimental values is 0.2 to 0.3 MeV.

[3] According to ref. [41], the most precise and robust nuclear mass predictions are given by the Duflo-Zuker model [42], which gives an rms deviation of 373 keV.

Table 2: Fission barriers used in GEF, part 1

N	Th	Pa	U	Np	Pu
134	5.75/5.87	4.99/4.79	4.12/3.57	3.41/2.46	3.20/1.83
135	5.84/6.01	5.53/5.39	4.45/3.95	4.18/3.29	3.48/2.18
136	5.64/5.85	5.25/5.15	4.54/4.10	4.07/3.25	3.81/2.57
137	5.70/5.96	5.64/5.60	4.84/4.46	4.67/3.91	4.30/3.13
138	5.67/5.98	5.44/5.45	5.00/4.67	4.64/3.94	4.37/3.27
139	5.78/6.13	5.88/5.93	5.35/5.07	5.22/4.58	4.79/3.75
140	5.70/6.09	5.91/6.43	5.37/5.15	5.24/4.66	4.89/3.92
141	5.91/6.34	6.03/6.18	5.85/5.67	5.81/5.29	5.43/4.52
142	5.72/6.19	5.60/5.70	5.69/5.56	5.60/5.13	5.37/4.53
143	5.84/6.35	6.03/6.18	5.95/5.87	6.08/5.66	5.80/5.01
144	5.65/6.19	5.72/5.91	5.76/5.73	5.70/5.34	5.65/4.92
145	5.87/6.46	6.06/6.30	6.04/6.06	6.19/5.88	6.08/5.41
146	5.56/6.18	5.48/5.84	5.64/5.71	5.68/5.43	5.70/5.09
147	5.71/6.37	5.77/6.17	5.82/5.94	5.97/5.76	5.97/5.41
148	5.19/5.89	5.48/5.84	5.44/5.59	5.63/5.47	5.61/5.10
149		5.77/6.17	5.63/5.83	5.98/5.87	5.89/5.44
150		5.28/5.72	5.19/5.43	5.36/5.30	5.49/5.09
151			5.29/5.57	5.77/5.75	5.65/5.31
152			5.63/5.95	5.04/5.07	5.30/5.01
153				5.96/6.03	5.34/5.10
154					5.11/4.91

Note: Height of first and second barrier used in the GEF code in MeV.

Table 3: Fission barriers used in GEF, part 2

N	Am	Cm	Bk	Cf	Es
137	4.35/2.73	3.77/1.67			
138	4.28/2.74	4.05/2.03	3.64/1.11		
139	4.98/3.51	4.45/2.51	4.27/1.82	3.89/0.89	
140	5.02/3.62	4.60/2.74	4.41/2.04	4.12/1.21	3.95/0.46
141	5.75/4.42	5.16/3.37	5.11/2.82	4.68/1.85	4.61/1.21
142	5.67/4.41	5.21/3.49	5.12/2.92	4.77/2.04	4.59/1.28
143	6.23/5.03	5.70/4.06	5.69/3.57	5.22/2.58	5.22/2.01
144	5.97/4.84	5.64/4.07	5.63/3.58	5.27/2.70	5.18/2.06
145	6.50/5.43	6.10/4.60	6.16/4.19	5.70/3.22	5.73/2.70
146	6.05/5.04	5.77/4.34	5.77/3.88	5.57/3.17	5.55/2.69
147	6.39/5.45	6.08/4.71	6.23/4.41	5.94/3.62	6.08/3.23
148	5.90/5.01	5.82/4.52	5.95/4.19	5.85/3.61	5.83/3.06
149	6.30/5.48	6.19/4.95	6.51/4.83	6.37/4.21	6.43/3.74
150	5.73/4.96	5.82/4.65	6.05/4.44	6.09/4.00	6.22/3.62
151	5.99/5.28	6.07/4.96	6.41/4.87	6.36/4.35	6.73/4.20
152	5.50/4.84	5.69/4.64	5.94/4.46	6.02/4.08	6.35/3.90
153	5.66/5.06	5.71/4.72	6.02/4.61	6.05/4.18	6.35/3.98
154	5.01/4.47	5.18/4.25	5.26/3.91	5.48/3.68	5.78/3.49
155	5.34/4.84	5.11/4.24	5.35/4.07	5.43/3.70	5.82/3.60
156		4.64/3.83	4.70/3.48	4.95/3.29	5.10/2.96
157			4.85/3.69	4.91/3.31	5.23/3.17
158			4.51/3.41	4.46/2.93	4.62/2.62
159				4.03/3.17	4.76/2.84
160				4.41/3.01	4.79/2.94
161					5.17/3.39
162					4.96/3.24

Note: Height of first and second barrier used in the GEF code in MeV. (Continuation of Table 2.)

3.2 Nuclear level densities

Nuclear level densities are another important ingredient of any nuclear model. There exist several descriptions that differ substantially, in particular in their low-energy characteristics. A recent analysis revealed that many of these descriptions are not consistent with our present understanding of nuclear properties [43]. The result can be summarised as follows:

1. Even-odd staggering of the nuclear binding energies proves that pairing correlations are present in essentially all nuclei at low excitation energies. Therefore, any kind of level-density formula based on the the so-called Fermi-gas level-density, which is derived under the independent-particle assumption, is not valid in the low-energy regime.

2. Since pairing correlations are only stable, if they enhance the nuclear binding, the binding energies of all nuclei are enhanced with respect to the value obtained in the independent-particle picture. Therefore, energy-shift parameters of the level-density description for energies above the regime of pairing correlations must be positive for all nuclei.

3. From an almost constant-temperature behaviour of measured level densities, high heat capacities are deduced for nuclei up to energies in the order of 10 MeV. Jumps in the heat capacity prove that the high heat capacity is caused by the consecutive creation of internal degrees of freedom by pair breaking, such that the energy per degree of freedom stays approximately constant as a function of excitation energy in the regime of pairing correlations.

In the GEF model, a simple and transparent analytical description is used that meets the above-mentioned requirements. The nuclear level density was modelled by the slightly simplified constant-temperature description of v. Egidy and Bucurescu [44] at low energies.

$$\rho = \frac{1}{T} e^{(E-E_0)/T} \tag{15}$$

with

$$E_0 = -n \cdot \Delta_0 \tag{16}$$

($n = 0, 1, 2$ for even-even, odd-A, and odd-odd nuclei, respectively, and $\Delta_0 = 12\ \mathrm{MeV}/\sqrt{A}$). The temperature parameter T depends on the mass A of the nucleus and the shell effect δU.

$$T/\mathrm{MeV} = \frac{A^{-2/3}}{0.0597 + 0.00198 \cdot \delta U/\mathrm{MeV}} \tag{17}$$

In the ground-state shape this is the ground-state shell effect. The same formula is applied in different configurations, e.g. at the fission barrier, where the shell effect is basically different from the ground-state shell effect, however with a larger pairing-gap parameter $\Delta_0 = 14\ \mathrm{MeV}/\sqrt{A}$.

The level density was smoothly joined at higher energies with the modified Fermi-gas description of Ignatyuk et al. [45, 46] for the nuclear-state density:

$$\omega \propto \frac{\sqrt{\pi}}{12\tilde{a}^{1/4}U^{5/4}} \exp(2\sqrt{\tilde{a}U}) \tag{18}$$

with $U = E + E_{cond} + \delta U(1 - \exp(-\gamma E))$, $\gamma = 0.55/\text{MeV}$ and the asymptotic level-density parameter $\tilde{a} = (0.078A + 0.115A^{2/3})/\text{MeV}$. The shift parameter $E_{cond} = -2$ MeV$-n\Delta_0$, $\Delta_0 = 12$ MeV$/\sqrt{A}$ ($\Delta_0 = 14$ MeV$/\sqrt{A}$ at the barrier) with $n = 0, 1, 2$, for odd-odd, odd-A and even-even nuclei, respectively, as proposed in ref. [43]. δU is the shell correction. A constant spin-cutoff parameter was used. The matching energy is determined from the matching condition (continuous level-density values and derivatives of the constant-temperature and the Fermi-gas part). Values slightly below 10 MeV are obtained. The matching condition also determines a scaling factor for the Fermi-gas part. It is related to the collective enhancement of the level density.

This picture is valid for the situation for near-symmetric mass splits. The increase of the even-odd effect in Z yields has no influence on the magnitude of the even-odd effect in total kinetic energy.

3.3 Empirical fragment shells

Figure 6 gives an overview on the measured mass and nuclear-charge distributions of fission products from low-energy fission. Fission of target nuclei in the actinide region, mostly induced by neutrons, shows predominantly asymmetric mass splits. A transition to symmetric mass splits is seen around mass 258 in spontaneous fission of fusion residues. Electromagnetic-induced fission of relativistic secondary beams covers the transition from asymmetric to symmetric fission around mass 226 [48]. A pronounced fine structure close to symmetry appears in ^{201}Tl [49] and in ^{180}Hg [50]. It is difficult to observe low-energy fission in this mass range. Thus, ^{201}Tl could only be measured down to 7.3 MeV above the fission barrier due to its low fissility, which explains the filling of the minimum between the two peaks. Only ^{180}Hg was measured at energies close to the barrier after beta decay of ^{180}Tl. Considering the measured energy dependence of the structure for ^{201}Tl [49], the fission characteristics of these two nuclei are rather similar. Also other nuclei in this mass region show similar features, which have been attributed to the influence of fragment shells [51]. Nuclei in this region are not further considered in this report that concentrates on heavier nuclei with mass numbers $A > 200$, which are more important for technical applications.

In the range where asymmetric fission prevails, e.g. from ^{227}Ra to ^{256}Fm, the light and the heavy fission-product components gradually approach each other, see Figure 6. A quantitative analysis revealed that the mean mass of the heavy component stays approximately constant at about $A = 140$ [52]. This has been explained by the influence of a deformed ($\beta \approx 0.6$) fragment shell at $N = 88$ and the spherical shell at $N = 82$

[53], suggesting that the position of the heavy fragment is essentially constant in neutron number.

More recent data on Z distributions over long isotopic chains [48], however, reveal very clearly that the position in neutron number varies systematically over more than 7 units, while the position in proton number is approximately constant at $Z = 54$ (see Figure 7). The rather short isotopic sequences covered in former experiments did not show this feature clearly enough and gave the false impression of a constant position in mass. Up to now it has not been possible to identify the fragment shells, which are behind the observed position of the heavy fragments in the actinides. Although the position of the heavy fragment is almost constant at $Z \approx 54$, it may be doubted that a proton shell is at the origin of the asymmetric fission of the actinides, because a proton shell in this region is in conflict with shell-model calculations [53, 55].

At present we limit ourselves in extracting the positions and the shapes of the fission valleys of the standard 1, the standard 2 and the super-asymmetric fission channels (in the nomenclature of Brosa et al. [56]), which form together the asymmetric fission component. This is done by a fit to the corresponding structures in the measured mass distributions. Eventually some shells in the complementary fragment are also assumed. The depths of

Figure 6: Systematics of fission-fragment distributions

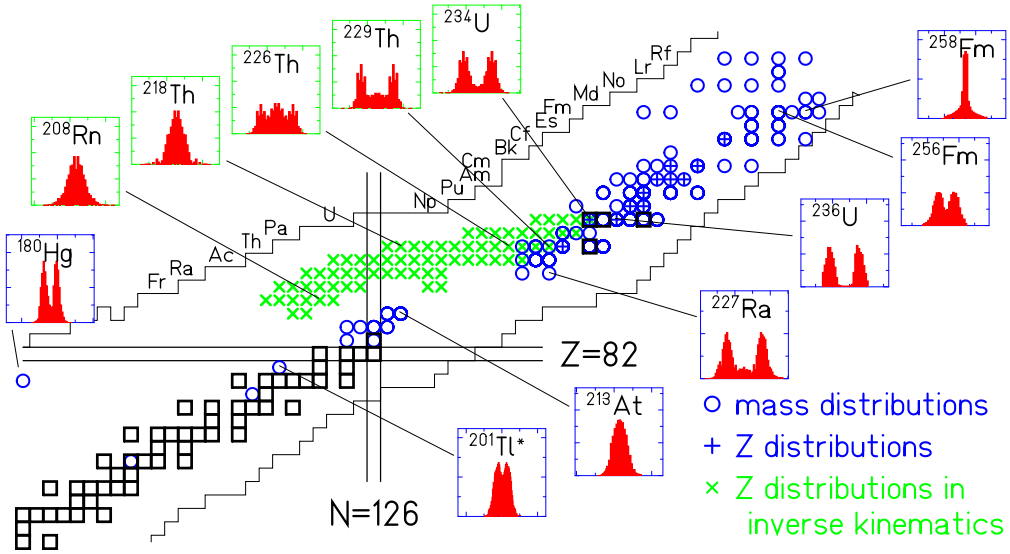

Note: General view on the systems for which mass or nuclear-charge distributions have been measured (from [47]). The distributions are shown for 12 selected systems. Blue circles (blue crosses): Mass (nuclear-charge) distributions, measured in conventional experiments [49, 50], and references given in [48]. Green crosses: Nuclear-charge distributions, measured in inverse kinematics [48].

Figure 7: Mean neutron and proton number of heavy mass peak

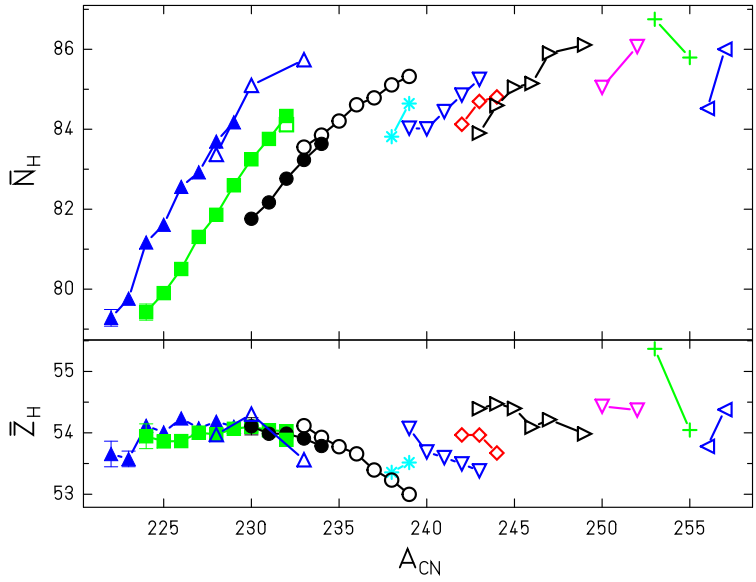

Note: Mean neutron and proton number of the heavy component in asymmetric fission in the actinide region before the emission of prompt neutrons (from [47]). The values were deduced from measured mass and nuclear-charge distributions using the GEF model for the correction of charge polarisation and prompt-neutron emission. Open symbols denote results from conventional experiments, full symbols refer to an experiment with relativistic projectile fragments of ^{238}U [48]. Data points for the same Z_{CN} are connected (see [54] for references of the underlying experimental data).

the fission valleys are deduced from the relative yields of the fission modes by assuming that the quantum oscillators in the different fission valleys are coupled, which implies that their populations in the vicinity of the outer barrier are in thermal equilibrium. The potential at this elongation is calculated as the sum of the macroscopic potential, which is a function of the fissionning nucleus, and of the shell effects. The magnitudes of the shell effects are assumed to be the same for all fissioning systems.

Figure 8 illustrates, how the observed transition from symmetric to asymmetric fission around ^{226}Th can be explained by the competition of the macroscopic potential that favours mass-symmetric splits and the shell effect around $Z = 55$, even if the shell strength is assumed to be constant. With increasing size of the system, the position of the shell assumed to be fixed at $Z = 55$ is found closer to symmetry, which is favoured by the macroscopic potential. In radium, the potential is lowest at mass symmetry, favouring single-humped mass distributions, in thorium, the potential at symmetry and near $Z = 55$ is about equal, creating triple-humped mass distributions, and in plutonium, the potential is lowest near $Z = 55$, favouring double-humped mass distributions.

Figure 8: Potential energy for mass-asymmetric distortions

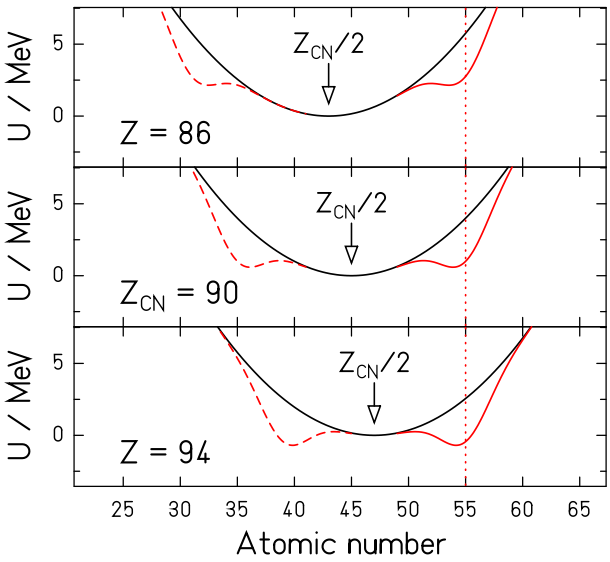

Note: Schematic illustration of the potential energy for mass-asymmetric shape distortions on the fission path, after an idea of M. Itkis et al. [57]. The black curve shows the macroscopic potential that is minimum at symmetry, while the red curve includes the extra binding due to an assumed shell appearing at Z=55 in the heavy fragment. This is not necessarily a proton shell (see text for details).

3.4 Charge polarisation

Besides the mass number, also the numbers of protons and neutrons in a fission fragment can vary independently. In mass-asymmetric fission, the mean Z/A value is found to be smaller on average in the heavy fragment. The cluster plot of a calculation with the GEF code, shown in Figure 9, demonstrates this finding on a nuclear chart. Figure 9 shows the yields of the fission fragments of the system ^{235}U(n$_{th}$,f) before emission of prompt neutrons. The model reproduces the measured mass-dependent prompt-neutron yields of ^{237}Np(n,f) [58] at different incident neutron energies and yields of the light fission-fragments after prompt-neutron emission of ^{235}U(n$_{th}$,f) [59]. Therefore, this calculation is expected to be quite realistic.

Figure 10 illustrates, how the Z/A degree of freedom is treated in the GEF model. First, a calculation minimises the energy of the system near scission with respect to the deformations and the charge densities (Z/A ratio) of the two fragments without considering structural effects. The macroscopic binding energies of the two fragments and the Coulomb repulsion between the fragments at a tip distance of 1 fm are considered. The neutron loss by emission of prompt neutrons that is consistent with the available data on

Figure 9: Nuclide distribution on the $N - Z$ plane

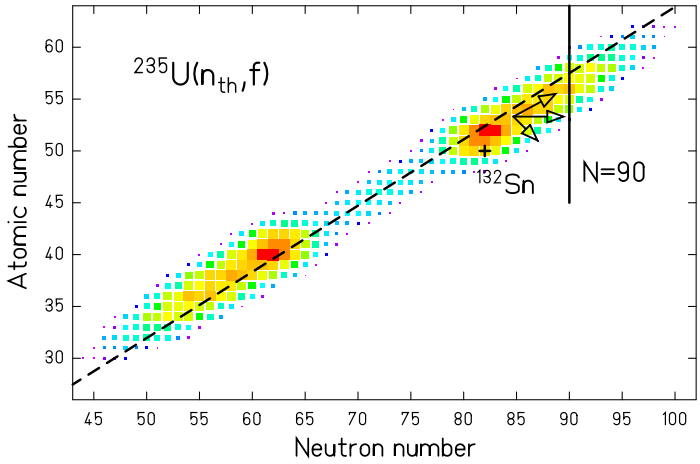

Note: Calculated nuclide distribution produced in thermal-neutron-induced fission of ^{235}U before the emission of prompt neutrons. The size of the clusters represents the yield in a logarithmic scale. The dashed line marks the nuclei with the same N/Z ratio as the fissioning nucleus ^{236}U. In addition, the position of the doubly magic ^{132}Sn and an assumed neutron shell at $N = 90$ are marked. See text for details.

mass-dependent prompt-neutron yields would not be sufficient to match the $Z_{mean} - Z_{UCD}$ values of the measured post-neutron nuclide distribution. In order to be consistent with the systematics of mass-dependent prompt-neutron yields, a charge polarisation of 0.32 units in $Z_{mean} - Z_{UCD}$ of the pre-neutron nuclide distribution, essentially constant over the whole mass range, before the prompt-neutron emission, must be assumed. Since it is further assumed that the fission process of all actinides is caused by essentially the same fragment shells, this polarisation is expected to be the same in the asymmetric fission channels for all systems.

The fine structure in the curves in Figure 10 results from the even-odd fluctuations in the fission-fragment yields as a function of atomic number Z and neutron number N.

Figure 9 illustrates the origin of this charge polarisation. The additional binding energy of spherical nuclei in the S1 fission channel in the vicinity of the $N = 82$ and the $Z = 50$ shells increases when approaching the doubly magic ^{132}Sn. This explains, why the fragments in the S1 fission channel tend to be more neutron-rich than expected from the optimisation of the macroscopic energy. The charge polarisation of the fragments with deformed shape in the S2 fission channel is explained by the force caused by a shell around $N = 90$. This force can be decomposed in a force towards mass asymmetry and a force towards higher N/Z values at constant mass as illustrated in Figure 9. Since the curvature of the binding energy against charge polarisation is much larger than the curvature of the macroscopic potential for mass-asymmetric distortions, the displacement of the mass

peak from symmetry ($\Delta A = 140\text{-}118 = 22$) is much larger than the displacement in charge polarisation (0.32 units).

Figure 10: Mean nuclear charge for fixed fragment mass

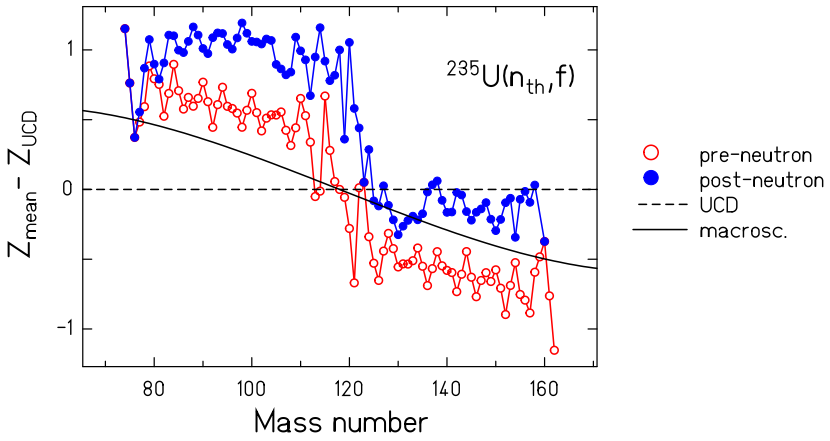

Note: Mean nuclear charge of isobaric chains for different cases for the system ^{235}U(n$_{th}$,f). Dashed line: UCD value. Full line: Macroscopic value at scission. Open symbols: Values before prompt-neutron emission as a function of pre-neutron mass. Full symbols: Values after prompt-neutron emission as a function of post-neutron mass.

This reasoning indicates that the S2 fission channel is mainly caused by a deformed neutron shell, because a proton shell in the heavy fragment would induce a charge polarisation in the opposite direction. Thus, the finding of an almost constant position in atomic number of the asymmetric fission component in the actinides cannot be attributed to a proton shell. It must rather be considered as the result of other influences, e.g. of the competition with the macroscopic potential or additional shells in the light fragment.

3.5 Quantum oscillators of normal modes

There is a long tradition in applying the statistical model to nuclear fission [60, 61, 62, 53]. However, it is well known [63] that the statistical model, applied to the scission-point configuration, is unable of explaining the variances of the mass and energy distributions and their dependence on the compound-nucleus fissility parameter. Studies of Adeev and Pashkevich [14] suggest that dynamical effects due to the influence of inertia and dissipation can be approximated by considering the properties of the system at an earlier time. That means that the statistical model may give reasonable results if it is applied to a configuration that depends on the typical time constant of the collective coordinate considered.

The potential U in the vicinity of a minimum as a function of a collective coordinate q is approximated by a parabola:

$$U = \frac{1}{2} C q^2 \tag{19}$$

Thus, the motion along the collective coordinate q corresponds to an excited state of an harmonic quantum oscillator. In an excited nucleus, there is an exchange of energy between the specific collective and all the other nuclear degrees of freedom that may be considered as a heat bath. In thermal equilibrium, the properties of the heat bath (e.g. state density and temperature T) determine the probability distribution of excited states of the harmonic oscillator considered. The probability distribution along the coordinate q is the sum of the contributions from different excited states of the oscillator:

$$P(q) = \sum_{0}^{i_{max}} W_i |\phi(q)|^2, \tag{20}$$

where W_i is the population probability of the state i of the oscillator with excitation energy $E_i = i \cdot \hbar\omega$. The upper limit i_{max} is given by the available energy of the system. If the temperature of the heat bath does not depend on the energy of the nucleus and if the energy of the nucleus is appreciably higher than the temperature of the heat bath, the solution is a Gaussian distribution with the variance:

$$\sigma_q^2 = \frac{\hbar\omega}{2C} \coth(\frac{\hbar\omega}{2T}). \tag{21}$$

Two limiting cases are the width of the zero-point motion:

$$\sigma_q^2 = \frac{\hbar\omega}{2C} \tag{22}$$

and the classical limit for $T >> \hbar\omega$:

$$\sigma_q^2 = T/C \tag{23}$$

The evolution of the width of the mass distribution of the symmetric fission channel at higher excitation energies, where shell effects are essentially washed out, has been the subject of many experimental and theoretical investigations, see refs. [64, 14, 65, 66]. It was found that the width of the mass distribution varies with energy E according to the relation $\sigma_q^2 = \frac{\sqrt{E/a}}{C}$ that corresponds to the classical limit with the temperature defined by the Fermi-gas nuclear level density. The values and the variation of the stiffness parameter C as a function of Z^2/A agree with theoretical estimations of the stiffness for mass-asymmetric distortions for a configuration between saddle and scission [66].

A more refined consideration is needed for understanding the mass distribution of a fission channel in asymmetric fission at energies little above the fission barrier. Here, the fission valley is formed by a shell effect, which also influences the level density. The

Figure 11: Widths of the asymmetric fission channels

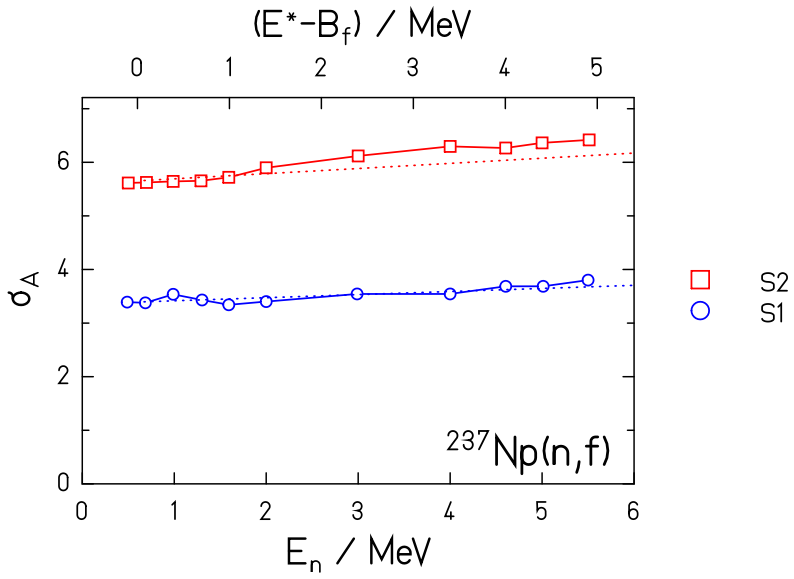

Note: Standard deviation of the mass distribution of the asymmetric fission channels (standard 1 and standard 2) in the fission of ^{237}Np(n,f) as a function of the neutron energy E_n (lower scale) and the excitation energy above the outer barrier (upper scale). The measured data [67] (symbols) are compared with the calculated widths of the corresponding quantum oscillators (dotted lines).

restoring force $F(q)$ of the corresponding oscillator is defined by the variation of the entropy S:

$$F(q) = T\frac{dS}{dq}, \tag{24}$$

and the effective potential $U(q)$ is obtained by integration:

$$U(q) = \int F(q)dq. \tag{25}$$

The stiffness C in the vicinity of the potential minimum is given by the second derivative:

$$C = d^2U/dq^2. \tag{26}$$

In Figure 11, the measured increase of the standard deviation of the mass distribution of the asymmetric fission channels (standard 1 and standard 2) [67] is compared with the result of a numerical calculation on the basis of the level-density description presented in Section 3.2.

The situation is again different for the charge-polarisation degree of freedom. Here, the potential is dominated by the macroscopic contribution. In addition, the zero-point

energy is so high that the quantum oscillator is not excited in low-energy fission [68, 69]. Therefore, the width of the charge polarization is essentially a constant value. That does not mean that the observed width of the isotopic or isobaric distributions is a constant, because it is broadened by neutron evaporation.

In the GEF code, the widths of the corresponding observables are described with analytical expressions that represent the physics ideas mentioned above.

3.6 Fission-fragment angular momentum

The empirical data on fission-fragment angular momenta mostly rely on the relative yields of fission fragments in their isomeric states and on the multiplicity of prompt gamma rays. Methods for deducing the original angular-momentum distributions from these data rely on the modelling of the statistical decay of the excited fragments by neutron emission and gamma de-excitation. The analysis of isomeric yields needs to estimate the angular momentum carried away by the neutrons and the gammas before reaching the isomer [70, 71]. The analysis of the gamma multiplicity relies on the distinction of statistical (dipole) and rotational or vibrational (quadrupole) radiation [72].

The mechanism that is responsible for creating the angular momenta of the fission fragments has long been controversially discussed. The thermal excitation of angular-momentum-bearing modes [64, 73, 74] within the statistical model requires temperatures as high as 2 or 3 MeV [75] that might only be possible if strong coupling between collective degrees of freedom and weak coupling to intrinsic degrees of freedom is assumed. This is in contradiction to large single-particle excitations found in near magic nuclei [76]. The pumping of fragment angular momenta by the zero-point motion of these modes has been found to explain the measured values [73, 77], however with the exception of spherical fragments in the vicinity of the doubly magic ^{132}Sn. Also, the torque by electrostatic repulsion between deformed fragments at scission has been considered [78, 73].

Recently, Kadmensky came up with an idea that seems to solve these problems: He pointed out that the assumption, often implicitly made, that the orbital angular momentum of the fission fragments is essentially zero, is in conflict with the uncertainty principle [79]. He assumes that the fluctuation of the orbital angular momentum according to the quantum-mechanical uncertainty is the true principal origin of the fission-fragment angular momenta. The orbital angular momentum is compensated by the fragment angular momenta, eventually also with single-particle excitations in spherical nuclei. The angular momentum $J_1 + J_2$ is shared between the two fragments according to the ratio of their momenta of inertia I_1 and I_2 in order to minimise the energy expense $E_{rot} = J_1^2/(2I_1) + J_2^2/(2I_2)$.

Since Kadmensky did not derive a quantitative formulation of his idea, the following semi-empirical description for the spin distribution of one fragment is used:

$$N(J) = (2J+1)\exp(-\frac{J(J+1)}{2b})^2 \tag{27}$$

The cut-off parameter b is related to the r.m.s. spin value by $J_{rms} = b/\sqrt{2}$ that is given by:

$$J_{rms} = \sqrt{2 I_{eff} T_{eff}} \tag{28}$$

The effective temperature

$$T_{eff} = \sqrt{T_{nuc}^2 + T_{zpm}^2} \tag{29}$$

considers in a simple way the effect of the zero-point motion of the orbital angular momentum by the parameter T_{zpm} and the effect of thermal excitations by the nuclear temperature T_{nuc}, defined by the energy-dependent nuclear level density.

The reduction of I_{eff} in the pairing regime:

$$I_{eff} = I_{rigid} \cdot (1 - 0.8 \cdot \exp(-0.693 E_{exc}/(5\ \mathrm{MeV}))), \tag{30}$$

of the rigid-body momentum of inertia of a fragment with mass number A_f with deformation α at scission [80]:

$$I_{rigid} = (1.16/\mathrm{fm})^2 \cdot A_f^{5/3}/(103.8415\ \mathrm{MeV}/\hbar^2) \cdot (1 + 1/2 \cdot \alpha + 9/7 \cdot \alpha^2). \tag{31}$$

is considered.

The initial spin distribution of the fissioning nucleus is included by considering the r.m.s. value J_{CN} in a classical approximation:

$$J_{rms} = \sqrt{2 I_{eff} T_{eff} + J_{CN}^2} \tag{32}$$

In spontaneous fission, J_{CN} is the ground-state spin J_0. In induced fission, it is the value of the entrance channel. Thus, in neutron-induced fission, the influence of the spin and the orbital angular momentum of the incident neutron (centre-of-mass energy E_{cm}) and the spin of the target nucleus J_0 is given by:

$$J_{CN} = \sqrt{J_0^2 + (1/2)^2 + (0.1699 A^{1/3} \sqrt{E_{cm}/\mathrm{MeV}})^2} \tag{33}$$

Finally, the observed enhancement of the angular momenta of odd-Z fission fragments[4] is considered by increasing J_{rms} by the amount $F_{odd} \cdot A_f^{2/3}$, which depends on the fragment mass A_f. This description has two parameters: $T_{zpm} = 0.8$ MeV is adjusted to the magnitude of measured fission-fragment angular momenta, and $F_{odd} = 0.0148$ is deduced from ref. [81].

For calculating the isomeric yields, once the angular-momentum population of the fragments is given, the de-excitation cascade by neutron evaporation and gamma emission should be calculated with full knowledge of the spectroscopic properties and the decay paths of all fission fragments. Since this knowledge is not available, the GEF model applies

[4]We would also expect an even-odd staggering of the fragment angular momentum in neutron number. However, this effect is not easily observable, because it is washed out by the fluctuations in the prompt-neutron emission.

a simple description, following the ideas of refs. [70, 71]. In the angular-momentum range considered, the emission of neutrons and statistical photons does not modify the angular-momentum distribution on the average. Therefore, the initial spin distribution of the fragments is assumed to be preserved until the entrance line is reached, where E2 radiation takes over. These transitions are assumed to follow essentially the yrast line towards the nuclear ground state. A certain isomeric state, or eventually the ground state, is assumed to be fed by the angular-momentum range on the entrance line between the angular momentum of the state considered and the next-higher isomeric state, or above the highest isomeric state, respectively. This procedure substantially differs from the often used descriptions of Madland and England [82] and of Rudstam [83]. Madland and England do not consider the preferred direction of the E2 transitions towards lower-lying states. Rudstam emphasises the change of the fragment spin due to E1 radiation, which is in conflict with refs. [70, 71], and, in our opinion he overestimates the possibility that neutron evaporation inhibits the population of high-energy isomers, because most fission fragments have initial excitation energies sufficiently above the yrast line in the angular-momentum range considered.

3.7 Energetics of the fission process

In low-energy fission, the available energy, consisting of the Q value of the reaction plus the initial excitation energy of the fissioning nucleus, ends up either in the total kinetic energy (TKE) or the total excitation energy (TXE) of the fragments. Moreover, the TXE is divided between the two fission fragments. In the GEF code, these values are not parametrised directly. In accordance with the general character of the model, the exchange of the available energy between the different degrees of freedom of the fissioning system is described along the fission path. This way, a consistent and complete description of all phenomena is obtained that depend on the energetics of the fission process. A schematic presentation of the evolution of the fissioning system is shown in Figure 12.

3.7.1 From saddle to scission

It is assumed that the energy available above the outer saddle (initial excitation energy of the fissioning nucleus minus the height of the outer fission barrier) is thermalised [11]. This implies that the available energy above the fission barrier is equally shared between the different degrees of freedom. Most of the available states are intrinsic excitations. Thus, most of the excitation energy available above the outer saddle is stored in intrinsic excitations. The intrinsic excitation energy grows on the way from saddle to scission, because part of the potential-energy release is dissipated into intrinsic excitations. Two-centre shell-model calculations documented in Figure 12 of ref. [12] show that there are many level crossings on the first section behind the outer saddle. Afterwards, the single-particle levels change only little. Level crossings lead to intrinsic excitations [85]. Consequently, the additional excitation energy is mostly dissipated in the vicinity of the

Figure 12: Energetics of the fission process

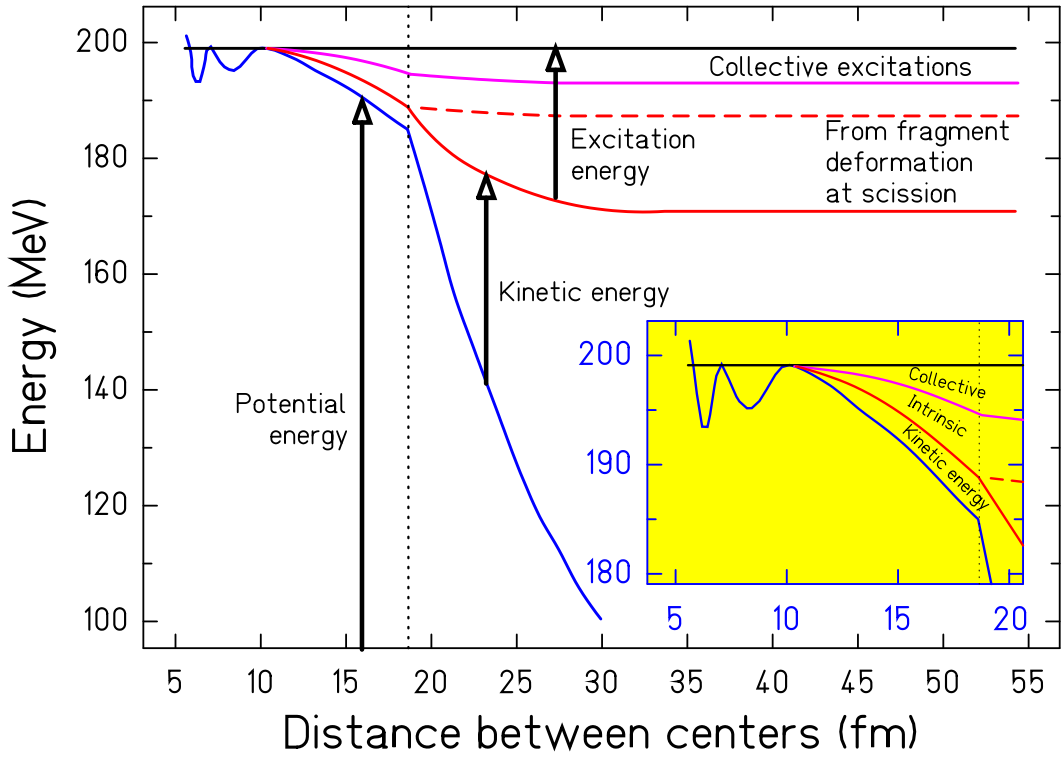

Note: Schematic presentation of the different energies appearing in the fission process (from [84]). The vertical dotted line indicates the scission point. The inset illustrates that the energy release due to the decreasing potential energy is partly dissipated into excitations of collective normal modes and intrinsic excitations. The remaining part feeds the pre-scission kinetic energy. The main figure demonstrates that the excitation energy of the fragments still increases right after scission, because the excess surface energy of the deformed fragments with respect to their ground states becomes available. Later also the collective excitations are damped into the intrinsic degrees of freedom. The figure represents the fission of ^{236}U with an initial excitation energy equal to the fission-barrier height.

outer saddle. The dissipated energy increases roughly with the mass of the fissioning nucleus, because the fission barrier is located at smaller deformations, and the range with a high number of level crossings is extended. Since both the deformation at the macroscopic barrier and the gain of potential energy from saddle to scission are related with the Coulomb parameter $Z^2/A^{1/3}$, the amount of dissipated energy from the outer saddle to scission is assumed to be a constant fraction of the calculated macroscopic potential energy gain from saddle to scission [86]. Additional intrinsic excitation may appear at neck rupture.

Theoretical investigations of the gradual transition from the mono-nuclear regime to

the di-nuclear system concerning shell effects [12], pairing correlations [87] and congruence energy [88] show that the properties of the individual fission fragments are already well established in the vicinity of the outer saddle. Therefore, close to the outer saddle the fissioning system consists of two well-defined nuclei in contact through the neck and a total amount of excitation energy E_{tot} that is equal to the intrinsic excitation energy above the outer saddle plus the energy acquired by dissipation on the first section behind the outer saddle. Intrinsic excitations are expected to be homogeneously distributed within the nuclear volume. This is likely to hold also in the transition from a mono-nuclear to a di-nuclear system that takes place very rapidly near the outer saddle [12]. Consequently, it is assumed that E_{tot} is initially shared among the fragments according to the ratio of their masses.

We assume that the system formed by the two nuclei in contact then evolves to a state of statistical equilibrium, the macro-state of maximum entropy, where all the available micro-states have equal probability [89]. This implies that the intrinsic excitation energy will be distributed among the two nascent fragments according to the probability distribution of the available microstates which is given by the total nuclear level density.[5]

Thus, the distribution of excitation energy E_1 of one fragment is given by the statistical weight of the states with a certain division of excitation energy between the fragments:

$$\frac{dN}{dE_1} \propto \rho_1(E_1) \cdot \rho_2(E_{tot} - E_1) \tag{34}$$

Note that ρ_1 and ρ_2 are the level densities of the fragments in their shape at scission, not in their ground-state shape. The remaining energy $E_{tot} - E_1$ is taken by the other fragment.

In the regime of pairing correlations, where the level density was found to grow almost exponentially with increasing excitation energy [88-95] energy sorting will take place, and the light fragment will transfer essentially all its excitation energy to the heavy one [98, 99]. At higher energies, in the independent-particle regime where pairing correlations die out, there is a gradual transition to a division closer to the ratio of the fragment masses according to the validity of the Fermi-gas level density.

The phenomenon of energy sorting explains in a straightforward and natural way the finding of [58] demonstrated in Figure 13 that the additional energy introduced in neutron-induced fission of ^{237}Np raises the neutron multiplicities in the heavy fragment, only. A similar result was reported for the system ^{235}U(n,f) [100], but data of this kind with good quality are scarce.

Part of the energy gain from saddle to scission may also be transferred to collective modes perpendicular to the fission direction (normal modes [101]). These excitations correspond to correlated motions of the whole system. The division between the fragments depends on the kind of collective motion. As an approximation, it is assumed that the collective excitation energy is equally shared between the fragments.

[5]The degeneracy of magnetic sub-states is not considered, because it contributes very little to the variation of the density of states as a function of excitation energy.

Figure 13: Variation of the prompt-neutron yield with excitation energy

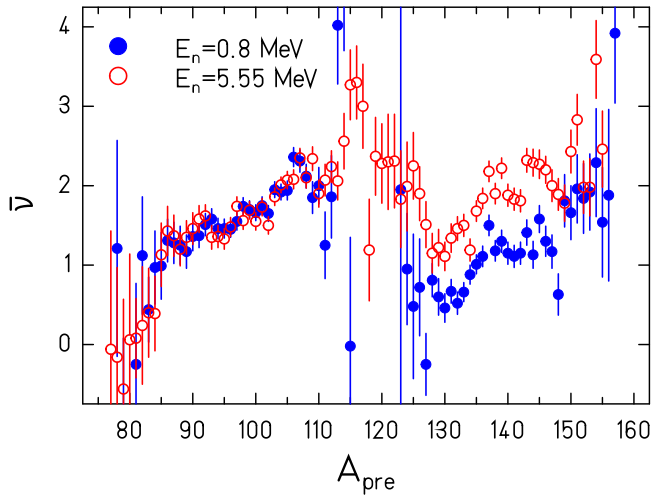

Note: Prompt-neutron multiplicity as a function of the pre-neutron fragment mass for the system ^{237}Np(n,f) for $E_n = 0.8$ MeV and 5.55 MeV [58]. (Figure from [84].)

3.7.2 Fully accelerated fragments

There is widespread agreement that the saw-tooth shape of the prompt- neutron yields (see Figure 13) is caused by the deformation energies of the nascent fragments at scission. The scission-point model of ref. [53] attributes it to the influence of fragment shells, the random-neck-rupture model [56] links it to the location of the rupture, and also microscopic calculations predict large deformation energies of the fragments near scission [102]. Large even-odd effects in the fragment Z distributions indicate that the intrinsic excitation energy at scission is generally much too low to account for the variation of the prompt-neutron yield by several units over the different fragments.

In the scission-point model of ref. [53], the deformation at scission is determined by minimising the potential energy for fixed tip distance. An alternative condition would be to require a fixed distance of the centres of mass of the two nascent fragments. The validity of one or the other case depends on the magnitude of dissipation [103]. The first case is valid in the case of strong dissipation, because the relative velocity of the fragments is slowed down by an attractive force which acts on the nascent fragments through the neck. The second case is valid for weak dissipation, where the relative velocity of the fragments reflects the action of the long-range Coulomb force between the nascent fragments. The magnitude of dissipation in low-energy fission in the regime of strong pairing correlations is a delicate problem [85]. The GEF model follows the idea of ref. [53]. In this scenario, the macroscopic forces favour fragments that are strongly deformed ($\beta \approx 0.5$ to 0.6). Thus, shell effects at these large deformations are favoured, while e.g. the influence of the ^{132}Sn

spherical shell is weakened by the macroscopic forces. According to ref. [53], this explains the weak relative yield of the standard 1 fission channel corresponding to spherical heavy fragments in the vicinity of ^{132}Sn, while the bulk of the yield of the asymmetric component is provided by the standard 2 fission channel with appreciably more strongly deformed heavy fragments.

In the GEF model, the mean deformation and the width of the different fragment shells that correspond to the different fission valleys are determined empirically by the deformation distribution of the light and the heavy fragment that is consistent with the observed prompt-neutron multiplicity distribution.

After fixing the intrinsic and the collective excitation energy at scission as well as the fragment deformation energy, the total kinetic energy is determined by energy conservation for a given A and Z split that defines the fission Q value.

The calculated two-dimensional A - E_{kin} distribution and the TKE distribution for the system ^{235}U(n$_{th}$,f) are shown in Figures 14 and 15. In addition, Figure 15 demonstrates that the numerical result of the GEF model is not well represented by a normal distribution. Deviations of measured TKE distributions from a normal distribution have already been described by Brosa et al. [56] and Zhdanov et al. [104].

Figure 14: $A - E_{kin}$ distribution

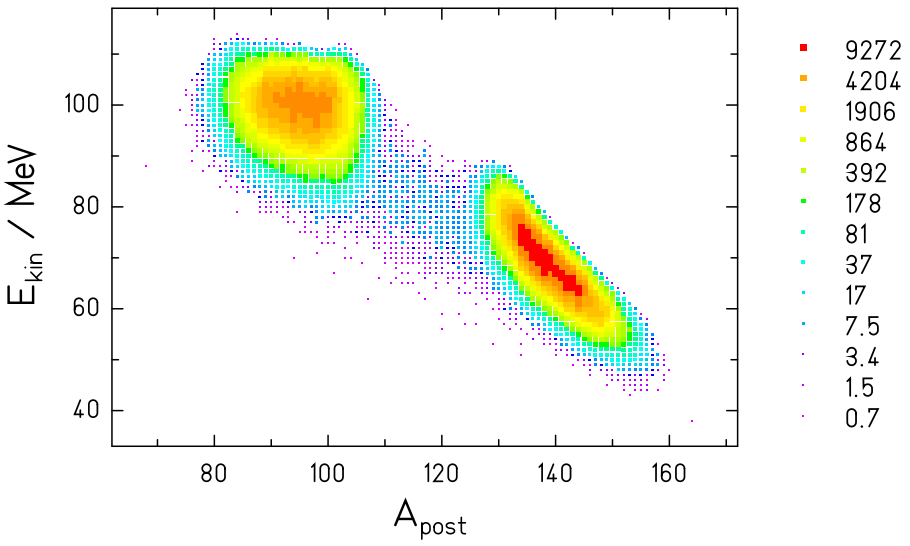

Note: Calculated 2-dimensional A - E_{kin} distribution for the system ^{235}U(n$_{th}$,f). The colour scale gives the number of events per bin.

Figure 15: TKE distribution

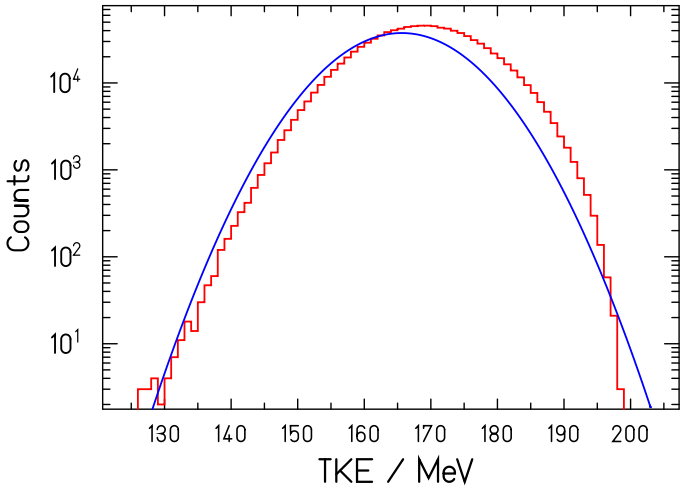

Note: Calculated post-neutron TKE distribution for the system ^{235}U(n$_{th}$,f) (histogram). The smooth curve shows a fit with a normal distribution.

3.8 Even-odd effects

Several quantities show a systematic staggering for fragments with even or odd number of protons. The most striking effect is the enhanced production of even-Z fragments, for which values up to 40% in the thermal-neutron-induced fission of ^{232}Th have been found. But also the yields of even-N fragments are found to be systematically higher. Moreover, the total kinetic energies of fragments in even-Z charge splits from even-Z fissioning systems were found to be enhanced.

3.8.1 Z distribution

The enhanced production of even-Z fragments is the most direct observation, because the number of protons in the fragments is generally not changed after scission since the probability for proton evaporation from the neutron-rich fission fragments is very low.

In the quasi-particle picture, the ground state is the only state in an even-even nucleus that is systematically lower than the states in an odd-odd nuclei on an absolute energy scale. The case of an odd-mass nucleus is in between. Therefore, we attribute the observed even-odd effect in fission fragment Z distributions to the population of the ground state or eventually some collective states in the vicinity of the ground state of even-Z fragments. It seems straightforward to attribute the observed enhanced production of even-Z light fragments [105] to the energy-sorting mechanism [106] that explained already the differential behaviour of the prompt-neutron yields [98]. If the time until scission is sufficiently

long for the energy sorting to be accomplished, the system can still gain an additional amount of entropy by predominantly producing even-even light fragments. Compared to the production of odd-odd light fragments, the excitation energy of the heavy fragment increases by two times the pairing gap, and its entropy increases due to the increasing number of available states.

The quantitative calculation of the even-odd effect is based on the assumption that the distribution of excited states in the two fragments at scission is in statistical equilibrium. This means that each state of the fissioning system is populated with the same probability.

For an even-even fissioning nucleus, the number of configurations with Z_1 even at fixed total reduced energy U_{tot} is given by:

$$N^{ee}_{Z_1=e}(Z_1) = \int_{-2\Delta_1}^{U_{tot}+2\Delta_2} \rho_1(U_1)_{(ee)}\rho_2(U_{tot}-U_1)_{(ee)}dU_1 + \tag{35}$$

$$\int_{-\Delta_1}^{U_{tot}+\Delta_2} \rho_1(U_1)_{(eo)}\rho_2(U_{tot}-U_1)_{(eo)}dU_1$$

where $\rho_i(U_i)_{(ee)}$ and $\rho_i(U_i)_{(eo)}$ are the level densities of representative even-even and even-odd nuclei, respectively, with mass close to A_1 or A_2. The reduced energy U is shifted with respect to the energy E above the nuclear ground state: $U = E - n\Delta$, $n = 0, 1, 2$ for odd-odd, odd-mass, and even-even nuclei, respectively.

The number of configurations with Z_1 odd for an even-even fissioning nucleus is:

$$N^{ee}_{Z_1=o}(Z_1) = \int_{-\Delta_1}^{U_{tot}-\Delta_2} \rho_1(U_1)_{(oe)}\rho_2(U_{tot}-U_1)_{(oe)}dU_1 + \tag{36}$$

$$\int_{0}^{U_{tot}} \rho_1(U_1)_{(oo)}\rho_2(U_{tot}-U_1)_{(oo)}dU_1$$

where $\rho_i(U_i)_{(oe)}$ and $\rho_i(U_i)_{(oo)}$ are the level densities of representative odd-even and odd-odd nuclei, respectively, with mass close to A_1 or A_2. The yield for even-Z_1 nuclei is $Y^{ee}_{Z_1=e}(Z_1) = N^{ee}_{Z_1=e}(Z_1)/N^{ee}_{tot}/(Z_1)$ with $N^{ee}_{tot}(Z_1) = N^{ee}_{Z_1=e}(Z_1) + N^{ee}_{Z_1=o}(Z_1)$. Similar equations hold for odd-even, even-odd and odd-odd fissioning systems. The total available reduced intrinsic excitation energy U_{tot} is assumed to be a fraction of the potential-energy difference from saddle to scission. Thus, it increases with the Coulomb parameter $Z^2/A^{1/3}$ of the fissioning nucleus.

This approach reproduces the observed salient features of the even-odd effect [105]: (i) The mean even-odd effect $(\Sigma Y_{Z=e} - \Sigma Y_{Z=o})$ / $(\Sigma Y_{Z=e} + \Sigma Y_{Z=o})$ decreases with the Coulomb parameter and with increasing intitial excitation energy. (ii) The local even-odd

effect
$\delta_p(Z+3/2) = 1/8(-1)^{Z+1}(\ln Y(Z+3) - \ln Y(Z) - 3[\ln Y(Z+2) - \ln Y(Z+1)])$
increases towards mass asymmetry. (iii) The local even-odd effect for odd-Z fissioning nuclei is zero at mass symmetry and approaches the value of even-Z nuclei for large mass asymmetry.

In the GEF code, an analytical function that parametrises the result of this approach with some adjustment to the measured values is used.

3.8.2 N distribution

In the GEF model it is assumed that the even-odd effect in the yields of the fission fragments as a function of the atomic number Z is also present in the yields as a function of the number of neutrons N. However, this structure cannot easily be observed. It is washed away by prompt-neutron emission, and another even-odd structure is established. This structure is generated by the influence of the neutron separation energy on the last stages of the evaporation process, which has also been observed in the cross-section of projectile fragments in reactions at relativistic energies [107, 108].

An interesting feature of the even-odd staggering of the fission-product yields in neutron number is that the structure generated by the evaporation process is not sensitive to the excitation energy of the fragments: The structure will remain unchanged with increasing excitation energy. That is in contrast to the even-odd staggering in atomic number.

3.8.3 Total kinetic energy

The even-odd effect in the Z distribution of the fission-fragment yields at constant TKE (or at constant kinetic energy of the light fragment) increases towards higher energy and decreases towards lower energy. This finding can also be expressed in a different way: The total-kinetic-energy (TKE) distributions of even-Z elements are shifted to higher values with respect to their odd-Z neighbours. The magnitude of this shift for thermal-neutron-induced fission of ^{229}Th, ^{233}U, ^{235}U, ^{239}Pu, ^{241}Pu, ^{245}Cm, and ^{249}Cf is correlated with the global even-odd effect in the Z yields. This can be deduced from the slope of the even-odd effect in the Z yields as a function of the kinetic energy of the light fragment shown in Figure 13 of [109]. In the GEF model, the even-odd fluctuation of the TKE is calculated by a simple description following an idea of ref. [59]. It is assumed that two components contribute to the even-Z yield. One component which contains at least one broken proton pair and the other where no proton pair is broken. If one proton pair is broken anywhere between the saddle and the scission point, it is assumed that the two unpaired protons will be distributed statistically on the two fragments. Therefore, the even-Z yield component with at least one broken pair is equal in amplitude to the odd-Z yield, and the energy distributions are expected to be the same, too. In contrast, the super-fluid component of the even-Z yield is shifted to higher kinetic energies. The shapes of the energy distributions of the two components of the even-Z yields are assumed to be

equal. The shift between the two components is the only free parameter of this description. The data are well described if the two components are assumed to be shifted by 1.7 MeV.

3.9 Spontaneous fission

Fission from excitation energies above or in the vicinity of the fission barrier and spontaneous fission, starting from the nuclear ground state, are very much related. Therefore, both processes must be described on a common footing. The potential-energy surface is the same.[6] The most important difference is that the passage across the barrier from the entrance point to the exit point, where the height of the potential exceeds the available excitation energy, is only possible by tunnelling in spontaneous fission.

In the GEF model, it is assumed that the exit point is located inside one of the fission valleys. Therefore, the relative yields of the fission channels are given by the relative values of the transmission coefficients, corresponding to the different fission channels. The potential energy along the fission path for ^{240}Pu is schematically shown in Figure 16. In addition to the passage over the lowest outer barrier, a second passage over another, 0.5 MeV higher, outer barrier of another fission channel is schematically shown.

By the systematics of spontaneous-fission half lives it is known that a variation of the binding energy of the fissioning nucleus (e.g. by a variation of the ground-state shell effect) by 1 MeV changes the fission half life by about 5 orders of magnitude [111, 112]. In that case, the energy deficit is modified over the whole path from entrance point to exit point. In the present case, it is only the potential around the outer barrier and beyond which is modified by the influence of fragment shells. Therefore, the relative population of the different fission valleys is much less sensitive to the magnitudes of the shell effects in the different fission valleys than the spontaneous-fission half-life is to the ground-state shell effect. A simple estimate for this sensitivity is given by the Hill-Wheeler formula, using the $\hbar\omega$ value of the outer barrier, which is in the order of 0.7 MeV [38, 113]. (We do not consider the appreciably larger value found for symmetric fission in ref. [113], which has a very low yield.) However, Figure 16 illustrates that the sensitivity is expected to be even much weaker, because the potential towards the second minimum is not affected by the shell effects that form the different fission valleys. In the GEF model, the potential energy forming the quantum oscillators in mass asymmetry inside the different fission valleys is assumed to be independent from the excitation energy of the fissioning nucleus. The sensitivity of the transmission coefficient to the influence of the shell effect that forms the fission valley is parametrised with the Hill-Wheeler formula with a $\hbar\omega$ value around 2 MeV, which is determined by a fit to the experimental fission-fragment yields in the different fission channels. In view of the above reasoning, this value that is much

[6] Note that the potential is defined as the binding energy of the nucleus in the respective shape at excitation energy zero. The driving force F in a stochastic process is given by the derivative of the entropy with respect to the collective coordinate q times the temperature: $F = TdS/dq$ [110], not by the potential. The concept of an excitation-energy-dependent potential-energy surface is only an effective way to express the properties of the level density above the potential.

Figure 16: Potential energy on the fission path

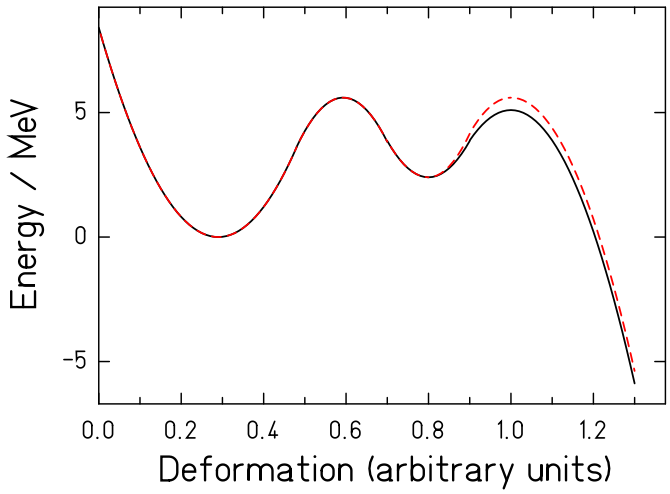

Note: Schematic drawing of the potential energy as a function of deformation in fission direction. The heights of the inner and the outer barrier as well as the depth of the second minimum are those determined for ^{240}Pu [38] (full line). The potential for another fission path with a 0.5 MeV higher outer barrier is shown in addition (dashed line).

larger than the value governing the tunnelling through the outer barrier appears to be reasonable. A theoretical estimation of the difference of the transmission for different fission channels would require a full dynamical quantum-mechanical calculation of the problem, which is not available with the necessary precision.

Another aspect in which the initial excitation energy of the fissioning nucleus matters is the energetics of the fission process. The excitation of the quantum oscillators for mass-asymmetric distortions is considered by a variation of the effective temperature. As mentioned in Section 3.5, the fluctuation of the charge polarisation is not expected to vary, because this mode is not excited in low-energy fission anyhow. A variation of the intrinsic excitation energy at scission is expected to influence the magnitude of the even-odd effect in Z yields, see Section 3.8. Unfortunately, for spontaneous fission this cannot be confirmed by experiment, because such kind of data is not available.

The description developed for the case of spontaneous fission is also used when the initial excitation energy falls below the height of the outer fission barrier of a specific fission channel. The only necessary modification to be considered is the finite initial energy of the system above the nuclear ground state.

3.10 Emission of prompt neutrons and prompt gammas

The de-excitation of the fission fragments after scission, including the acceleration phase, is obtained within the statistical model. Neutron emission during fragment acceleration reduces especially the laboratory energies of the first neutrons emitted at short times from highly excited fragments. As discussed in Section 3.8, it is assumed that both the emission of neutrons and the emission of E1 gammas do not change the angular momentum on the average, which seems to be a good approximation in the relevant angular-momentum range [70]. When the yrast line is reached, the angular momentum is carried away by a cascade of E2 gammas. A global reduction of the momentum of inertia as a function of the ground-state shell effect according to ref. [114] was applied. Inverse total neutron cross-sections with the optical-model parameters of ref. [115] were used. Gamma competition at energies above the neutron separation energy was considered. The gamma strength of the giant dipole resonance (GDR) following the description proposed in [116] was applied. The modelling of the level density of the fragments is described in Section 3.2.

4 Particle-induced fission

For practical reasons, it is desirable that the GEF code also provides a description of the processes that happen in induced fission before the formation of an excited compound nucleus. The technically most important reaction is the interaction of a neutron with a heavy nucleus.

Neutrons with energies below a few MeV are absorbed, forming a compound nucleus with an excitation energy equal to the full centre-of-mass energy. Interactions at higher energies are characterised by the interaction of the incoming neutron with another nucleon and successive interactions of the excited nucleons with more and more nucleons of the heavy nucleus. The single-particle configurations develop by more and more complex patterns towards an equilibrated compound nucleus. During this process, some of the excited nucleons may be emitted.

The basic idea for the description of this pre-equilibrium emission is the evolution of the system towards an increasing number of excited particles and holes (excitons). Particles are emitted from each of these configurations with a characteristic energy spectrum and with essentially equal probability [117].

More sophisticated pre-equilibrium models were developed, e.g. refs. [118, 119, 120], which describe the spectra of the emitted nucleons and eventually also of light clusters with better quality, often with specific empirical adjustments.

Guided by elaborate calculations [121], the probability of pre-equilibrium neutron emission (P_{pe}) up to $N_{exciton} = 10$ and statistical emission (P_{stat}) is assumed to follow a linear dependence as a function of the incident-neutron energy E_{in}:

$$P_{pe}/P_{stat} = (E_{in}/(MeV) - 2)/30. \tag{37}$$

The shape of the pre-equilibrium neutron spectrum is essentially given by:

$$dN/dE_n \sim v_n \cdot (E_{in} - E_n)^{N_{exciton}}. \tag{38}$$

(v_n is the velocity of the emitted neutron.) This simple description represents the influence of pre-equilibrium emission on the prompt-neutron spectrum and the fission-fragment yields for a fixed incident-neutron energy rather well.

Another aspect of particle-induced fission is the spin distribution of the entrance channel. This aspect is described in Section 3.6.

5 Multi-chance fission

If the excitation energy of a heavy nucleus is high enough that the excitation energy after particle emission falls near or above the fission barrier of the daughter nucleus, the observed fission events are a mixture from the fission of the mother (first-chance fission) and of the daughter nucleus (second-chance fission). With increasing excitation energy, also the fission of the grand-daughter nucleus begins to contribute (third-chance fission), and so on. For the GEF code, it is important to know the relative contributions of the different chances.

Modelling of multi-chance fission requires calculating the competition between particle and gamma decay and fission as a function of excitation energy and angular momentum for determining the relative contributions of the different nuclei and the corresponding excitation-energy distributions at fission. Moreover, the variation of the fission characteristics, e.g. the nuclide distributions, needs to be described. Both topics are described in other sections of this report. Figure 17 shows the calculated relative contributions of the different fission chances to the fission events in the system ^{235}U(n,f) as a function of the energy of the incident neutron.

The excitation energies at fission corresponding to the different fission chances are shown in Figure 18 for the system ^{235}U(n,f) at E_n = 14 MeV.

Figure 17: Probabilities of fission chances

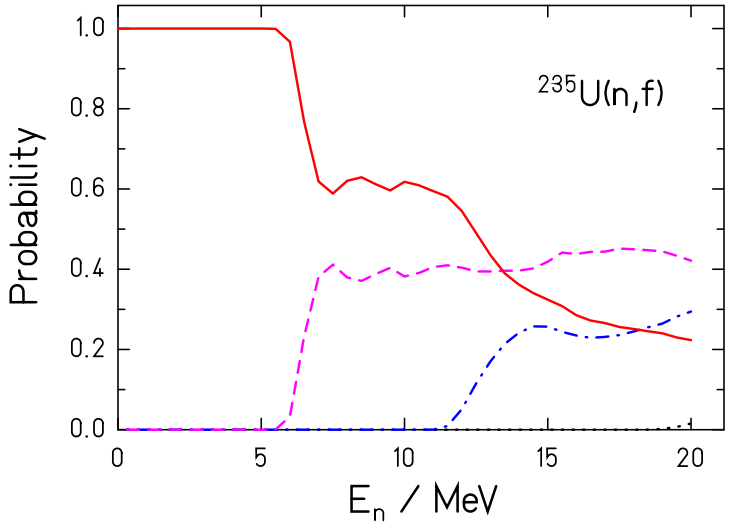

Note: Relative contributions of the different fission chances to the fission events of the system ^{235}U(n,f) as a function of the energy of the incident neutron. Full line: first-chance fission, dashed line: second-chance fission, dot-dashed line: third-chance fission.

Figure 18: Excitation energies at fission

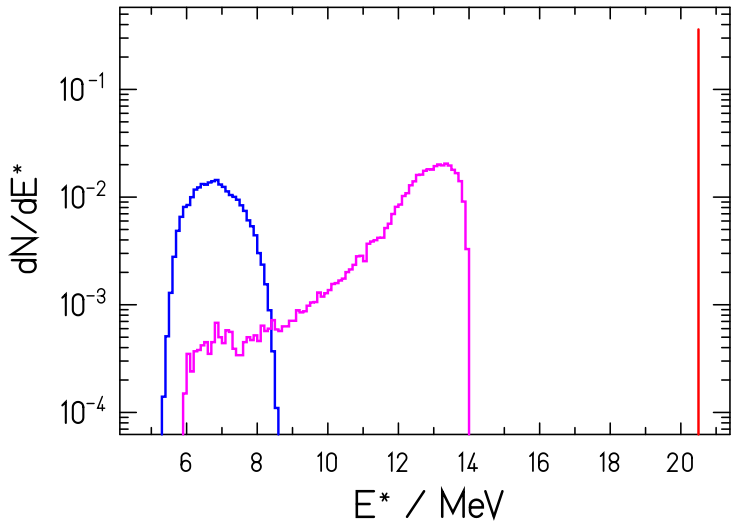

Note: Distribution of excitation energies at fission for the system ^{235}U(n,f) at E_n = 14 MeV. The rightmost peak shows events from first-chance fission (fission of ^{236}U), the middle curve corresponds to second-chance fission (fission of ^{235}U), and the left curve corresponds to third-chance fission (fission of ^{234}U).

Detailed information on the characteristics of multi-chance fission, in particular at the threshold energies where a new fission chance opens, is very scarce, because there exist no comprehensive high-precision data on nuclide distributions with a fine grid of excitation energies.

6 Parameter values

According to the concept of the GEF model, a number of parameters were determined from a systematic analysis of empirical data. In the following, the parameters that are relevant for the physics of the model are listed. Some details of predominantly technical interest are not documented in full detail. They may be searched for in the open source of the code [54].

6.1 Positions of the fission channels

The mean positions of the shell-stabilised heavy fragments of the different fission channels in thermal-neutron-induced fission are given by the following empirical relations:

For the S1 channel:

$$\bar{Z}_{S1} = 51.5 + 25 \cdot (\frac{Z_{CN}^{1.3}}{A_{CN}} - 1.5) \tag{39}$$

For the S2 channel:

$$\bar{Z}_{S2} = 53.4 + 21.67 \cdot (\frac{Z_{CN}^{1.3}}{A_{CN}} - 1.5) \tag{40}$$

For the S3 channel:

$$\bar{Z}_{S3} = 58.0 + 21.67 \cdot (\frac{Z_{CN}^{1.3}}{A_{CN}} - 1.5) \tag{41}$$

The exact position of the shell around $Z = 42$ in the light fragment that enhances the yield of the S1 channel in fissioning nuclei around Pu is:

$$\bar{Z}_{light} = 42.15. \tag{42}$$

The shell in the light fragment that enhances the yield of the S3 channel in fissioning nuclei around Cf has a slightly different position:

$$\bar{Z}_{light} = 39.7. \tag{43}$$

These two values probably refer to the same shell. In addition to the uncertainties of this analysis, the displacement can be explained by the correlation between particle number and deformation for deformed shells as discussed in Section 6.4. The spherical heavy fragment of the S1 channel induces a stronger Coulomb force and thus drives the light fragment to larger deformation and the shell to larger particle number than the strongly deformed heavy fragment of the S3 channel. When this shell in the light fragment meets one of the shells in the heavy fragment, it enhances the yield of the corresponding fission channel, but it is apparently too weak to shift its position. There are indications, however, that this shell has an influence on the deformation of the light fragment at scission, see Section 6.4.

According to the assumption that fragment shells are behind the structural effects that form the fission valleys, this is the same fragment shell, which creates the double-humped fission-fragment mass distributions for several fissioning systems around $Z = 80$ [49, 51, 50].

The positions of the fission channels in fragment mass vary with increasing excitation energy. They are determined by maximising the level density in the mass-asymmetry degree of freedom, considering the macroscopic potential in mass-asymmetry and the shell effects.

6.2 Widths of the fission channels

The shape of the potential for mass-asymmetric distortions at the moment of freeze-out of this degree of freedom is the sum of the macroscopic and the microscopic contribution. All these contributions are approximated by parabolas $U = U_0 + c \cdot (Z - Z_0)^2$ in the vicinity of their minima, except for the S2 fission channel, where the potential has a more complex shape. The values of the stiffness coefficients c are listed in Table 4.

Table 4: Stiffness coefficients

macroscopic	S1	S3	$Z \approx 42$
systematics [15]	0.30	0.076	0.28

Note: Stiffness coefficients of the different contributions to the potential for mass-asymmetric distortions at freeze out of this degree of freedom. The stiffness of the macroscopic potential depends on the system. It is taken from ref. [15].

The shell that forms the S2 channel is parametrised as a rectangular distribution in particle number with a width of $\Delta Z = 5.6$. The borders are smoothed by a parabolic shape with $c = 0.174$ at the lower side and with $c = 0.095$ at the upper side. This is technically performed by convoluting the rectangular distribution with two Gaussian distributions with different width around the two borders of the rectangle. This kind of shape is consistent with the general feature of deformed shells obtained from shell-model calculations [52,54], which show an extended valley in the 2-dimensional plane of particle number and deformation that starts at a specific particle number at small deformation and extends to a larger particle number at large deformation with a rather constant amount of additional binding over the whole range.

6.3 Strength of the fragment shells

The strengths of the fragment shells are listed in Table 5. These values refer to the configuration, where the population of the fission valleys is determined. This is assumed to be the case little behind the outer fission barrier. The strength of the shell behind the

S1 fission channel varies as a function of neutron excess, because it is created by both, the $Z = 50$ and the $N = 82$ shells. Thus, its strength decreases if the N/Z ratio of the fissioning system deviates from the one of the doubly magic ^{132}Sn.

$$\delta U_{eff} = -1.8 \cdot (1 - 4.5 \cdot |82/50 - N_{CN}/Z_{CN}|) \tag{44}$$

The maximum value of the effective shell strength δU_{eff} is the sum of the shell strength $\delta U = -4.6$ MeV and the expense $\Delta U_{mac} = 2.8$ MeV to be paid to the macroscopic potential due to the unfavourable spherical shape.

Table 5: Strengths of the fragments shells near the outer fission barrier.

S2	S3	$Z \approx 42$
-4.0 MeV	-6.0 MeV	-1.3 MeV

6.4 Fragment deformation

The shape of the nascent fragments at scission is assumed to be governed by a global feature that is shown by shell-model calculations [53, 55]. Although the results differ in their details, the calculations show regular patterns of valleys and ridges extending from lower particle number and smaller deformation to higher particle number and larger deformation both for neutron and proton shells. This correlation between shell-stabilised shape and size of the nucleus is assumed to govern the deformation of the fission fragments at scission and to explain the saw-tooth behaviour of the prompt-neutron yields.

The deformation of the fragments at scission is approximated by a second-order spheroid with a tip distance of 1 fm. The deformation parameter β of the heavy fragment of the S2 fission channel is parametrised as a linear function of the atomic number Z_{heavy}:

$$\beta_{heavy} = 0.0275(Z_{heavy} - 48.0). \tag{45}$$

The deformation of the light fragment of the S1 and the S2 fission channels is given by:

$$\beta_{light} = 0.0325(Z_{light} - 24.5). \tag{46}$$

We assume that this is due to a shell, roughly in the region $28 < Z < 50$. It was not possible to deduce the strength of this shell from the fission observables, but it is certainly weaker than the shells in the heavy fragment, because this shell in the light fragment does not influence the positions of the S1, S2 and S3 fission channels.

Deviating from this behaviour, the nascent heavy fragment of the S1 channel is assumed to be spherical.

The deformation parameters of the nascent fragments of the super-long (symmetric) fission channel were determined by minimising the potential energy (binding energies of the fragments plus Coulomb interaction potential) at the scission configuration.

The deformation parameter of the heavy fragment of the S3 fission channel is given by:

$$\beta_{heavy} = 0.0275(Z_{heavy} - 48.0) + 0.2. \tag{47}$$

The deformation of the light fragment of the S3 fission channel is:

$$\beta_{light} = 0.0325(Z_{light} - 24.5) - 0.1. \tag{48}$$

In all cases, oblate deformation resulting from these formulae was replaced by spherical shape ($\beta = 0$).

For fissioning nuclei around Pu, where the shell around ^{132}Sn in the heavy fragment meets the shell near $Z = 42$ in the light fragment, the deformation of the light fragment deviates from the above description. The TKE values and the prompt-neutron yields indicate that the shell near $Z = 42$ favours less deformed fragments at scission. This deviation is parametrised accordingly in the GEF code.

After scission, the Coulomb repulsion between the fragments and the condition of a quasi-fixed tip-distance are not present any more, and, therefore, the fragments snap to a less deformed shape. In this process, a certain amount of energy is liberated and adds up to the intrinsic energy of the respective fragment. This energy is assumed to be dominated by the macroscopic deformation-energy difference given by the liquid-drop model [122]. Therefore, the contribution due to shell effects is neglected. For the heavy fragments of the S1 fission channel around ^{132}Sn this is obviously a realistic assumption, because these nuclei are nearly spherical at scission and in their ground state. Thus, the shell effect, which is rather strong, does not change. The shell effects of the other fragments, typically in the order of a few MeV, are small compared to the variation of the macroscopic deformation energy, which reaches up to more than 10 MeV.

6.5 Charge polarisation

The charge polarization at scission (related to the deviation of the N/Z ratios of the fragments from the value of the fissioning nucleus) is calculated by minimising the potential energy of the corresponding scission configuration for a given mass division. In order to obtain agreement with experimental data, the mean number of protons in the light (heavy) fragment for a fixed fragment mass is reduced (increased) by 0.32 units, except for the super-long fission channel. This additional charge polarisation is attributed to the influence of fragment shells. Because the fragment shells do not depend on the fissioning system, the polarisation is assumed to be the same for all systems.

6.6 Energies and temperatures

6.6.1 Temperatures

The width σ of the distribution of the coordinate in a quantum oscillator can be expressed by an effective temperature T_Z that includes the effect of the zero-point motion:

$$\sigma = \sqrt{T_Z/C} \tag{49}$$

with

$$T_Z = \frac{\hbar\omega}{2}\coth(\frac{\hbar\omega}{2T}). \tag{50}$$

The minimum value of the $T_Z = \hbar\omega/2$ is not only specific to the collective coordinate, but, for example for the mass-asymmetry degree of freedom, also to the fission channel considered.

The temperature parameter for the symmetric fission channel that is created by the macroscopic potential is given by the parametrisation on the basis of the Fermi-gas level density of ref. [15] with a minimum value of 0.72 MeV in the constant-temperature regime. The calculation of the widths of the other fission channels, which are caused by shell effects, is more complex, see above. They are directly parametrised to reproduce the empirical values and their variation with excitation energy. The values for the quantum oscillator for the charge-polarisation degree of freedom are $\hbar\omega = 2$ MeV and stiffness coefficient $c = 3.16$ MeV (variation of Z for fixed A). The width is dominated by the zero-point motion.

6.6.2 Excitation energy at scission

The total excitation energy at scission consists of three contributions $E^*_{scission} = E^*_B + E_{diss} + E_{coll}$:

1. The initial excitation energy of the fissioning nucleus minus the height of the outer fission barrier:

$$E^*_B = E^*_{CN} - EB. \tag{51}$$

2. The intrinsic energy acquired through dissipation on the way from the barrier to scission:

$$E_{diss} = 0.35 \cdot \Delta E^{intr}_{pot} \tag{52}$$

with

$$\Delta E^{intr}_{pot}/\mathrm{MeV} = 0.08 \cdot (Z^2_{CN}/A^{1/3}_{CN} - 1358) + 11. \tag{53}$$

This is roughly 35% of the potential-energy gain from saddle to scission given in ref. [86] with a slight modification.

3. The collective energy acquired through coupling between collective degrees of freedom on the way from the outer barrier to scission:

$$E_{coll} = 0.065 \cdot \Delta E^{coll}_{pot} \tag{54}$$

with

$$\Delta E_{pot}^{coll}/\mathrm{MeV} = 0.08 \cdot (Z_{CN}^2/A_{CN}^{1/3} - 1390) + 11. \quad (55)$$

This is roughly 6.5% of the potential-energy gain from saddle to scission given in ref. [86] with a slight modification.

The dissipated energy at scission E_{diss} is assumed to fluctuate with a standard deviation of 70 %, not including negative values. The total intrinsic excitation energy at scission $E_B^* + E_{diss}$ is subject to energy sorting [98]. The collective energy E_{coll} at scission is shared equally between the fragments.

Note that the excitation-energy-dependent prompt-neutron multiplicities and total kinetic energies show that due to the lack of suitable transition states below the pairing gap ($2 \cdot \Delta$ for even-even nuclei and Δ for odd-mass nuclei), fission at excitation energies above the barrier proceeds by an effective barrier that is correspondingly higher. Therefore, E_{diss} is correspondingly reduced.

6.6.3 Deformation energy

After scission, the deformation of the nascent fragments at scission, which is described above, invokes an additional excitation energy. It is estimated by the macroscopic deformation energy [122]. The observed fluctuation of the prompt-neutron multiplicity is mostly explained by the width $\Delta\beta = 0.165$ of the distribution of the fragment deformation at scission.

6.6.4 Tunneling

Fission at energies below the outer barrier of a specific fission channel, either in the ground state or at low excitation energies, is characterised by tunneling and a reduced value of E_{diss}. The effective transmission coefficients that determine the populations of the different fission channels are calculated with the Hill-Wheeler formula. The effective $\hbar\omega$ values are expressed by effective temperature parameters $T_{eff} = \hbar\omega/(2\pi)$. Slightly different values are used for the different fission channels as listed in Table 6. The slightly larger value for the S1 channel is clearly proven by the data. It is very important for a good reproduction of the data. It may be connected with a smaller effective mass or with the more compact configuration at the scission point for this channel.

The reduced value of E_{diss} is obtained by the formula:

$$E_{diss} = 0.35 \cdot \Delta E_{pot}^{intr} \quad (56)$$

with

$$\Delta E_{pot}^{intr}/\mathrm{MeV} = 0.08 \cdot (Z_{CN}^2/A_{CN}^{1/3} - 1358) + 11 - EB + E_{CN}^*. \quad (57)$$

Also the value of E_{coll} is modified:

$$E_{coll} = 0.065 \cdot \Delta E_{pot}^{coll} \quad (58)$$

with

$$\Delta E^{coll}_{pot}/\mathrm{MeV} = 0.1 \cdot (Z^2_{CN}/A^{1/3}_{CN} - 1390) + 11 - EB + E^*_{CN}. \quad (59)$$

Table 6: Effective temperature parameter for tunneling

SL	S1	S2	S3
0.31 MeV	0.342 MeV	0.31 MeV	0.31 MeV

Note: Effective temperatures T_{eff} for the calculation of the effective transmission coefficients through the outer fission barrier.

6.7 Concluding remarks

Most of the parameters discussed in this section have a physical meaning and, thus, can be rather directly compared with results of microscopic theoretical models. Since these parameters comprise already the knowledge on systematic properties of a large number of systems, this might give a more valuable constraint than the rather complex body of direct experimental information.

Altogether, the number of about 50 parameter values from the simultaneous description of a variety of fission observables for almost 100 systems covering from spontaneous fission to fission at excitation energies of about 100 MeV is astonishingly modest. One should consider that about the same number of parameter values was used by Wahl [1] for describing only the fission-fragment yields of only one single system with his empirical description.

The physical background of the description and its simplicity give confidence that the GEF model has a good predictive power for nuclei in the neighbourhood of the cases which were used to constrain the model. Exceptions may exist due to very local structural effects.

7 Uncertainties and covariances

Experimental data or results of a model calculation are not expected to be precise. Generally they are subject to an uncertainty margin. In both cases, it is important to provide a realistic estimation of the uncertainty. However, for estimating the uncertainty of an integral derived quantity that depends on many values, e.g. a whole distribution, the knowledge of the uncertainty of individual data points is not sufficient.

Often, the variations of different data points are correlated by a contribution from a common source. A simple case for a common error source for all measured data concerned is a global normalisation. The uncertainty of the normalisation acts on all data points in a fully correlated way. In the case of an efficiency curve that is known to be smooth, the correlation will decrease with the distance between the points of interest. Also, in the calculated distribution of some observables there exist correlations between different values, but they have a different origin. If a specific property of the system is changed, this has an influence on the values of many observables. For example, a decreased dissipation strength lowers the intrinsic excitation energy at scission and raises the even-odd effect of the element yields, leading to higher yields for even-Z and lower yields for odd-Z elements. The fission-fragment yields in the same fission channel are connected by a positive correlation.

The GEF code provides uncertainties and covariance data for the element yields, the mass yields and the nuclide yields (depending on Z and A), the latter ones before and after emission of prompt neutrons. Covariances between any other pair of observables can be determined by analysing the list-mode output of the GEF code. The covariance between two observables x and y is determined by performing a large number N of calculations with different sets of parameters $\vec{p}_i = \left(\; p_1, \;\; p_2, \;\; \cdots, \;\; p_n \; \right)_i$. The index i denotes a specific set of parameters. In each set of parameters $\vec{p}_i$ the values of the different parameters are chosen randomly from a normal distribution with a central value given by the nominal parameter value of the model and a standard deviation defined by the uncertainty range of this parameter. The uncertainty range of a specific parameter of the GEF model was determined by investigating, how much the parameter value can deviate from the nominal value, until the agreement with the body of empirical data deteriorates substantially. This analysis was done with some caution, considering that the comprehensive comparison of the data with the GEF results gave occasion to distrust some of the experimental or evaluated data. The determined uncertainties are listed in Table 7. Each parameter is varied independently from the others. The covariance between the two observables x and y is defined by:

$$\mathrm{Cov}(x,y) = \sum_{i=1}^{N} \frac{(x_i - \bar{x})(y_i - \bar{y})}{N}. \tag{60}$$

x_i and y_i are the values of the observables x and y from the individual calculations with perturbed parameters, $\bar{x}$ is the mean value of the observable x and $\bar{y}$ is the mean value of the observable y of all N calculations. The values of the covariances of a set of observables, e.g. the yields of the fission-fragment Z distribution form a matrix.

Table 7: Standard deviations of perturbed parameter values

Quantity	σ	unit
Position of the shell for S1 channel	0.1	Z units
Position of the shell for S2 channel	0.1	Z units
Rectangular contribution to the width of S2 channel	0.05	Mass units
Position of the shell for S3 channel	0.1	Z units
Position of the shell at $Z \approx 42$	0.1	Z units
Shell effect at mass symmetry	0.1	MeV
Shell effect for S1 channel	0.1	MeV
Shell effect for S2 channel	0.1	MeV
Shell effect for S3 channel	0.2	MeV
Shell at $Z \approx 42$	0.05	MeV
Curvature of shell for S1 channel	5	%
Curvature of shell for S2 channel	5	%
Curvature of shell for S3 channel	5	%
Curvature of shell at $Z \approx 42$	5	%
$(\hbar\omega)_{eff}$ for tunneling of S1 channel	3	%
$(\hbar\omega)_{eff}$ for tunneling of S2 channel	3	%
$(\hbar\omega)_{eff}$ for tunneling of S3 channel	3	%
$(\hbar\omega)_{eff}$ for tunneling of channel at $Z \approx 42$	3	%
Weakening of the S1 shell with $82/50 - N_{CN}/Z_{CN}$	20	%
Width of the fragment distribution in N/Z	10	%
Charge polarization ($\bar{Z}$ for fixed A)	0.1	Z units

Note: Standard deviations of the parameter values used for determining the uncertainties and the covariances of the GEF results.

Figure 19: Covariance matrix of fragment mass yields

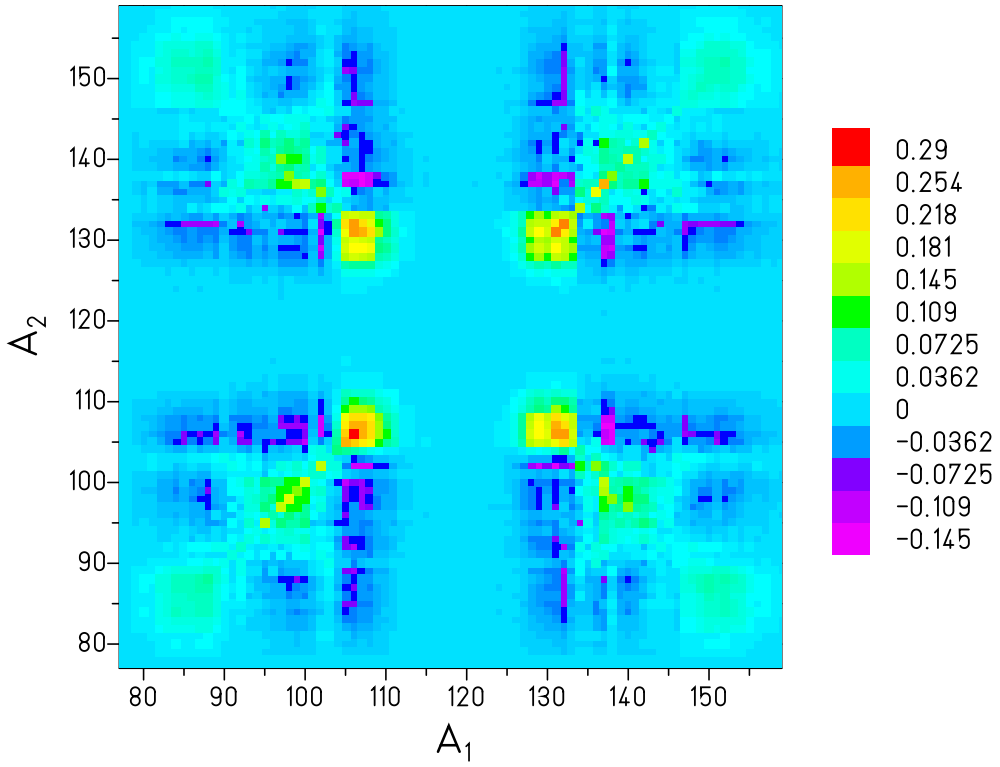

Note: Covariance matrix of the fission-fragment mass yields after prompt-neutron emission from the thermal-neutron-induced fission of ^{239}Pu.

Figure 19 shows the covariance matrix of the mass yields after prompt-neutron emission for the system ^{239}Pu(n_{th},f). The values on the diagonal from the lower-left corner to the upper-right corner show the largest positive values. They are identical with the variances of the mass yields. Also, the values from the upper-left corner to the lower-right corner are positive. These are the covariances between complementary masses. Due to emission of prompt neutrons, the largest covariance values are slightly smaller and a bit shifted from the diagonal to the left-lower side. The values of the covariances between the yields of masses from different fission channels are negative. This is a consequence of the normalisation of the yields to 200%. The post-neutron mass yields of ^{239}Pu(n_{th},f) including the error bars determined with perturbed-parameter calculations from the GEF code are compared with the evaluated data from ENDF/B-VII in Figure 20. The estimated uncertainties of the evaluated data can be seen in Figures 41 and 42.

Assuming that the model is realistic, the covariances between different observables of a model calculation provide valuable information on the inherent relations between the

Figure 20: Uncertainties of mass yields from perturbed-parameter calculations

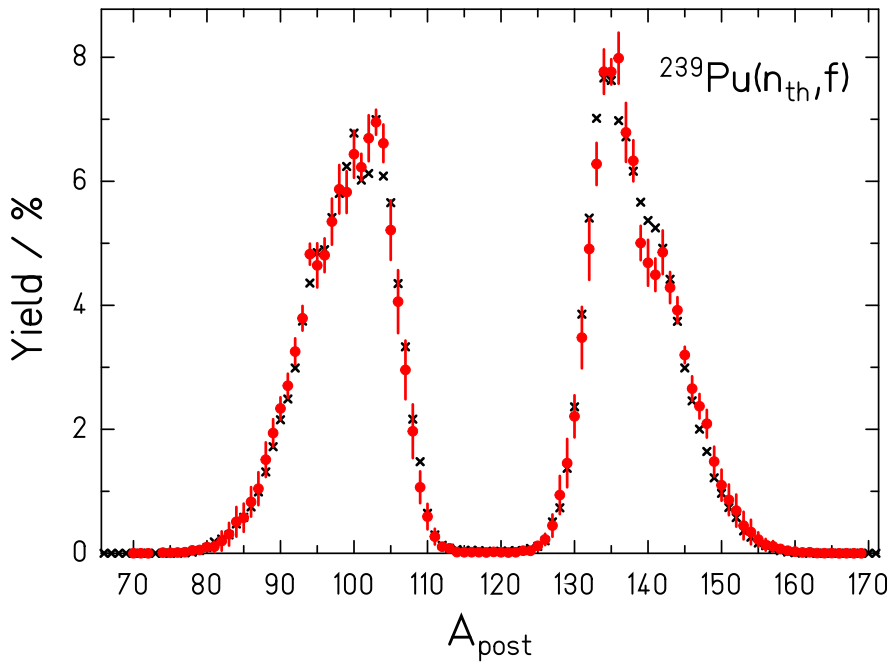

Note: Mass yields after prompt-neutron emission from the thermal-neutron-induced fission of ^{239}Pu . The GEF result (red full points) with error bars is compared with the evaluated data from ENDF/B VII (black crosses).

different observables imparted by the physics of the fission process. This information can be used as a tool to verify the consistency of experimental data and to make evaluations more efficient.

8 Assessment

8.1 Fission probability

8.1.1 Introduction

The description of fission observables above the threshold of multi-chance fission requires the knowledge of the competition between fission, neutron emission and gamma decay as a function of excitation energy and angular momentum of the compound nucleus, because they determine the relative weights of the different chances. Entrance-channel-specific pre-compound processes must eventually be considered in addition. They are not included in the present study. Since the GEF code aims for modelling the fission process in a global way without being locally adjusted to experimental data of specific systems, global descriptions of the relevant decay widths are required. This ensures that the GEF code can predict fission observables for systems for which no experimental data are available. However, this also means that specific nuclear-structure effects can only be considered in an approximate way.

8.1.2 Formulation of the fission probability

The fission probability is calculated as:

$$P_f = \Gamma_f/(\Gamma_f + \Gamma_n + \Gamma_\gamma). \tag{61}$$

The gamma-decay width is calculated by the global formula:

$$\Gamma_\gamma = 0.62410^{-9} \cdot A_{CN}^{1.6} \cdot T_i^5 MeV \tag{62}$$

proposed by Ignatyuk [46]. A_{CN} is the mass number and T_i is the temperature of the compound nucleus with energy E_i.

The neutron-decay width is calculated by the global formula:

$$\Gamma_n = 0.13 \cdot (A_{CN} - 1)^{2/3} \cdot T_n^2 / \exp(< S_n > /T_n) \tag{63}$$

proposed in ref. [123], which is valid for an exponential neutron-energy spectrum. S_n is the neutron separation energy, T_n is the maximum temperature of the daughter nucleus at the energy $E_i - < S_n >$. This expression was multiplied by:

$$1 - \exp(-(E_i - < S_n >)/(1.6 \cdot T_n)) \tag{64}$$

in order to approximately adapt to the Maxwellian shape of the neutron-energy spectrum. The use of $< S_n >= S_{2n}/2$ is another way to consider the shift of the level density by Δ and 2Δ in odd-mass and even-even nuclei, respectively, with respect to odd-odd nuclei. Γ_n is set to zero at energies below the neutron separation energy S_n.

The calculation of the fission-decay width is based on the following equations proposed in ref. [124] with a few extensions:

$$\Gamma_f = F_{rot} \cdot T_f/(G \cdot \exp(B_m/T_f)). \tag{65}$$

B_m is the maximum value of the inner fission barrier B_A and the outer barrier B_B, T_f is the temperature of the compound nucleus at the barrier B_m. $F_{rot} = exp((I_{rms}/15)^2)$ considers the influence of the root-mean square value I_{rms} of the angular-momentum distribution of the compound nucleus.

$$G = G_A \cdot \exp((B_A - B_{max})/T_f) + G_B \cdot \exp((B_B - B_{max})/T_f) \tag{66}$$

whereby G_A and G_B consider the collective enhancement of the level densities on top of the inner barrier(assuming triaxial shapes) and the outer barrier (assuming mass-asymmetric shapes) and of tunneling through the corresponding barrier:

$$G_A = F_A \cdot 0.14/\sqrt{\pi/2}, \tag{67}$$

$$F_A = 1/(1 + \exp(-(E - B_A)/T_{equi}), \tag{68}$$

$$G_B = F_B/2, \tag{69}$$

and

$$F_B = 1/(1 + \exp(-(E - B_B)/T_{equi}). \tag{70}$$

T_{equi} is related to the values of $\hbar\omega_A$ and $\hbar\omega_B$ at the inner and outer barriers by $T_{equi} = \hbar\omega/2\pi$, assuming $\hbar\omega_A = \hbar\omega_B = 0.9$ MeV.

In order to account for the low level density above B_m at energies below the pairing gap 2Δ in even-even nuclei, the value of Γ_f was multiplied at energies in the vicinity of the barrier B_m by a reduction factor that was deduced from the average behaviour of measured fission probabilities. The function is shown in Figure 21.

The collective-enhancement factors at the inner and outer barrier with respect to the daughter nucleus after neutron decay that is assumed to have a quadrupole shape (the inverse of $0.14/\sqrt{\pi/2}$ and 0.5, respectively) are assumed to fade out at higher energies, where the shape of the fissioning nucleus at scission becomes mass symmetric. They are multiplied by the attenuation factor:

$$F_{att} = \exp(0.05(E - B_A))/(1/G_A + \exp(0.05(E - B_A))) \tag{71}$$

for the inner barrier and an analogous factor for the outer barrier.

The temperature values were determined as the inverse logarithmic derivative of the nuclear level density with respect to excitation energy. The nuclear level density both in the ground-state minimum and at the fission barrier was modelled by the constant-temperature description of v. Egidy and Bucurescu [44] at low energies. The level density was smoothly joined at higher energies with the modified Fermi-gas description of Ignatyuk et al. [45, 46] for the nuclear-state density:

Figure 21: Reduction of fission-decay width

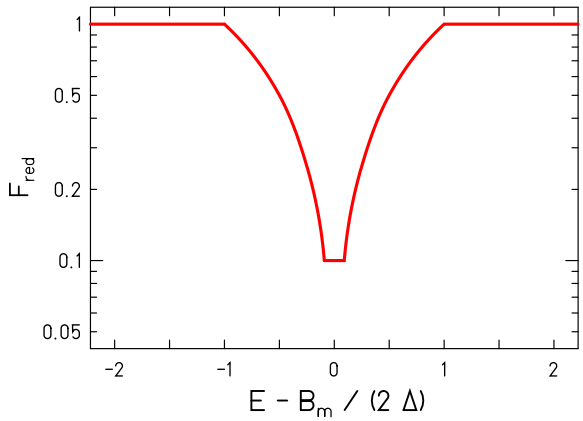

Note: Adapted reduction of the fission-decay width around the fission barrier for even-even nuclei

$$\omega \propto \frac{\sqrt{\pi}}{12\tilde{a}^{1/4}U^{5/4}} exp(2\sqrt{\tilde{a}U}) \tag{72}$$

with $U = E + E_{cond} + \delta U(1 - \exp(-\gamma E))$, $\gamma = 0.55$ and the asymptotic level-density parameter $\tilde{a} = 0.078A + 0.115A^{2/3}$. The shift parameter $E_{cond} = 2$ MeV $- n\Delta_0$, $\Delta_0 = 12/\sqrt{A}$ with $n = 0, 1, 2$, for odd-odd, odd-A and even-even nuclei, respectively, as proposed in ref. [43]. δU is the ground-state shell correction. Because the level density in the low-energy range is described by the constant-temperature formula, a constant spin-cutoff parameter was used. The matching energy is determined from the matching condition (continuous level-density values and derivatives of the constant-temperature and the Fermi-gas part). Values slightly below 10 MeV are obtained. The matching condition also determines a scaling factor for the Fermi-gas part. It is related with the collective enhancement of the level density.

The fission barriers were modelled on the basis of the Thomas-Fermi fission barriers of Myers and Swiatecki [36], using the topographical theorem of the same authors [20] to account for the contribution of the ground-state shell effect. Adjustments to measured barrier values [40] were applied. Details are described in Section 3.

8.1.3 Comparison with experimental data

Figures 22 to 30 show a survey on measured fission probabilities in comparison with the results of the GEF code. The data are taken from the following publications: [125, 126, 127, 128, 129, 130]. Some of the figures show the data from different reactions with different symbols. (See the original publications for details.)

Figure 22: Benchmark of fission probabilities, part 1

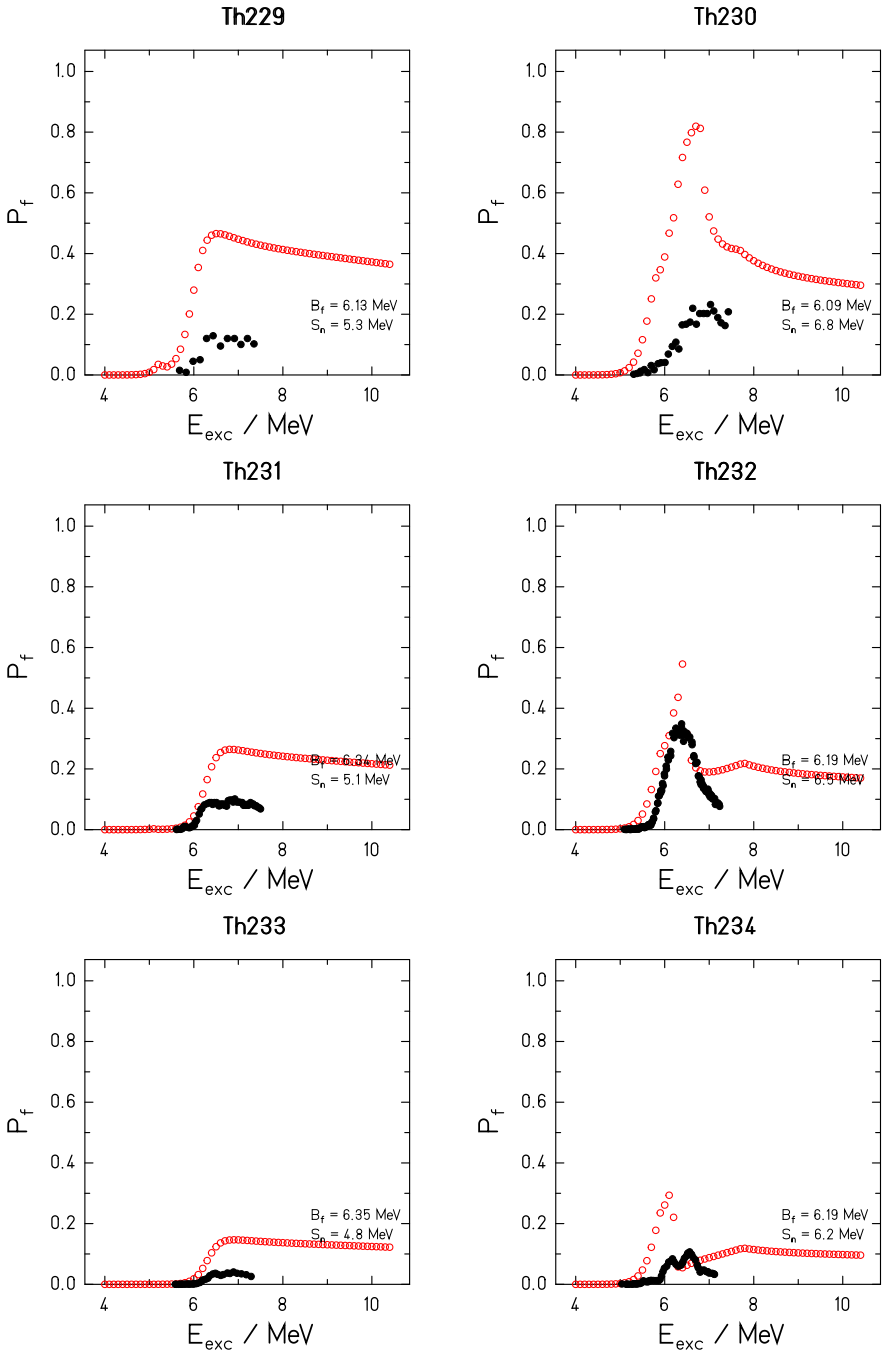

Note: Comparison of the measured fission probabilities (black symbols) with calculations with the GEF code (red symbols). The fission barrier and the neutron separation energy used in the calculations are listed.

Figure 23: Benchmark of fission probabilities, part 2

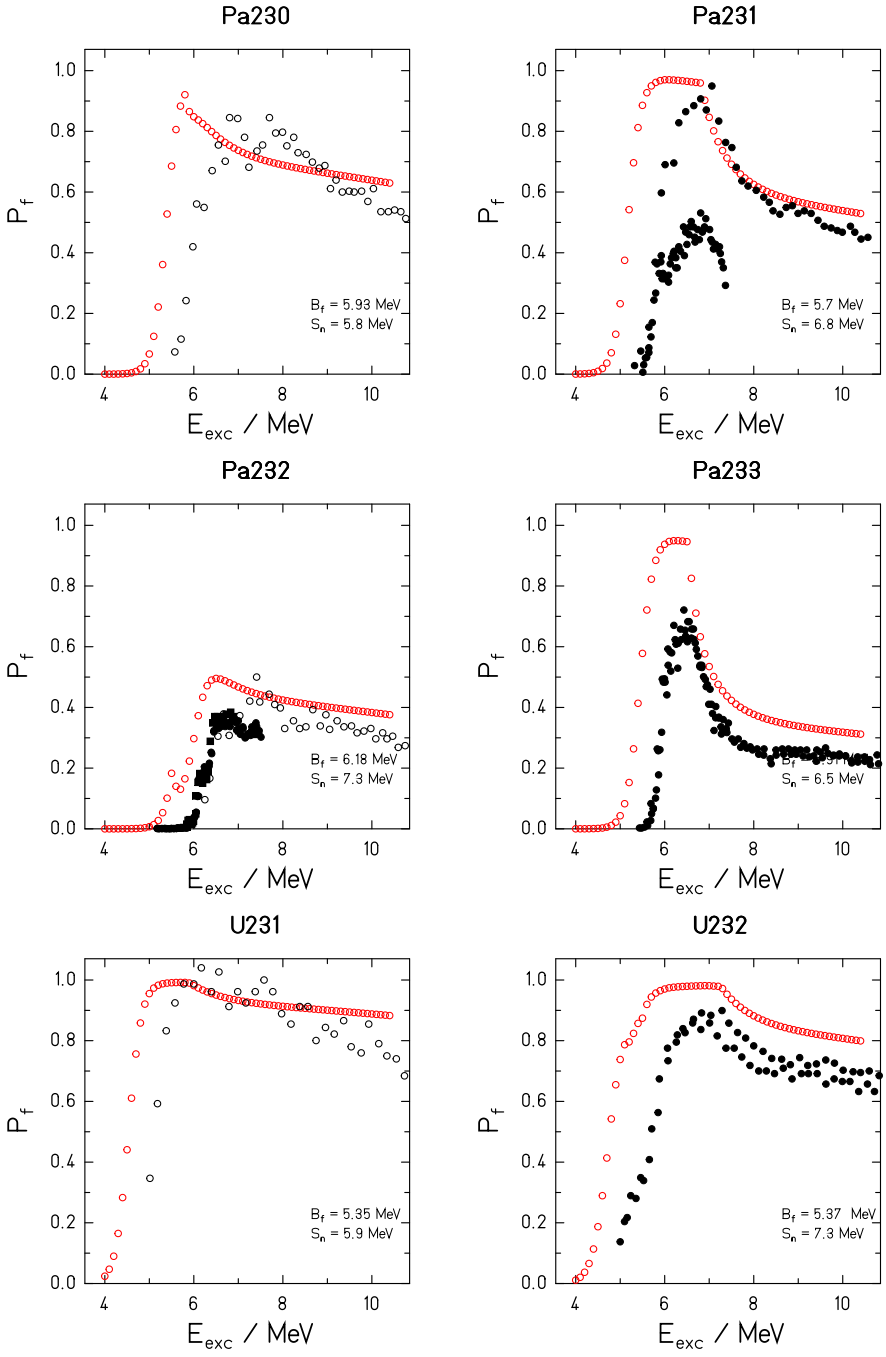

Note: Comparison of the measured fission probabilities (black symbols) with calculations with the GEF code (red symbols).

Figure 24: Benchmark of fission probabilities, part 3

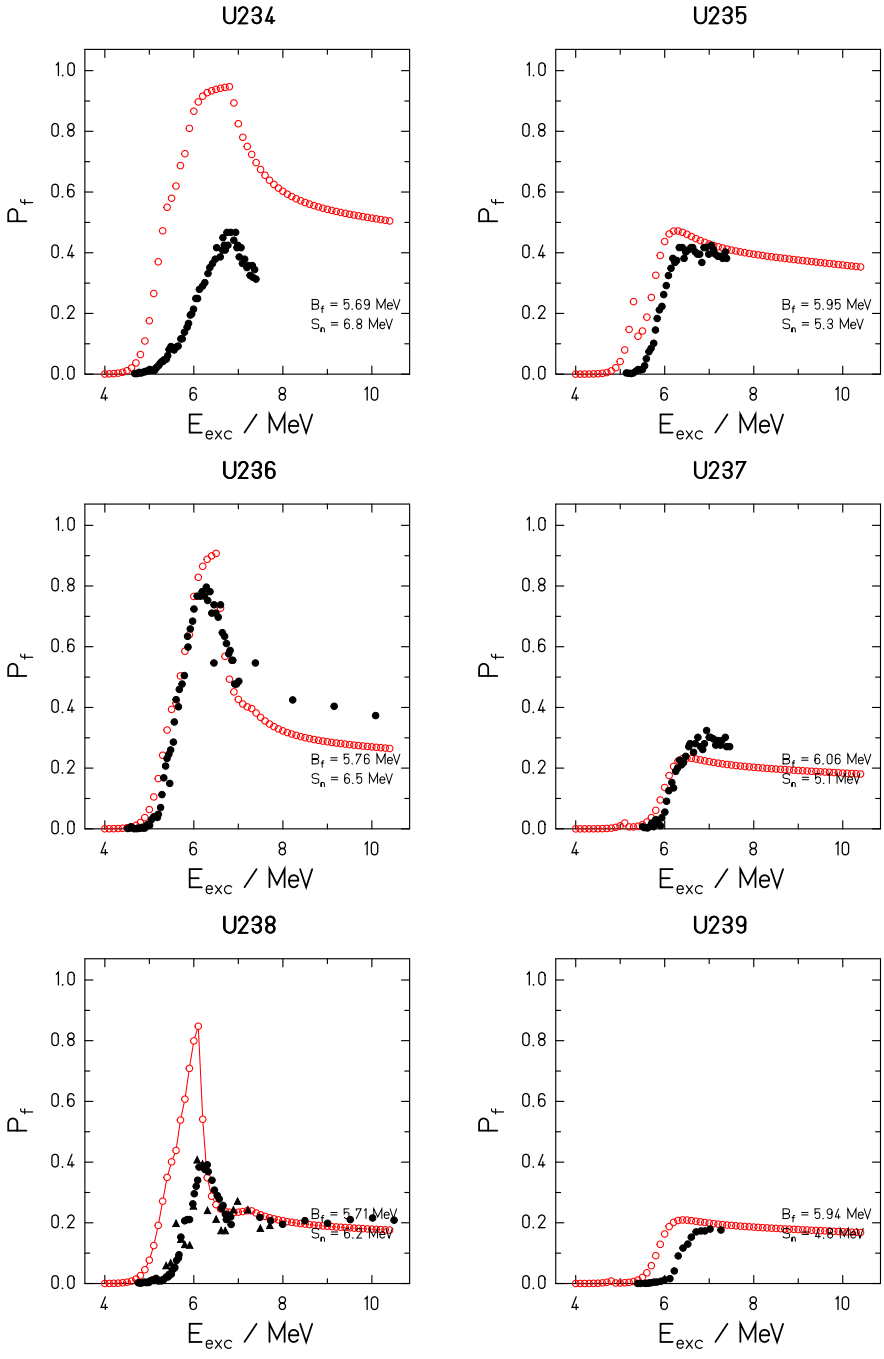

Note: Comparison of the measured fission probabilities (black symbols) with calculations with the GEF code (red symbols).

Figure 25: Benchmark of fission probabilities, part 4

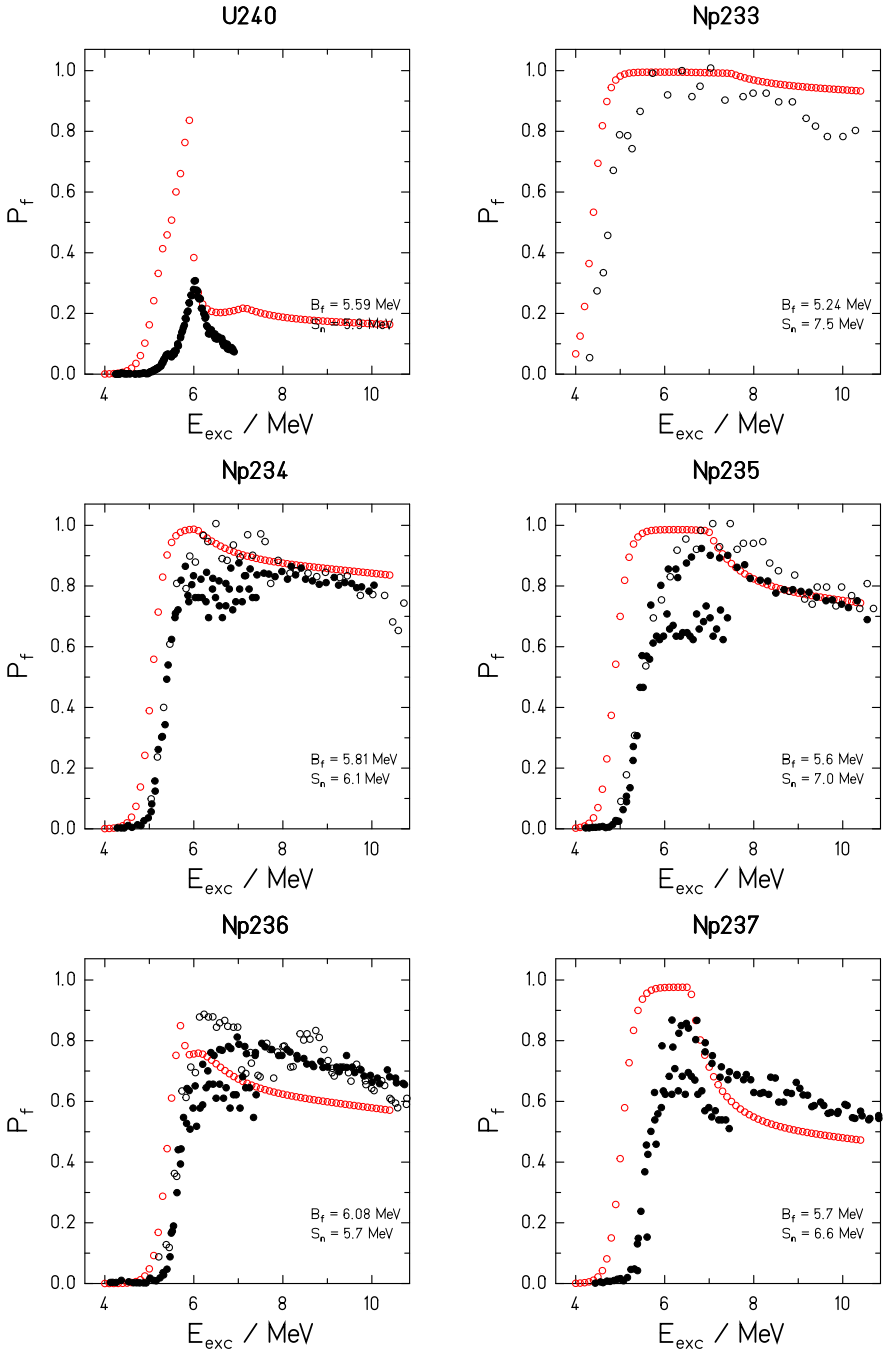

Note: Comparison of the measured fission probabilities (black symbols) with calculations with the GEF code (red symbols).

Figure 26: Benchmark of fission probabilities, part 5

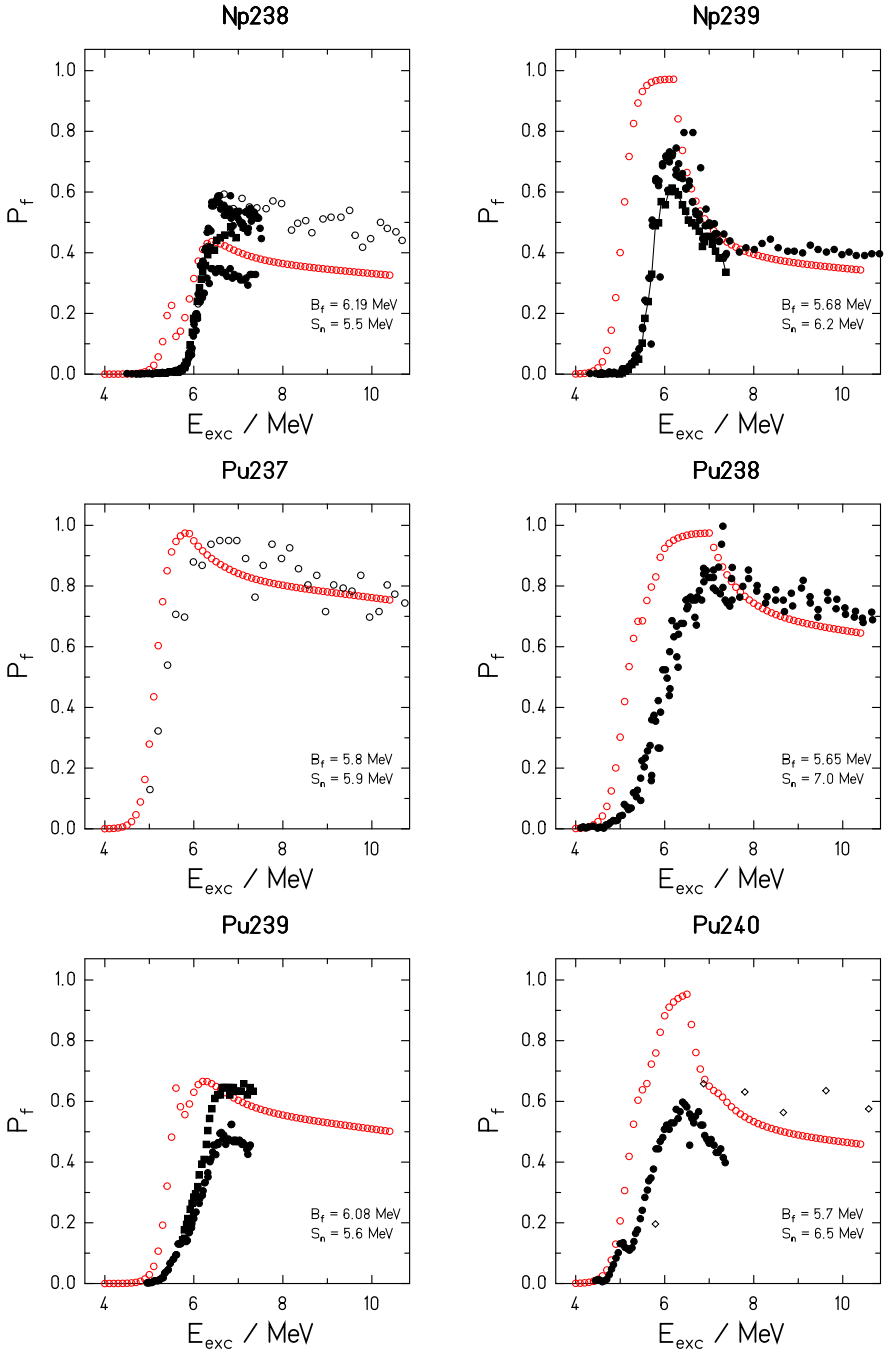

Note: Comparison of the measured fission probabilities (black symbols) with calculations with the GEF code (red symbols).

Figure 27: Benchmark of fission probabilities, part 6

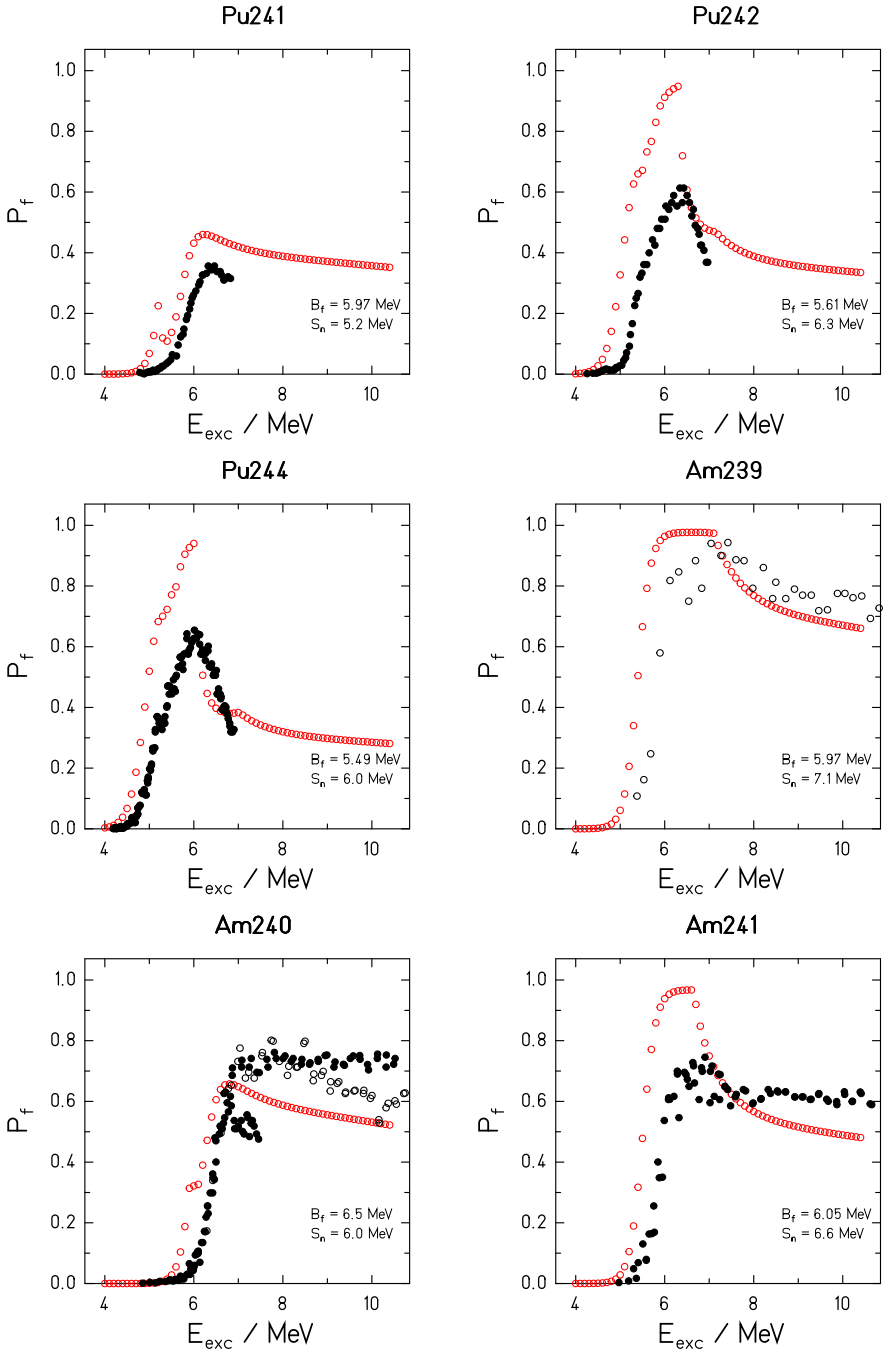

Note: Comparison of the measured fission probabilities (black symbols) with calculations with the GEF code (red symbols).

Figure 28: Benchmark of fission probabilities, part 7

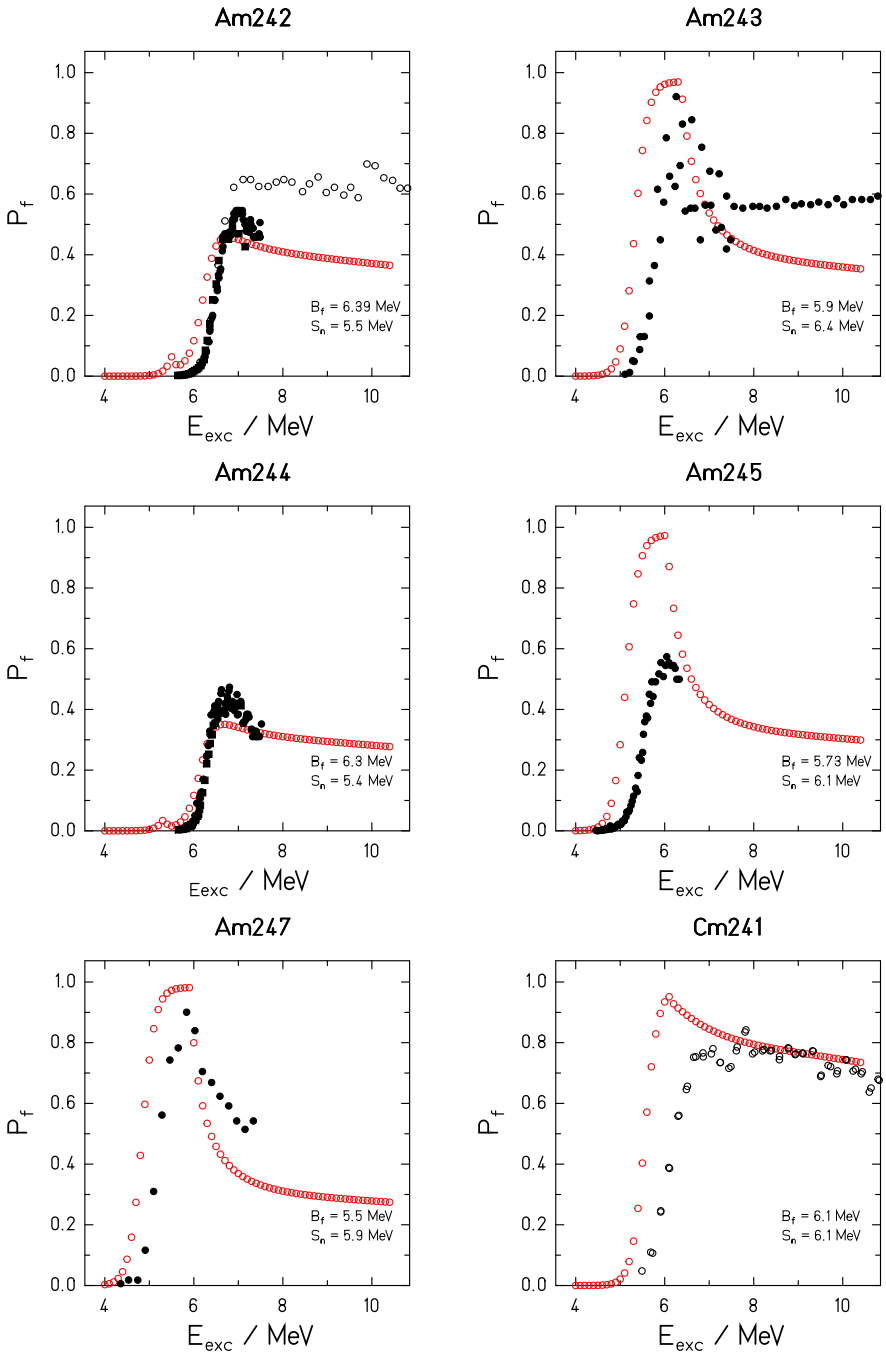

Note: Comparison of the measured fission probabilities (black symbols) with calculations with the GEF code (red symbols).

Figure 29: Benchmark of fission probabilities, part 8

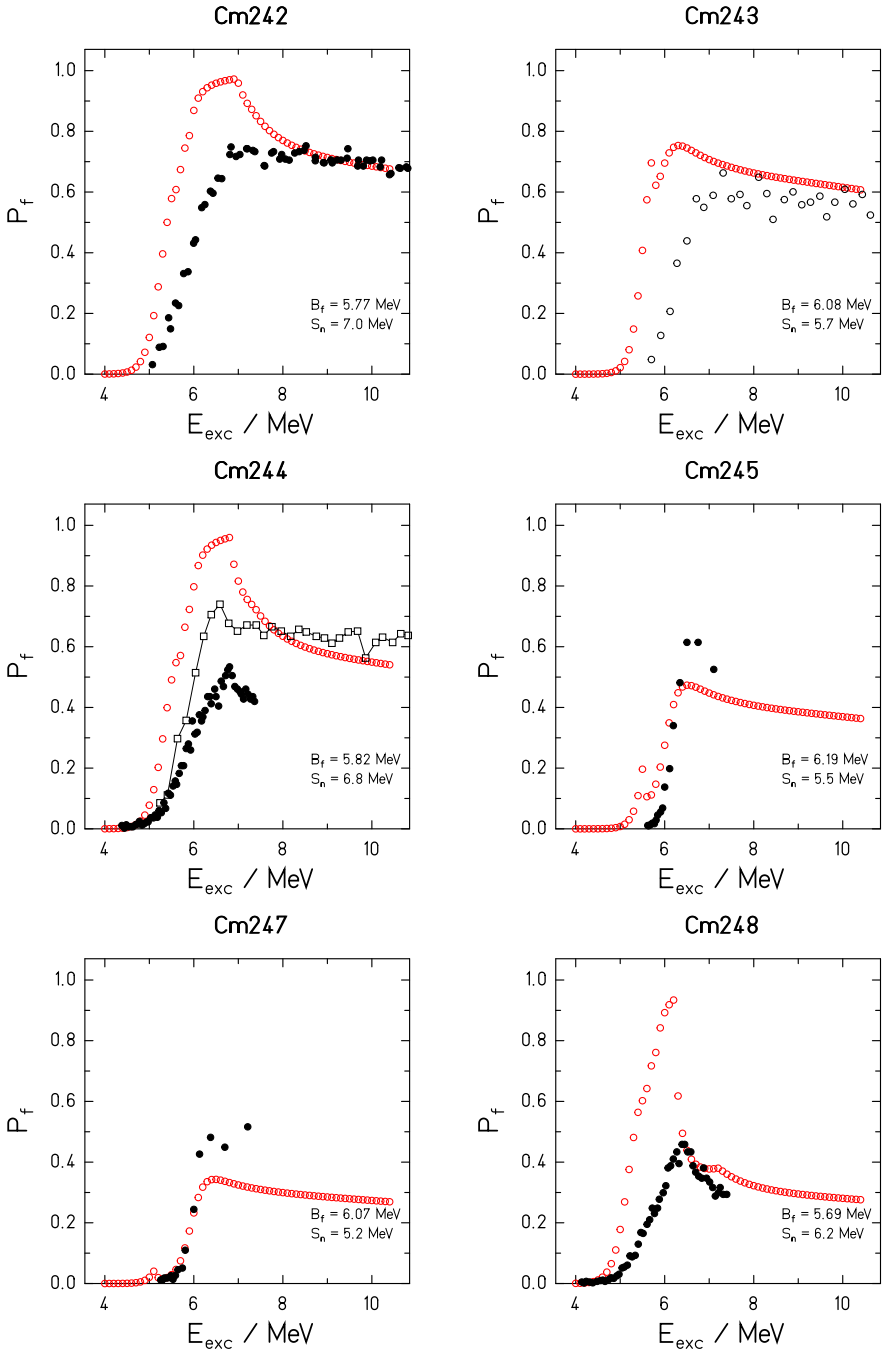

Note: Comparison of the measured fission probabilities (black symbols) with calculations with the GEF code (red symbols).

Figure 30: Benchmark of fission probabilities, part 9

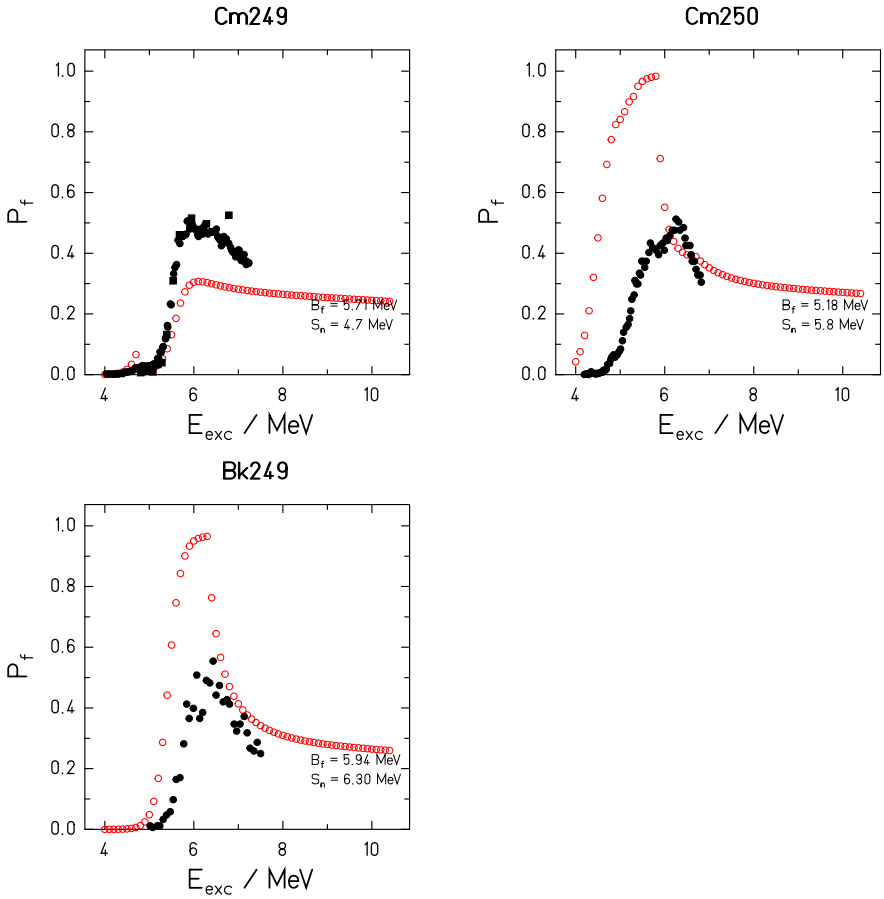

Note: Comparison of the measured fission probabilities (black symbols) with calculations with the GEF code (red symbols).

8.1.4 Discussion

The absolute values and the energy dependence of the fission probabilities of most systems reaching from Pa to Cm are rather well reproduced by the GEF code at energies above the fission barrier. However, in many cases, fission sets in at too low energies in the calculation. In a few cases, the measured fission probabilities are considerably lower than the calculated ones, while the threshold and the energy dependence are rather similar. The most pronounced cases are ^{229}Th, ^{230}Th, ^{231}Th, ^{233}Th, and ^{234}U.

A possible key to the latter problem may be seen in the figures for ^{231}Pa, ^{235}Np, ^{239}Pu, ^{240}Pu, and ^{244}Cm, where different sets of measured data exist. In all these cases, one of the data sets gives appreciably higher values than the other one, and the higher values agree rather well with the model calculations. For fission probabilities obtained

with transfer reactions, there may be a background originating from reactions on target contaminants (e.g. oxygen) or from other parasitic reactions like the breakup of the projectile (deuteron-breakup in particular). This may explain the differences encountered between the different groups of experimental data. Thus, this problem might have its origin in the experimental data at least in some of the cases.

The deviations at the threshold may be attributed to the shortcoming of the model due to its global description. Specific structural effects at low excitation energies, in particular structural information on the levels above the fission barrier are not properly considered. The observed deviations correspond to a shift of the effective threshold in the order of several 100 keV. Considering that the fission barriers extracted by different authors for the same nucleus often differ by 0.5 MeV and more [40], the deviations are not too surprising. The kind of disagreement seen in the figures gives a realistic impression about the quality of the predictions of the model for cases, where no experimental data exist.

8.1.5 Conclusion

A global description of the fission probability of the actinides has been derived which reproduces the experimental data rather well. Discrepancies in the absolute values over the whole energy range might be caused by a background contribution due to the presence of light target contaminants in the experiment. The global description of the nuclear level densities near the ground state and near the fission threshold used in the code can only give a rather crude approximation of the behaviour of the fission probability near the fission threshold. This explains the discrepancies in the fission probabilities near the fission threshold found for several systems. The energy-dependent fission probabilities are important to calculate the relative weights of the different fission chances at higher energies.

8.2 Fission-fragment yields

8.2.1 Introduction

Several hundred different nuclides are produced in the fission of a heavy nucleus. They essentially contribute to the radioactive inventory of a fission reactor, and they are the source of most part of the decay heat that incurres in the fuel rods even long time after the shut-down of a fission reactor. The relative yields of the different nuclides depend on the fissioning nucleus and on the excitation energy at fission. Moreover, the radioactive-decay properties of the different fission products differ very much. Therefore, a very good knowledge on the yields of the different fission products is of paramount importance for the operation of a fission reactor and for the storage of used fuel rods.

New data are required when new generations of fission reactors are developed, e.g. when fission is induced by neutrons of higher energies, or when eventually other kind of fuel is used. Reliable model calculations of the fission-product yields are urgently required which can replace time-consuming and expensive experiments.

The GEF code [131, 54, 132] has been developed with the aim to provide this kind of information. In the following, the quality and the predictive power of the GEF code for calculating fission-fragment yields for different fissioning systems and a large range of energy is assessed.

8.2.2 Experimental techniques

It is worthwhile to have a look on the different most often used experimental techniques applied to measure fission-product yields, because they determine the nature of the data.

The traditional approach is based on the identification of gamma rays that are characteristic for the radioactive decay of a specific fragment [133]. Fission-product masses after the emission of prompt neutrons are determined. This technique is able to identify the emitting nuclide unambiguously, but it requires additional knowledge on the decay properties, e.g. branching ratios, in order to deduce quantitative yields. Moreover, this technique is not well suited for measuring the yields of short-lived fission products and unable to determine the yields of stable nuclides.

The masses of the fission products can also be determined by particle detectors that measure the energies and/or the velocities of the fission products [134, 135, 136]. These methods are suited to deduce the masses of the fission products before and after the emission of prompt neutrons. However, the resolution is not sufficient to determine the mass unambiguously in most cases.

Unambiguous determination of fission-product masses is achieved by use of the Lohengrin spectrograph [137] at the high-flux reactor of the ILL, Grenoble. Also, the nuclear charge in the light group of the fission products can be determined. However, this technique is restricted to thermal-neutron-induced fission and a limited choice of target material.

A novel kind of experiments in inverse kinematics [138, 48, 139] succeeded to determine

the mass A and the atomic number Z of all fission products unambiguously in Coulomb fission of short-lived neutron-deficient projectile fragments at relativistic energies. The full identification of all fission products in A and Z was also achieved in the fission of transfer products from ^{238}U projectiles at energies above the Coulomb barrier [140]. Besides the unprecedented resolution in kinematical measurements, these experiments offer a wide choice of fissionning systems, not accessible before.

8.2.3 Mass distributions

Fission-fragment mass distributions have a particular importance. First, they are determined with full resolution for a large number of systems by gamma-spectroscopic measurements. The data which are often incomplete are completed with the Wahl systematics [1]. Moreover, the beta decay which is the predominant decay path follows the mass chain. Thus, the mass distribution can also be deduced from cumulative yields. Second, the mass distributions allow estimating the long-term radioactive decay characteristics rather well, because beta decay that connects nuclei with the same mass number is the predominant decay path in most cases.

In the following, experimental and evaluated mass distributions in four different energy classes and from different experimental sources are compared with the result of the GEF code. Depending on the experimental technique, mass distributions before emission of prompt neutrons (A_{pre}) and after emission of prompt neutrons (A_{post}) are given. In a few cases, A_{prov}, the provisional mass, is shown. It is directly deduced from the ratio of the kinetic energies E_1 and E_2 of the fragments, assuming that $A_1/A_2 = E_2/E_1$, and, thus, it is not corrected for neutron emission.

The calculated individual contributions from the different fission modes are shown in addition. The comparison is not exhaustive, but it gives a rather complete view on the variation of the mass distributions from protactinium to rutherfordium. The error bars represent the uncertainties given in the indicated references (see Table 8).

Although the GEF code is able to produce uncertainties by calculations with perturbed parameters, they are not shown in order not to overload the figures.

8.2.3.1 Spontaneous fission: Figures 31 to 38 show the calculated mass distributions for spontaneous fission in comparison with measured or evaluated data of a number of systems in linear and in logarithmic scale. Although spontaneous fission is less important for technical applications, these figures are essential for revealing the dependence of the fission-fragment yields upon excitation energy on the fission path. Note that the kinematical measurements of pre-neutron masses are subject to a finite resolution and uncertainties due to the correction for detector response and prompt-neutron emission.

Figure 31: Mass distributions, spontaneous fission, part 1, linear scale

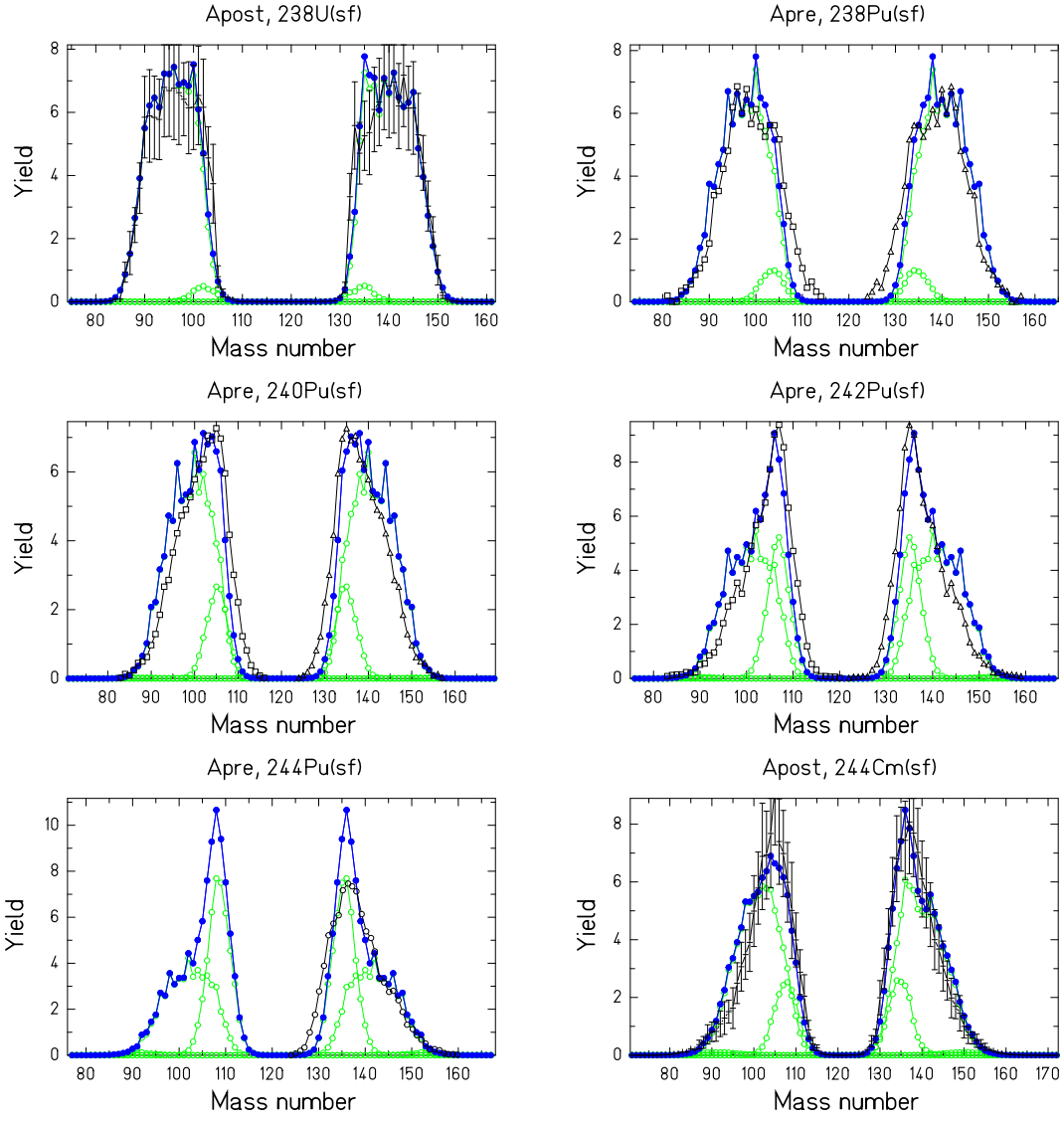

Note: Evaluated and experimental mass distributions (black symbols) of fission fragments in comparison with the results of the GEF code (green and blue symbols) in a linear scale. Spontaneous fission, part 1.

Figure 32: Mass distributions, spontaneous fission, part 1, logarithmic scale

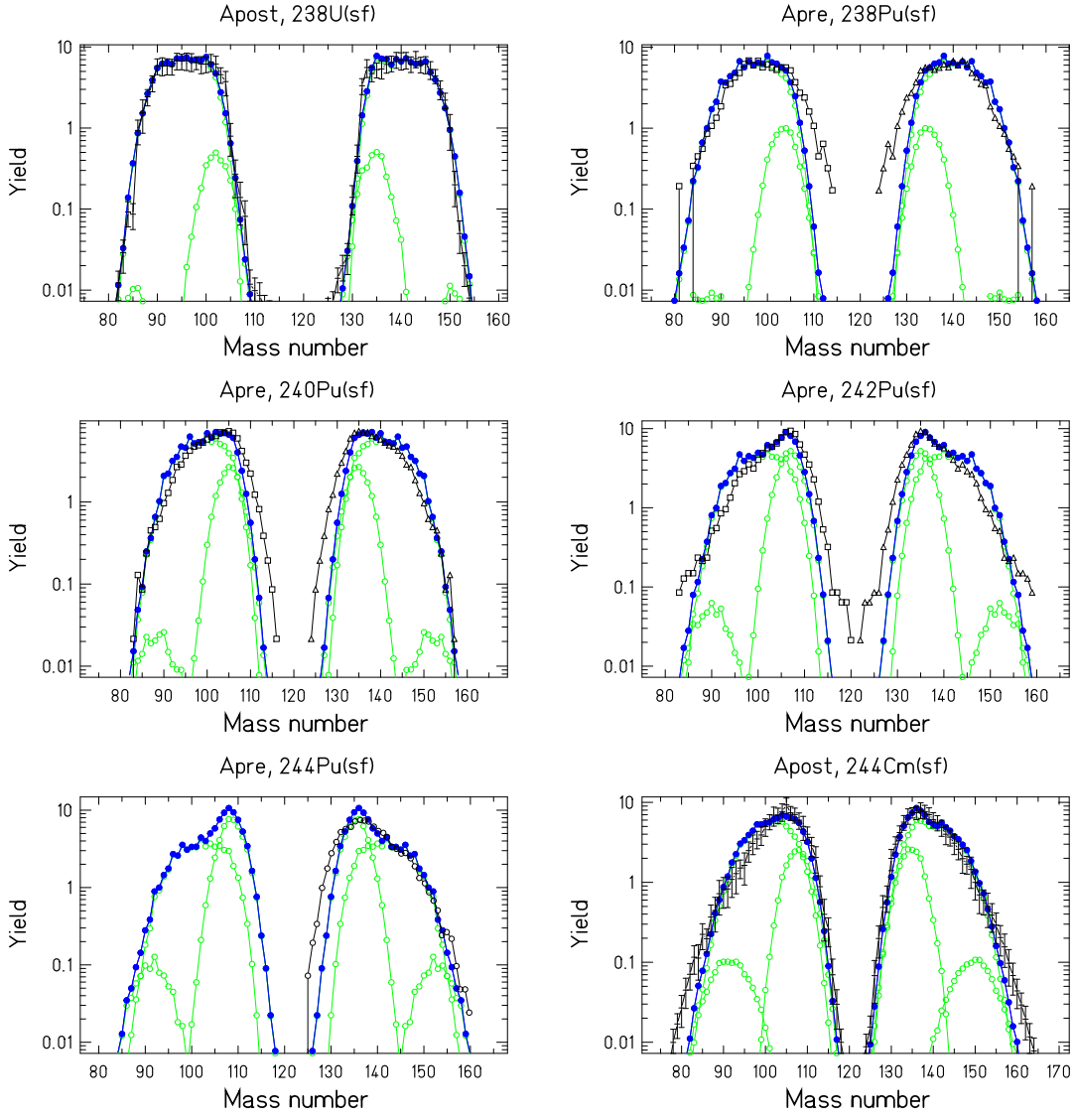

Note: Evaluated and experimental mass distributions (black symbols) of fission fragments in comparison with the results of the GEF code (green and blue symbols) in a logarithmic scale. Spontaneous fission, part 1.

Figure 33: Mass distributions, spontaneous fission, part 2, linear scale

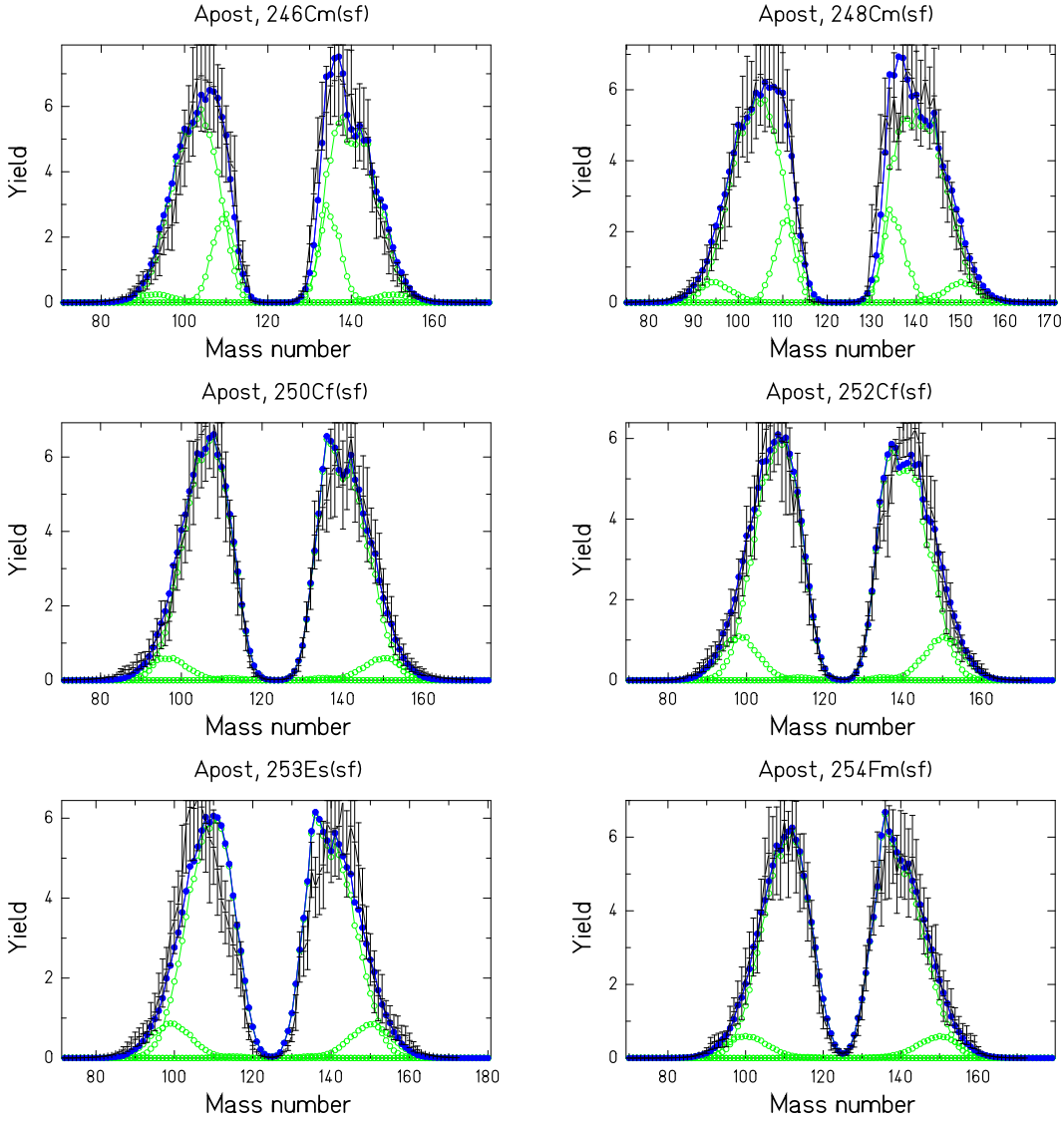

Note: Evaluated and experimental mass distributions (black symbols) of fission fragments in comparison with the results of the GEF code (green and blue symbols) in a linear scale. Spontaneous fission, part 2.

Figure 34: Mass distributions, spontaneous fission, part 2, logarithmic scale

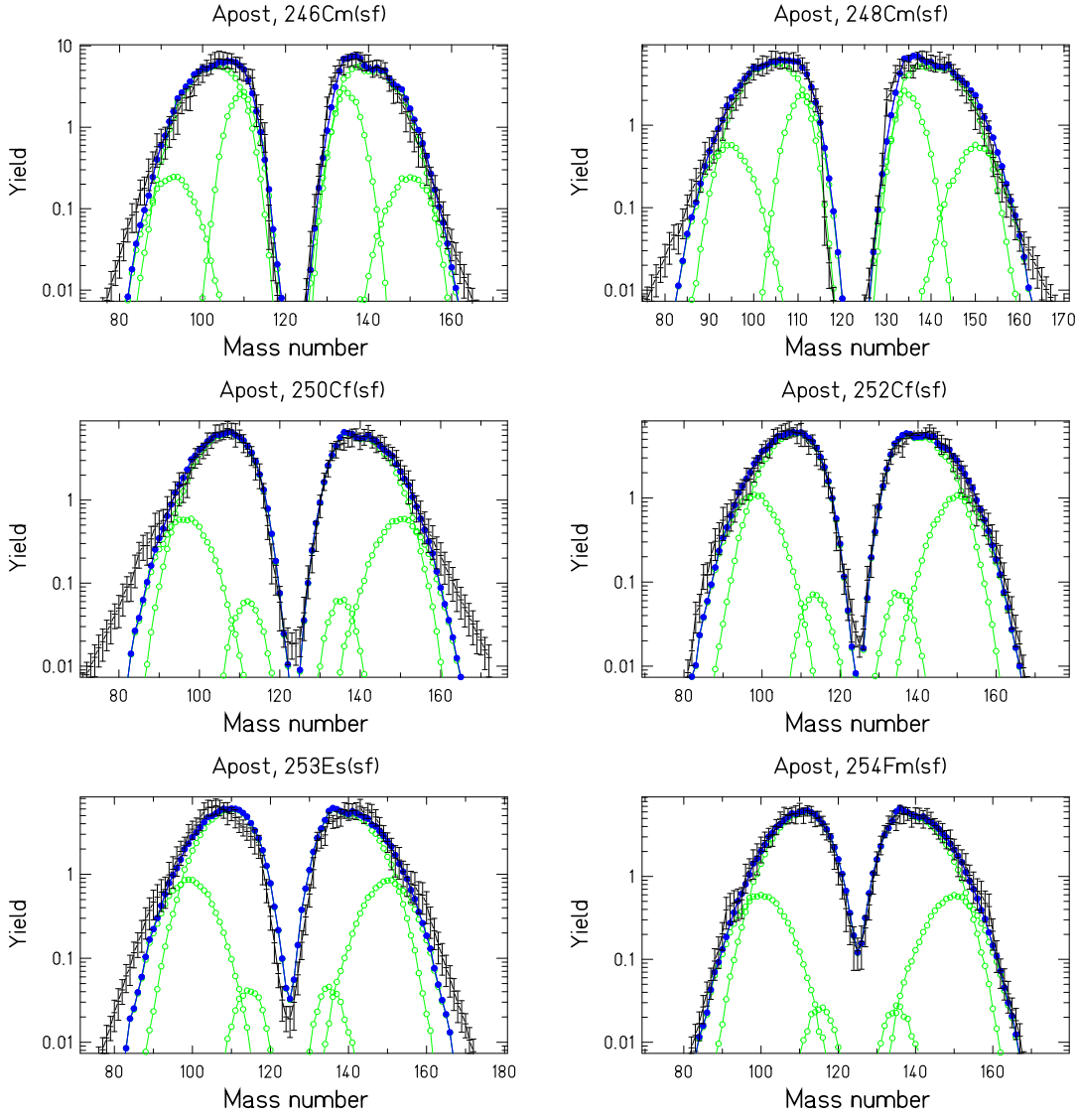

Note Evaluated and experimental mass distributions (black symbols) of fission fragments in comparison with the results of the GEF code (green and blue symbols) in a logarithmic scale. Spontaneous fission, part 2.

Figure 35: Mass distributions, spontaneous fission, part 3, linear scale

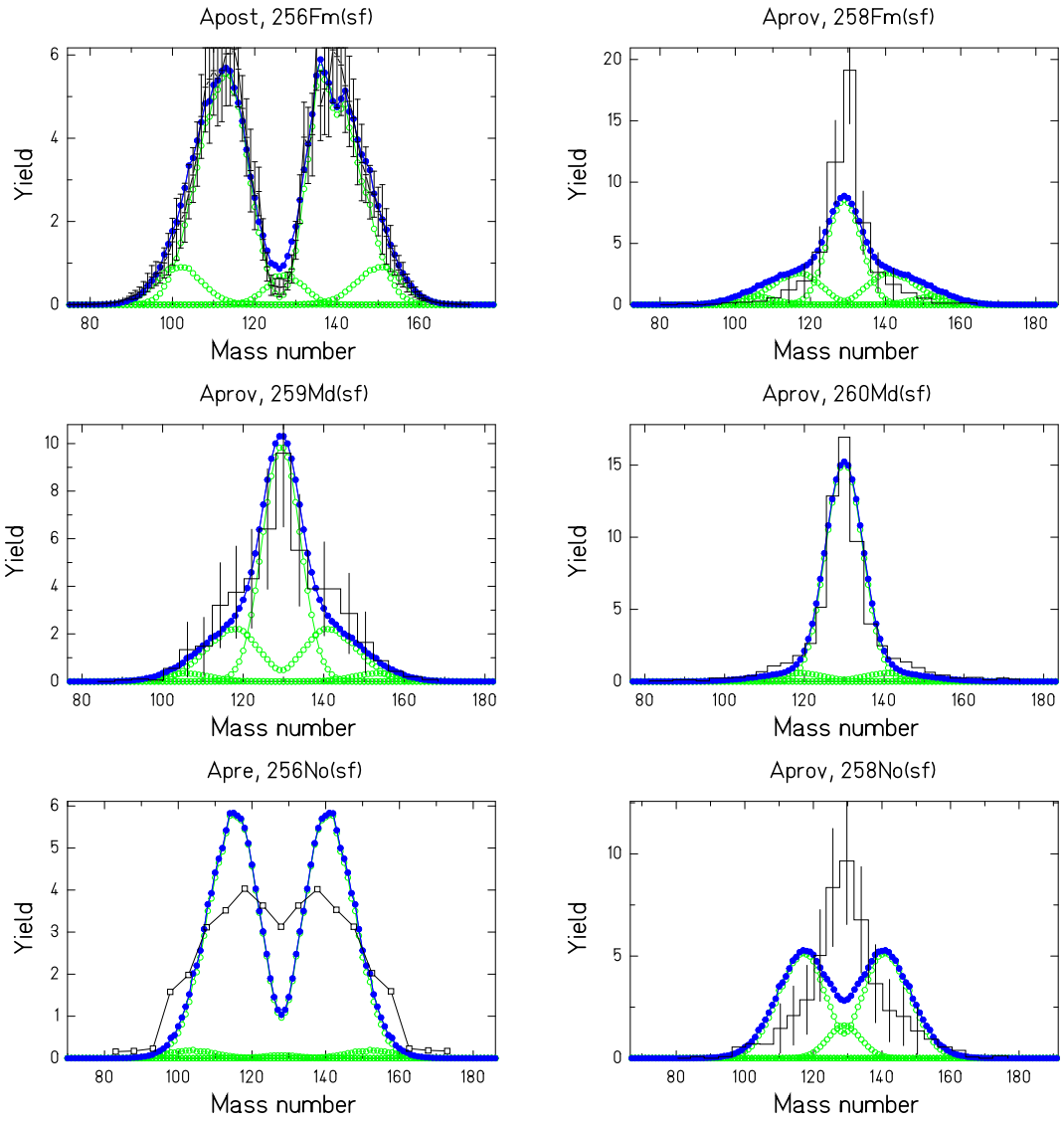

Note: Evaluated and experimental mass distributions (black symbols) of fission fragments in comparison with the results of the GEF code (green and blue symbols) in a linear scale. Spontaneous fission, part 3.

Figure 36: Mass distributions, spontaneous fission, part 3, logarithmic scale

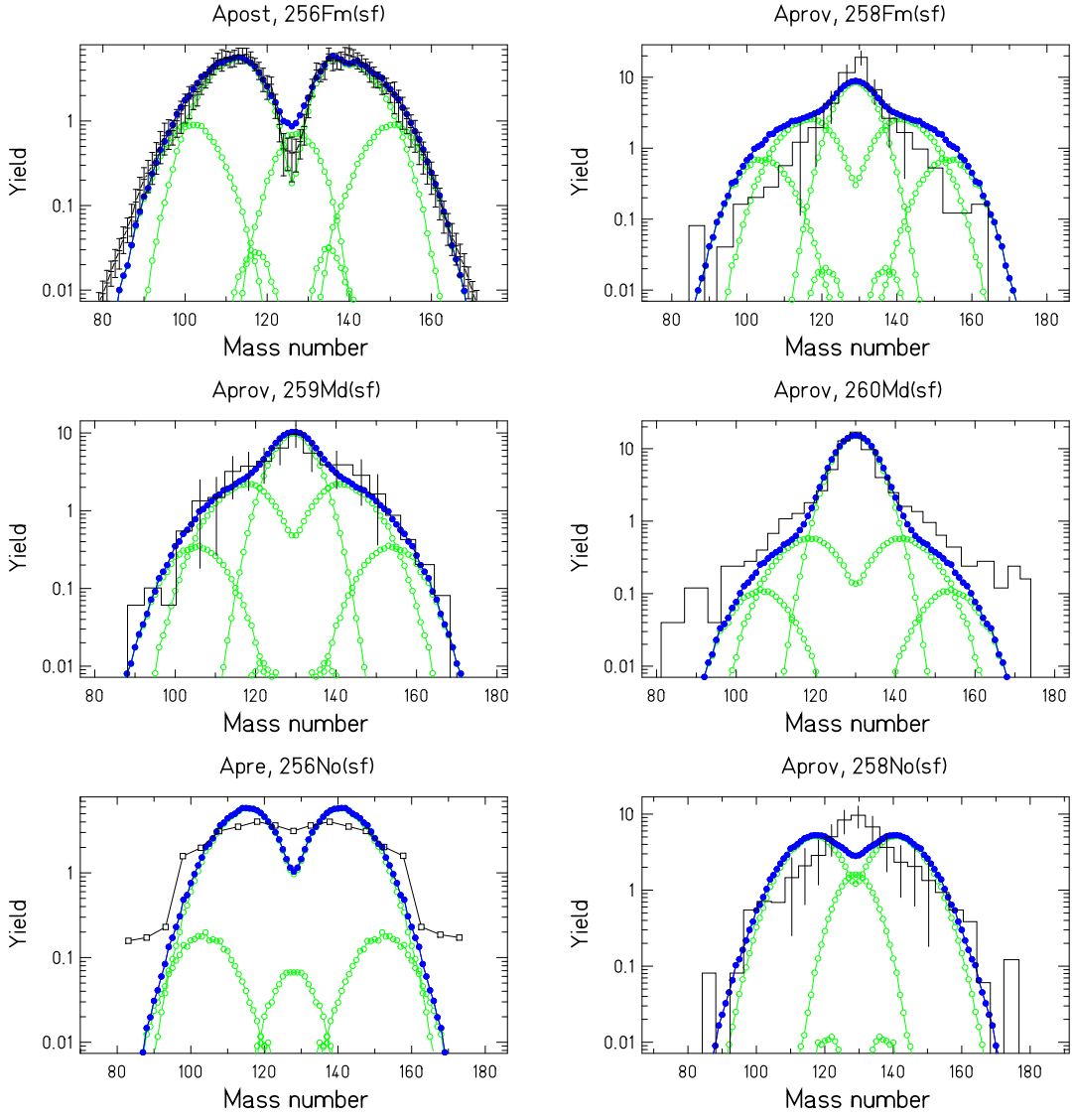

Note: Evaluated and experimental mass distributions (black symbols) of fission fragments in comparison with the results of the GEF code (green and blue symbols) in a logarithmic scale. Spontaneous fission, part 3.

Figure 37: Mass distributions, spontaneous fission, part 4, linear scale

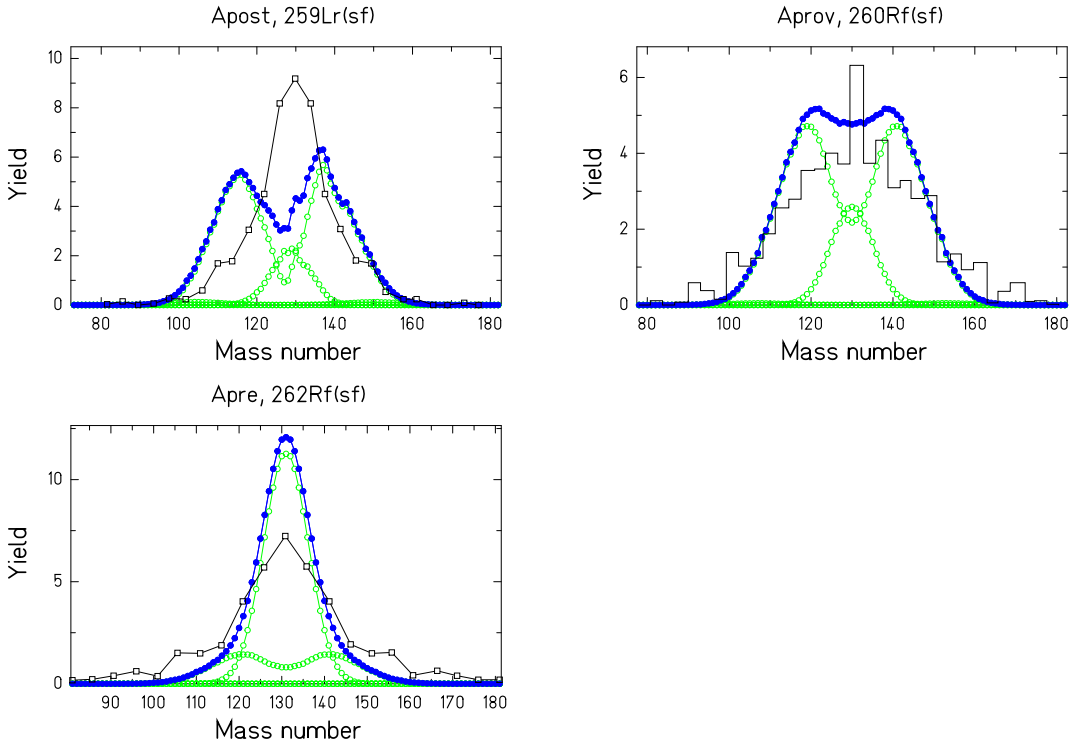

Note: Evaluated and experimental mass distributions (black symbols) of fission fragments in comparison with the results of the GEF code (green and blue symbols) in a linear scale. Spontaneous fission, part 4.

Figure 38: Mass distributions, spontaneous fission, part 4, logarithmic scale

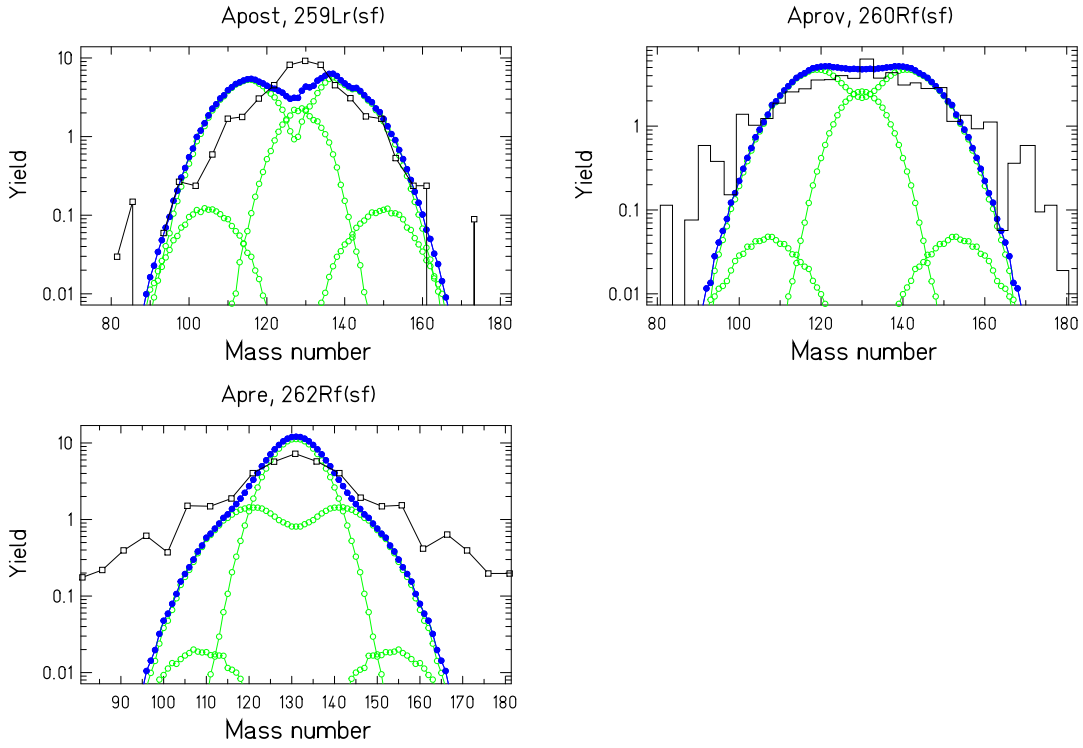

Note: Evaluated and experimental mass distributions (black symbols) of fission fragments in comparison with the results of the GEF code (green and blue symbols) in a logarithmic scale. Spontaneous fission, part 4.

8.2.3.2 Fission induced by thermal neutrons: Mass distributions from thermal-neutron-induced fission are shown in Figures 39 to 44.

Figure 39: Mass distributions, (n_{th}, f), part 1, linear scale

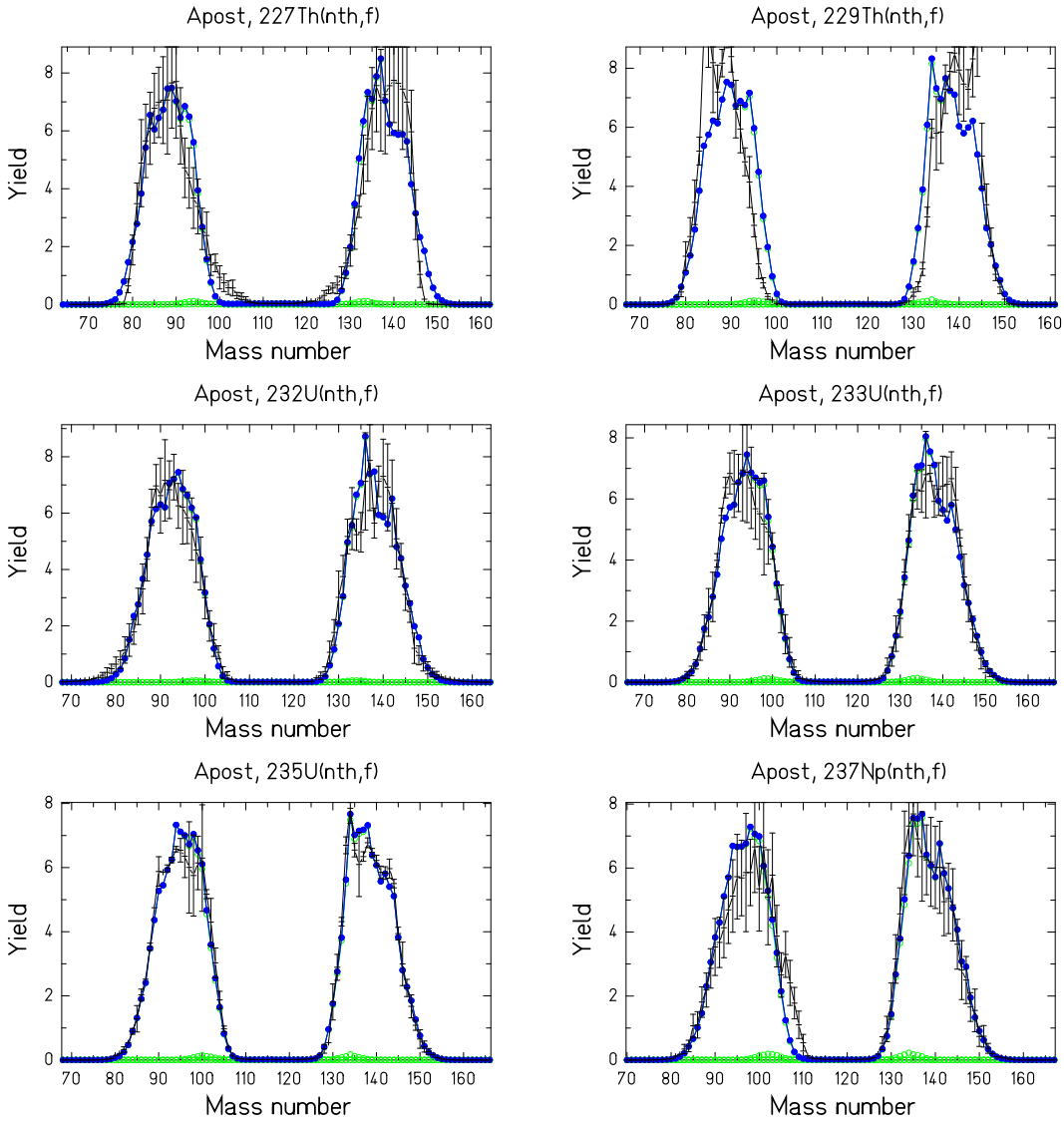

Note: Evaluated and experimental mass distributions (black symbols) of fission fragments in comparison with the results of the GEF code (green and blue symbols) in a linear scale. Thermal-neutron-induced fission, part 1.

Figure 40: Mass distributions, (n_{th}, f), part 1, logarithmic scale

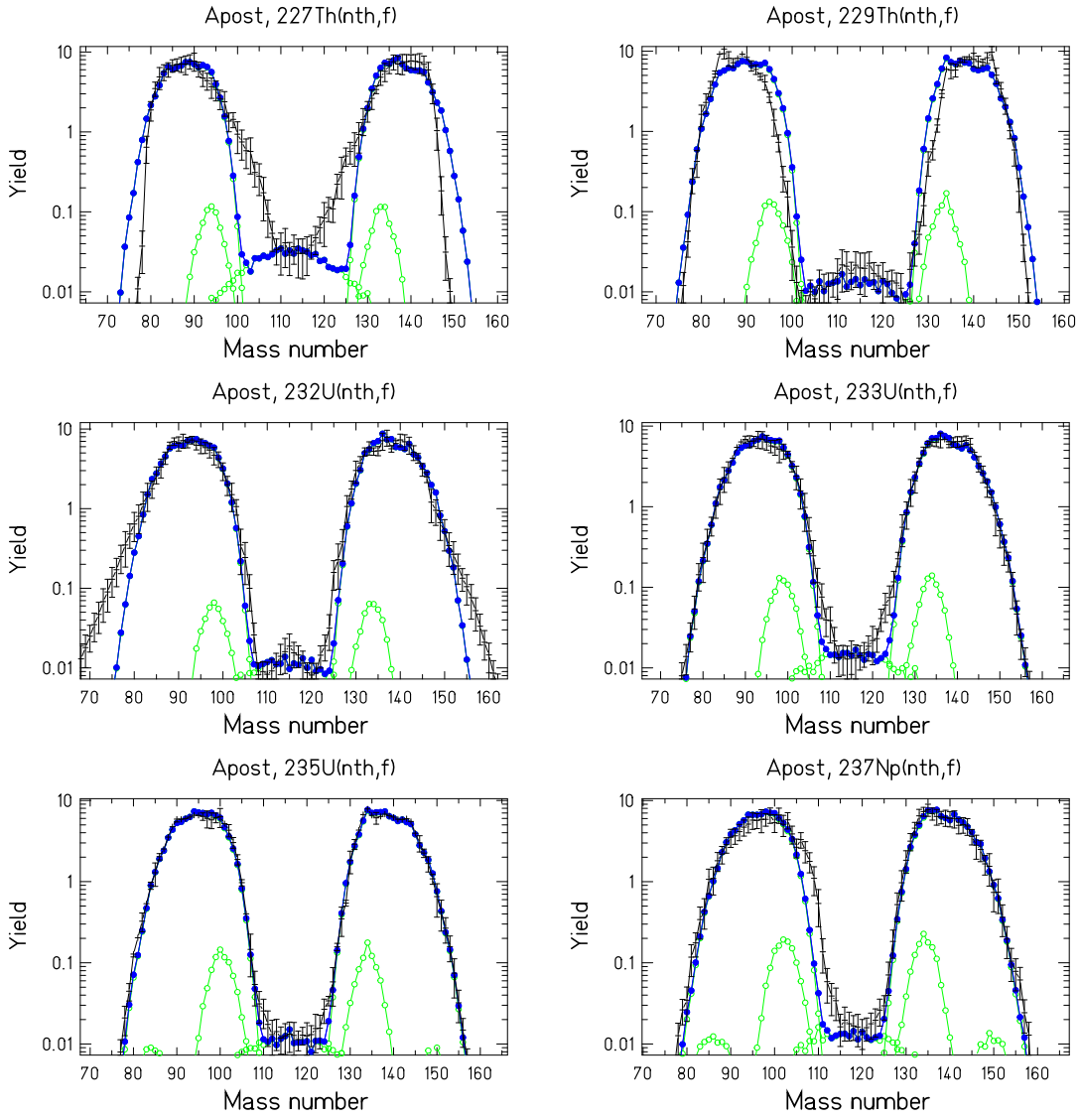

Note: Evaluated and experimental mass distributions (black symbols) of fission fragments in comparison with the results of the GEF code (green and blue symbols) in a logarithmic scale. Thermal-neutron-induced fission, part 1.

Figure 41: Mass distributions, (n_{th}, f), part 2, linear scale

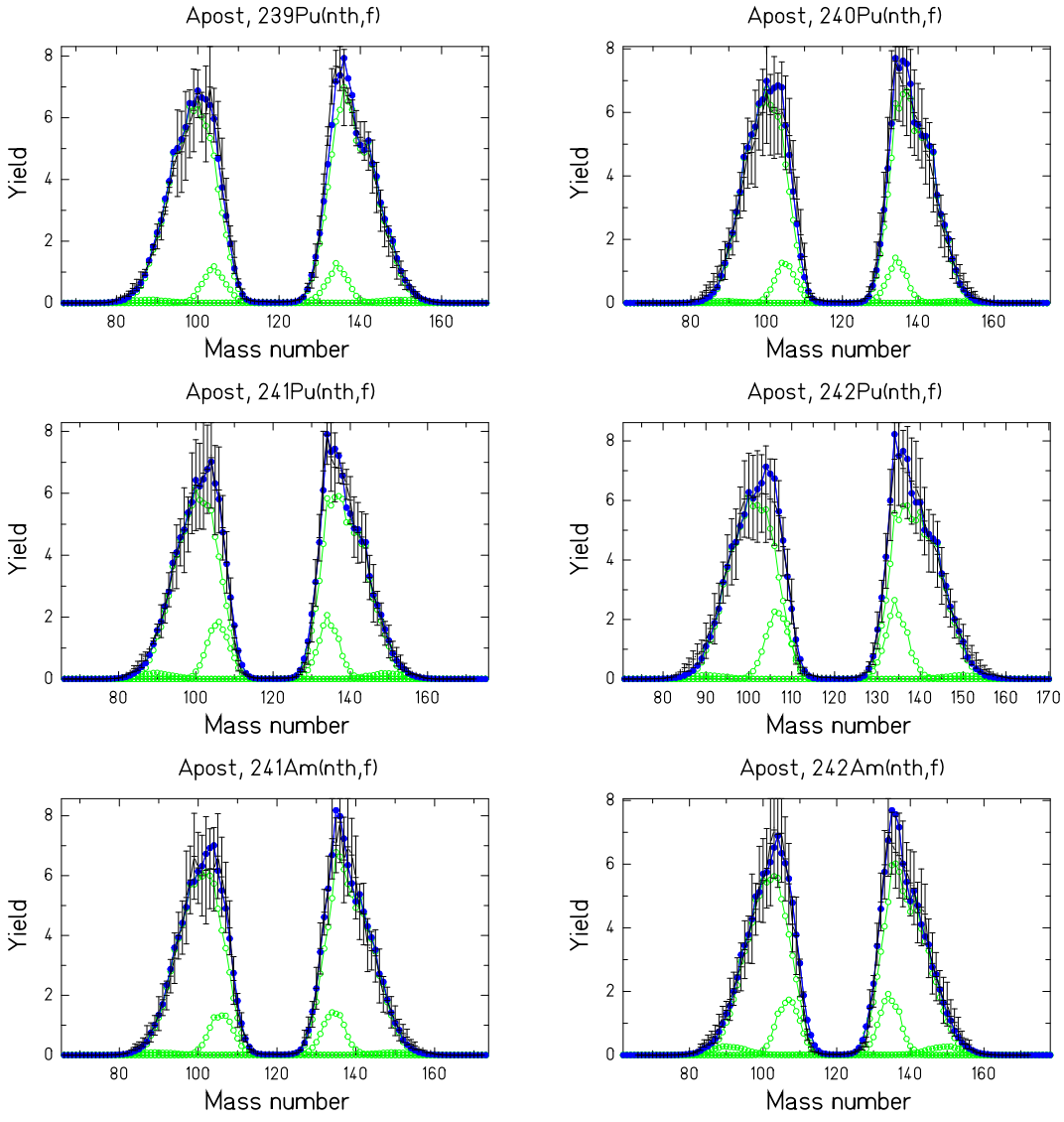

Note: Evaluated and experimental mass distributions (black symbols) of fission fragments in comparison with the results of the GEF code (green and blue symbols) in a linear scale. Thermal-neutron-induced fission, part 2.

Figure 42: Mass distributions, (n_{th}, f), part 2, logarithmic scale

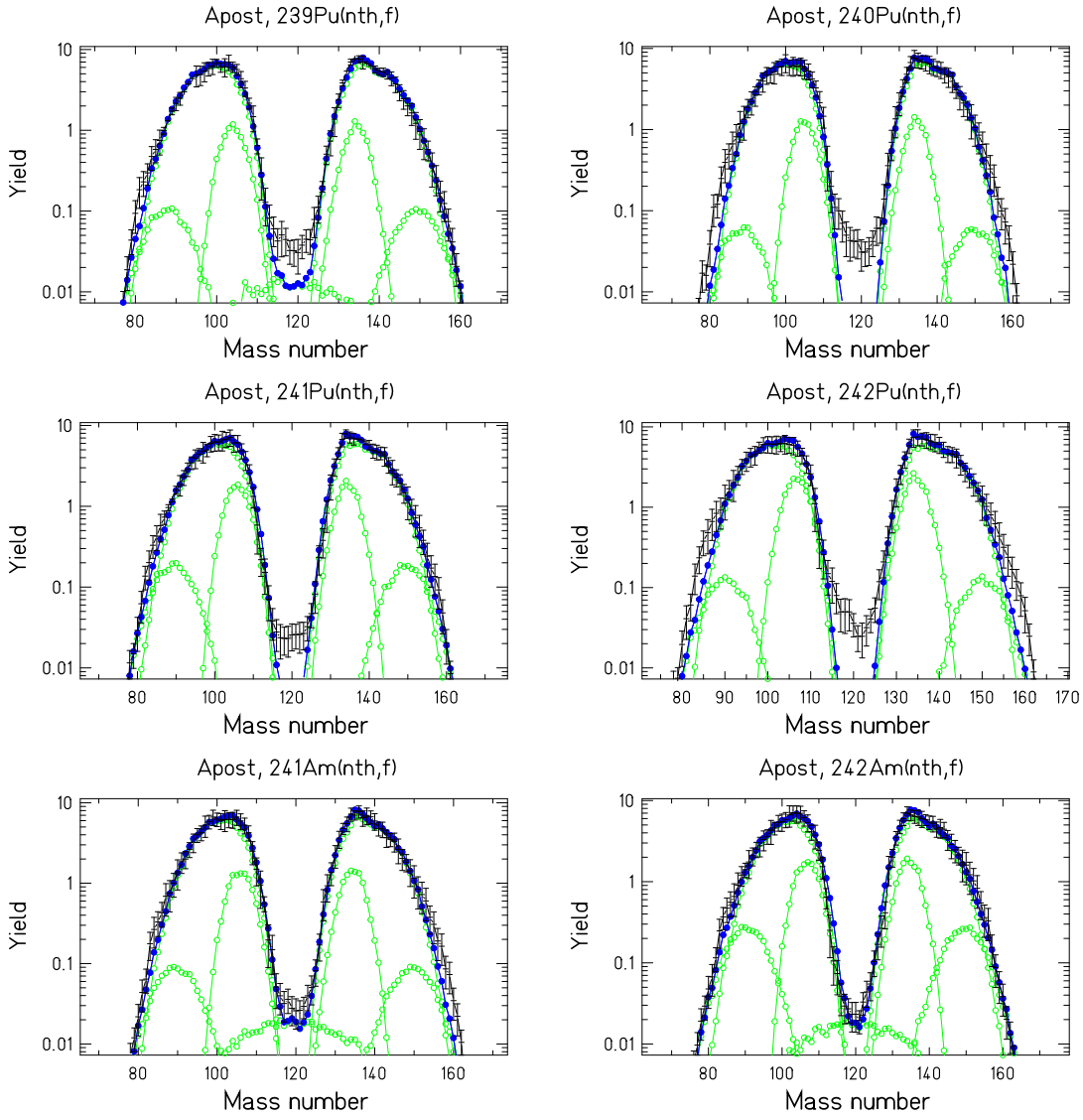

Note: Evaluated and experimental mass distributions (black symbols) of fission fragments in comparison with the results of the GEF code (green and blue symbols) in a logarithmic scale. Thermal-neutron-induced fission, part 2.

Figure 43: Mass distributions, (n_{th}, f), part 3, linear scale

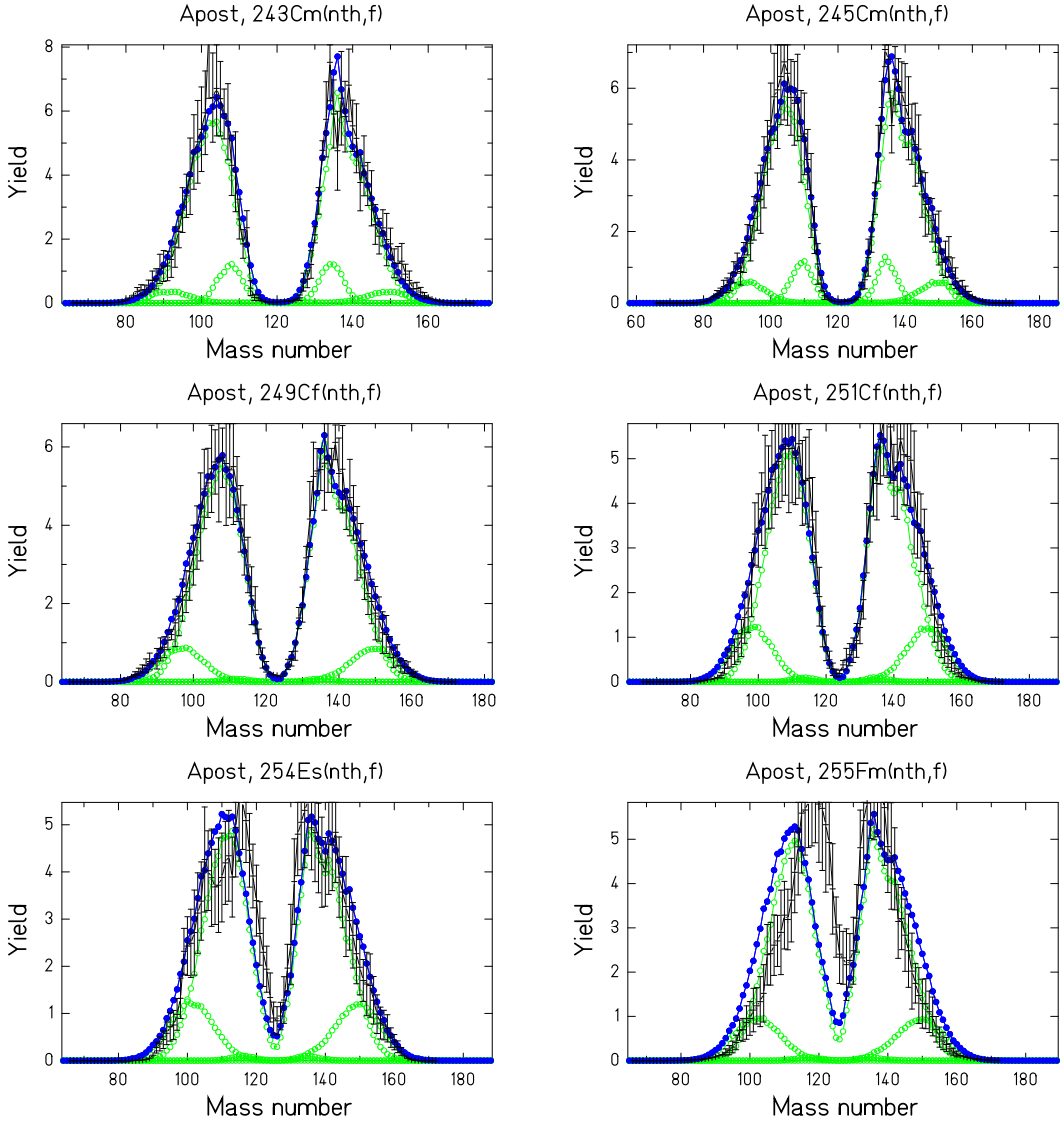

Note: Evaluated and experimental mass distributions (black symbols) of fission fragments in comparison with the results of the GEF code (green and blue symbols) in a linear scale. Thermal-neutron-induced fission, part 3.

Figure 44: Mass distributions, (n_{th}, f), part 3, logarithmic scale

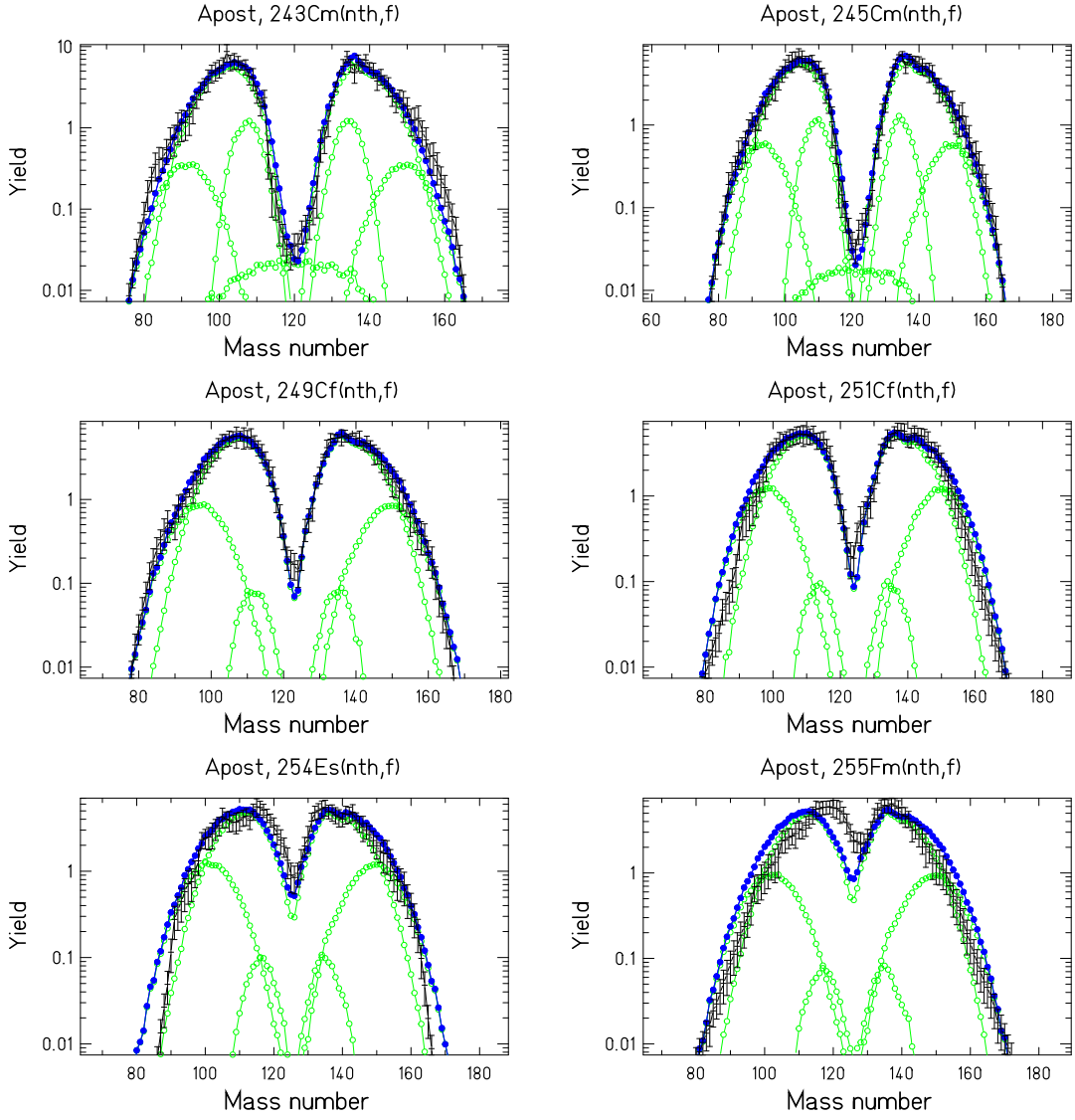

Note: Evaluated and experimental mass distributions (black symbols) of fission fragments in comparison with the results of the GEF code (green and blue symbols) in a logarithmic scale. Thermal-neutron-induced fission, part 3.

8.2.3.3 Fission induced by fast neutrons: Fast-neutron-induced fission comprises the energy range of fission neutrons up to a few MeV. Some data refer to well defined energies of e.g. 0.4 MeV or 2 MeV, some correspond to rather broad energy distributions. In the case of a strongly energy-dependent fission cross section, the mean energy of the fissioning nuclei may be rather high. Therefore, in Figures 45 to 8.2.3 the strongly energy-dependent yield at symmetry may often not be correctly reproduced by the calculations, which were performed with an incoming-neutron energy of 2 MeV in all cases.

Figure 45: Mass distributions, (n_{fast}, f), part 1, linear scale

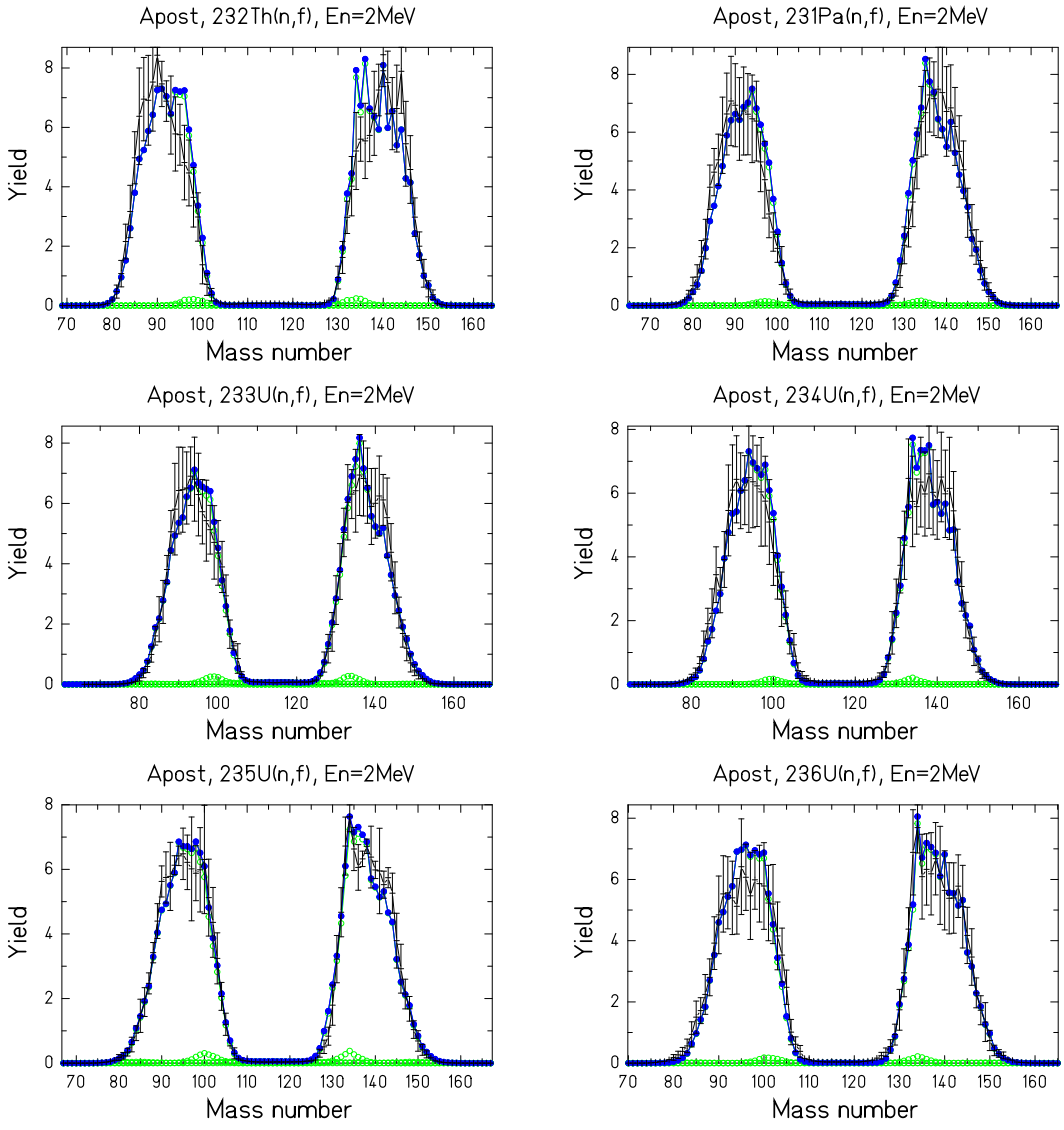

Note: Evaluated and experimental mass distributions (black symbols) of fission fragments in comparison with the results of the GEF code (green and blue symbols) in a linear scale. Fast-neutron-induced fission, part 1.

Figure 46: Mass distributions, (n_{fast}, f), part 1, logarithmic scale

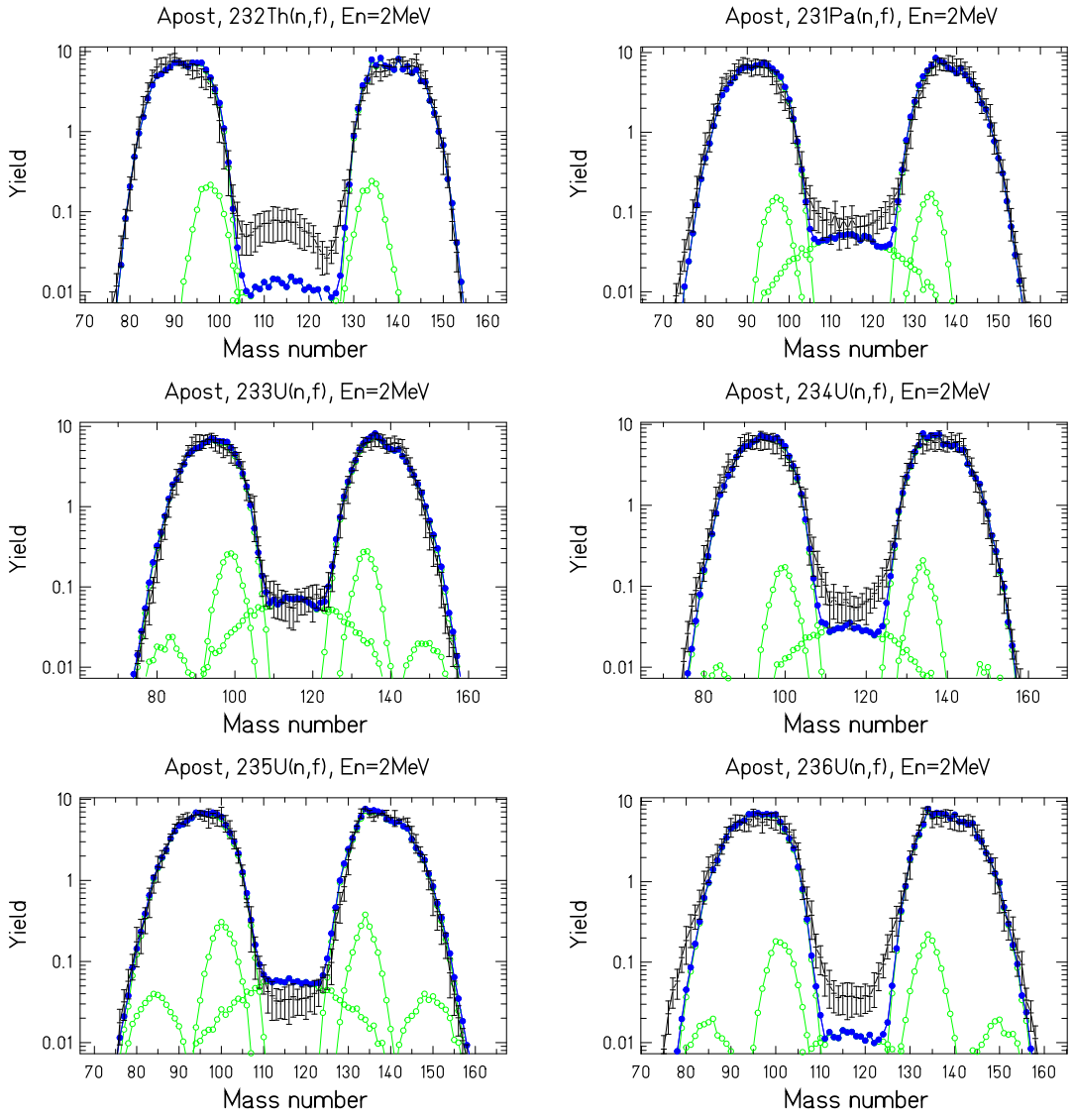

Note: Evaluated and experimental mass distributions (black symbols) of fission fragments in comparison with the results of the GEF code (green and blue symbols) in a logarithmic scale. Fast-neutron-induced fission, part 1.

Figure 47: Mass distributions, (n_{fast}, f), part 2, linear scale

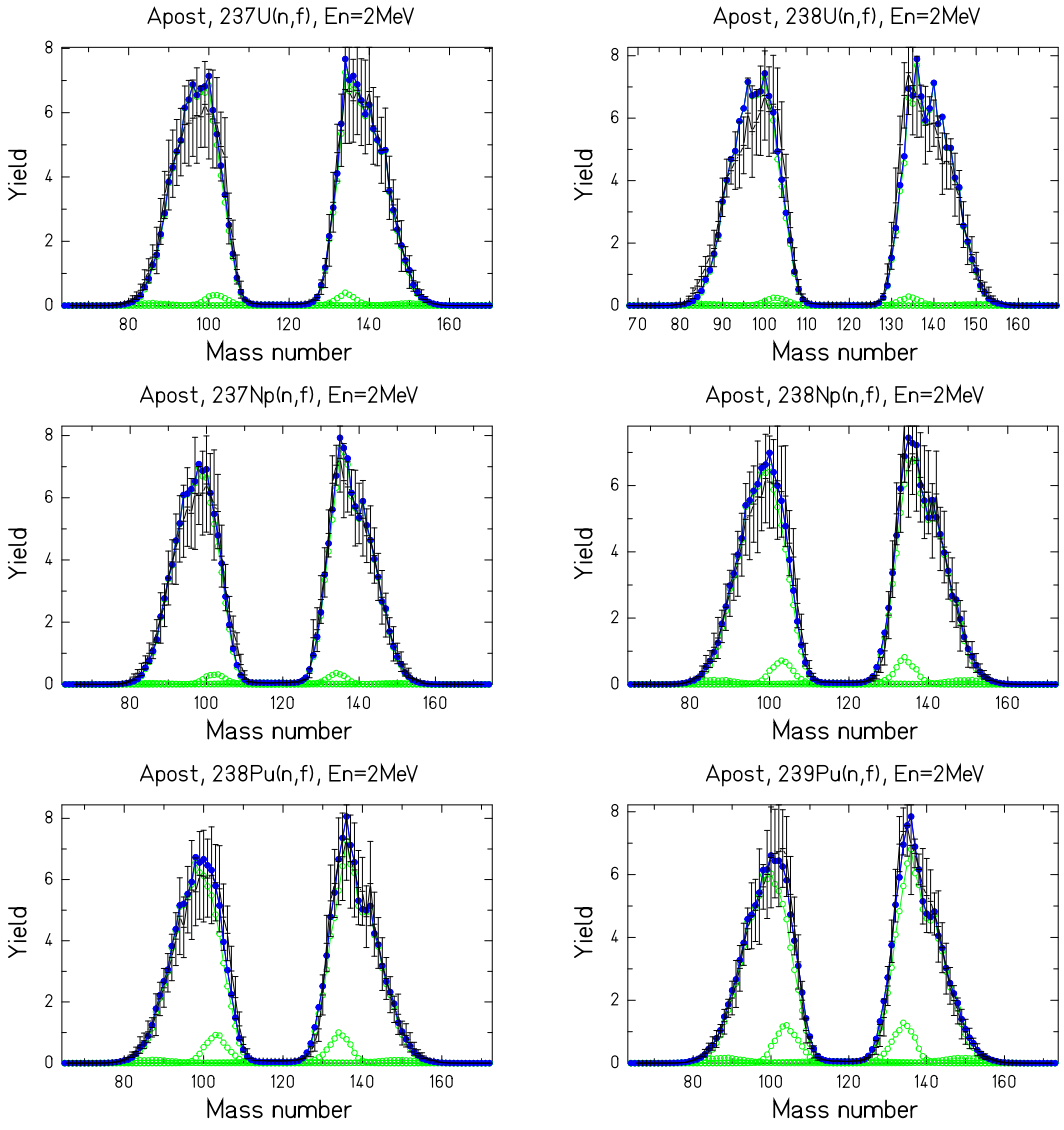

Note: Evaluated and experimental mass distributions (black symbols) of fission fragments in comparison with the results of the GEF code (green and blue symbols) in a linear scale. Fast-neutron-induced fission, part 2.

Figure 48: Mass distributions, (n_{fast}, f), part 2, logarithmic scale

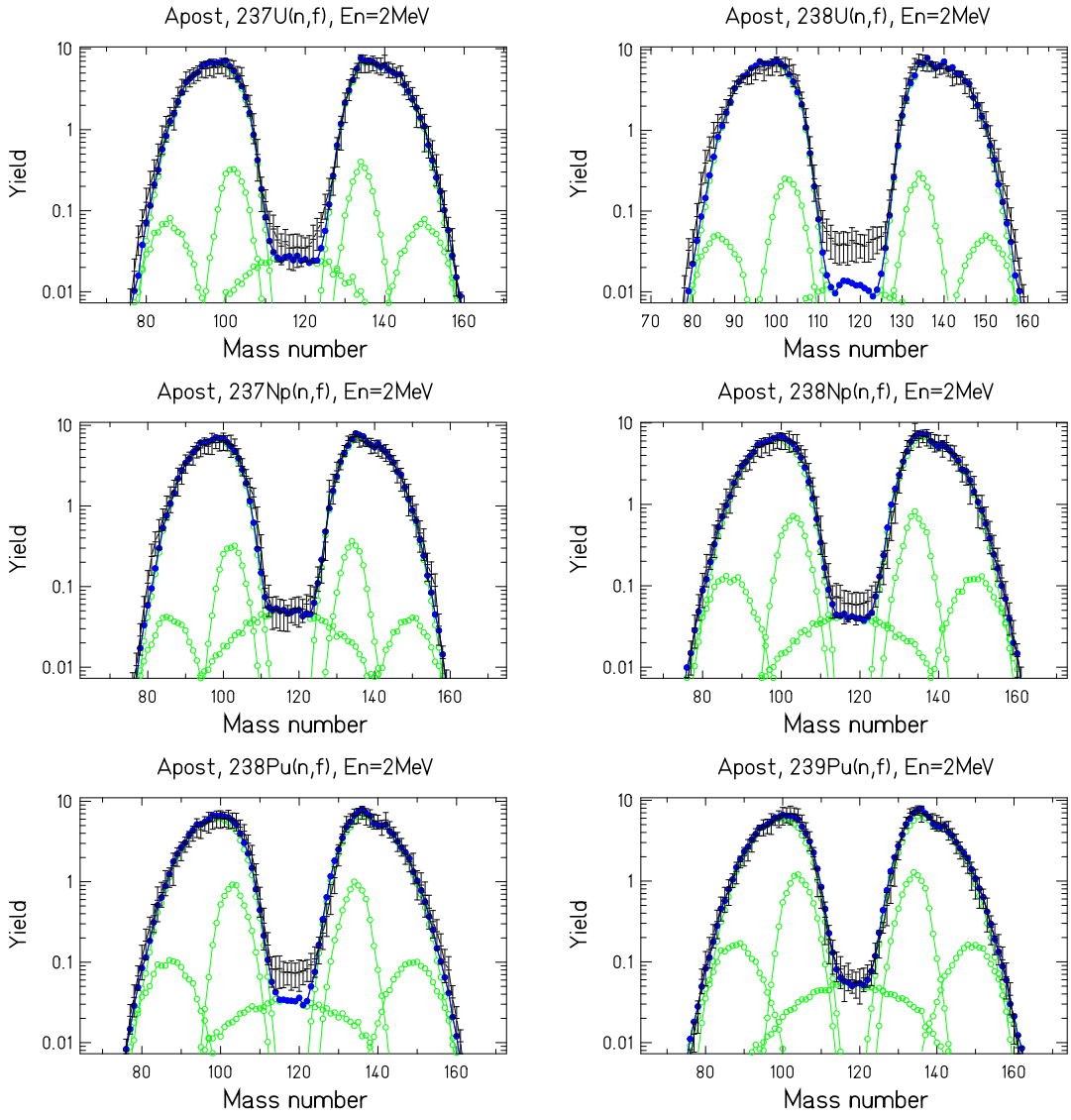

Note: Evaluated and experimental mass distributions (black symbols) of fission fragments in comparison with the results of the GEF code (green and blue symbols) in a logarithmic scale. Fast-neutron-induced fission, part 2.

Figure 49: Mass distributions, (n_{fast}, f), part 3, linear scale

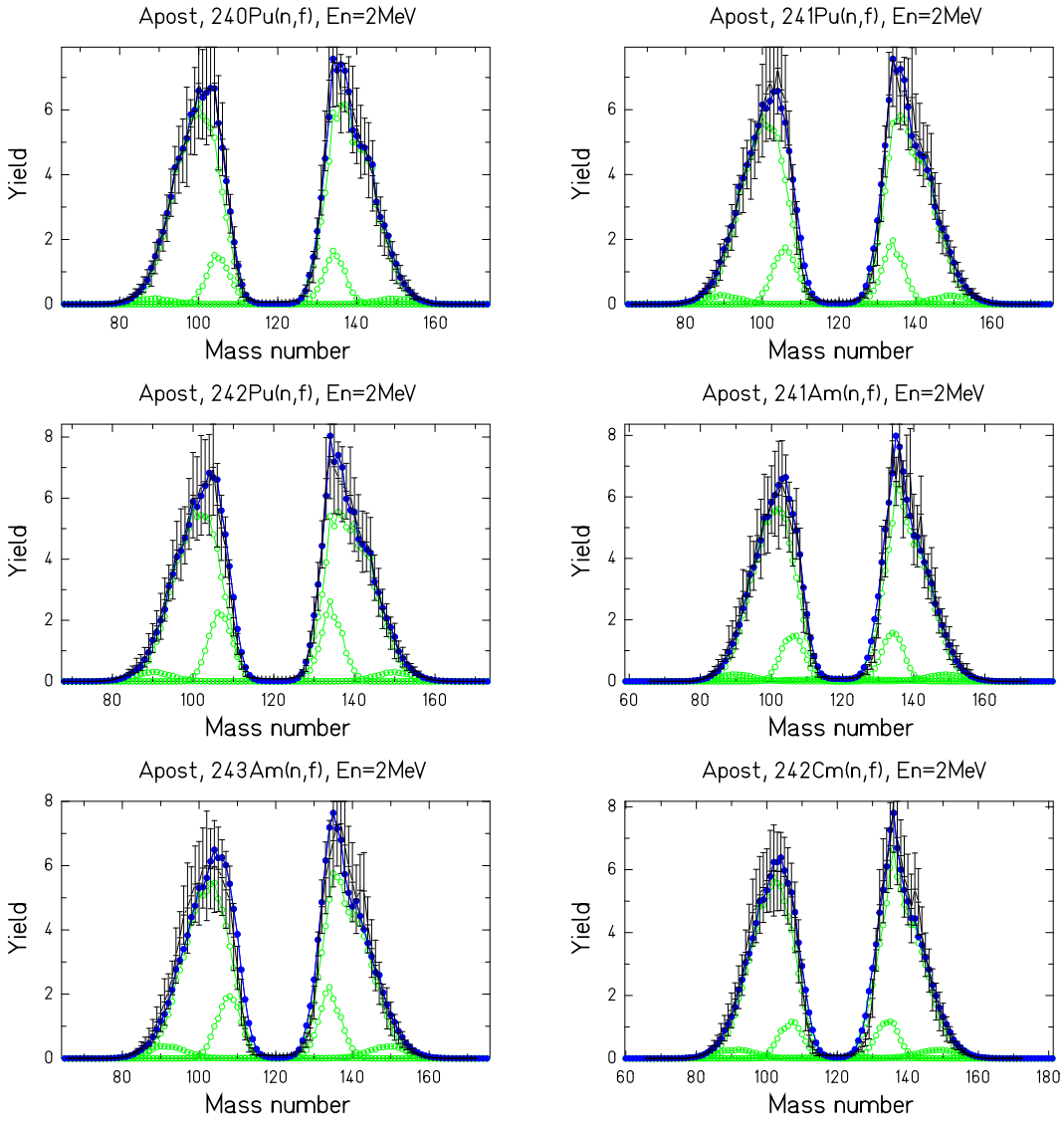

Note: Evaluated and experimental mass distributions (black symbols) of fission fragments in comparison with the results of the GEF code (green and blue symbols) in a linear scale. Fast-neutron-induced fission, part 3.

Figure 50: Mass distributions, (n_{fast}, f), part 3, logarithmic scale

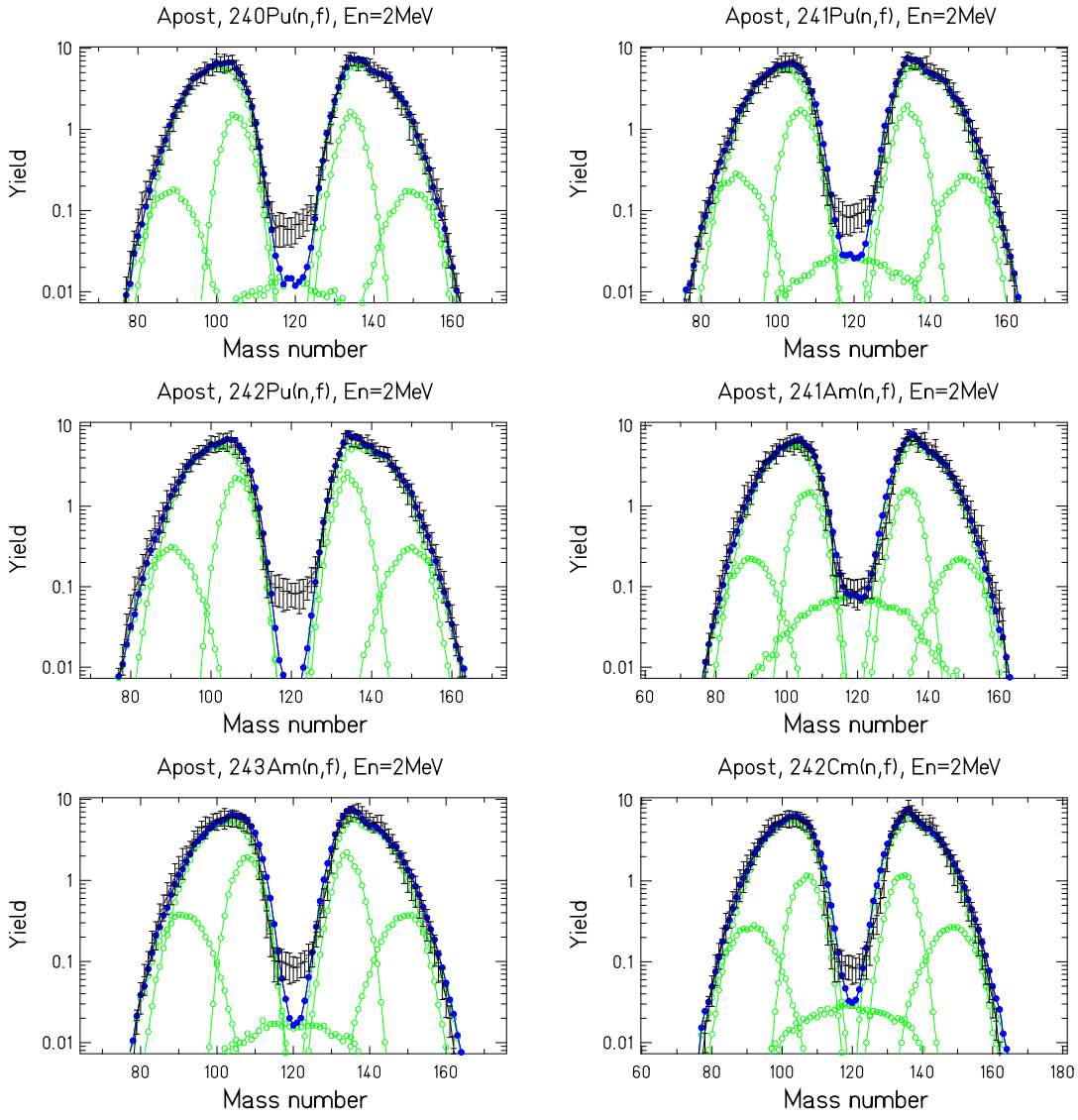

Note: Evaluated and experimental mass distributions (black symbols) of fission fragments in comparison with the results of the GEF code (green and blue symbols) in a logarithmic scale. Fast-neutron-induced fission, part 3.

Figure 51: Mass distributions, (n_{fast}, f), part 4, linear scale

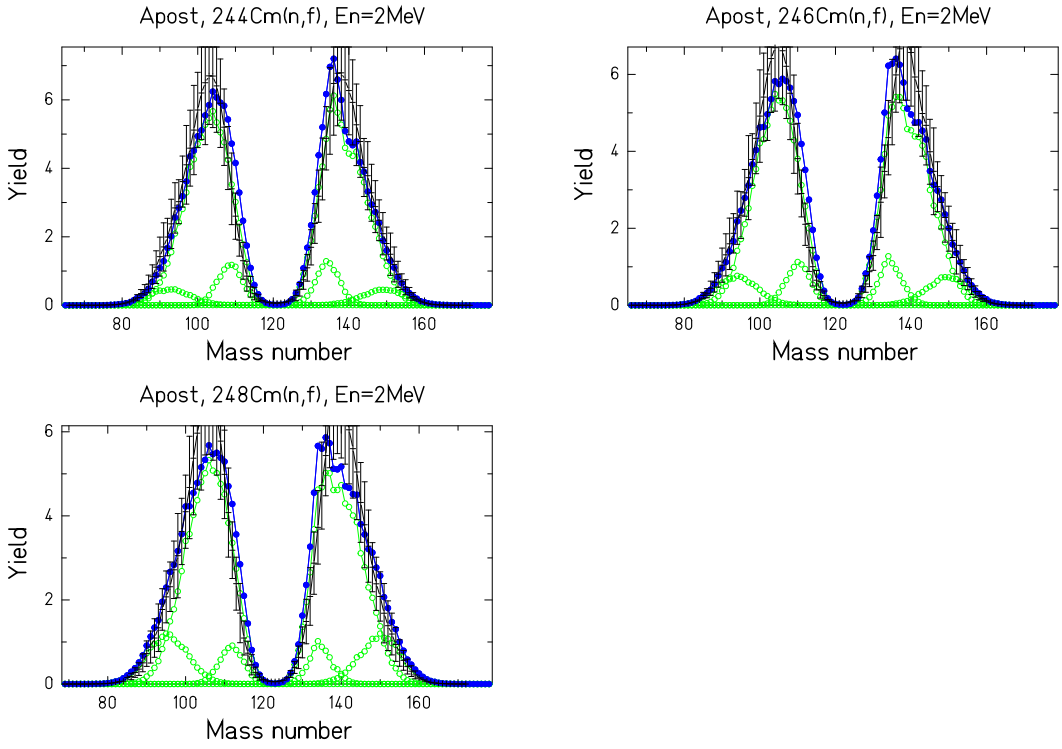

Note: Evaluated and experimental mass distributions (black symbols) of fission fragments in comparison with the results of the GEF code (green and blue symbols) in a linear scale. Fast-neutron-induced fission, part 4.

Figure 52: Mass distributions, (n_{fast}, f), part 4, logarithmic scale

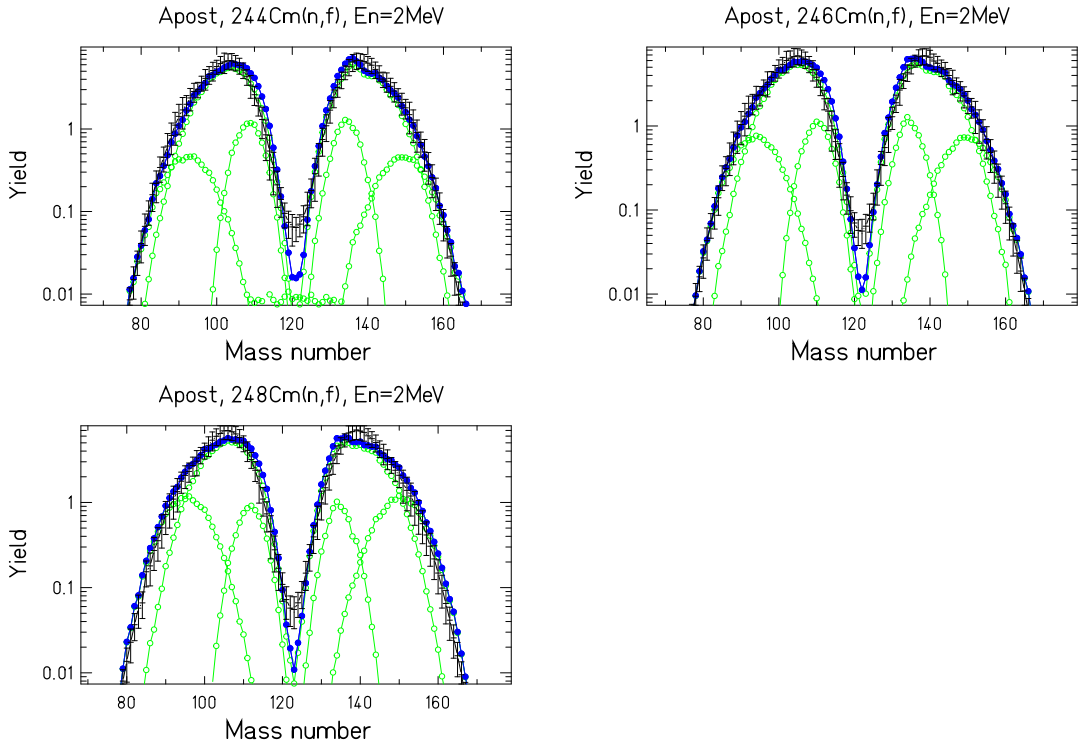

Note: Evaluated and experimental mass distributions (black symbols) of fission fragments in comparison with the results of the GEF code (green and blue symbols) in a logarithmic scale. Fast-neutron-induced fission, part 4.

8.2.3.4 Fission induced by 14-MeV neutrons: A few mass distributions were measured for fission induced by 14-MeV neutrons. They are compared with results of the GEF code in Figures 53 to 56.

Figure 53: Mass distributions, E_n = 14 MeV, part 1, linear scale

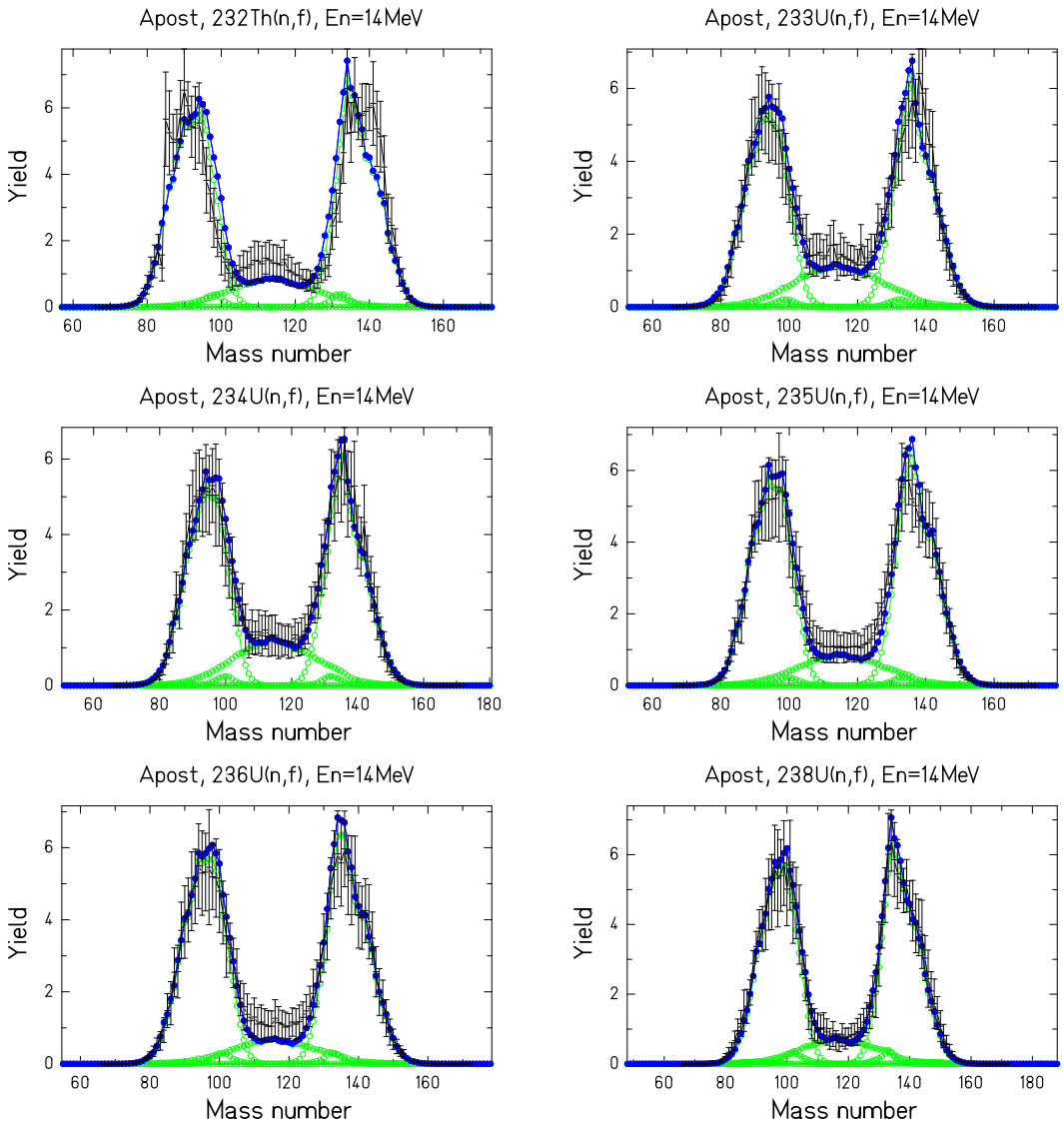

Note: Evaluated and experimental mass distributions (black symbols) of fission fragments in comparison with the results of the GEF code (green and blue symbols) in a linear scale. 14-MeV-neutron-induced fission, part 1.

Figure 54: Mass distributions, E_n = 14 MeV, part 1, logarithmic scale

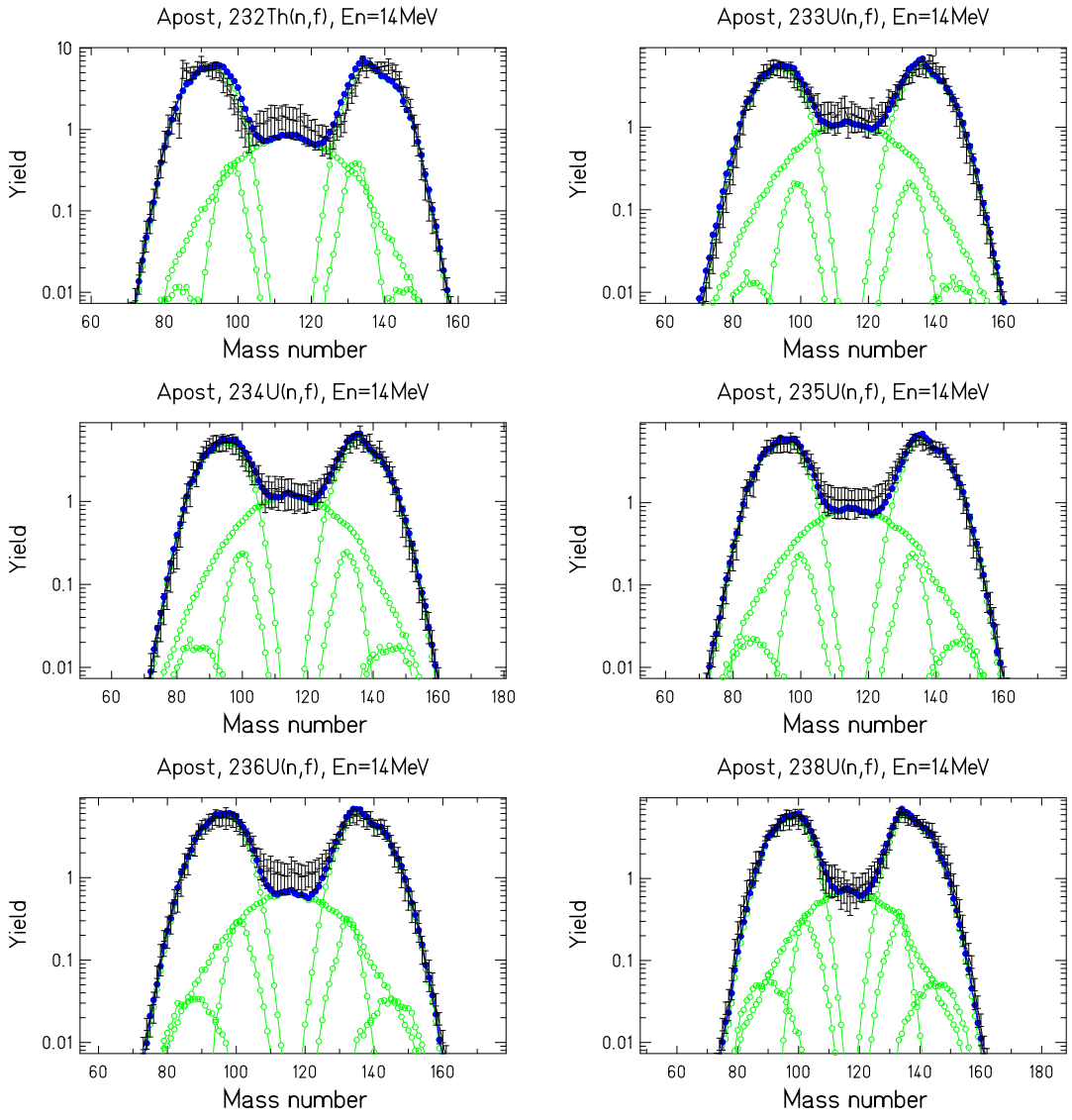

Note: Evaluated and experimental mass distributions (black symbols) of fission fragments in comparison with the results of the GEF code (green and blue symbols) in a logarithmic scale. 14-MeV-neutron-induced fission, part 1.

Figure 55: Mass distributions, E_n = 14 MeV, part 2, linear scale

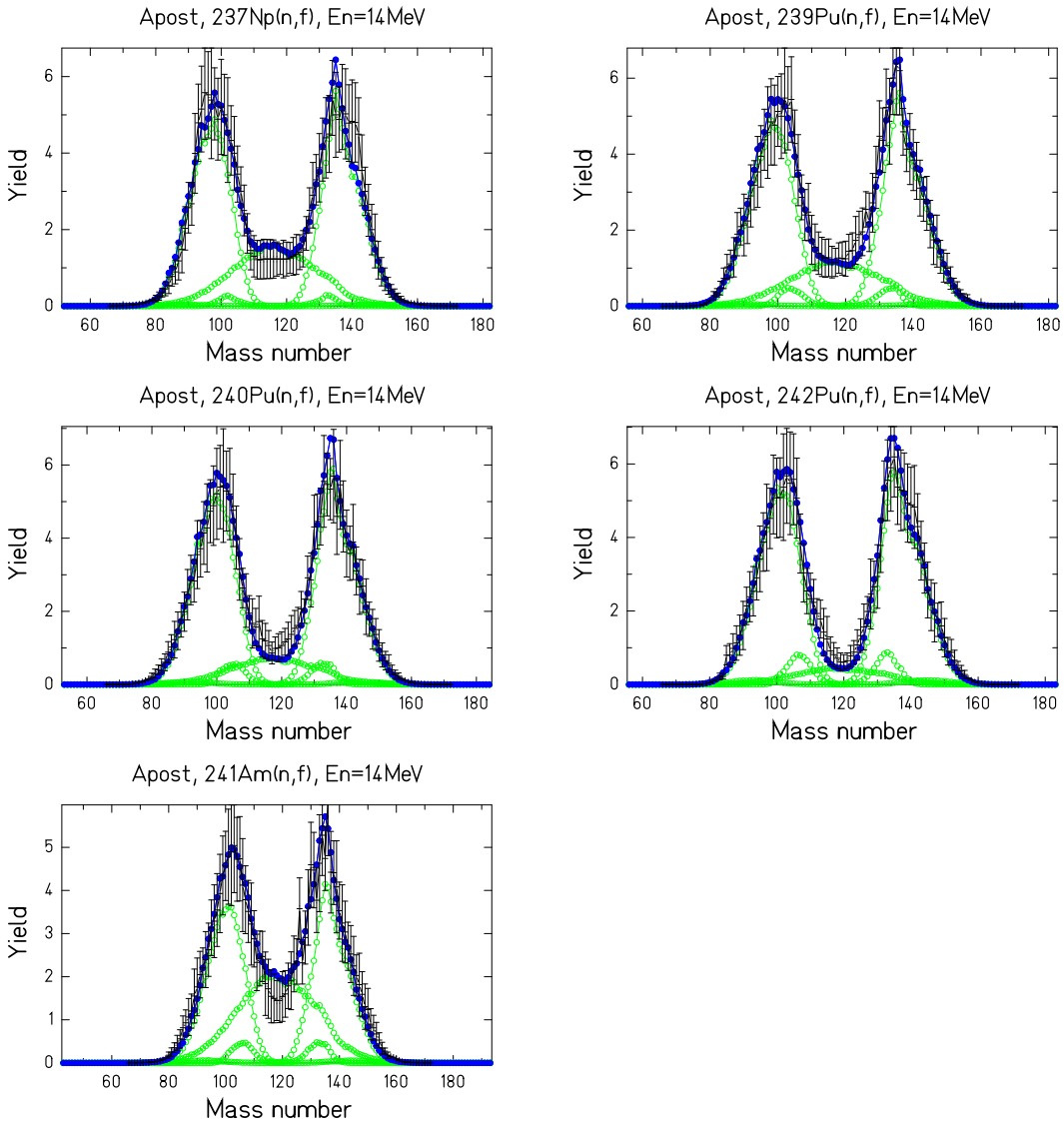

Note: Evaluated and experimental mass distributions (black symbols) of fission fragments in comparison with the results of the GEF code (green and blue symbols) in a linear scale. 14-MeV-neutron-induced fission, part 2.

Figure 56: Mass distributions, E_n = 14 MeV, part 2, logarithmic scale

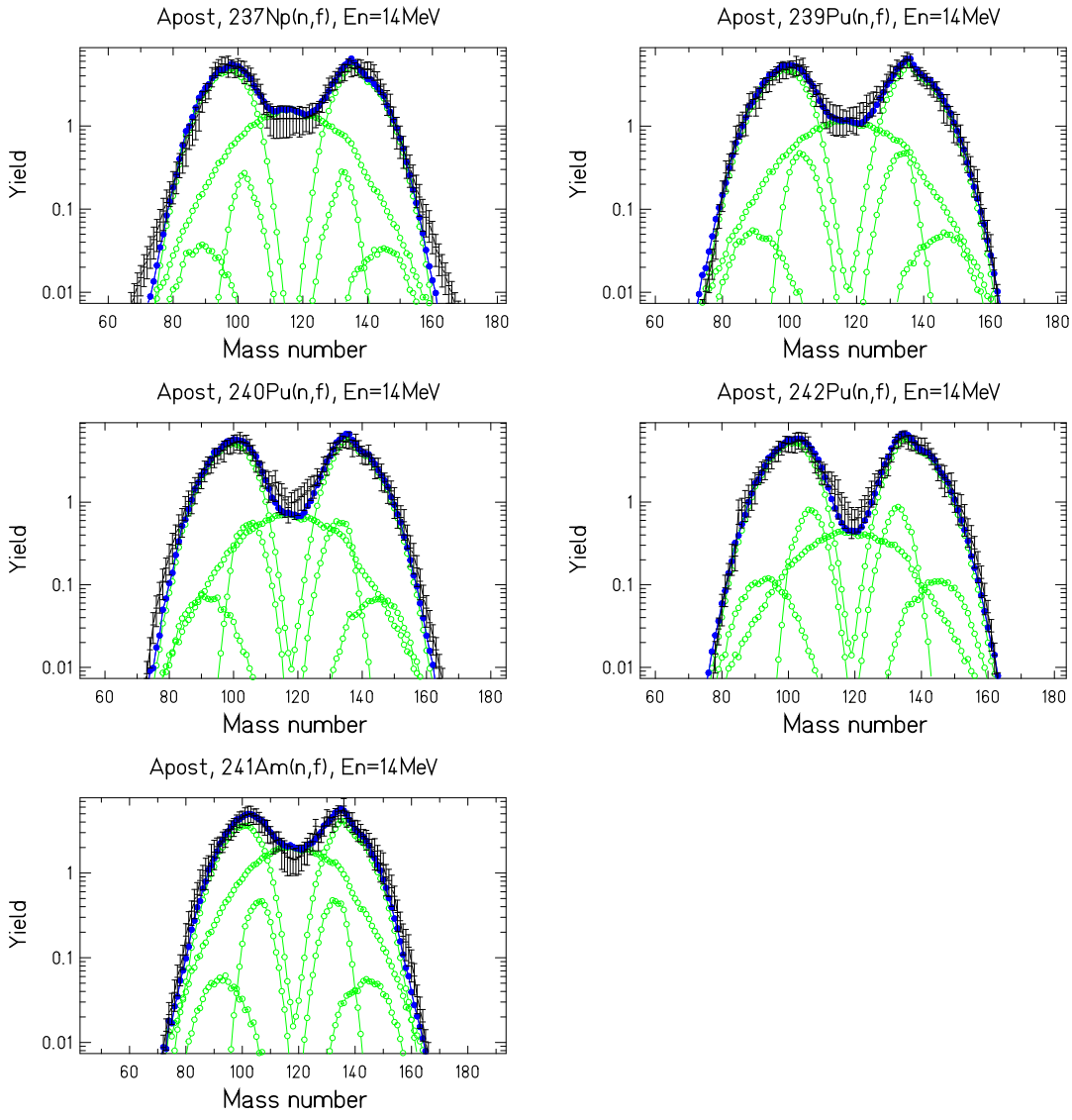

Note: Evaluated and experimental mass distributions (black symbols) of fission fragments in comparison with the results of the GEF code (green and blue symbols) in a logarithmic scale. 14-MeV-neutron-induced fission, part 2.

8.2.4 Deviations

The reduced Chi-squared values of the deviations between GEF results and evaluated data are given in Tables 8 to 10. There are no Chi-squared values given for distributions of pre-neutron or provisional masses because of several reasons. In some cases, the uncertainties are not available. Moreover, the data are disturbed by the finite mass resolution and possible problems in the corrections for prompt-neutron emission [19]. The tables also give the references to the sources of the data shown in Figures 31 to 56.

Table 8: Measured and evaluated mass distributions, part 1

System	Measured quantity	Reference	reduced Chi-squared
^{238}U(sf)	A_{post}	[141]	3.2
^{238}Pu(sf)	A_{pre}	[142]	—
^{240}Pu(sf)	A_{pre}	[142]	—
^{242}Pu(sf)	A_{pre}	[142]	—
^{244}Pu(sf)	A_{pre}	[143]	—
^{244}Cm(sf)	A_{post}	[141]	1.4
^{246}Cm(sf)	A_{post}	[141]	1.1
^{248}Cm(sf)	A_{post}	[141]	7.8
^{250}Cf(sf)	A_{post}	[141]	0.9
^{252}Cf(sf)	A_{post}	[141]	0.6
^{253}Es(sf)	A_{post}	[141]	3.7
^{254}Fm(sf)	A_{post}	[141]	0.4
^{256}Fm(sf)	A_{post}	[141]	0.8
^{258}Fm(sf)	A_{prov}	[144]	—
^{259}Md(sf)	A_{prov}	[144]	—
^{260}Md(sf)	A_{prov}	[144]	—
^{256}No(sf)	A_{pre}	[145]	—
^{258}No(sf)	A_{prov}	[144]	—

Note: Measured and evaluated mass distributions used for the comparison in Figures 31 to 56, their nature and their references. The last column gives the sum of the squared deviations of the GEF results from the evaluated yields divided by the uncertainties of the empirical data per degrees of freedom (reduced Chi-squared). This value should be around 1 for a good description. Only yields larger than 0.01% have been considered.

Table 9: Measured and evaluated mass distributions, part 2

System	Measured quantity	Reference	reduced Chi-squared
^{259}Lr(sf)	A_{post}	[146]	—
^{260}Rf(sf)	A_{prov}	[144]	—
^{262}Rf(sf)	A_{pre}	[147]	—
^{227}Th(n$_{th}$,f)	A_{post}	[141]	420
^{229}Th(n$_{th}$,f)	A_{post}	[141]	26
^{232}U(n$_{th}$,f)	A_{post}	[141]	1.6
^{233}U(n$_{th}$,f)	A_{post}	[141]	1.2
^{235}U(n$_{th}$,f)	A_{post}	[141]	7.4
^{237}Np(n$_{th}$,f)	A_{post}	[141]	1.1
^{239}Pu(n$_{th}$,f)	A_{post}	[141]	1.2
^{240}Pu(n$_{th}$,f)	A_{post}	[141]	0.9
^{241}Pu(n$_{th}$,f)	A_{post}	[141]	0.7
^{242}Pu(n$_{th}$,f)	A_{post}	[141]	0.8
^{241}Am(n$_{th}$,f)	A_{post}	[141]	0.6
^{242}Am(n$_{th}$,f)	A_{post}	[141]	0.9
^{243}Cm(n$_{th}$,f)	A_{post}	[141]	1.7
^{245}Cm(n$_{th}$,f)	A_{post}	[141]	0.5
^{249}Cf(n$_{th}$,f)	A_{post}	[141]	0.7
^{251}Cf(n$_{th}$,f)	A_{post}	[141]	4.9
^{254}Es(n$_{th}$,f)	A_{post}	[141]	9.5
^{255}Fm(n$_{th}$,f)	A_{post}	[141]	5.6
^{232}Th(n,f), E$_n$=fast	A_{post}	[141]	1.7
^{231}Pa(n,f), E$_n$=fast	A_{post}	[141]	1.0
^{233}U(n,f), E$_n$=fast	A_{post}	[141]	1.0
^{234}U(n,f), E$_n$=fast	A_{post}	[141]	1.0
^{235}U(n,f), E$_n$=fast	A_{post}	[141]	1.5
^{236}U(n,f), E$_n$=fast	A_{post}	[141]	1.2
^{237}U(n,f), E$_n$=fast	A_{post}	[141]	0.4
^{238}U(n,f), E$_n$=fast	A_{post}	[141]	1.1
^{237}Np(n,f), E$_n$=fast	A_{post}	[141]	0.5

Note: Table 8 continued

Table 10: Measured and evaluated mass distributions, part 3

System	Measured quantity	Reference	reduced Chi-squared
^{238}Np(n,f), E_n=fast	A_{post}	[141]	0.5
^{238}Pu(n,f), E_n=fast	A_{post}	[141]	0.7
^{239}Pu(n,f), E_n=fast	A_{post}	[141]	0.6
^{240}Pu(n,f), E_n=fast	A_{post}	[141]	0.6
^{241}Pu(n,f), E_n=fast	A_{post}	[141]	0.7
^{242}Pu(n,f), E_n=fast	A_{post}	[141]	0.6
^{241}Am(n,f), E_n=fast	A_{post}	[141]	0.7
^{243}Am(n,f), E_n=fast	A_{post}	[141]	1.4
^{242}Cm(n,f), E_n=fast	A_{post}	[141]	1.4
^{244}Cm(n,f), E_n=fast	A_{post}	[141]	1.0
^{246}Cm(n,f), E_n=fast	A_{post}	[141]	1.0
^{248}Cm(n,f), E_n=fast	A_{post}	[141]	1.5
^{232}Th(n,f), E_n=14 MeV	A_{post}	[141]	1.7
^{233}U(n,f), E_n=14 MeV	A_{post}	[141]	0.7
^{234}U(n,f), E_n=14 MeV	A_{post}	[141]	0.3
^{235}U(n,f), E_n=14 MeV	A_{post}	[141]	0.5
^{236}U(n,f), E_n=14 MeV	A_{post}	[141]	0.4
^{238}U(n,f), E_n=14 MeV	A_{post}	[141]	0.3
^{237}Np(n,f), E_n=14 MeV	A_{post}	[141]	0.6
^{239}Pu(n,f), E_n=14 MeV	A_{post}	[141]	0.5
^{240}Pu(n,f), E_n=14 MeV	A_{post}	[141]	0.7
^{242}Pu(n,f), E_n=14 MeV	A_{post}	[141]	0.5
^{241}Am(n,f), E_n=14 MeV	A_{post}	[141]	0.6

Note: Table 8 continued

8.2.5 Charge polarisation and emission of prompt neutrons

The two fission products are not fully determined by their mass, because the protons and neutrons of the fissioning nucleus can be distributed in a different portion to the fragments at scission by charge polarisation. Furthermore, the emission of prompt neutrons from the excited fragments tends to decrease the neutron excess of the fragments. For calculating the nuclide distributions after prompt-neutron emission for which the most precise data are available, both the charge polarisation and the prompt-neutron emission must be considered. Data on the mass-dependent prompt-neutron multiplicity exist for a few fissioning systems. They provide the necessary information for disentangling the influence of charge polarisation and prompt-neutron emission on the neutron excess of the fission products.

Figure 57 shows the mean values and the standard deviations of the Z distributions for fixed post-neutron mass. Available experimental data in the light fission-fragment group of four fissioning systems [148, 59, 149, 150, 151] are compared with the result of the GEF code. The agreement is generally very good, except for the heaviest nuclei of the system ^{249}Cf(n$_{th}$,f). However, it is not clear, whether this discrepancy can be attributed to a shortcoming of the model, because the experiment suffered from insufficient Z resolution in this range.

The mass-dependent mean prompt-neutron multiplicity for ^{237}Np(n,f) [58] and ^{252}Cf(sf) [152] are shown below in the dedicated section. Also here one can observe a good reproduction of the experimental data by the GEF code.

Figure 57: Charge density of post-neutron fragments

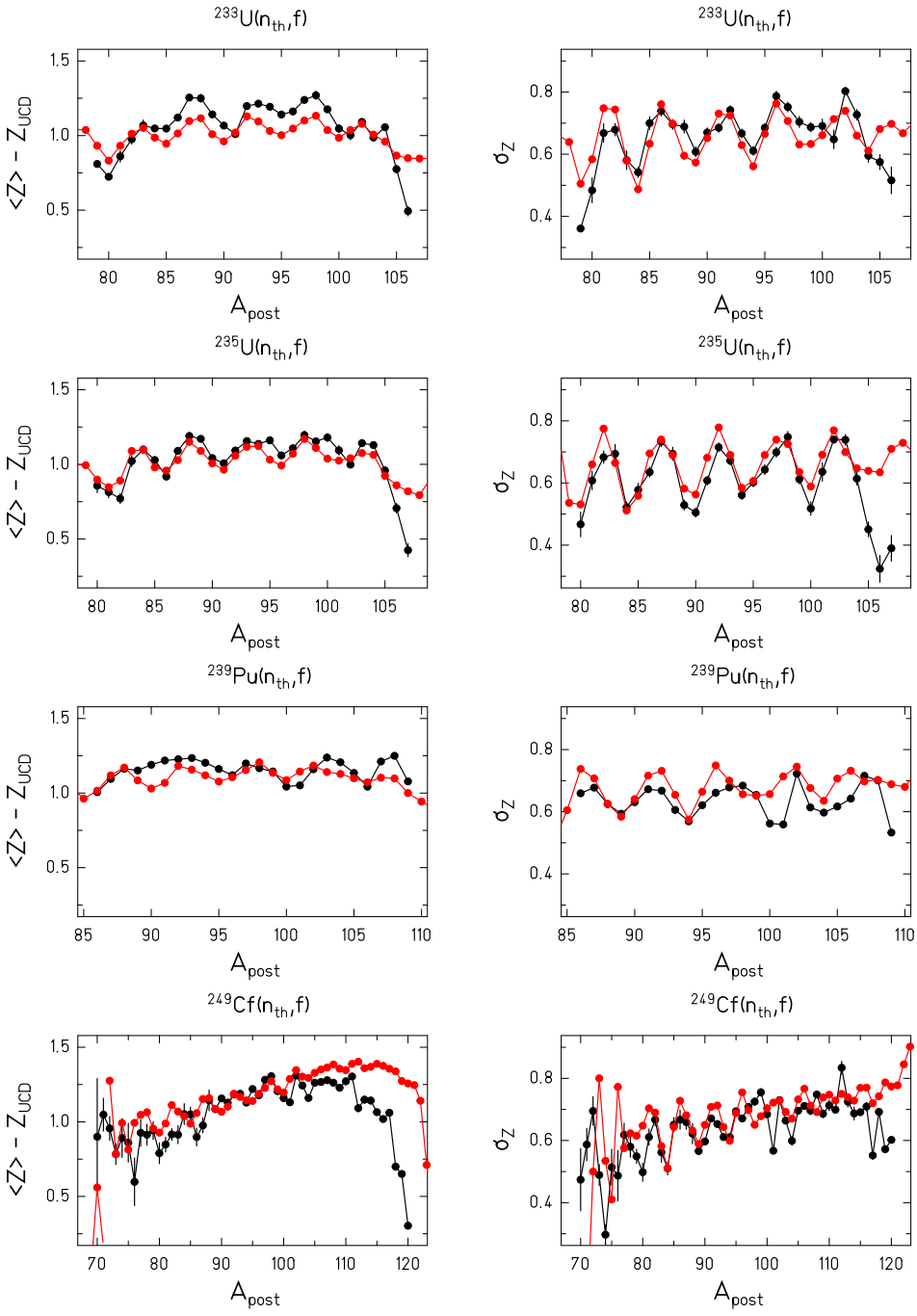

Note: Deviation of the mean fission-product nuclear charge for a fixed mass after prompt-neutron emission from the UCD value. Experimental data (black symbols) are compared with the results of the GEF code (red symbols).

8.2.6 Nuclide distributions

A detailed overview on the nuclide distribution is shown in Figures 58 to 67 for only one representative system because of the large quantity of this kind of data. In these figures, the empirical mass-chain yields for the system ^{235}U(n$_{th}$,f) are compared with the result of the GEF code. In the light fission-product group, the data measured at the Lohengrin spectrograph have been chosen [59], while the evaluation of A. Wahl [1] was used for the heavy group. However, only those elements of this evaluation were taken for which at least two data points were directly derived from experimental data.

In Figures 58 to 62, a logarithmic scale has been chosen, spanning the same range from 10^{-4}% to 10%. The error bars of the empirical data represent the uncertainties given in [59, 1]. The error bars of the GEF results represent the estimated uncertainties that were obtained by calculations with perturbed parameters. The relevant parameters were varied within their uncertainty range.

Figure 58: Isobaric Z distributions for ^{238}U(n$_{th}$,f), part 1, logarithmic scale

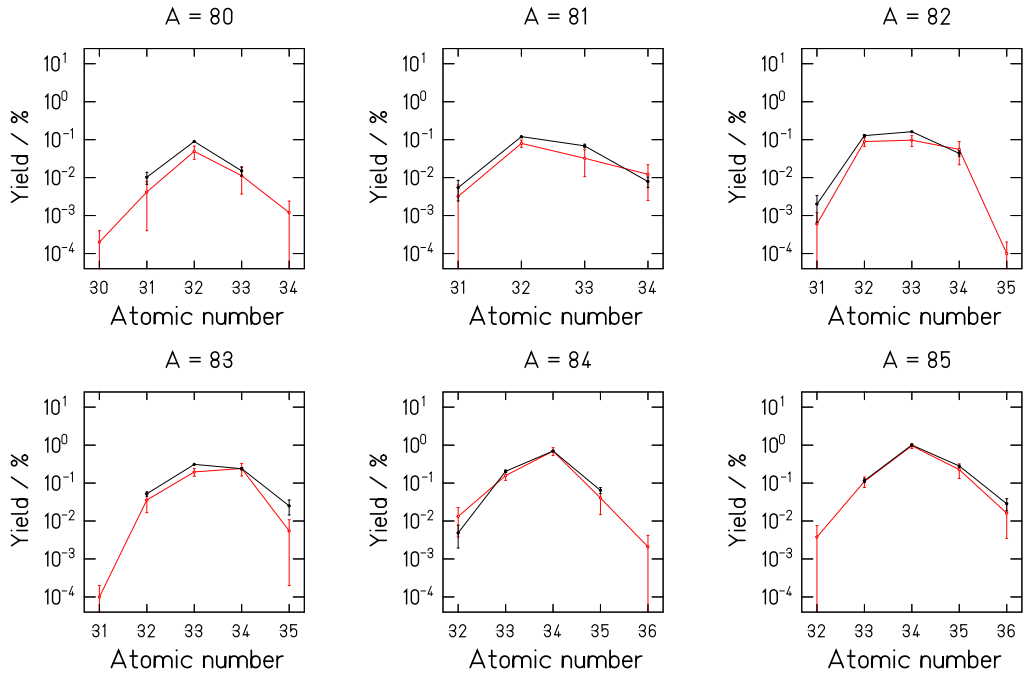

Note: Post-neutron isobaric element distributions in logarithmic scale. The experimental data [59] (black symbols) are compared with the results of the GEF code (red symbols). The mass numbers are specified in the figures.

Figure 59: Isobaric Z distributions for ^{238}U(n$_{th}$,f), part 2, logarithmic scale

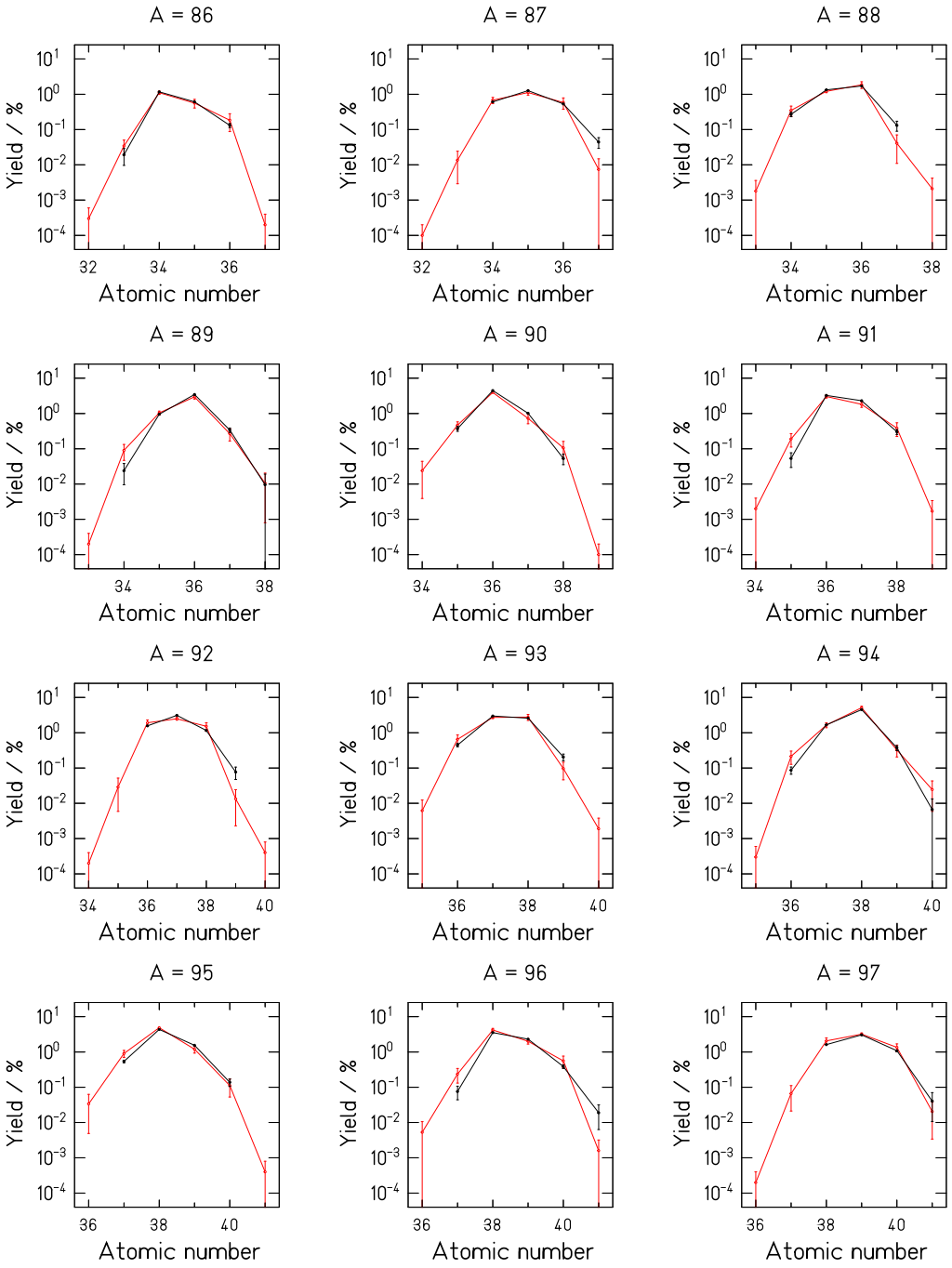

Note: Post-neutron isobaric element distributions in logarithmic scale. The experimental data [59] (black symbols) are compared with the results of the GEF code (red symbols). The mass numbers are specified in the figures.

Figure 60: Isobaric Z distributions for ^{238}U(n$_{th}$,f), part 3, logarithmic scale

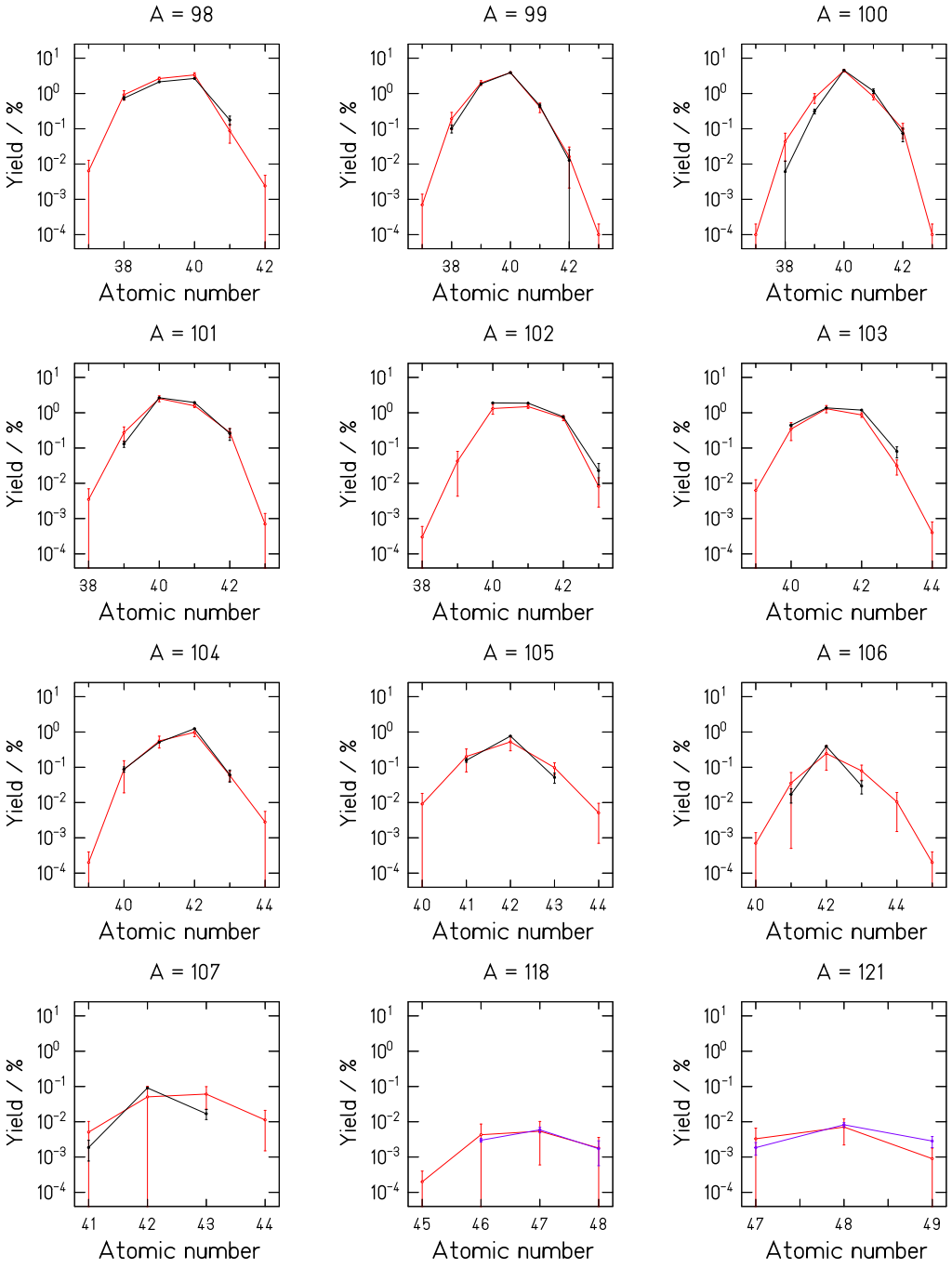

Note: Post-neutron isobaric element distributions in logarithmic scale. The experimental data [59] (black symbols) and the evaluated data [1] (violet symbols) are compared with the results of the GEF code (red symbols). The mass numbers are specified in the figures.

Figure 61: Isobaric Z distributions for ^{238}U(n$_{th}$,f), part 4, logarithmic scale

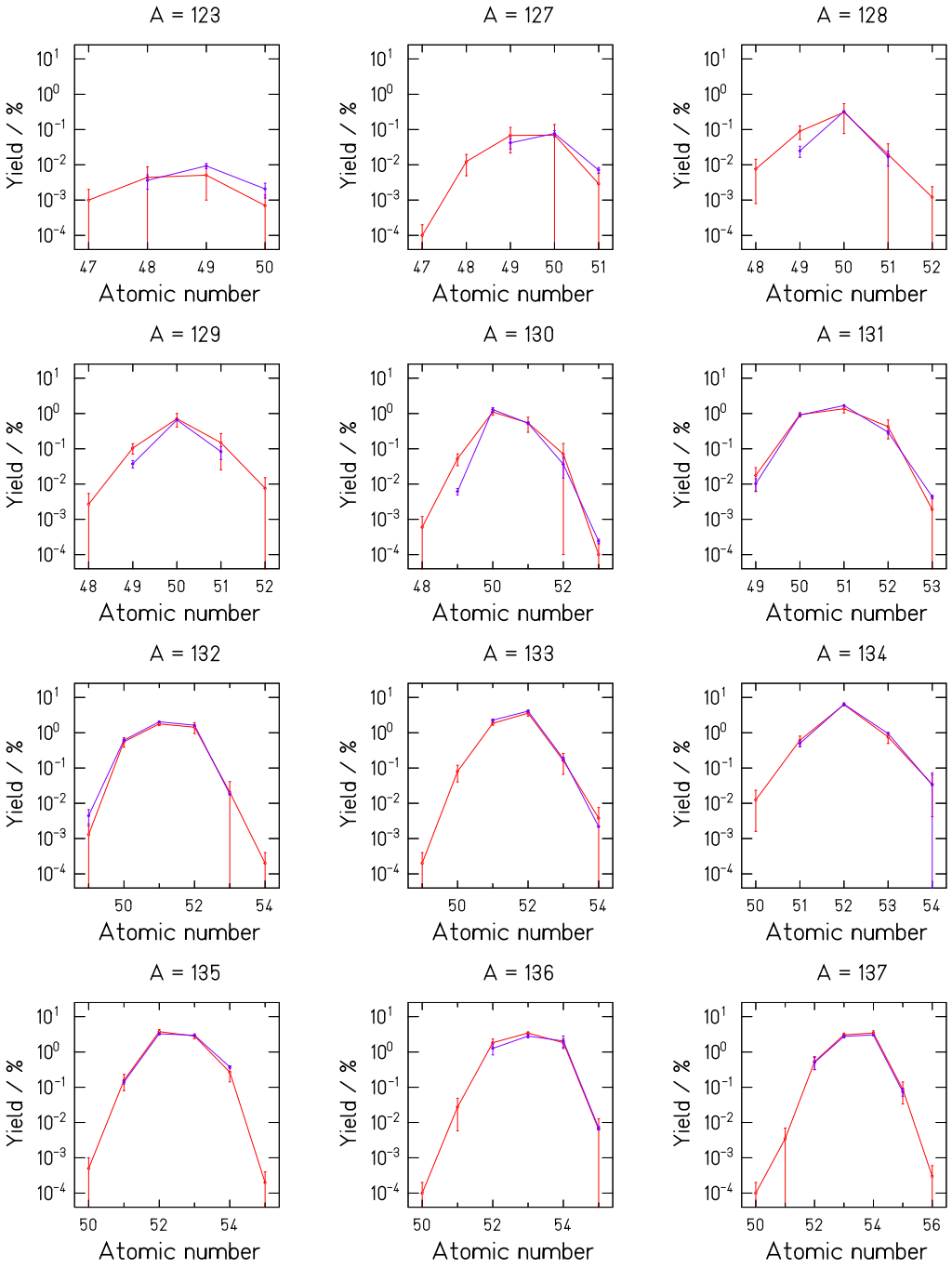

Note: Post-neutron isobaric element distributions in logarithmic scale. The evaluated data [1] (violet symbols) are compared with the results of the GEF code (red symbols). The mass numbers are specified in the figures.

Figure 62: Isobaric Z distributions for ^{238}U(n$_{th}$,f), part 5, logarithmic scale

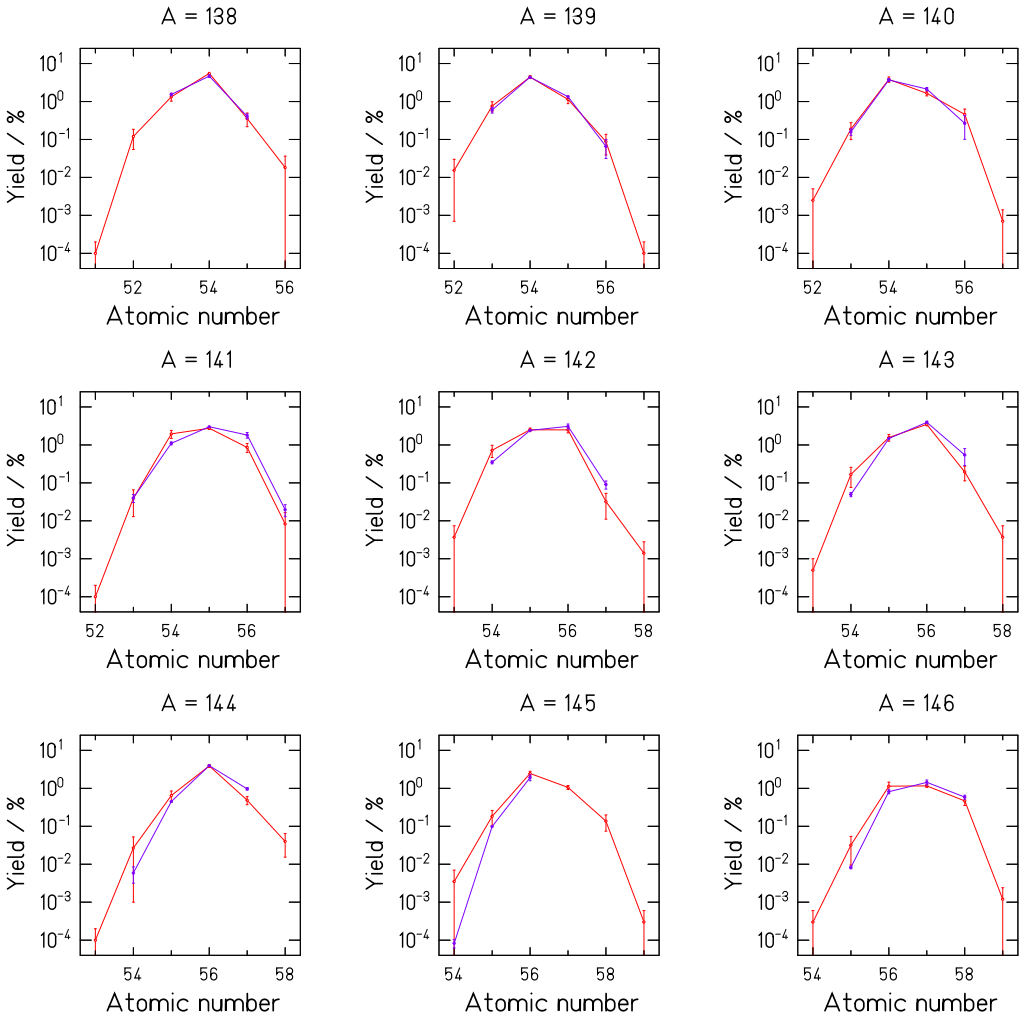

Note Post-neutron isobaric element distributions in logarithmic scale. The evaluated data [1] (violet symbols) are compared with the results of the GEF code (red symbols). The mass numbers are specified in the figures.

In Figures 63 to 67, the same data are shown in a linear scale. The range is adjusted to the range of the data in each case individually.

Figure 63: Isobaric Z distributions for ^{238}U(n$_{th}$,f), part 1, linear scale

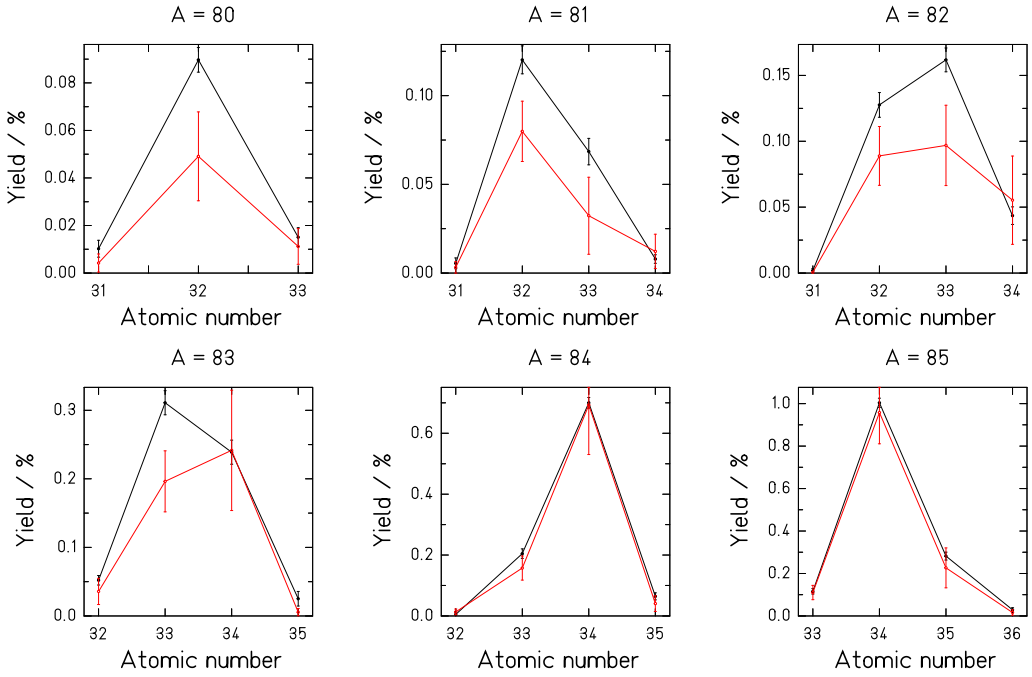

Note: Post-neutron isobaric element distributions in linear scale. The experimental data [59] (black symbols) are compared with the results of the GEF code (red symbols). The mass numbers are specified in the figures.

Figure 64: Isobaric Z distributions for ^{238}U(n$_{th}$,f), part 2, linear scale

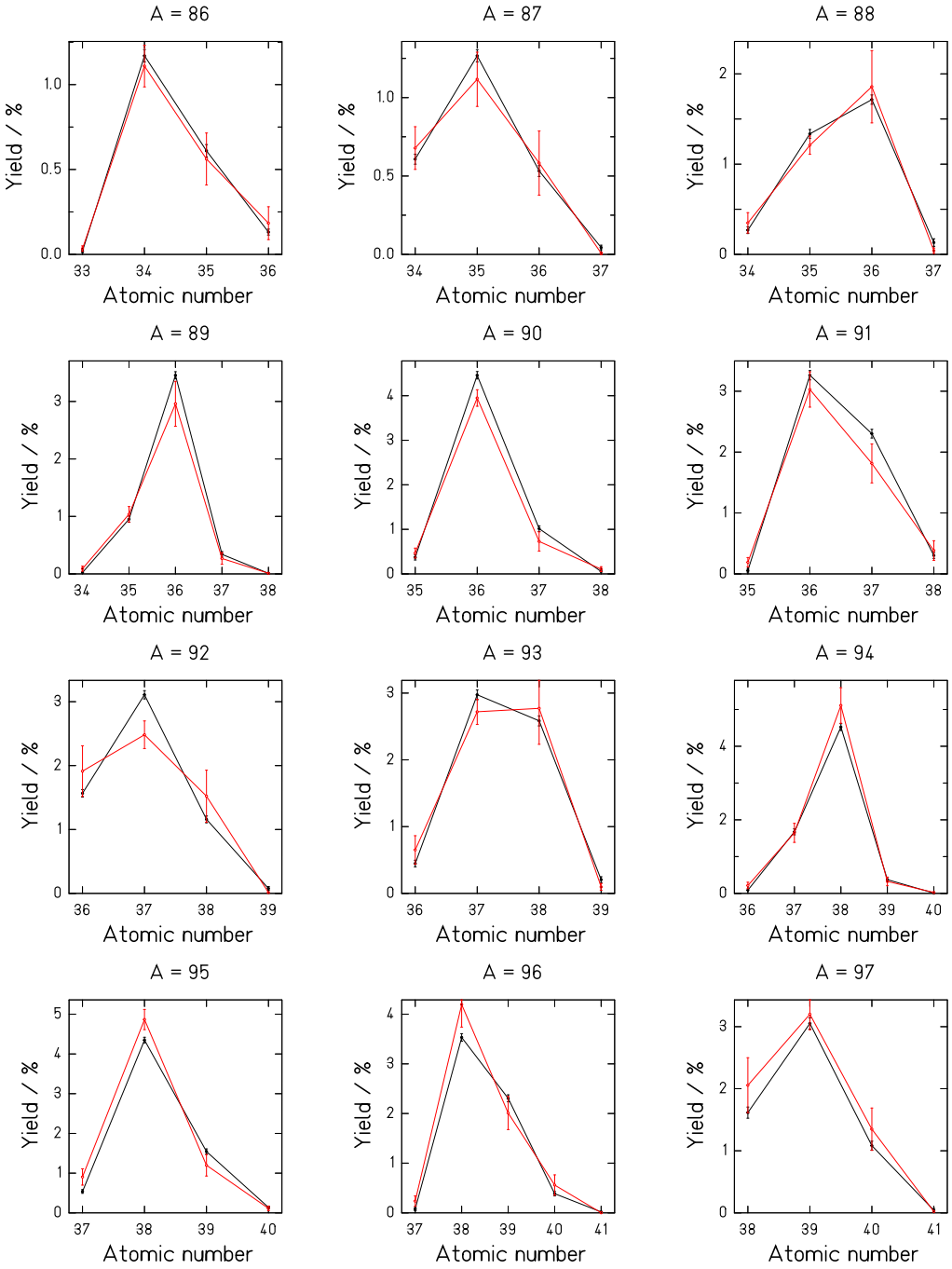

Note: Post-neutron isobaric element distributions in linear scale. The experimental data [59] (black symbols) are compared with the results of the GEF code (red symbols). The mass numbers are specified in the figures.

Figure 65: Isobaric Z distributions for ^{238}U(n$_{th}$,f), part 3, linear scale

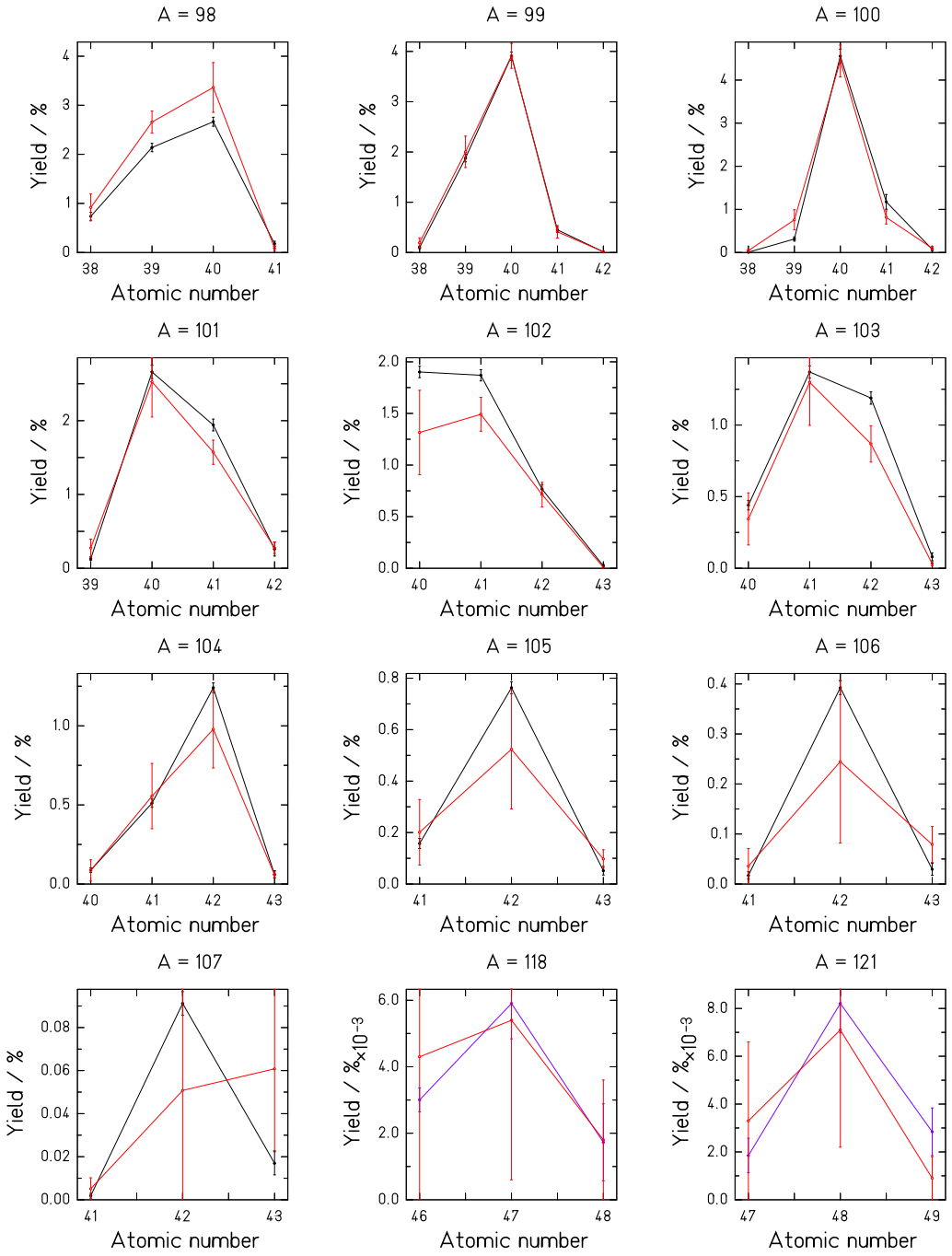

New: Post-neutron isobaric element distributions in linear scale. The experimental data [59] (black symbols) and the evaluated data [1] (violet symbols) are compared with the results of the GEF code (red symbols). The mass numbers are specified in the figures.

Figure 66: Isobaric Z distributions for ^{238}U(n$_{th}$,f), part 4, linear scale

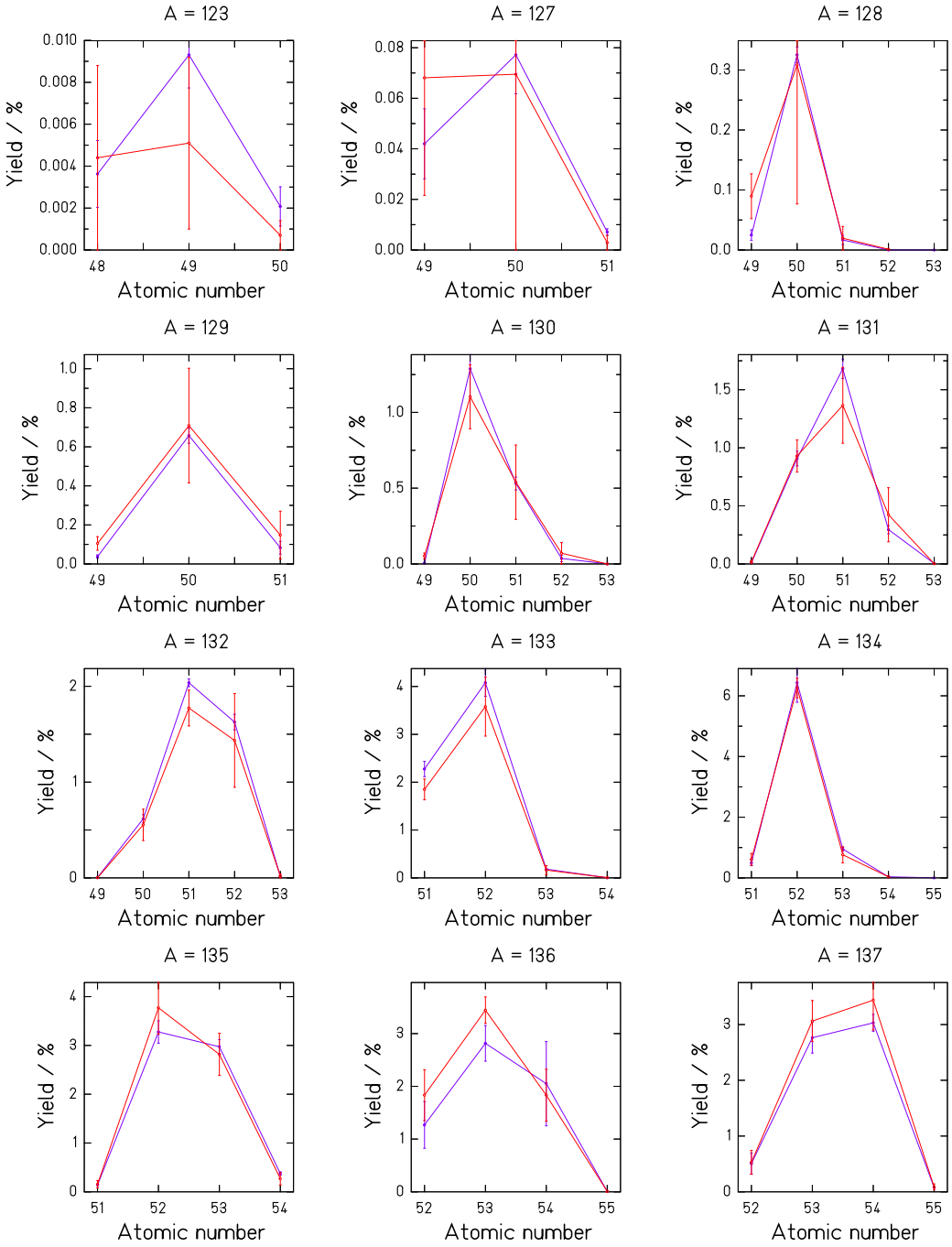

Note: Post-neutron isobaric element distributions in linear scale. The evaluated data [1] (violet symbols) are compared with the results of the GEF code (red symbols). The mass numbers are specified in the figures.

Figure 67: Isobaric Z distributions for ^{238}U(n$_{th}$,f), part 5, linear scale

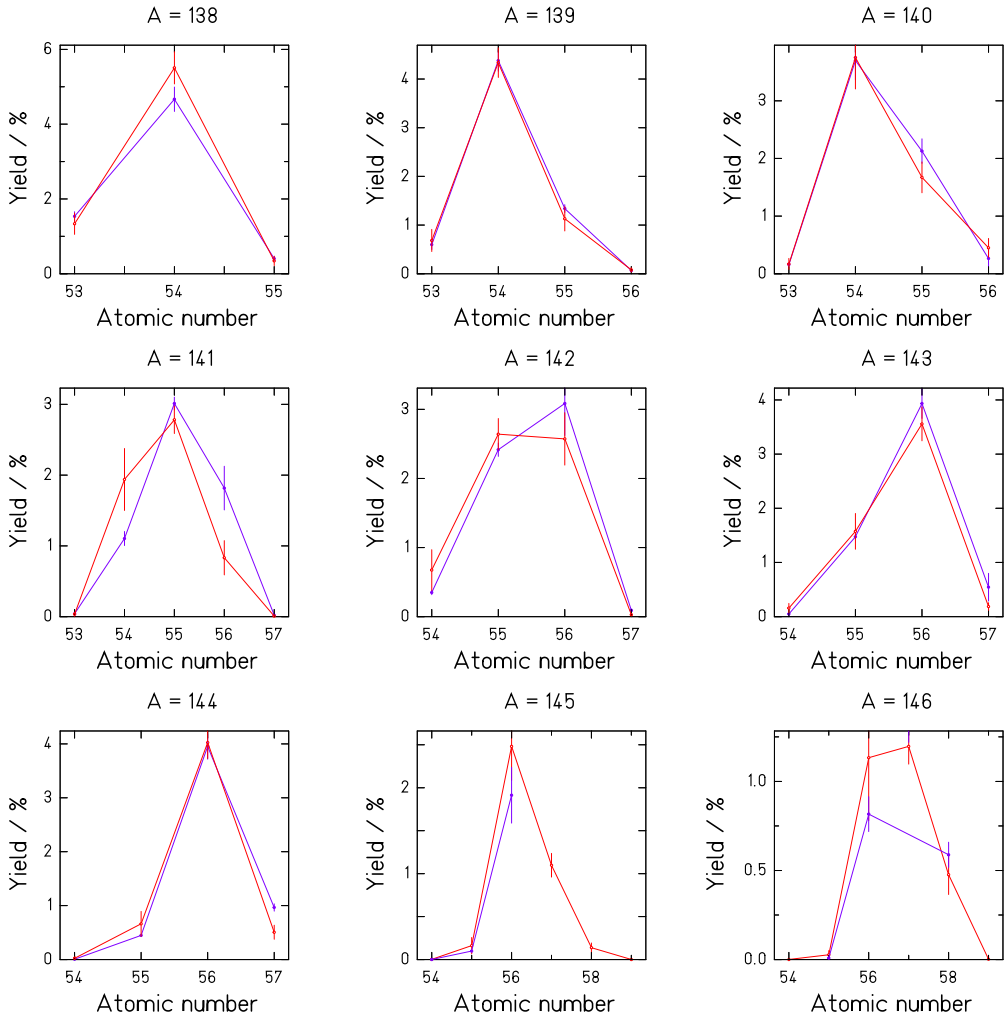

Note: Post-neutron isobaric element distributions in linear scale. The evaluated data [1] (violet symbols) are compared with the results of the GEF code (red symbols). The mass numbers are specified in the figures.

8.2.7 Energy dependence

In order to benchmark the GEF code up to 14 MeV, the fission yields of 3 masses are compared with the available data. As suggested in Reference [153], the masses 111, 115 and 140 were chosen. In order to be comparable, the shell effect at symmetry was set to +0.3 MeV for all systems, corresponding to a weak anti-shell. First, the ratio $Y(A = 115)/Y(A = 140)$ is shown in Figure 68. The GEF code is able to reproduce the global trend for all systems. Also the absolute values agree very well for the systems ^{238}U

Figure 68: Evolution of $Y(A = 115)/Y(A = 140)$ with excitation energy

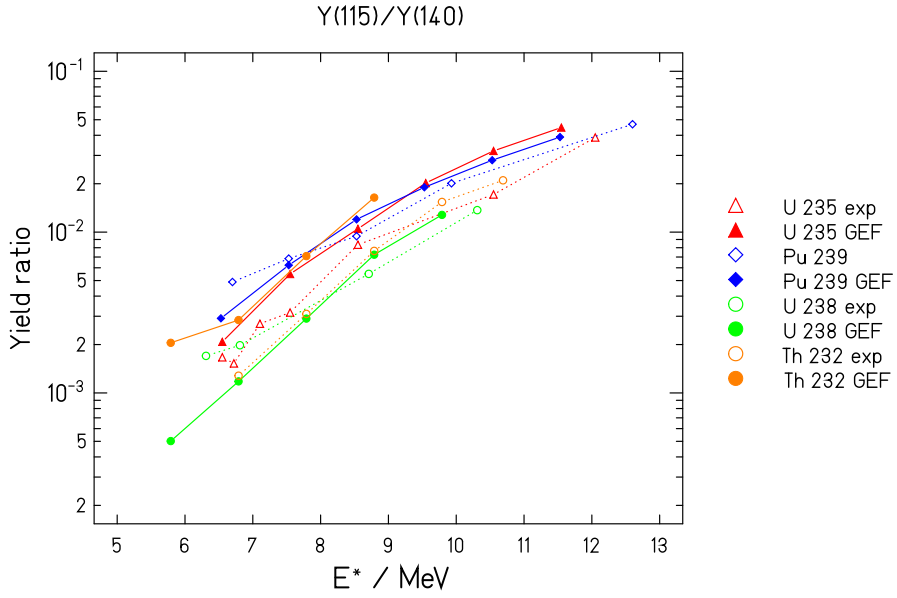

Note: $Y(A = 115)/Y(A = 140)$ for different fissioning nuclei as a function of the excitation energy. Experimental data [154, 155, 156, 157] are compared with the result of the GEF code.

and ^{239}Pu, while they are slightly overestimated for ^{235}U and ^{232}Th. Thus, the conditional barrier for symmetric fission seems to be slightly higher for these two systems.

Two regions in energy domain should be studied: before the second-chance threshold, where the fissioning nucleus is always the same but with different excitation energy and after this threshold, where multi-chance fission must be taken into account. While Figure 68 shows the evolution of the valley/peak ratio, represented by the $A = 115/A = 140$ ratio, before the threshold (≈10-12 MeV) for neutron-induced fission of ^{232}Th, ^{235}U, ^{238}U, and ^{239}Pu, the fission yields of two masses near symmetry ($A = 111$, $A = 115$) and one mass near the heavy peak ($A = 140$) are compared in Figures 69 and 70 for the systems ^{235}U and ^{239}Pu in an extended energy range. Obviously, the values above the threshold for second-chance fission ($E_n \approx 6$ MeV) and third-chance fission $E_n \approx 12$ MeV are well reproduced. The calculation slightly underestimates the yields of the system ^{235}U near symmetry above the threshold of second-chance fission, a deviation which is opposite to the deviation found at lower energies revealed in Figure 68. However, the yield near the asymmetric peak at $A = 140$ is underestimated in this low-energy range for both systems.

According to Tables 11 and 12, the calculated probabilities for first-chance fission at $E = 8$ MeV and $E = 14$ MeV are somewhat higher, but still close to the values given in the ENDF/B-VII library [141].

As the difference of some specific masses can be the result of some local effects, the complete fission-yield distributions were studied for 4 MeV, 8 MeV and 14 MeV where

Figure 69: Energy dependence of mass yields in ^{235}U(n,f)

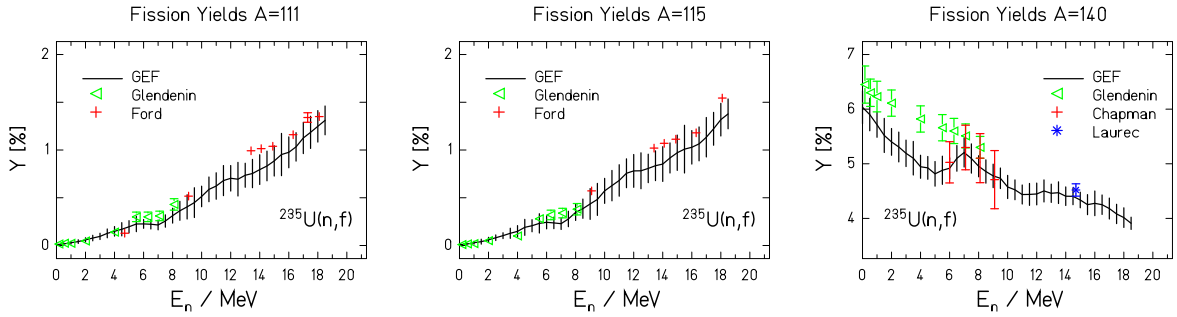

Note: Measured fission yields of $A = 111$ (left), $A = 115$ (middle) and $A = 140$ (right) for ^{235}U(n,f) as a function of E_n [154, 158, 159] are compared with the GEF results. The hatched band indicates the uncertainty of the calculated values.

Table 11: First-chance probability for ^{235}U(n,f), $E_n = 8$ MeV and 14 MeV.

Energy	GEF first-chance relative probability	Library first-chance relative probability
8 MeV	54.3 %	46.1 %
14 MeV	25.2 %	29.6 %

Table 12: First-chance probability for ^{239}Pu(n,f), $E_n = 8$ MeV and 14 MeV.

Energy	GEF first-chance relative probability	Library first-chance relative probability
8 MeV	80.4 %	65.6 %
14 MeV	59.5 %	44.8 %

Figure 70: Energy dependence of mass yields in ^{239}Pu(n,f)

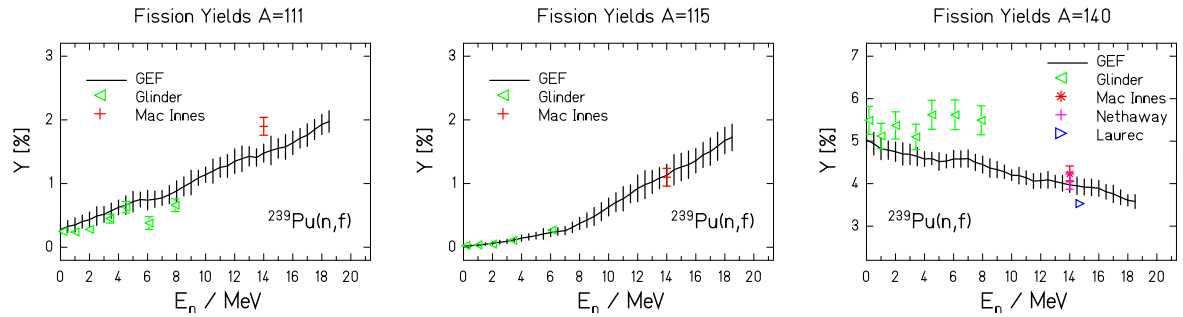

Note: Measured fission yields of $A = 111$ (left), $A = 115$ (middle) and $A = 140$ (right) for ^{239}Pu(n,f) as a function of E_n [155, 159, 160] are compared with the GEF results. The hatched band indicates the uncertainty of the calculated values.

library evaluations are also available. Figure 71 shows the fission-yield distributions for ^{235}U at 4 and 8 MeV. The predicted fission-yield distribution at 4 MeV overestimates the experimental data slightly. At 8 MeV, there exist two data-sets from different experiments. The GEF prediction is close to the symmetric data of Glendenin et al. but higher than the data from Chapman et al.. This is in line with an analysis reported in [153], where comparisons were made with the Ford experimental data which are consistent with the Glendenin data, according to which the Chapman data seem to systematically underestimate the symmetric part.

The fission yields of the system ^{239}Pu(n,f) at 4 and 8 MeV shown in Figure 72 are rather well reproduced by the GEF code.

In addition to the comparison at the lower energies (4 and 8 MeV), the fission yields of ^{235}U and ^{239}Pu at $E_n = 14$ MeV are shown in Figure 73. Some deviations to the evaluated data are found: The calculated fission yields at symmetry are slightly lower than the evaluated values. However, in view of the scattering of the data from different experiments this deviation is not very significant. Moreover, the calculated yield distribution shows a more pronounced structure in the peak regions if compared to the evaluation. Also, this deviation is not very significant due to the uncertainties and the large scattering of the experimental data.

Figure 71: Mass yields for ^{235}U(n,f), E_n = 4 MeV and 8 MeV

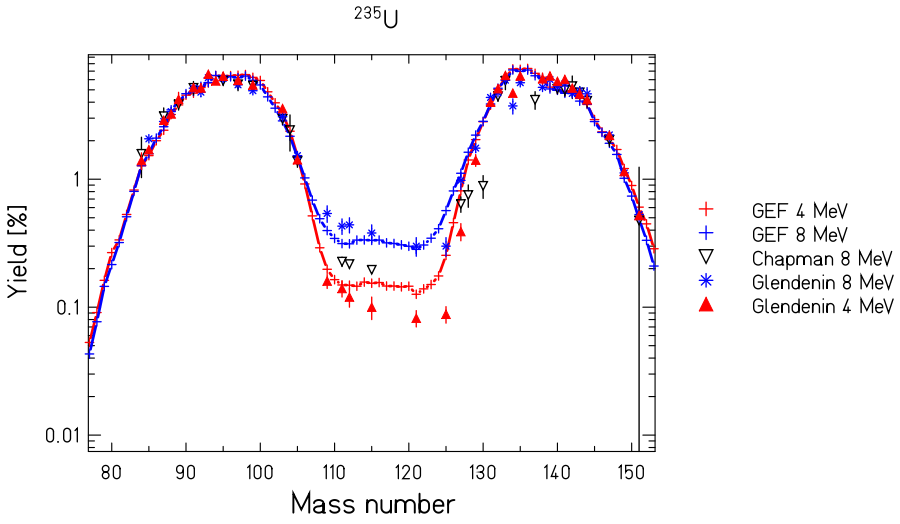

Note: Fission-yield distribution for ^{235}U(n,f) for E_n = 4 MeV and E_n = 8 MeV. Experimental data [154, 161] are compared with the GEF results.

Figure 72: Mass yields for ^{239}Pu(n,f), E_n = 4 MeV and 8 MeV

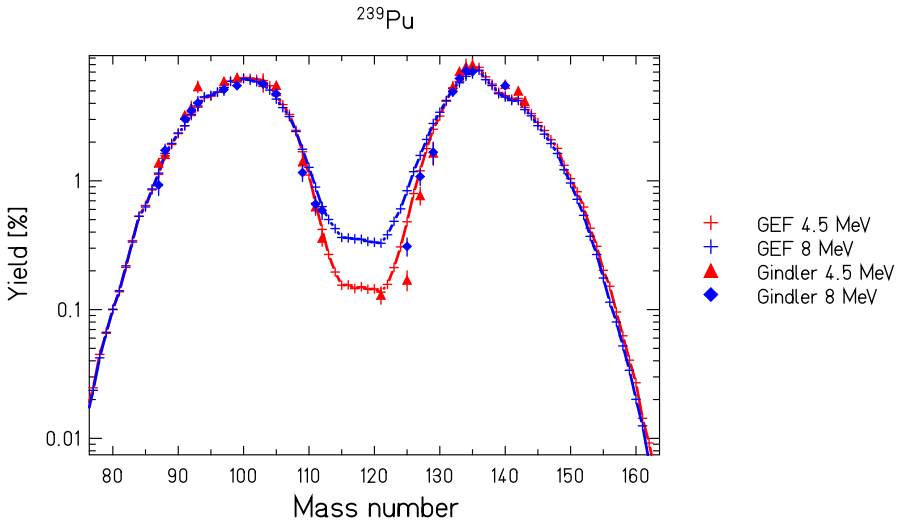

Note: Fission-yield distribution for ^{239}Pu(n,f) for E_n = 4 MeV and E_n = 8 MeV. Experimental data [155] are compared with the GEF results.

Figure 73: Mass yields for ^{235}U(n,f) and ^{239}Pu(n,f), E_n = 14 MeV

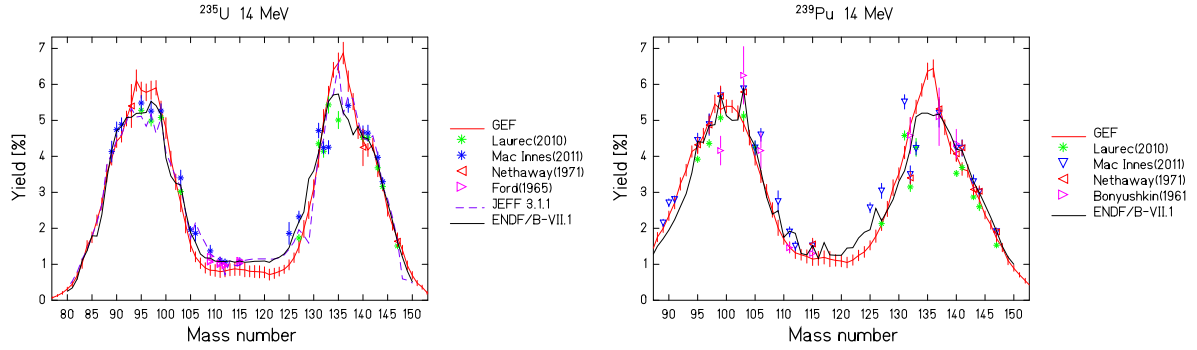

Note: Fission-yields distributions for ^{235}U(n,f) and ^{239}Pu(n,f) at E_n=14 MeV. The result of the GEF model is compared with values from data libraries and experimental data. Colour points correspond to experimental data [158, 160, 159]. The calculated values are given together with their estimated uncertainties

8.2.8 Discussion

8.2.8.1 Mass distributions: Figures 31 to 56 demonstrate an overall rather good agreement between the empirical mass distributions and the results of the GEF code. In particular, the variation of the global shape for different systems and as a function of energy, which can be rather drastic in some cases, are rather well reproduced. When looking in detail, however, more or less severe discrepancies can also be found for several systems. In this comparison, it must be considered that the quality of the experimental data that are shown in the figure or that were used for the evaluation may differ strongly from one system to another one. In many cases, the evaluation is based on incomplete data of limited quality due to the difficulties of the experiment. In other cases, there are plenty of high-quality data. The mass distributions from double-energy or double-velocity measurements generally suffer from a limited resolution. The data from spontaneous fission of the heaviest nuclei are important for revealing the strong variation of the global shape from system to system, but the uncertainties are rather large, e.g. due to low statistics. Thus, a careful analysis is needed to decide whether the discrepancies between empirical data and calculated spectra are to be attributed to shortcomings of the model or to uncertainties of the empirical data.

A first step towards a quantitative assessment is the determination of the reduced Chi-squared values of the differences between empirical data and calculated values. The Chi-squared values were only determined for the evaluated data, because they are mostly based on radio-chemical methods with full identification of the fission-product mass, while the mass spectra from kinematical measurements are distorted by the limited resolution. These Chi-squared values are listed in Table 8.

The Chi-squared values are also shown in an histogram in Figure 74. The distribution

has a main peak around unity, containing 50 of the 59 cases. It reaches from 0.3 to 1.7 and, thus, seems to be essentially in agreement with the expected scattering caused by the uncertainties of the evaluated data. This picture already does not give indications for a shortcoming of the model in these 50 cases which represent 85 % of the cases. The uncertainties of the model seem to contribute little to the Chi-squared values of the systems in the main peak, because this peak centres at about unity without taking the uncertainties of the model into account. The remaining 9 cases will be investigated in more detail.

Figure 74: Chi-squared deviations for mass distributions

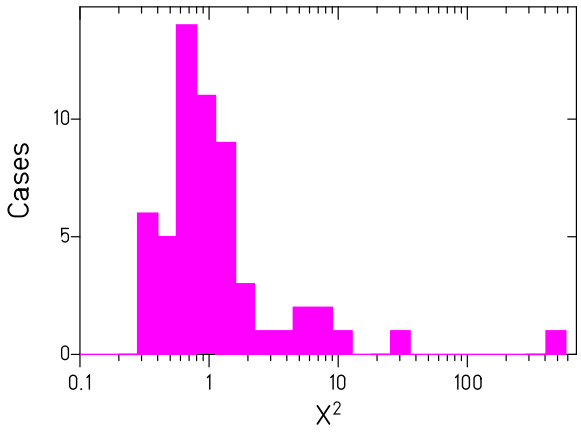

Note: Chi-squared deviations of the mass distributions from GEF calculations from the empirical data (Figures 31 - 56) in a logarithmic binning. The height of the histogram represents the number of cases per bin.

The largest Chi-squared value is observed for the system ^{227}Th(n$_{th}$,f). An inspection of the figure, in particular in the logarithmic scale, reveals that the evaluated spectrum has a very unusual shape that differs substantially from the other spectra of near-by systems: The descent from the asymmetric mass peaks towards symmetry is exceptionally gradual. This observation is a strong argument for assuming that the problem is caused by an unrealistic result of the evaluation in this case.

The second-highest Chi-squared value is found for the system ^{229}Th(n$_{th}$,f). Also in this case, the largest deviations occur on the inner wings of the asymmetric peaks. This time, the slope agrees, but the borders towards symmetry are shifted in the calculation. In this case, there exist very reliable and precise data from different sources, including an experiment at the Lohengrin spectrograph [148]. Thus, this problem must be attributed to a shortcoming of the model. This displacement of the inner wing of the asymmetric mass peak with respect to the global description of the model, which agrees in practically all other cases, is very astonishing. It indicates a local effect that is not considered in the model.

Seven other systems show larger Chi-squared values between 3.2 and 9.5: ^{238}U(sf), ^{248}Cm(sf), ^{253}Es(sf), ^{235}U(n$_{th}$,f), ^{251}Cf(n$_{th}$,f), ^{254}Es(n$_{th}$,f), and ^{255}Fm(n$_{th}$,f). The deviations for ^{238}U(sf) are not severe and look unsystematical. ^{248}Cm(sf), ^{253}Es(sf), ^{251}Cf(n$_{th}$,f), ^{254}Es(n$_{th}$,f), and ^{255}Fm(n$_{th}$,f) form a group of nuclei that seem to suffer from incomplete data and/or large uncertainties. A closer look reveals two abnormalities: All systems show rather schematic shapes at the outer wings of the mass distributions that differ substantially from the spectrum of ^{252}Cf(sf) which has been investigated in great detail. In addition, ^{254}Es(n$_{th}$,f) and even more clearly ^{255}Fm(n$_{th}$,f) show a shift of the minimum around symmetry with respect to the calculation. The mass distribution of ^{255}Fm(n$_{th}$,f) is symmetric around A=128 $\pm$ 0.5, which is half the mass of the fissioning system. Thus, there is no room for neutron evaporation, although the systematics suggests a mean prompt-neutron yield around 5. Finally, ^{235}U(n$_{th}$,f) is a very peculiar case. For this nucleus, the measurements are so precise that the experimental uncertainties are appreciably smaller than the general uncertainties of the model calculation. Thus, although the evaluated mass spectrum is very well reproduced by the calculation, relatively small deviations lead to a large Chi-squared value.

In summary, from the 59 evaluated mass distributions, we found one case where a shortcoming of the model is clearly proven. In 6 cases, it seems that the evaluation suffers from poor data. In addition, the uncertainties of the evaluation have been underestimated, causing large Chi-squared values. A closer look to these cases does not give indications for a shortcoming of the model but rather for somewhat faulty evaluations. In one case, the measured yields (and thus the evaluated data) are so precise that the uncertainties of the model exceed the uncertainties of the evaluation substantially. This leads to large Chi-squared values, although the mass distribution is well reproduced.

A closer view to the mass distributions reveals some additional somewhat minor problems either in the evaluation or in the model. The calculated yields around symmetry often deviate from the empirical data. The prediction of the low yields at symmetry is very demanding due to their high sensitivity to excitation energy and the strong variation from system to system. This is particularly critical for fast-neutron-induced fission, where the neutron-energy distribution in the experiment might be rather broad, and the energy distribution of fissioning systems is weighted with the energy-dependent fission probability of the specific system. Moreover, experimental data in the region of very low yields near symmetry are very scarce, and the uncertainties are large. In the right wing of the left peak for the system ^{237}Np(n$_{th}$,f) appears a structure, which is probably caused by a contamination of the target by a heavier nucleus. Note that the position of the heavy fission-product group is roughly independent of the fissioning nucleus, while the position of the light fission-fragment group moves accordingly. There are several systems, where the outer wings of the evaluated mass distribution appear to have a schematic, unrealistic shape, probably due to the lack of reliable data (in addition to the systems already mentioned above): ^{250}Cf(sf), ^{232}U(n$_{th}$,f), and ^{237}Np(n,f) at E_n = 14 MeV are the most prominent cases.

8.2.8.2 Charge polarisation and emission of prompt neutrons: There is a rather limited amount of data on the neutron excess of the fission products. Figure 57 proves that the mean neutron excess and the fluctuations are well reproduced over the large range from ^{233}U(n$_{th}$,f) to ^{249}Cf(n$_{th}$,f). The reason for the deviations for $A_{post} > 105$ from ^{249}Cf(n$_{th}$,f) is not clear, because the resolution of the experiment was insufficient to distinguish the energy-loss signals from the different elements. The data show very nicely the influence of an even-odd staggering, predominantly in the Z distribution. The good reproduction of the mass-dependent mean prompt-neutron multiplicity for ^{237}Np(n,f) as a representative for a lighter system and ^{252}Cf(sf) as a representative for a heavier system that will be discussed in Section 8.4 shows that the influence of charge polarisation and prompt-neutron emission is correctly modelled in the GEF code. In particular, the transport of the additional energy from the 5.55 MeV neutron to the heavy fragment is correctly reproduced [98].

8.2.8.3 Nuclide distributions: The isobaric Z distributions shown in Figures 58 to 67 demonstrate a very good agreement of the GEF calculations with the measured data for the system ^{235}U(n$_{th}$,f). For almost all mass chains, the error bars of the evaluation and the error bars from the estimated uncertainties of the model calculation overlap. Due to the good agreement of the mean value and the standard deviation of the isobaric Z distributions also for other systems shown in Figure 57 one expects that the nuclide distributions of other systems are described with a similar quality.

8.2.8.4 Energy dependence: The relative intensities of the fission fragments at symmetry are most sensitive to the excitation energy of the fissioning system. The general increase of the valley-to-peak ratio of the mass distributions is rather well described by the GEF model. This validates the statistical approach assumed for the population of the fission channels, including the parametrisation of the level densities. There are mostly minor deviations in the absolute values, but they do not seem to be systematical.

On the basis of this analysis one can expect that the GEF model is suited to give reliable estimations of the complete fission-fragment yields at higher energies, at least up to excitation energies around 20 MeV, where experiments are scarce and in most cases very incomplete.

8.2.9 Conclusion and outlook

The overall quality of the GEF code for predicting the fission-product yields was demonstrated on the basis of all mass distributions of the ENDF/B-VII evaluation and other data, comprising measured fission-product mass distributions, mass-dependent prompt-neutron yields and mass-chain Z yields. Severe shortcomings of the model appeared only for the system ^{229}Th(n$_{th}$,f), while deficiencies of the evaluation were found for a number of other systems.

From the careful comparison of the evaluated data and the predictions of the GEF code it becomes evident that the GEF code can be applied to substantially improve the quality of evaluated data.

8.3 Isomeric yields

The angular-momentum distribution cannot be directly measured and is often extracted from the isomeric ratio. In order to reduce the bias due to the model used for the extraction of the angular momentum, the only benchmark on the prediction of the angular momentum detailed here are the isomeric ratios.

The Naik compilation [162, 163] was used as a reference for experimental data. These isomeric ratios are usually extracted from γ-ray spectroscopy coupled with radio-chemistry technique. This technique relays on the values of the branching ratio I_γ which are often known with an uncertainty larger than 5-10%, which consequently leads to large uncertainties on the isomeric ratio. Moreover, the nuclei studied have a long life time (> 1 minute) and are in the heavy peak. Very few measurements were performed on the light peak. As the angular momentum depends on the mass of the fragment, new measurements on the light peak will be welcome.

The isomeric ratio predicted by the GEF model depends on the mass of the fragment, the deformation of the fragment, the Z parity of the fragment, the excitation energy, the spin of the compound nucleus, and on the spin difference between the isomeric state and the ground state. These dependencies will be studied in this section.

Figure 75 represents the ratio of the isomeric yield (Y_m) over the sum of the isomeric

Figure 75: Isomeric ratios for ^{239}Pu(n$_{th}$,f).

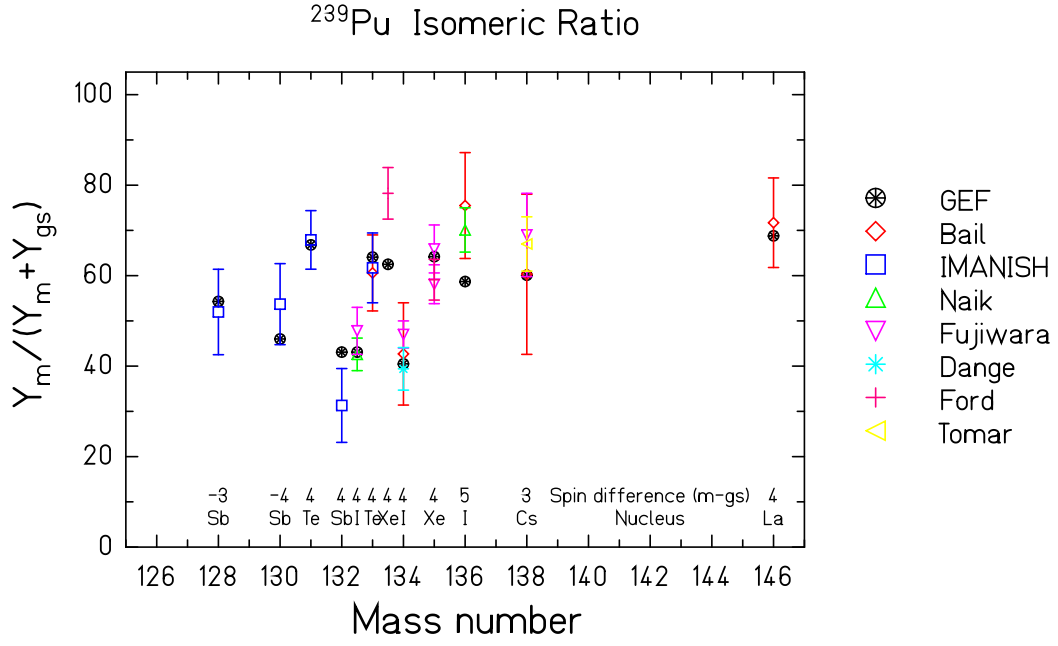

Note: Measured isomeric ratios for ^{239}Pu(n$_{th}$,f) [162, 163, 164] are compared with the GEF results.

yield and the ground-state yield ($Y_m + Y_{gs}$) for the ^{239}Pu(n$_{th}$,f) reaction. The GEF prediction agrees with the experimental data within the 1σ- uncertainty in the majority of cases. The agreement does not depend on the Z parity : the odd-Z isomeric ratios (Sb, I, Cs, La) are predicted with the same quality as the even-Z isomeric ratios (Te, Xe). The quality does not seem to be influenced by the mass of the fragment, at least on the heavy peak. The spin difference, defined as $Spin(isomer) - Spin(groundstate)$ is nearly always the same (values around four in most cases), so the influence of this difference cannot be studied. However, it can be seen on the chain of the Sb isotopes that a negative spin difference is not problematic for the GEF model.

Figure 76: Isomeric ratios for odd-Z compound nuclei

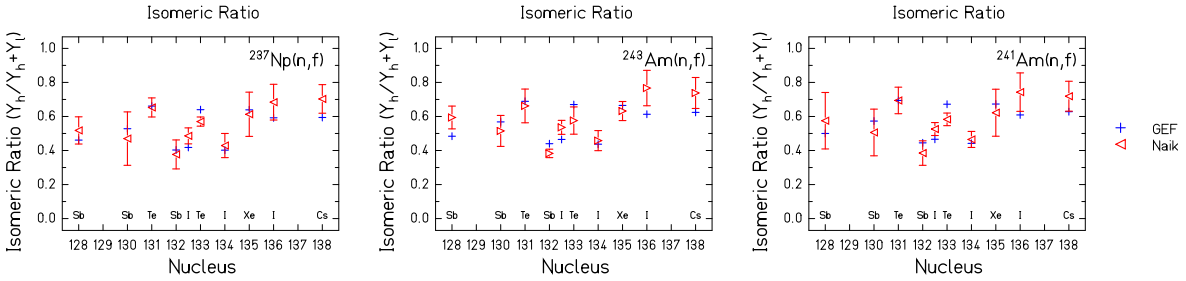

Note: Measured isomeric ratios for odd-Z compound nuclei: ^{237}Np (5/2+) (n,f), ^{241}Am (5/2-) (n,f), ^{243} Am (5/2+) (n,f) [165] are compared with the GEF results.

Figure 77: Isomeric ratios for even-Z compound nuclei

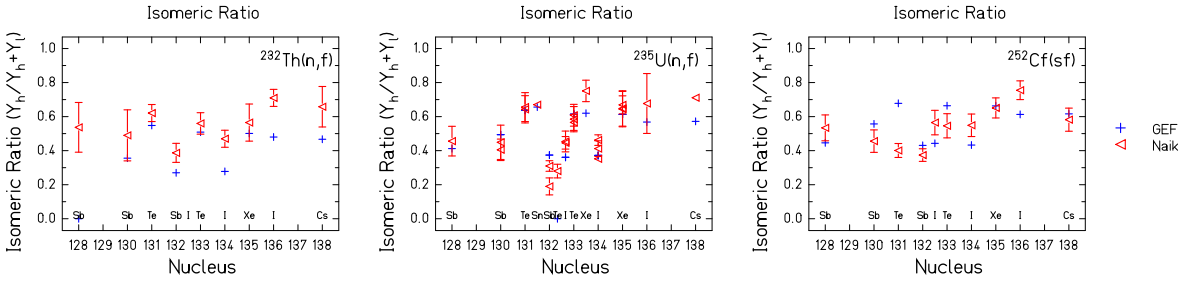

Note: Measured isomeric ratios for even-Z compound nuclei: ^{232}Th (0+) (n,f), ^{235}U (7/2-) (n,f), ^{252}Cf (0+) (sf) [162] are compared with the GEF results.

The ratios of the high-spin yield (Y_h) over the sum of the low-spin and the high-spin yields ($Y_l + Y_h$) were compared for 6 different nuclei in Figures 76 and 77: ^{237}Np (5/2+) (n,f), ^{241}Am (5/2-) (n,f), ^{243}Am (5/2+) (n,f), ^{232}Th (0+) (n,f), ^{235}U (7/2-) (n,f), ^{252}Cf (0+) (sf). The conclusions are the same as the previous ones on ^{239}Pu(n$_{th}$,f). The agreement between the experimental data and the GEF prediction is good whatever the parity and the spin of the compound nucleus.

In order to extend our benchmark of the GEF prediction as a function of the compound nucleus, four isomeric ratios (the Sb chain and ^{135}Xe) are compared for 15 fissioning systems in Figures 78 and 79. The ^{132}Sb isomeric ratios are clearly over-predicted whereas the ^{128}Sb ratios are under-predicted. The ^{135}Xe isomeric ratio is well reproduced. In each case, the tendency with the variation of the compound nucleus is good.

Figure 78: Isomeric ratio for Sb isotopes.

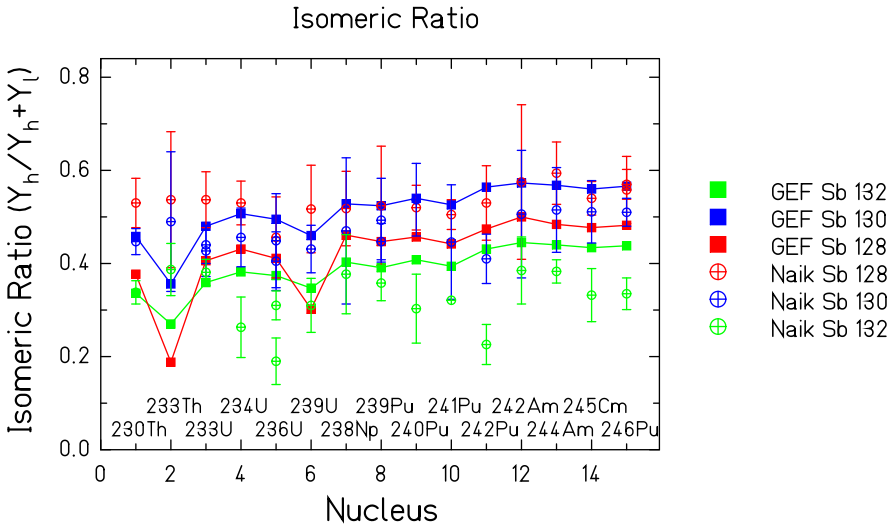

Note: Measured isomeric ratios for the Sb chain for different fissioning nuclei [162, 163] are compared with the GEF results.

Even if few data are available for the light group, Figure 80 shows that the GEF code tends to overestimate the few ones available on the average. According to the experimental data on the heavy peak that indicate a small influence of the compound nucleus on the isomeric ratio, the experimental ^{99}Nb value for ^{235}U can be wrong as the experimental ^{99}Nb value for ^{239}Pu is the complementary to 1. This can be due to the inversion $Y_m/Y_{gs} = Y_l/Y_h$ for the nucleus contrary to a lot of nuclei where $Y_m/Y_{gs} = Y_h/Y_l$.

In order to study the influence of the excitation of the compound nucleus on the isomeric ratio, the ^{135}Xe and ^{133}Xe isomeric ratios are also compared as a function of the excitation energy with the Ford measurement (thermal, 2 MeV, 14 MeV) in Figure 81. Ford observed an increase of the Y_m/Y_g ratio for ^{133}Xe whereas he saw no increase for ^{135}Xe. The GEF code does not reproduce the nearly constant behaviour before 3 MeV. A larger number of data is however required to extend this observation more especially in the range $E_n = 2 - 14$ MeV.

Photo-fission reactions also give some hints that the excitation energy does not have a huge influence on the isomeric ratio at least in the range $E^* = 9.7 - 14.1$ MeV ($E_n = 4 - 8$ MeV). Figure 82 shows the isomeric ratio for ^{134}I for ^{235}U and ^{238}U as a function

Figure 79: Isomeric ratio for ^{135}Xe

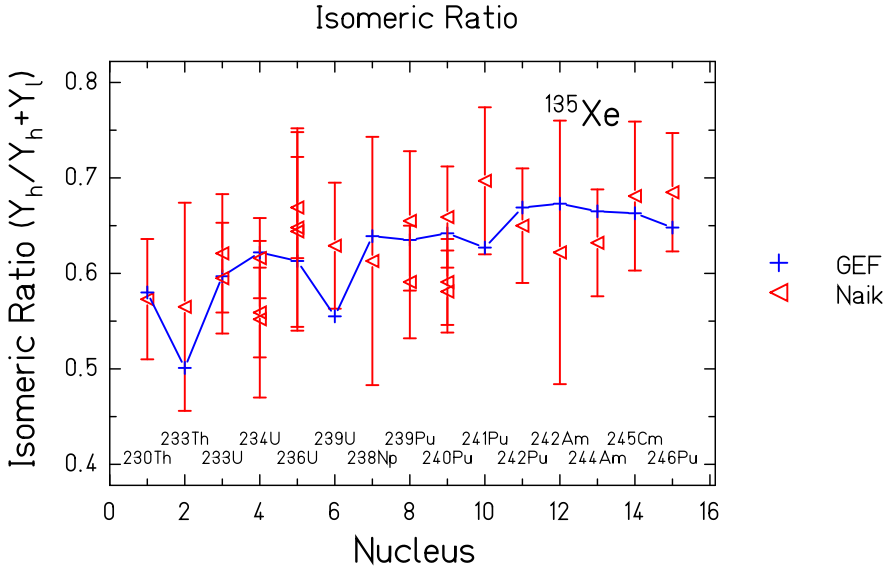

Note: Measured isomeric ratio for ^{135}Xe for different fissioning nuclei [162, 163] is compared with the GEF result.

Figure 80: Isomeric ratios for light fragments

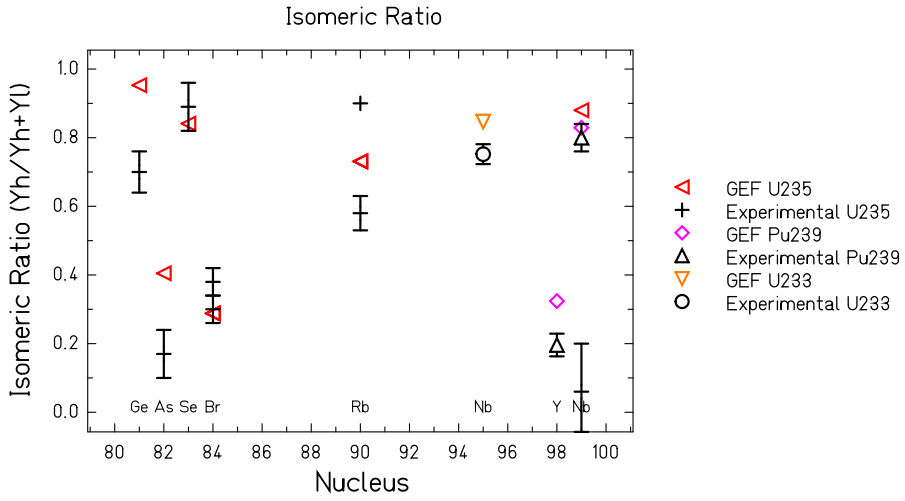

Note: Measured isomeric ratios for light fragments from different thermal-neutron-induced reactions [166, 164, 167] are compared with the GEF results.

of the excitation energy of the compound nucleus. The experimental ratios are nearly constant for both compound nuclei in the domain $E^* = 9.7 - 14.1$ MeV. The GEF

Figure 81: Energy dependence of isomeric ratios for ^{133}Xe and ^{135}Xe

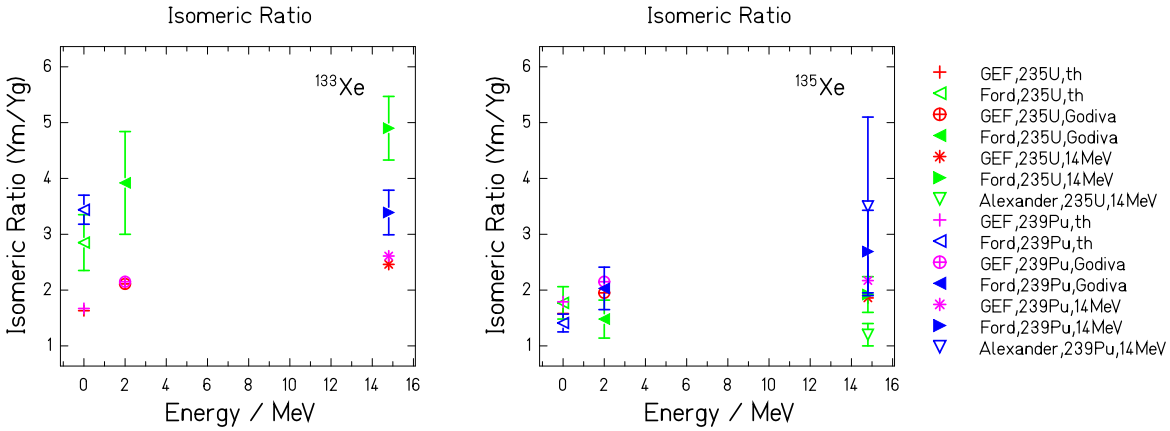

Note: Measured isomeric ratios for ^{133}Xe and ^{135}Xe from ^{235}U(n,f) and ^{239}Pu(n,f) for different neutron energies [168] are compared with the GEF results.

predictions are also nearly constant. The excitation-energy dependence of the isomeric ratio as parametrised in the GEF code seems to be correct. The absolute values, however, are substantially underestimated.

Figure 82: Isomeric ratio for ^{134}I from photofission

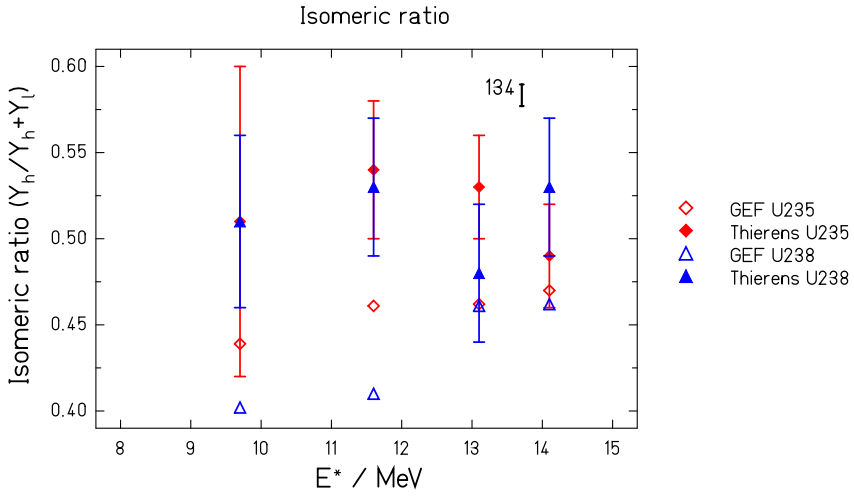

Note: Measured isomeric ratios for ^{134}I from ^{235}U(γ,f) and ^{238}U(γ,f) at different excitation energies [169] are compared with the GEF results.

In conclusion, the GEF prediction is in very good agreement with the data in a large number of cases.

8.4 Prompt-neutron multiplicities

The multiplicities of prompt fission neutrons contain valuable information and, thus, provide a stringent test for the understanding of the fission process. Moreover, this quantity is very important for nuclear technology. The prompt-neutron multiplicity is rather directly connected with the excitation energies of the fragments. Fortunately, prompt-neutron yields have been measured for many fissioning systems. In a few cases, the variation of the prompt-neutron yield as a function of excitation energy and fragment mass has been determined.

8.4.1 System dependence

There exist extended systematics of prompt-neutron multiplicities for spontaneous fission and for thermal-neutron-induced fission. They are compared in Figures 83 and 84 with results of the GEF code. It is obvious that the data cannot be parametrised by a simple function of a macroscopic parameter, e.g. the fissility parameter Z^2/A or the Coulomb parameter $Z^2/A^{1/3}$.

8.4.1.1 Spontaneous fission: In spontaneous fission, the most striking structural effects are the horizontal slope for the Pu isotopes that deviates from the average slope of the other isotopic chains and the decrease towards the heaviest Fm isotopes. The first effect is the consequence of the large yield of the standard 1 fission channel, which is characterised by a 17 MeV higher TKE value [143] and a correspondingly reduced TXE. Let us remind that the large yield of the S1 fission channel for these nuclei is attributed to the influence of a shell in the light fragment around $Z = 42$ in the GEF model. The yield of the standard 1 channel increases gradually from ^{236}Pu to ^{244}Pu, which explains the almost constant prompt-neutron multiplicity for the Pu isotopes. The reduction of the prompt-neutron yield due to the increasing yield of the S1 channel compensates the general trend that shows an increase of the prompt-neutron yield with increasing mass number, as can be seen in the behaviour of the uranium, curium, and californium isotopic sequences. The second effect reflects the rather sudden appearance above ^{256}Fm of a narrow symmetric fission component with TKE values which are higher by about 30 MeV [170].

The measured values are very well reproduced by the GEF model with a few exceptions. The experimental value for ^{232}Th has a large uncertainty, and the one for ^{253}Es was reported without mentioning the uncertainty range. Thus, these values may be considered with some caution. Moreover, the increase of the measured values from ^{256}Fm to ^{257}Fm seems to be in conflict with the increase of the measured yield of the narrow symmetric component and its high total kinetic energy, because the TKE and the TXE are connected through the Q value by energy conservation. The expected further decrease of the prompt-neutron yield towards ^{258}Fm is demonstrated by the calculated value in Figure 83. Therefore, the measured value for ^{256}Fm may be doubted. The rms deviation between the remaining 19 experimental values and the corresponding calculations

Figure 83: Systematics of prompt-neutron multiplicities for spontaneous fission

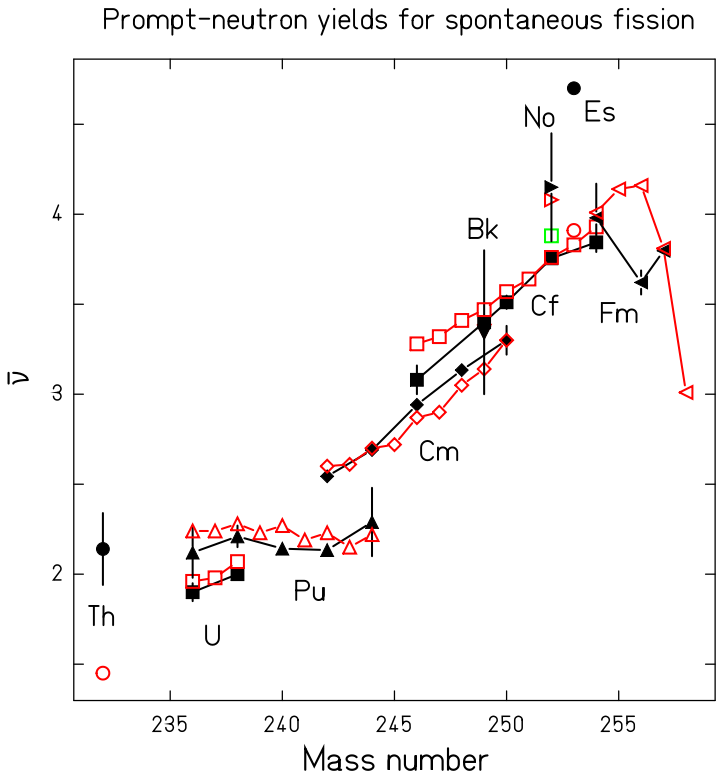

Note: Measured mean prompt-neutron multiplicities for spontaneous fission (black full symbols) as a function of the mass number of the fissioning nucleus [171] in comparison with the result of the GEF model (red open symbols). Experimental error bars are not shown when they are smaller than the symbols. The value for ^{253}Es is reported without an experimental uncertainty.

amounts to 0.086. This is also the order of magnitude of the expected uncertainty for the predictions of the prompt-neutron yields of nuclei in the vicinity of the systems shown in Figure 83. Thus, the GEF model is expected to be able to estimate the prompt-neutron multiplicity for spontaneous fission with a precision better than 0.1 units.

8.4.1.2 Thermal-neutron-induced fission: In the case of thermal-neutron-induced fission, the situation is more complex. A number of data are rather well reproduced by the GEF model, see Figure 84, but there are also large deviations. The value for ^{232}U reported in ref. [171] deviates by exactly one unit from the value obtained by the GEF model. Unfortunately, ref. [171] cites another publication [173] that is not easily accessible. Therefore, the possibility of a misprint, which is tentatively assumed in Figure 84, could not be verified. For the large discrepancies for ^{229}Th, ^{233}U, ^{238}Pu, ^{241,243}Am, and ^{245,247}Cm there is no obvious explanation. There is no obvious systematics in these

Figure 84: Systematics of prompt-neutron multiplicities for n_{th}-induced fission

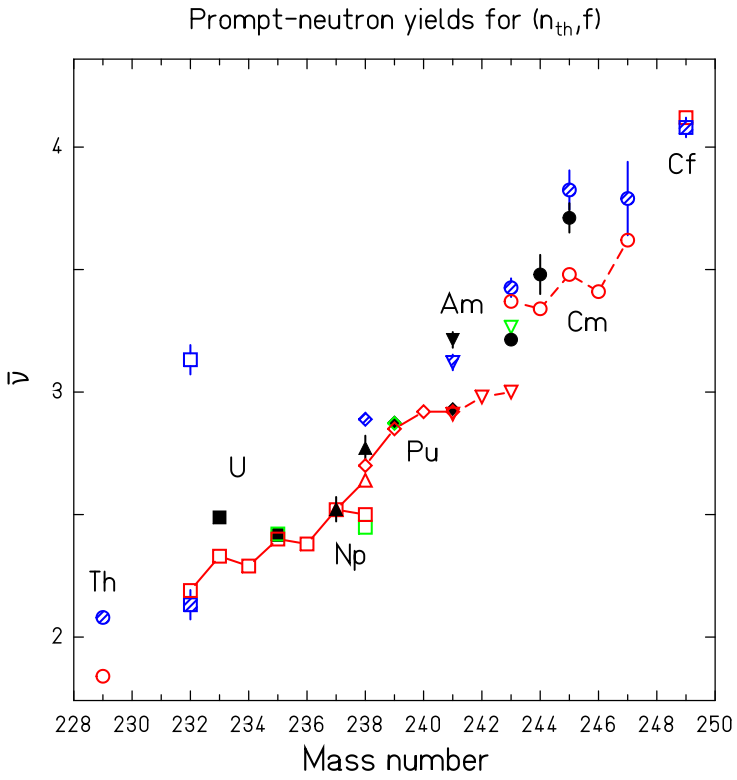

Note: Measured mean prompt-neutron multiplicities for thermal-neutron-induced fission as a function of the mass number of the target nucleus [172] (black full symbols), [171] (blue shaded symbols), and [141] (green open symbols) in comparison with the result of the GEF model (red open symbols). We assumed that the value 3.132 for ^{232}U given in [171] (blue open symbol) is wrong due to a misprint. The tentatively corrected value (2.132) is marked by a blue shaded symbol. Experimental error bars are not shown when they are smaller than the symbols.

deviations. It is striking that the data for the following systems with easily available target material (^{235,238}U, ^{237}Np, ^{239,241}Pu, ^{252}Cf), and also ^{232}U are very well reproduced.

The situation is not clear. More experimental work would be desirable in order to better understand the structural effects, which are eventually responsible for the observed deviations, and in order to verify the result and to exclude possible systematic uncertainties of one or the other experiment. The rms deviation between all 21 experimental values, including those with large error bars, amounts to 0.17, which is about twice the value found for spontaneous fission. For ^{232}U, the tentatively corrected value was used. Thus, the GEF model is expected to be able to estimate the prompt-neutron multiplicity for thermal-neutron-induced fission with a precision better than 0.2 units.

8.4.2 Energy dependence

For a few target nuclei, the prompt-neutron multiplicity has been measured in neutron-induced fission as a function of the incident-neutron energy. Great part of these data are compared with the results of the GEF model in Figure 85. The experimental data are taken from ref. [171]. Only part of the data are shown if they overlap in order not to overload the figures. The overall slope of the neutron multiplicity as a function of neutron energy is well reproduced by the model. The data for the two systems ^{235}U(n,f) and ^{239}Pu(n,f), which have been studied most extensively, are very well reproduced over the whole energy range up to almost 30 MeV. The data for ^{232}Th(n,f) show a structure at the onset of second-chance fission, which is well reproduced by the model as well. The strong increase of the neutron multiplicity just above the threshold for second-chance fission can be explained by the fact that second-chance fission is only possible in this energy range, if the kinetic energy of the emitted pre-fission neutron is so low that the excitation energy of the daughter nucleus falls above its fission barrier. Thus, the average prompt-neutron energy is exceptionally low, and the corresponding neutron multiplicity is exceptionally high. Also, another peculiarity of this system, the weak increase of the prompt-neutron multiplicity in the low-energy range up to 3 MeV is present in the model results. This effect is connected with the fact that for this even-even nucleus low incident neutron energies lead to excitation energies around the fission barrier. In the tunneling regime, at energies below the fission barrier, the TXE values do not directly follow the variations of the initial excitation energy. A similar, however much weaker structure than in ^{232}Th(n,f) at the onset of first-chance fission of ^{238}U(n,f) in the calculated values is not seen in the data. The structures seen in the model results at the threshold for third-chance fission near 15 MeV for ^{235}U(n,f) and ^{239}Pu(n,f) cannot be compared, because there are no data measured between 15 and 22 MeV.

It is interesting to note that the energy-dependent prompt-neutron multiplicity is perfectly reproduced by the GEF model for the odd-A targets ^{235}U(n,f) and ^{239}Pu(n,f), in contrast to the even-A targets ^{232}Th(n,f) and ^{238}U(n,f), where the neutron yield is overestimated above the threshold for second-chance fission. This problem is probably connected with the difficulties in describing the fission probabilities of systems with relatively low fissility and high neutron-separation energies, which were already reported in Section 8.1. In general, the specific behaviour of the prompt-neutron multiplicity at the onset of a higher-chance fission strongly depends on the behaviour of the fission probability around the fission threshold, which shows a gradual increase in part of the systems and a more or less pronounced peak structure in other systems. In the first case, the mean neutron energy tends to increase, in the second case it tends to decrease with the opening of another fission chance. This feature strongly depends on structural effects in the level density (see the discussion in Section 8.1). In addition, the neutron yield for ^{232}Th(n,f) is underestimated at incident-neutron energies below 5 MeV. Possibly, this problem is related in some way with the discrepancies observed in the fragment yields from the fission of several thorium isotopes.

Figure 85: Energy dependence of mean prompt-neutron multiplicities

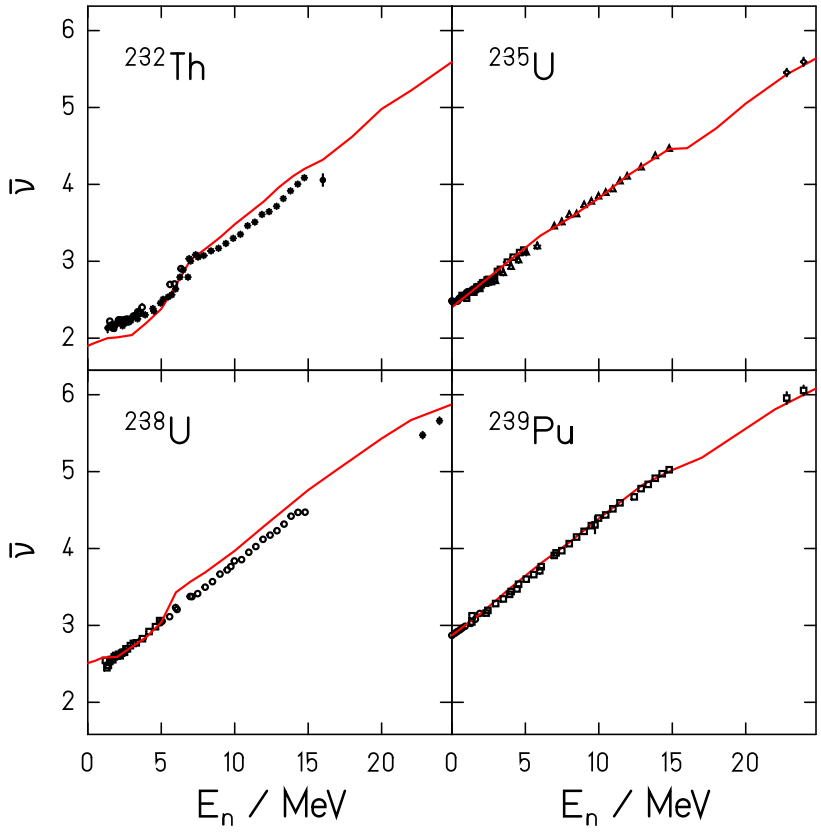

Note: Measured prompt-neutron multiplicity for ^{232}Th(n,f), ^{235}U(n,f), ^{238}U(n,f), and ^{239}Pu(n,f) (black symbols, different symbols are used for different experiments) as a function of neutron energy (data from ref. [171]) in comparison with the result of the GEF model (red line).

8.4.3 Fragment-mass dependence

In the actinides, the prompt-neutron multiplicity has the typical saw-tooth behaviour as a function of fragment mass. Figure 86 shows the measured data for the system ^{237}Np(n,f) for two incident-neutron energies. The data for ^{252}Cf(sf) are shown in Figure 87. The data are rather well reproduced by the GEF model.

Figure 86: Variation of the mass-dependent prompt neutron yield with E^*

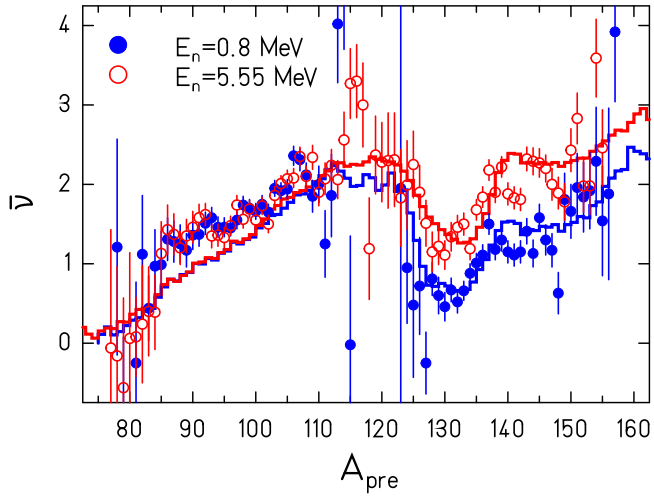

Measured prompt-neutron yield in ^{237}Np(n,f) as a function of pre-neutron mass at two different incident-neutron energies [58] (data points) in comparison with the result of the GEF model (histograms).

Figure 87: Mass dependent prompt-neutron yield in ^{252}Cf(sf)

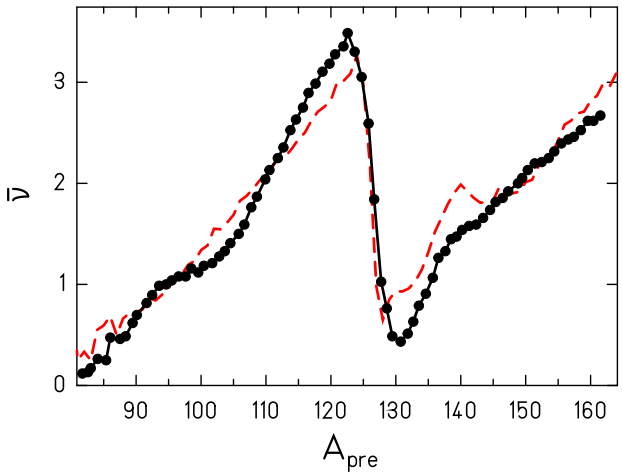

Measured prompt-neutron yield in ^{252}Cf(sf) [174] as a function of pre-neutron mass (data points) in comparison with the result of the GEF code (dashed line). The experimental uncertainties are smaller than the symbols.

There are two prominent features in the model: First, the increasing yields are caused by the fragment deformation at scission which increases with the fragment mass in the range of the light and in the range of the heavy fragments. This feature is a consequence of a general characteristics of shells in deformed nuclei, already mentioned in Section 6.4: these shells extend over a broad range of neutron, respectively proton number, but the optimum deformation is correlated with the size of the system [53, 55]. Secondly, the intrinsic excitation energy at scission is subject to energy sorting [98]. Thus, the higher incident neutron energy in ^{237}Np(n,f) leads to an increased neutron yield in the heavy fragment, only.

It is remarkable that the data of the two systems are well reproduced by the model with the fundamental assumption that the fragment deformation at scission is a unique function of the fragment shells.

8.4.4 Multiplicity distributions

The distribution of prompt-neutron multiplicities provides a test for the fluctuation of the total excitation energy of the fragments. In the GEF model, the largest contribution to these fluctuations is caused by the distribution of fragment deformations around the equilibrium value at scission. The distributions for ^{239}Pu(n$_{th}$,f) and ^{252}Cf(sf) shown in Figure 88 are perfectly reproduced, whereas the calculated distribution for ^{235}U(n$_{th}$,f) is slightly too narrow.

Figure 88: Distribution of prompt-neutron multiplicities

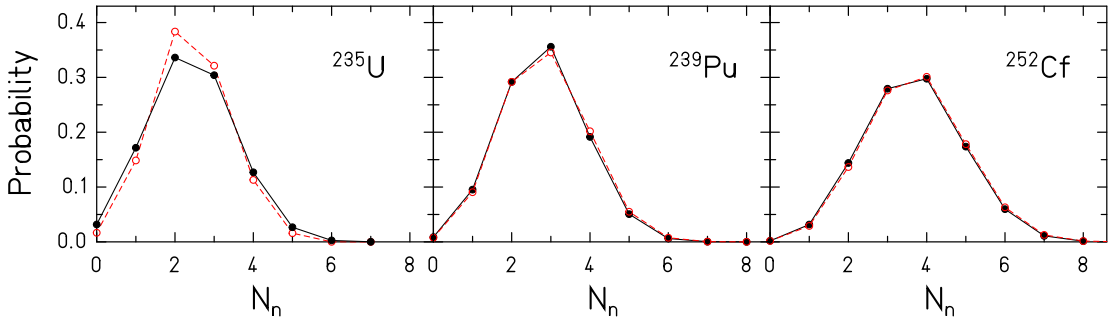

Note: Measured distribution of prompt-neutron multiplicities in ^{235}U(n$_{th}$,f), ^{239}Pu(n$_{th}$,f) and ^{252}Cf(sf) [175, 176] (black full points) in comparison with the result of the GEF model (red open points).

8.4.5 Conclusion

The manifold data on prompt-neutron multiplicities show a large variety of gross and subtle features. The GEF model is able to reproduce most of them with a satisfactory

quality. Even more importantly, the model traces these features back to peculiar aspects of the physics governing the fission process. This way, the model provides a link to other observables which are consistently described by the model.

8.5 Prompt-neutron energies

8.5.1 Key systems

8.5.1.1 Prompt-neutron spectra The experimental prompt-fission-neutron spectra for the systems ^{235}U(n$_{th}$,f) [177] and ^{252}Cf(sf) [178] are compared with results of the GEF code in Figure 89. In order to better visualise the deviations, the lower panels show a reduced presentation with the spectra normalised to a Maxwellian distribution with the parameter $T = 1.32$ MeV.

In this calculation, the de-excitation of the separated fragments has been obtained within the statistical model. It is assumed that both the emission of neutrons and the emission of E1 gammas do not change the angular momentum on the average, which seems to be a good approximation in the relevant angular-momentum range [70]. When the

Figure 89: Prompt-neutron spectra for ^{235}U(n$_{th}$,f) and ^{252}Cf(sf)

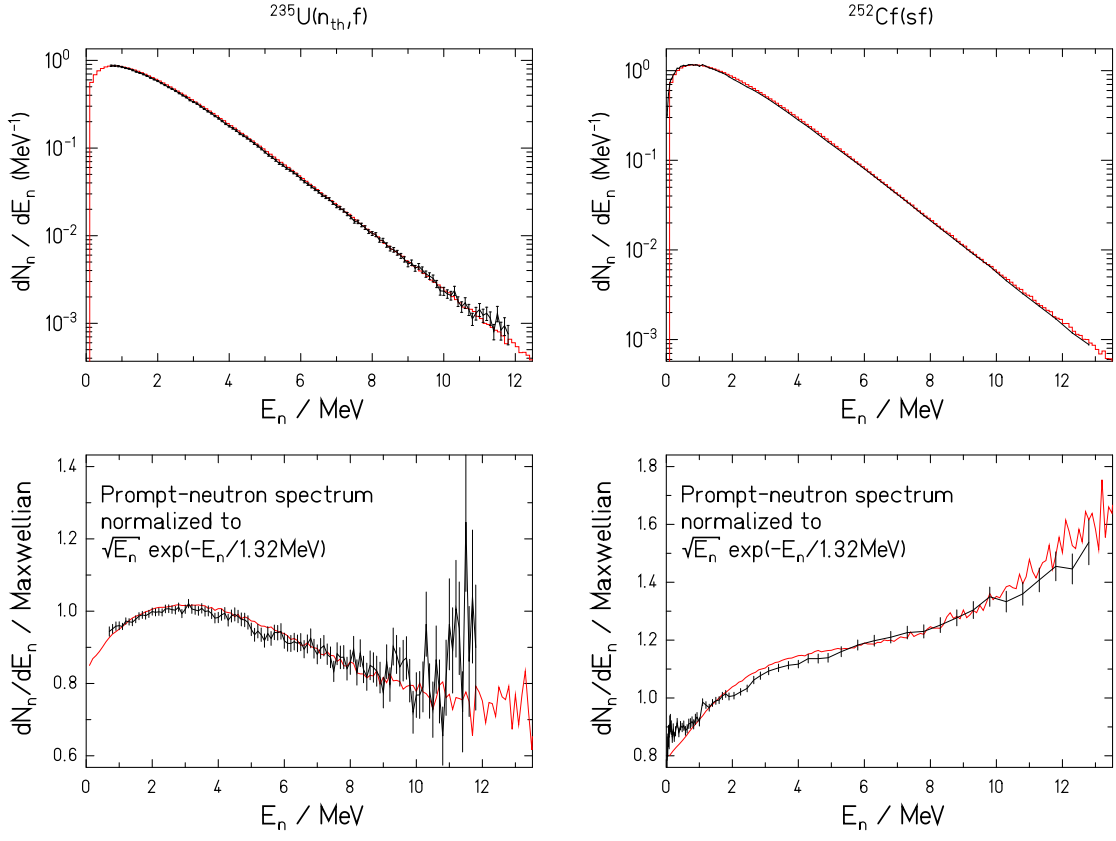

Note: Experimental prompt-fission-neutron spectra (black lines and error bars) for ^{235}U(n$_{th}$,f) [177] (left panels) and ^{252}Cf(sf) [178] (right panels) in comparison with the result of the GEF model (red lines) in logarithmic scale. In the lowest panels, all spectra have been normalised to a Maxwellian with $T = 1.32$ MeV.

yrast line is reached, the angular momentum is carried away by a cascade of E2 gammas. The inverse neutron absorption cross-section has been described by the parametrisation from [115]. Since the fast-neutron spectrum in fission is composed of the contributions from many emitting fragments, the use of this global description that is computed very quickly is probably not too critical. Gamma competition at energies above the neutron separation energy was considered. The gamma strength of the giant dipole resonance (GDR) following the description proposed in ref. [116] was applied. The nuclear level density was modelled by the constant-temperature description of v. Egidy and Bucurescu [44] at low energies. The level density was smoothly joined at higher energies with the modified Fermi-gas description of Ignatyuk et al. [45, 46] for the nuclear-state density:

$$\omega \propto \frac{\sqrt{\pi}}{12\tilde{a}^{1/4}U^{5/4}} exp(2\sqrt{\tilde{a}U}) \tag{73}$$

with $U = E + E_{cond} + \delta U(1 - exp(-\gamma E))$, $\gamma = 0.55$ and the asymptotic level-density parameter $\tilde{a} = 0.078A + 0.115A^{2/3}$. The shift parameter $E_{cond} = 2$ MeV $- n\Delta_0$, $\Delta_0 = 12/\sqrt{A}$ with $n = 0, 1, 2$, for odd-odd, odd-A and even-even nuclei, respectively, as proposed in ref. [43]. δU is the ground-state shell correction. A constant spin-cutoff parameter was used. The matching energy is determined from the matching condition (continuous level-density values and derivatives of the constant-temperature and the Fermi-gas part). Values slightly below 10 MeV are obtained. The matching condition also determines a scaling factor for the Fermi-gas part. It is related with the collective enhancement of the level density (see Section 3.2).

The resulting prompt-neutron spectra are shown in Figure 89. The transformation of the neutron-energies into the laboratory frame was performed considering the acceleration phase [179, 180] after scission by a numerical trajectory calculation. The mean pre-scission total kinetic energy was assumed to be 40% of the potential-energy gain from saddle to scission derived by Asghar and Hasse [86] as:

$$< TKE >_{pre} = 0.032(Z^2/A^{1/3} - 1527) MeV \tag{74}$$

with a standard deviation of the same amount. The distribution was truncated at negative values.

The good reproduction of the measured neutron spectra, especially for the lighter system ^{235}U(n$_{th}$,f), does not give indication for additional neutron emission at scission [181, 182, 183, 184].

The emission during the acceleration phase is stronger for the system ^{252}Cf(sf), since higher excitation energies and, thus, shorter emission times are involved in this system. Neutron emission during fragment acceleration reduces especially the laboratory energies of the first neutrons emitted at short times from the most highly excited fragments in ^{252}Cf(sf) and allows for a decently consistent description of the two systems with the GEF code, using the same parameter set. Experimental prompt-fission-neutron spectra of the systems ^{239}Pu(n$_{th}$,f) and ^{240}Pu(sf) are compared with the result of the GEF code

in Figures 90 and 91, again using the same model parameters. Obviously, the data are very well reproduced.

Figure 90: Prompt-neutron spectrum for ^{239}Pu(n$_{th}$,f)

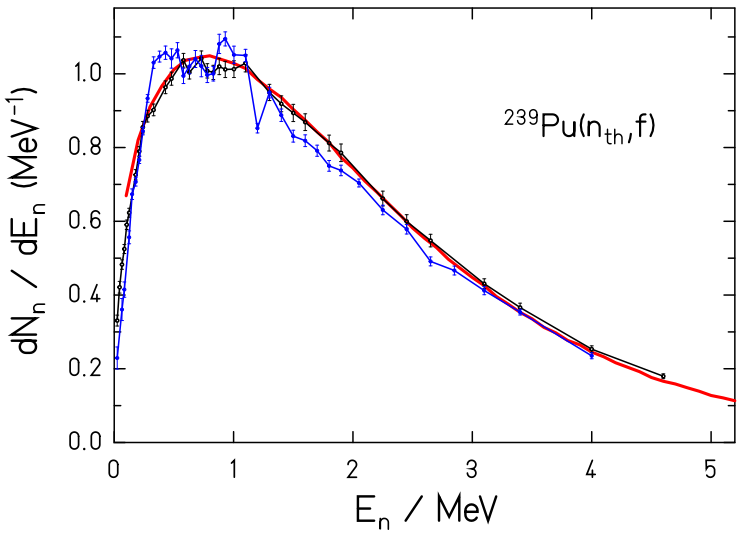

Note: Experimental prompt-fission-neutron spectrum for the system ^{239}Pu(n$_{th}$,f) from ref. [185] (black open symbols) and from [186] (blue full symbols) in comparison with the result of the GEF code (red thick full line). The calculated spectrum was normalised to the measured total neutron multiplicity ($\bar{\nu} = 2.88$ [175]). The measured spectra are slightly scaled for minimising the overall deviations from the calculated spectrum in order to better compare the spectral shapes.

In general, the GEF code reproduces the available experimental fission-prompt-neutron spectra rather well. This qualifies the GEF code for estimating prompt-neutron spectra in cases where experimental data do not exist. These data can be generated by downloading the code [54] and by performing the calculations for the appropriate fissioning system. The code also seems to be a suitable tool for improving evaluations.

8.5.1.2 Correlations: Since the prompt-neutron spectra measured in the laboratory frame are the result of a convolution due to the emission under different angles from the moving fragments, they are not very sensitive to the yield of neutrons with very low energies in the frame of the fragments. Therefore, one may look for other experimental signatures that are more sensitive to specific features of the neutron emission. One of these signatures is the variation of the neutron multiplicity as a function of the angle between the directions of the emitted neutrons and the light fission fragment. Figure 92 shows the experimental data [188] in comparison with the result of the GEF code. The measured data are well reproduced over almost the complete angular range. The code

Figure 91: Prompt-fission-neutron spectrum for ^{240}Pu(sf)

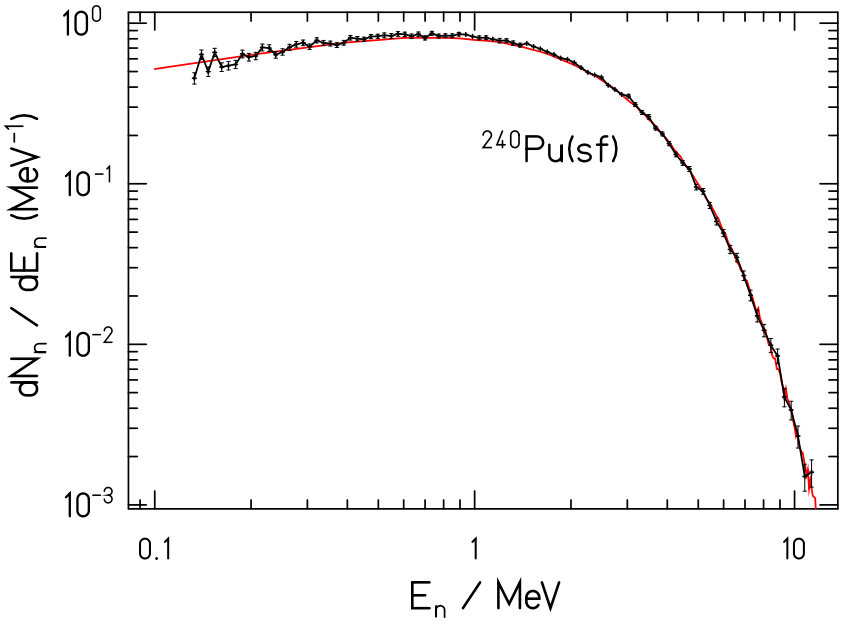

Note: Experimental prompt-fission-neutron spectrum for the system ^{240}Pu(sf) from ref. [187] (black symbols) in comparison with the result of the GEF code (red line). The measured data were scaled to the height of the calculated spectrum. Since the experiment covers especially well the lower-energy range, a double-logarithmic presentation was chosen.

underestimates the yield only very close to the direction of the light fragments. The two right-most points of the distribution correspond to angles of 5.7 and 9.9 degrees, corresponding to neutron energies in the fragment frame of 30 and 10 keV, respectively. Thus, these deviations can be explained by a slight underestimation of the neutron-absorption cross-sections in the very restricted low-energy regime below 50 keV. In the prompt-neutron spectrum, Figures 89 to 91, these events appear at laboratory energies around 1 MeV due to the velocity of the emitting fragment. Here, no indication for this deviation can be seen. It seems that the description by the GEF code is very well suited for estimating the prompt-neutron spectra in the laboratory frame of heavy fissioning systems, which are most important for technical applications. The slight deviations in the angular distributions, Figure 92, have practically no influence on the energy distribution of the prompt neutrons in the laboratory frame.

In the following, we investigate the prompt-neutron yield as a function of the fission-fragment total kinetic energy. Figure 93 shows a comparison of the result of the GEF code with experimental data [189, 190] and a previous calculation of Kornilov [191]. The GEF calculation has been performed using Thomas-Fermi masses of Myers and Swiatecki [20] with recommended shell corrections and schematic even-odd fluctuations. The variation

Figure 92: Prompt-neutron multiplicities versus neutron direction

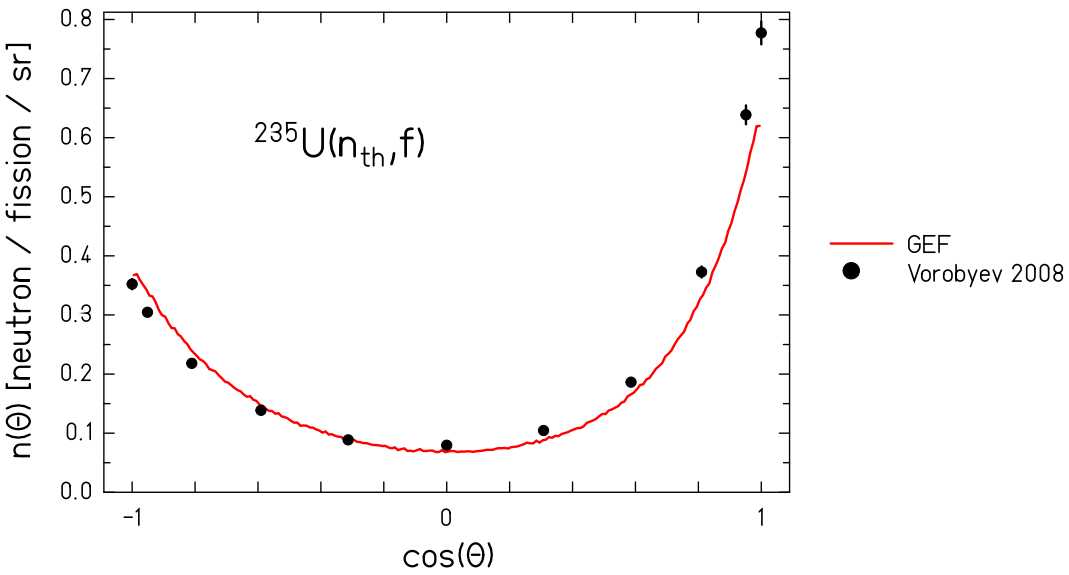

Note: Variation of the prompt-neutron multiplicities versus the neutron direction relative to the light fission fragment. The result of the GEF code is compared with experimental data from ref. [188]. The nominal threshold in the experiment was 0.15 to 0.2 MeV.

of the prompt-neutron yields from the light and the heavy fragment are assumed to be uncorrelated for a given split in Z and N.

The GEF calculation, in particular the slope, is rather close to the experimental data in the region between 155 MeV and 185 MeV. Also, the low-energy point of Boldeman et al. is well reproduced. For energies higher than 185 MeV, all calculations, also the calculation of Kornilov, are appreciably below the experimental data. The cut-off of the neutron multiplicity slightly below 200 MeV is probably realistic, because even for the splits with the highest Q values the excitation energies of the fragments fall below the corresponding neutron separation energy for these high TKE values.

One should not forget that scattering phenomena can considerably disturb experimental data in regions of low yield as e.g. demonstrated in ref. [192]. Such processes would tend to flatten the variation of the measured prompt-neutron yield as a function of TKE. In this context, it is interesting to note that the data of Boldeman et al. have a steeper slope than the data of Vorobyev et al., especially in the wings of the TKE distribution. The data of Vorobyev et al. even extend to TKE values, where there is hardly any yield expected, and neutrons are still seen above TKE = 200 MeV, where neutron emission is suppressed in the GEF code due to the Q-value limit. This puts also doubts on the data of Vorobyev et al. for total kinetic energies below 150 MeV, where the yield is low, and scattering phenomena may have an important influence.

Figure 93: Mean prompt-neutron yield as a function of TKE

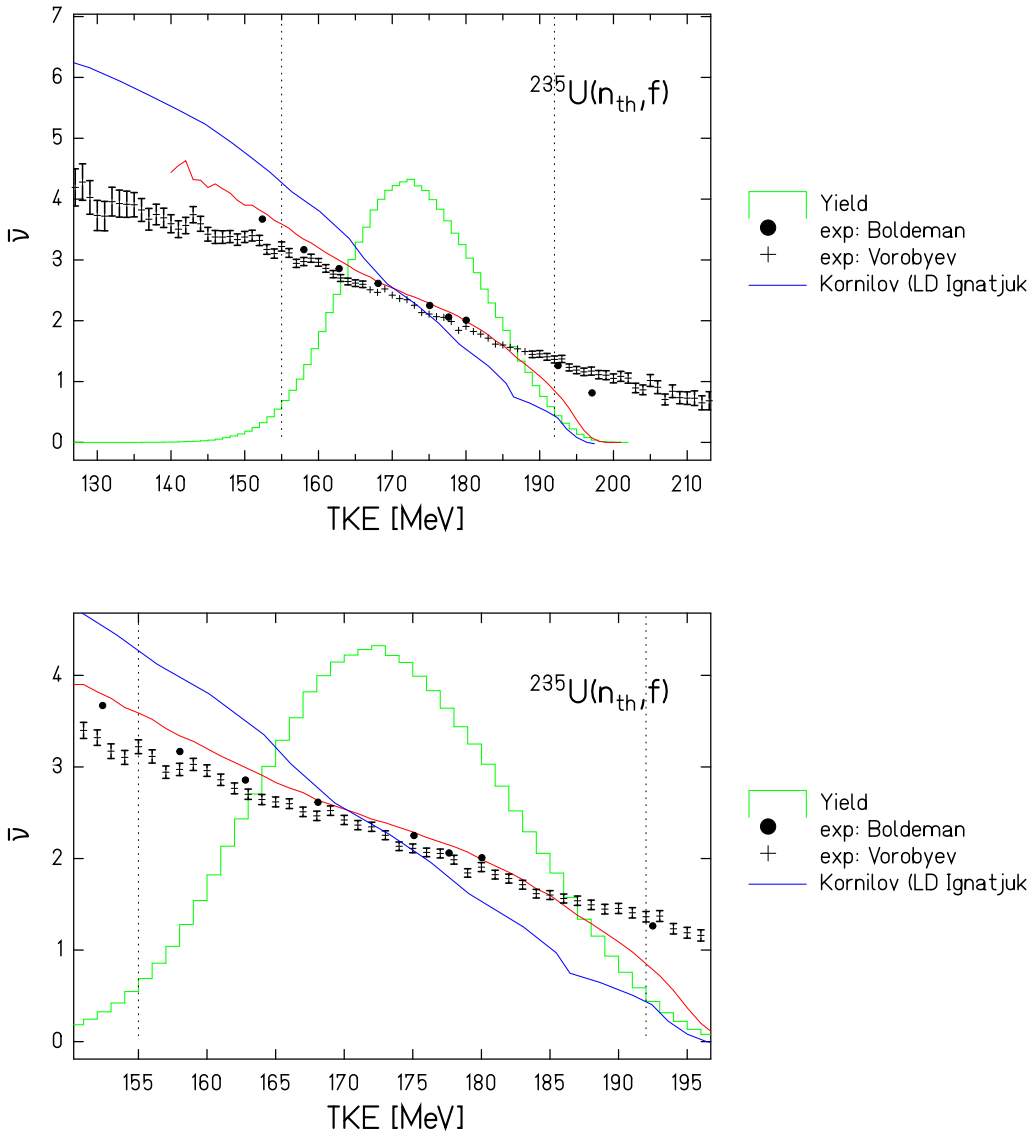

Note: Mean prompt-neutron yield as a function of fission-fragment total kinetic energy for the system ^{235}U(nth,f). The experimental data of Boldeman et al. [189] and Vorobyev et al. [190] are compared with a calculation of Kornilov [191] (labelled as LD Ignatyuk) and the result of the GEF model (red line). The lower part shows a zoom on the central part of the TKE distribution. The green histogram shows the calculated pre-neutron TKE distribution in an arbitrary scale. The dotted vertical lines denote the region that contains 95 % of the fission events.

The GEF code reproduces also well the measured mean prompt-neutron yields as a function of the total fission-fragment total kinetic energy for spontaneous fission of ^{252}Cf

Figure 94: Mean prompt-neutron yield as a function of TKE for ^{252}Cf(sf)

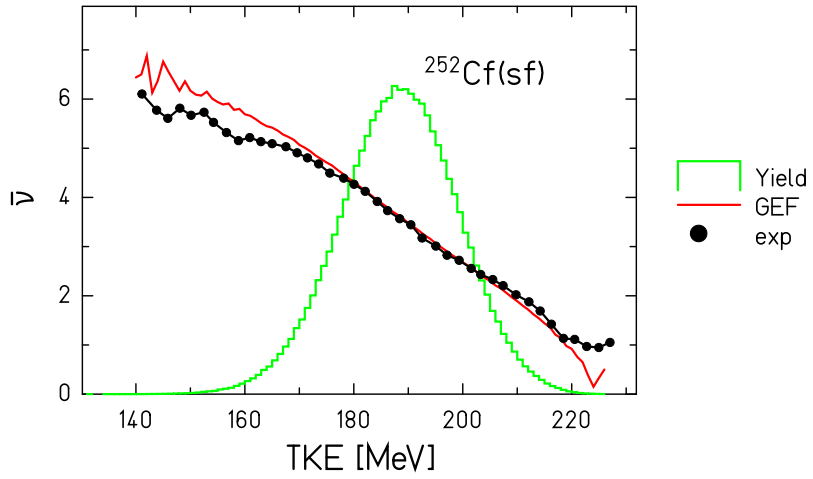

Note: Mean prompt-neutron yield as a function of fission-fragment total kinetic energy for the system ^{252}Cf(sf). The experimental data of Budtz-Jorgensen et al. [174] are compared with the result of the GEF model. The green histogram shows the calculated pre-neutron TKE distribution in an arbitrary scale.

of ref. [174], see Figure 94. The deviations at high TKE appear in a region of extremely low yield. They may be explained by a background of events with lower TKE due to random coincidences of fragment and prompt-neutron signals in the experiment. Also the deviations at low TKE appear in a region with low yield. They may be caused at least to a part by incompletely measured TKE values due to scattering phenomena in the experiment.

One may speculate that the transport of a multitude of correlations along the fission process in the GEF code without any intermediate averaging has an important influence on correlations between different fission observables. These correlations might not have been fully considered in other models. The calculations with the GEF code do not give strong hints for additional phenomena like scission neutrons; the data of Figures 93 and 94 can rather well be reproduced with the assumption of prompt-neutron emission from the fragments after scission, only.

8.5.1.3 Conclusion: The GEF model reproduces a large variety of observables with a good precision in a consistent way without further adjustment to specific fissioning systems with a unique parameter set. With this global approach one is able to predict several characteristic quantities of the fission process, e.g. the energy and multiplicity distribution of prompt-fission neutrons, without the need for specific experimental information of the respective system, e.g. measured mass-TKE distributions. All properties of the fission

fragments that are considered in the code (e.g. nuclear charge, mass, excitation energy, angular momentum) are sampled in the corresponding multi-dimensional parameter space by a Monte-Carlo technique. Thus, all respect ive correlations are preserved. Moreover, correlations between all observables considered in the code are provided on an event-by-event basis. It should be stressed that it is straightforward to deduce covariances for the calculated prompt-neutron spectrum determined by the inner logic of the GEF model in analogy to the covariances of the fission-fragment yields from the list-mode data of the perturbed-parameter calculations.

The measured prompt-neutron spectra in fission induced by thermal neutrons are very well reproduced by the GEF code without any specific adjustment of the model for all systems that were investigated. It is to be expected that this agreement is preserved for fission induced by neutrons of higher energies. There are no systematic deviations which suggest the presence of scission neutrons in these cases.

8.5.2 Energy dependence

8.5.2.1 Introduction: This section deals with the description of prompt-neutron spectra in neutron-induced fission reactions over a larger excitation-energy range extending from spontaneous fission to multi-chance fission. A number of measured prompt-neutron spectra from elaborate experiments are compared with the results of the GEF code [131, 54]. The GEF code calculates the contributions from the excited nucleus before scission and from the fragments simultaneously with the statistical model in a consistent way together with many other fission observables. The calculation is done without using an analytical formula with adjustable parameters for the shape of the prompt-neutron spectrum and without any input on fission-fragment properties for specific systems. Therefore, this study aims to give a coherent picture on the variation of the prompt-neutron spectrum for different fissioning systems as a function of excitation energy.

8.5.2.2 Description of the calculation: The following figures show comparisons of measured fission prompt-neutron spectra extracted from EXFOR with results of the GEF code [131, 54]. All measurements have been performed relative to the system ^{252}Cf(sf). Thus, the data marked as ratio or R are directly measured. If the deduced prompt-neutron spectra are also given in EXFOR, they are shown as well, marked as yield or Y. The scale is dN/dE in units of 1/MeV.

GEF calculations on neutron yields and energy distributions have been performed for the indicated systems and for ^{252}Cf(sf). All calculations have been performed without any adjustment to specific systems with the very same parameter set. No particular information from experimental data, e.g. A-TKE spectra, has been used. The GEF model exploits three general laws of dynamics, quantum mechanics and statistical mechanics in order to model the fission process in a comprehensive and consistent way with a modest input of empirical information and a minimum of computational effort: the influence of inertia and friction on the fission dynamics is implicitly considered by a dynamical freeze-out, the influence of nuclear structure is traced back to the early influence of fragment shells, and the transport of thermal energy between the fragments before scission is assumed to be driven by entropy.

In order to clearly distinguish the calculation of prompt-neutron yields with the general approach of the GEF model from other models, a short summary of alternative approaches seems to be appropriate. One of the first widespread descriptions of the prompt-neutron spectrum was introduced by Watt [193]. He proposed a closed formula, deduced from a Maxwell-type energy spectrum from one or two average fragments and the transformation into the frame of the fissioning system with at least two adjustable parameters: the temperature and the velocity of the average fragment. The "Los-Alamos model" [194] extended this approach essentially by the use of a triangular temperature distribution of the fragments to a four-term closed expression for an average light and an average heavy fragment. A similar two-fragment model was also used by Kornilov et al. in [181]. In 1989, Madland et al. [195] introduced the point-by-point model by considering the

emission from all individual fragments, specified by Z and A. This model was further developed e.g. by Lemaire et al. [196], Tudora et al. [197] and Vogt et al. [198]. In refs. [199, 200, 201, 202], the spectral shape was parameterised by the Watt formula [193] or an empirical shape function that had been introduced by Mannhart [203] in order to better model the shape of the neutron energy spectra in the fragment frame. Kornilov [204] proposed a phenomenological approach for the parameterisation of a model-independent shape of the prompt-neutron spectrum. This approach was later also used by Kodeli et al. [205] and Maslov et al. [206]. These models often reach a high degree of agreement with the measured prompt-neutron spectra for particular fissioning systems with especially adjusted parameters. All models cited above are based on empirical data: the Watt model and the Lost-Alamos model are directly fitted to the measured prompt-neutron spectrum, while the point-by-point model is based on the measured A-TKE distribution. Manea et al. [207] proposed a scission-point model that predicts the TKE(A) distribution, in order to allow for calculations of prompt-neutron spectra with the boint-by-point method if only the mass distribution is known. For completeness, we also mention a paper of Howerton [208], who developed a method for predicting (Z, A, E_n) distributions. The required input values are the charge and mass numbers (Z and A) and the binding energy of the last neutron in the $(A + 1)$ nucleus. This method was used in [209].

As a result of the GEF model, the prompt-neutron spectra and the ratios to the calculated ^{252}Cf(sf) spectrum are shown. Note that the measured and calculated spectrum for ^{252}Cf(sf) are shown in Figure 89. Due to the Monte-Carlo method used in the GEF code, the spectra show statistical fluctuations, especially in the high-energy tail. The calculated total prompt-neutron multiplicity is given in addition in the figures. Note that the deviations between GEF results and experimental data in the two representations (ratio and yield) are not consistent, because the GEF yield ratios and the experimental yields (measured yield ratios times neutron yields for ^{252}Cf(sf)) have been obtained with different prompt-neutron reference spectra: For the GEF ratios the calculated ^{252}Cf(sf) spectrum was used, for the experimental yields an evaluated ^{252}Cf(sf) spectrum was used. It seems that most of the experiments aimed only to determine the shape of the spectra. Therefore, an arbitrary scaling factor was applied, such that the total prompt-neutron multiplicity agrees approximately with the GEF result. These scaling factors are listed in the legends of the figures. All figures are shown in logarithmic and in linear scale.

8.5.2.3 Results:

Spectra:

Figure 95: Prompt-neutron spectrum from ^{232}Th(n,f), E_n = 2.9 MeV

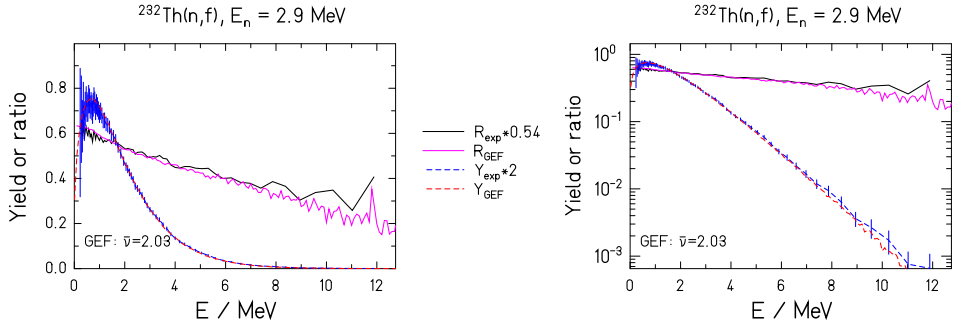

Note: Data from EXFOR dataset 411100081.

Figure 96: Prompt-neutron spectrum from ^{232}Th(n,f), E_n = 14.7 MeV

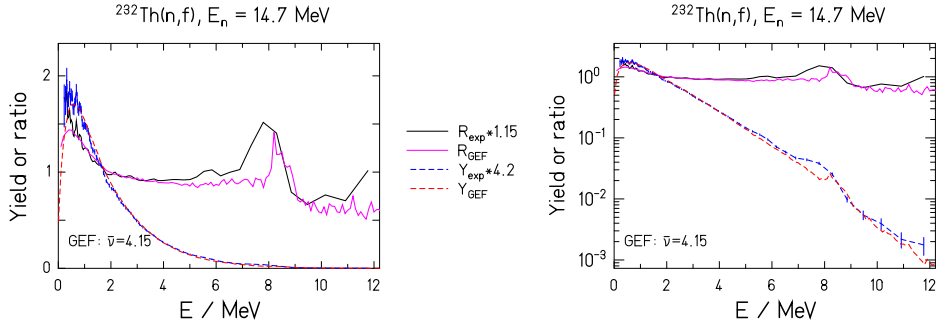

Note: Data from EXFOR dataset 411100081.

Figure 97: Prompt-neutron spectrum from ^{233}U(n_{th},f)

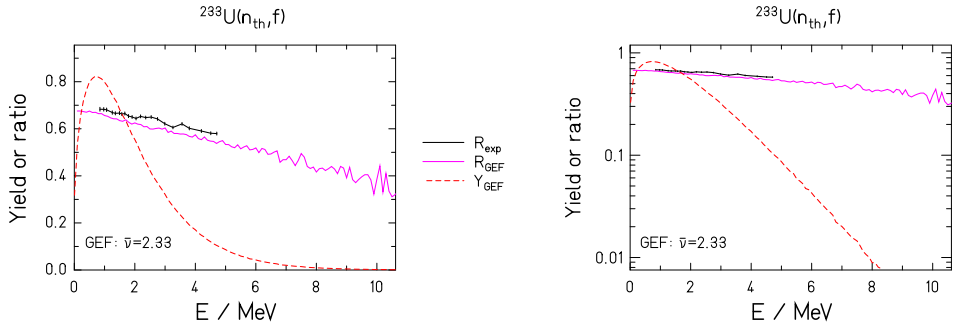

Note: Data from EXFOR dataset 40871013.

Figure 98: Prompt-neutron spectrum from ^{235}U(n,f), E_n = 100 K

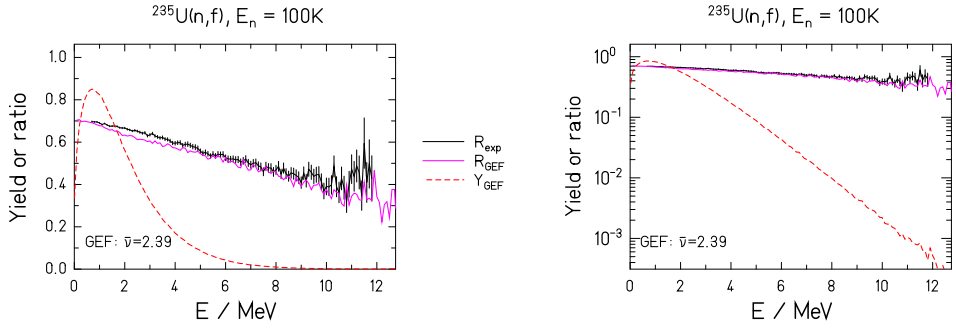

Note: Data from EXFOR dataset 31692006.

Figure 99: Prompt-neutron spectrum from ^{235}U(n_{th},f)

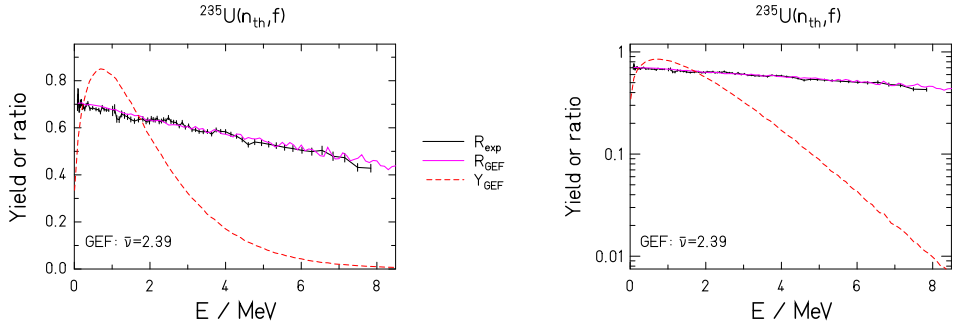

Note: Data from EXFOR datasets 40871011, 40871012.

Figure 100: Prompt-neutron spectrum from ^{238}U(n,f), E_n = 2.9 MeV

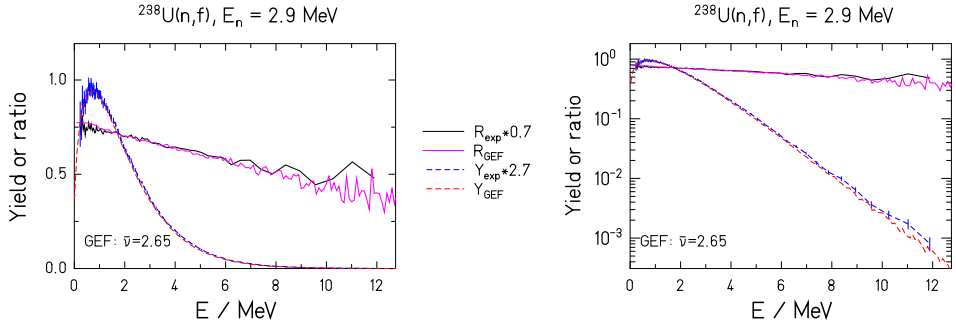

Note: Data from EXFOR dataset 411100101.

Figure 101: Prompt-neutron spectrum from ^{238}U(n,f), E_n = 5 MeV

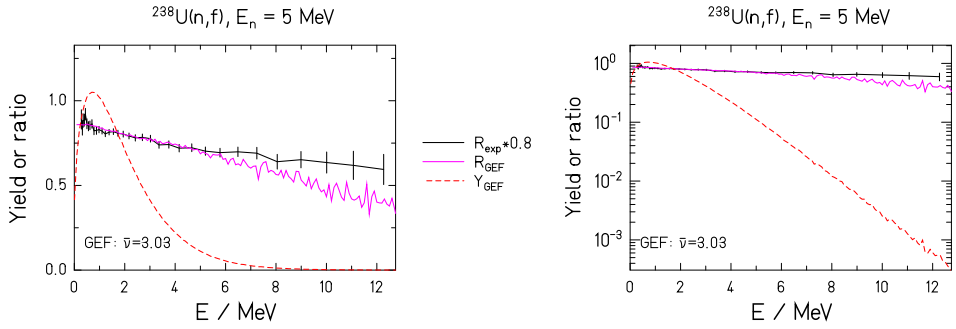

Note: Data from EXFOR dataset 41450003.

Figure 102: Prompt-neutron spectrum from ^{238}U(n,f), E_n = 6 MeV

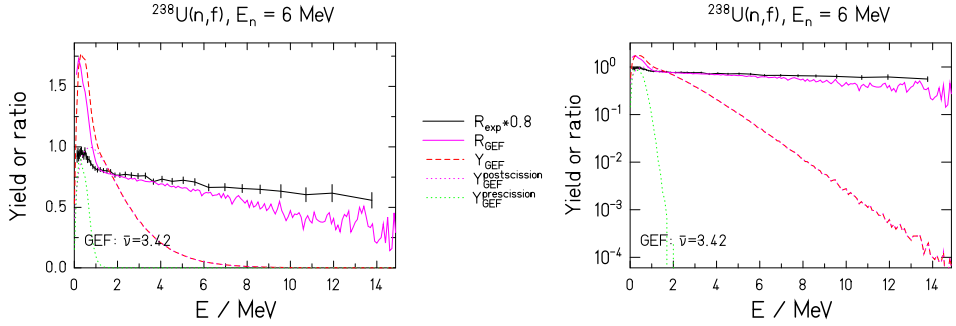

Note: Data from EXFOR dataset 41447003.

Figure 103: Prompt-neutron spectrum from ^{238}U(n,f), E_n = 7 MeV

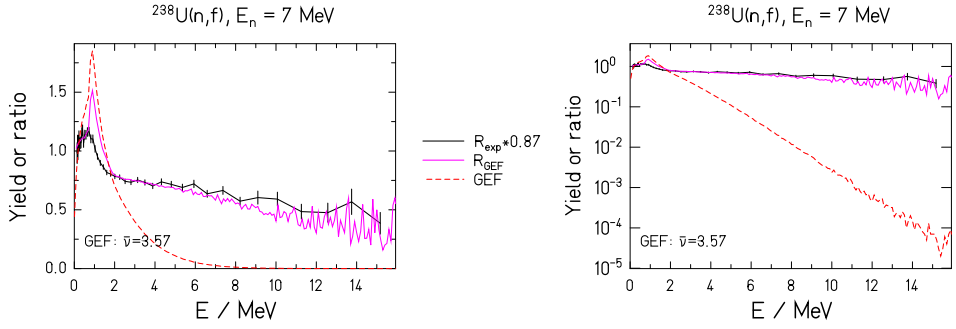

Note: Data from EXFOR dataset 41447003.

Figure 104: Prompt-neutron spectrum from ^{238}U(n,f), E_n = 10 MeV

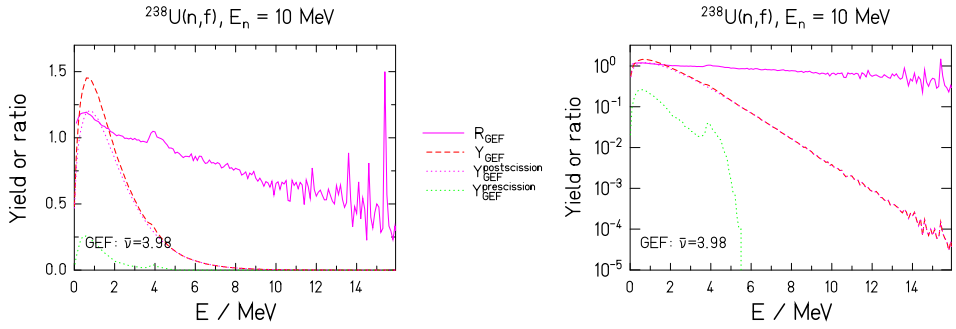

Note: No data available.

Figure 105: Prompt-neutron spectrum from ^{238}U(n,f), E_n = 13.2 MeV

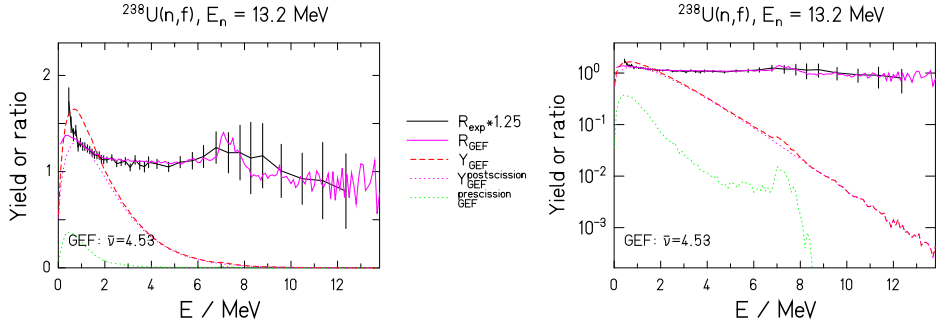

Note: Data from EXFOR dataset 41450003.

Figure 106: Prompt-neutron spectrum from ^{238}U(n,f), E_n = 14.7 MeV

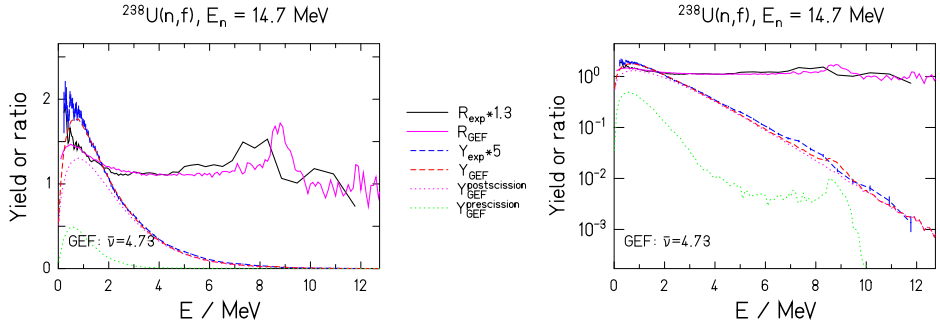

Data from EXFOR dataset 411100101.

Figure 107: Prompt-neutron spectrum from ^{239}Pu(n$_{th}$,f)

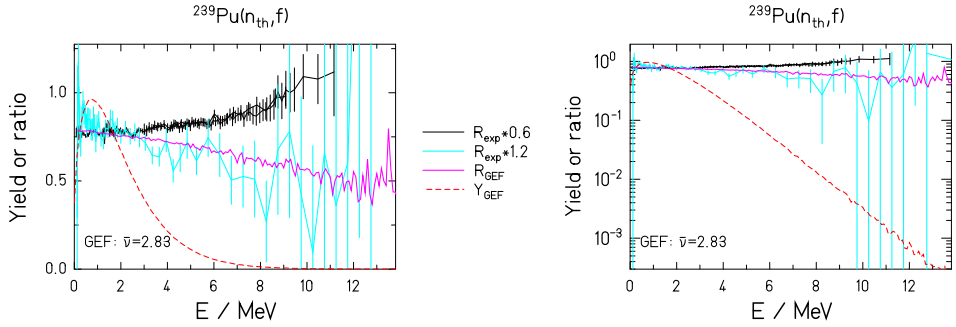

Note: Data from EXFOR datasets 40871009, 40871010, 40872006, 41502004.

Figure 108: Prompt-neutron spectrum from ^{240}Pu(sf)

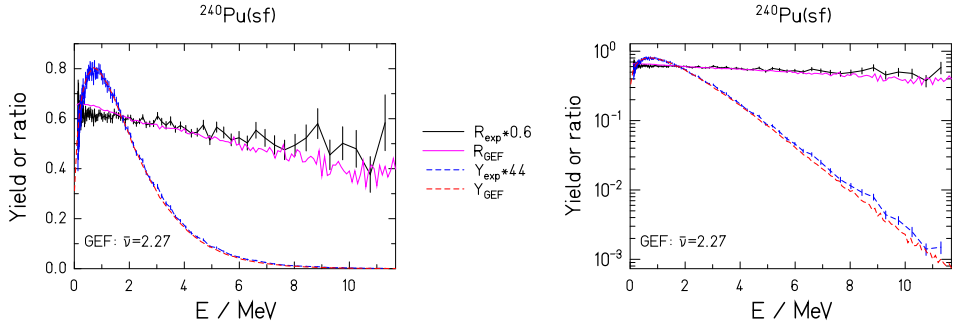

Note: Data from EXFOR dataset 414210021.

Figure 109: Prompt-neutron spectrum from ^{242}Pu(sf)

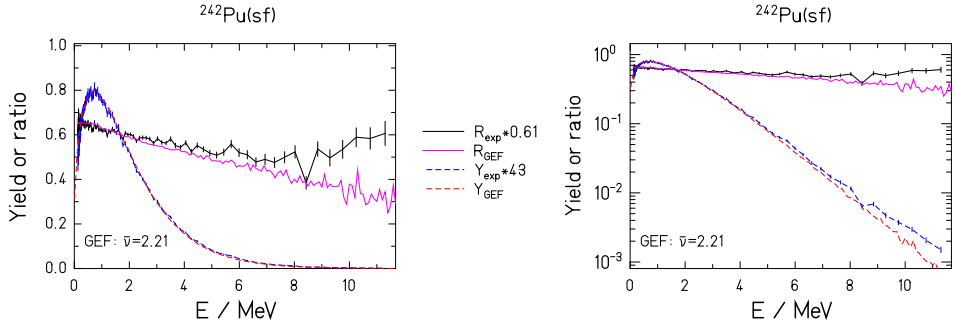

Note: Data from EXFOR dataset 414210031.

Figure 110: Prompt-neutron spectrum from ^{241}Am(n,f), E_n = 2.9 MeV

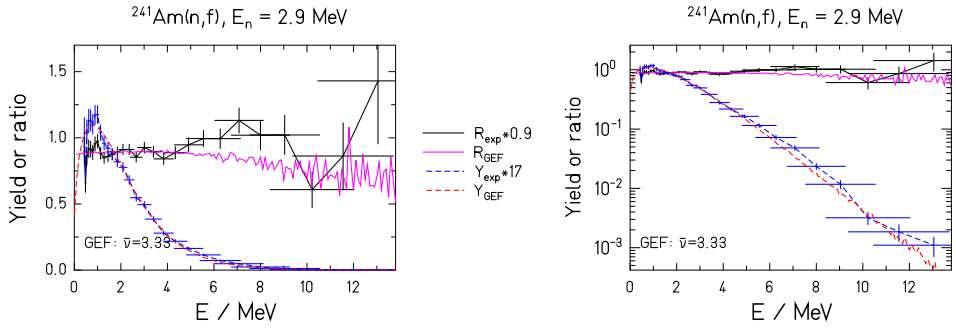

Note: Data from EXFOR dataset 415890021.

Figure 111: Prompt-neutron spectrum from ^{241}Am(n,f), E_n = 4.5 MeV

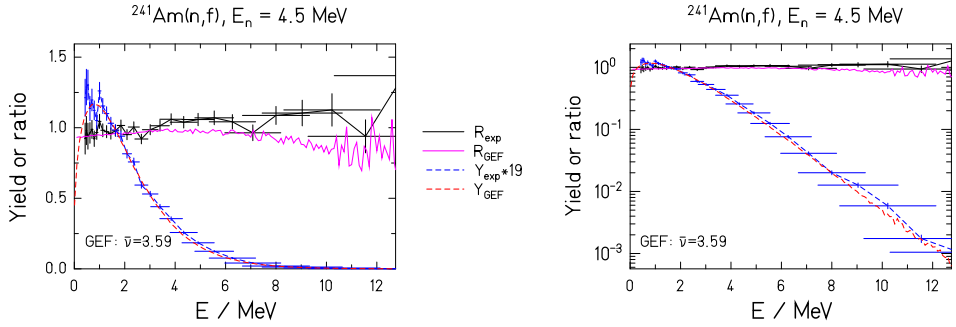

Note: Data from EXFOR dataset 415890031.

Figure 112: Prompt-neutron spectrum from ^{241}Am(n,f), E_n = 14.6 MeV

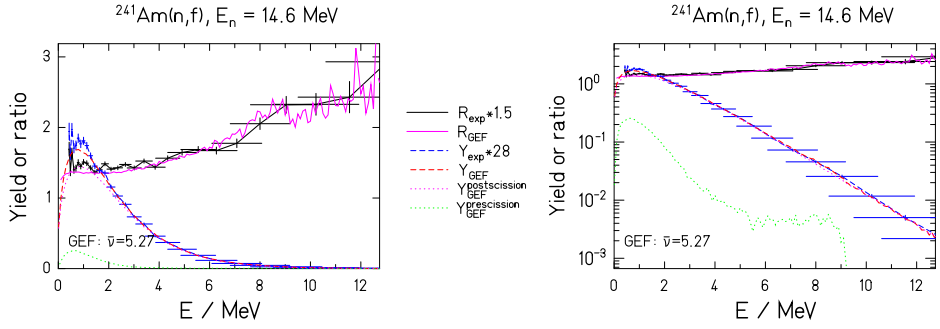

Note: Data from EXFOR dataset 415890041.

^{232}Th(n,f), E_n=2.9 MeV: The measured spectrum is very well reproduced up to 7 MeV. At higher energies, the measured spectrum shows strange fluctuations, which points at experimental uncertainties.

^{232}Th(n,f), E_n=14.7 MeV: Most part of the spectrum is very well reproduced by the calculation. However, there is a local enhancement at very low energies, which is not strong enough in the calculation below 0.5 MeV. The structure around 8 MeV is narrower and slightly shifted in the calculation.

^{233}U(n_{th},f): The calculated spectrum is very well reproduced in the range between 0.8 and 4.7 MeV that is covered by the experiment. (The spectrum was not normalised.)

^{235}U(n,f), E_n=100 K: The spectrum is well reproduced over the whole energy range. Between 1 MeV and 5 MeV, the calculated spectrum is a little bit lower. (This spectrum is not normalised.)

^{235}U(n_{th},f): The measured spectrum is very well reproduced over the whole energy range.

^{238}U(n,f), E_n=2.9 MeV: The measured spectrum is very well reproduced in the energy range below 6 MeV. At higher energies, the measured spectrum shows strange fluctuations, which points at experimental uncertainties.

^{238}U(n,f), E_n=5 MeV: The measured spectrum is very well reproduced up to 5 MeV. At 5 MeV there is a kink in the measured data, and the data have a smaller slope at higher energies. This may point at a background in the experiment.

^{238}U(n,f), E_n=6 MeV: The calculated spectrum above 1 MeV has a steeper slope than the measured one. In addition, the calculated spectrum is enhanced at the lowest energies due to a contribution from second-chance fission. This enhancement is overestimated by the calculation.

^{238}U(n,f), E_n=7 MeV: The calculated spectrum above 1 MeV has a slightly steeper slope than the measured one. The spectrum is enhanced at the lowest energies due to a contribution from second-chance fission. Amplitude, width and position of this structure are not correctly reproduced by the calculation.

^{238}U(n,f), E_n=10 MeV: This spectrum, for which no data are available, is added in order to allow a systematic view on the variation of the structure caused by the threshold of second- chance fission.

^{238}U(n,f), E_n=13.2 MeV: The spectrum is well reproduced by the model within the experimental uncertainties. However, there is a local enhancement at very low energies, which is not strong enough in the calculation. The structure due to the threshold of second-chance fission is slightly shifted to lower energies and narrower in the calculation.

^{238}U(n,f), E_n=14.7 MeV: Again, there is a local enhancement at very low energies below 0.6 MeV, which is not strong enough in the calculation. The shape and the position of the structure due to the threshold of second-chance fission are not correctly reproduced by the calculation.

Figure 113: Prompt-neutron spectrum from ^{242}Am(n$_{th}$,f)

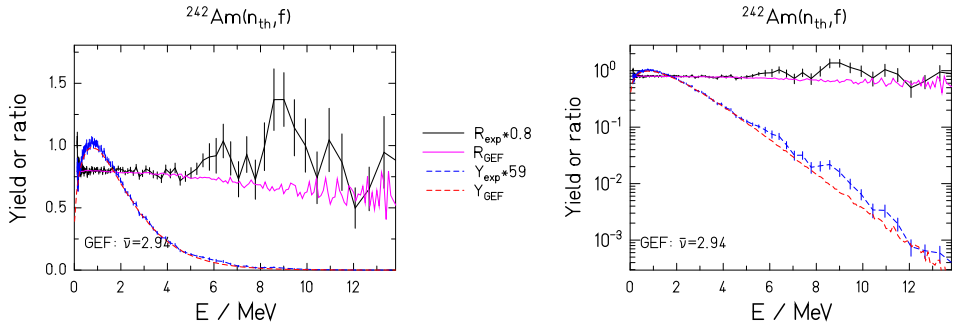

Note: Data from EXFOR dataset 414210081.

Figure 114: Prompt-neutron spectrum from ^{243}Am(n,f), E_n = 2.9 MeV

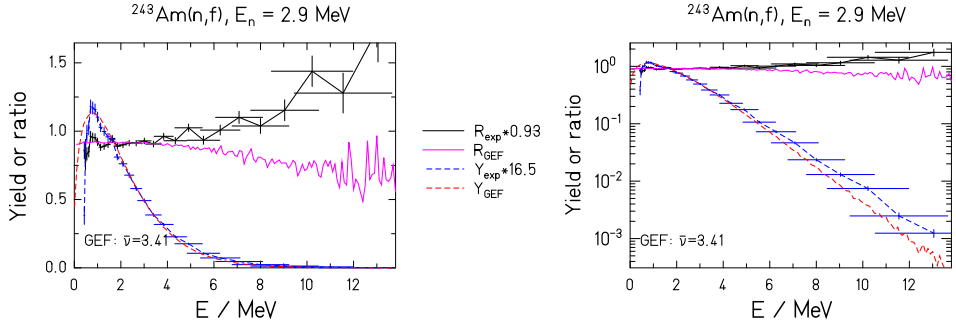

Note: Data from EXFOR dataset 415890051.

Figure 115: Prompt-neutron spectrum from ^{243}Am(n,f), E_n = 4.5 MeV

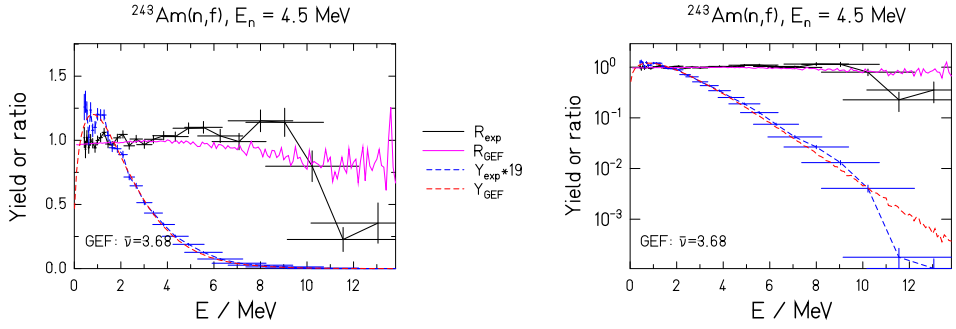

Note: Data from EXFOR dataset 415890061.

Figure 116: Prompt-neutron spectrum from ^{243}Am(n,f), E_n = 14.6 MeV

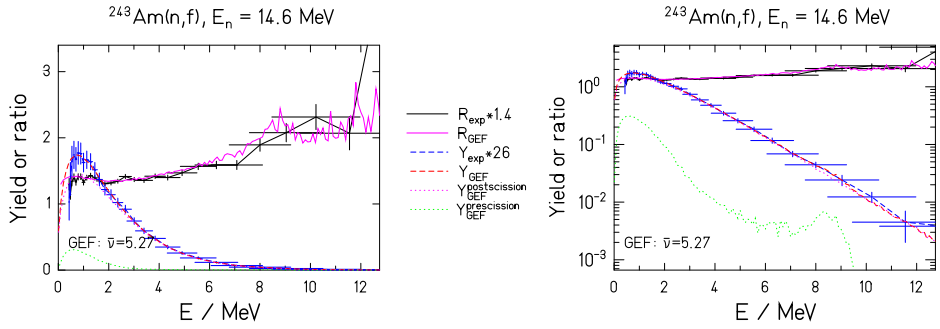

Note: Data from EXFOR dataset 415890071.

Figure 117: Prompt-neutron spectrum from ^{243}Cm(n$_{th}$,f)

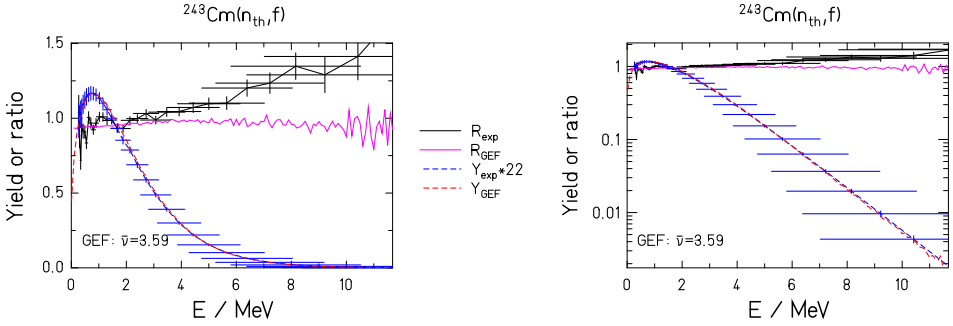

Note: Data from EXFOR dataset 415890081.

Figure 118: Prompt-neutron spectrum from ^{244}Cm(sf)

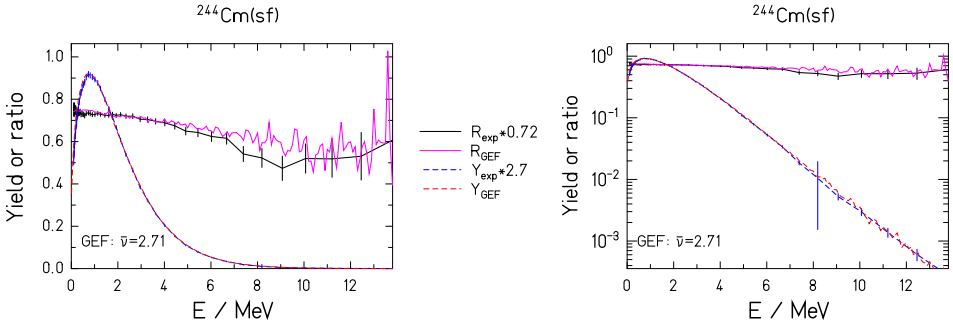

Note: Data from EXFOR dataset 413400041.

Figure 119: Prompt-neutron spectrum from ^{245}Cm(n_{th},f)

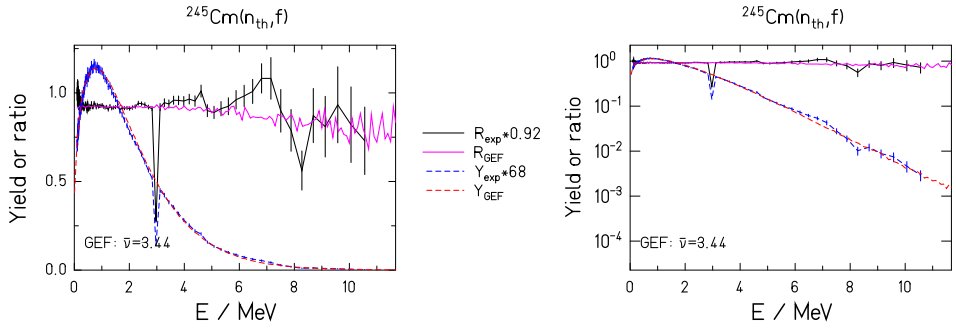

Note: Data from EXFOR dataset 414210091.

Figure 120: Prompt-neutron spectrum from ^{246}Cm(sf)

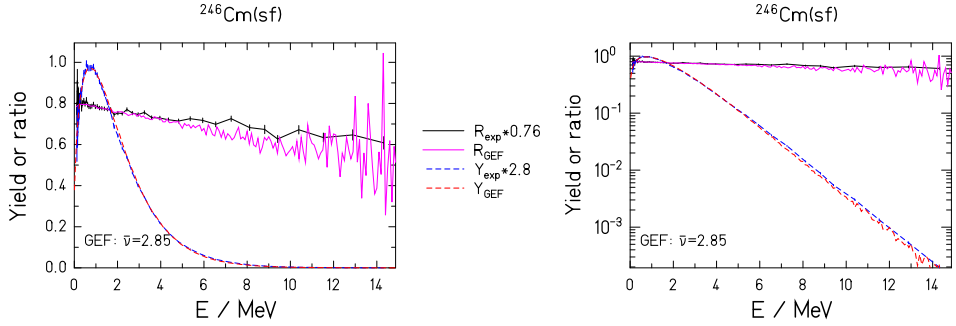

Note: Data from EXFOR dataset 413400051.

Figure 121: Prompt-neutron spectrum from ^{248}Cm(sf)

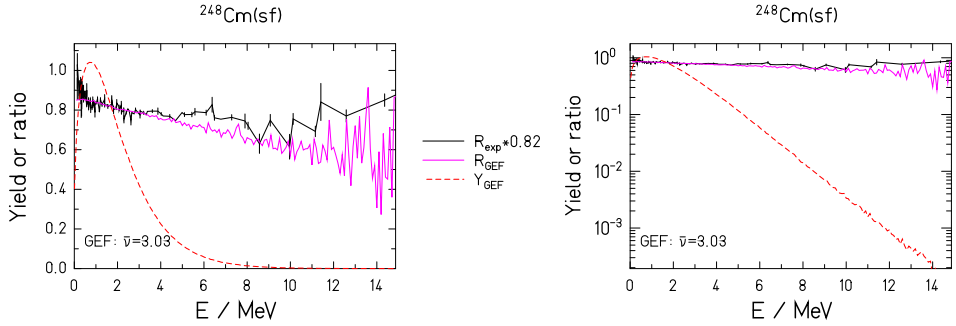

Note: Data from EXFOR dataset 41113004.

^{239}Pu(n_{th},f): There are two experimental results with different slopes of the high-energy tail. The slope of the calculated spectrum agrees better with the steeper slope of one of the experiments, although this spectrum shows strong local fluctuations. The steeper slope is also much closer to the ones of the systems ^{238}U(n,f), E_n=2.9 MeV and ^{246}Cm(sf), which have similar total prompt-neutron yields as ^{239}Pu(nth,f). Since all these cases are restricted to first-chance fission, one should expect that the total prompt-neutron yield is a measure of the mean excitation energies of the primary fragments, which means that it should be correlated with the slope of the high-energy tail of the prompt-neutron spectrum. Due to this argument, the spectrum with the steeper slope appears to be more likely the correct one.

^{240}Pu(sf), ^{242}Pu(sf): The measured spectra are well reproduced by the calculation, if the fluctuations in the experiment at higher energies are disregarded.

^{241}Am(n,f), E_n=2.9 MeV: Below 4 MeV, the measured spectrum is well reproduced by the calculation. A comparison at higher energies is difficult due to the strong fluctuations in the measured spectrum.

^{241}Am(n,f), E_n=4.5 MeV: The measured spectrum is well reproduced by the calculation below 2.5 MeV. Above this energy the experimental data fluctuate rather strongly.

^{241}Am(n,f), E_n=14.6 MeV: The measured spectrum is very well reproduced by the calculation, including the structure around 9 MeV.

^{242}Am(n_{th},f): Below 4.5 MeV, the measured spectrum is very well reproduced by the calculation. A comparison is difficult at higher energies due to the strong fluctuations in the measured spectrum.

^{243}Am(n,f), E_n=2.9 MeV: The measured spectrum is well reproduced below 4 MeV. The calculated spectrum is much softer in the high-energy tail than the measured one. It is remarkable that the measured spectrum is appreciably stiffer than the spectrum of ^{252}Cf(sf), although the total prompt neutron yield is almost the same. This points at an experimental problem.

^{243}Am(n,f), E_n=4.5 MeV: The measured spectrum is well reproduced below 4 MeV. A comparison at higher energies is difficult due to the strong fluctuations of the measured spectrum.

^{243}Am(n,f), E_n=14.6 MeV: The measured spectrum is generally well reproduced by the calculation. The structure around 8 MeV is slightly shifted to lower energies.

^{243}Cm(n_{th},f): When comparing the measured and the calculated ratios to the spectrum of ^{252}Cf(sf), the calculated spectrum appears to be much softer than the measured one. It is astonishing that the measured spectrum is as stiff as the one for ^{243}Am(n,f) at E_n=14.6 MeV which has a much higher total prompt-neutron yield. The measured spectrum is also much stiffer than the one of the system ^{252}Cf(sf), although the total prompt-neutron yield is about the same. However, when comparing the empirical prompt-neutron spectrum, already multiplied with the reference spectrum of ^{252}Cf(sf), which is also listed in EXFOR, with the calculated spectrum, in particular in logarithmic scale in the right panel, there is very good agreement. That means that the ratio to ^{252}Cf and the spectrum given in EXFOR are not consistent. This kind of inconsistency is not observed for any

other case.

^{244}Cm(sf): The measured spectrum is well reproduced below 6 MeV. At higher energies, the measured spectrum has an unusual shape with a dip around 9 MeV. This dip is not found in the calculated spectrum.

^{245}Cm(n$_{th}$,f): The measured spectrum is well reproduced at energies below 2.5 MeV. One value at 3 MeV seems to be in error. At higher energies, the measured spectrum shows strong fluctuations, making a comparison difficult.

^{246}Cm(sf) and ^{248}Cm(sf): Both measured spectra are well reproduced by the calculation up to 4 MeV. There are deviations and fluctuations in the experiment at higher energies.

8.5.2.4 Discussion:

General observations: The most salient features of this comparison are:

1. There is a qualitatively rather good reproduction of the shape of the spectra, including the structural effects. There are some deviations in the quantitative reproduction of the structure at the threshold of second-chance fission.

2. In some cases, the exponential slope of the calculated spectrum exceeds the slope of the measured spectrum. The most important deviations are found for ^{238}U(n,f), E_n=5 and 6 MeV, ^{239}Pu(n$_{th}$,f) with respect to one experiment, ^{243}Am(n,f), E_n=2.9 MeV, and ^{243}Cm(n$_{th}$,f).

3. There are some fluctuations in the data for which the model does not provide an explanation. The most severe cases are ^{241}Am(n,f), E_n=2.9 MeV, ^{242}Am(n$_{th}$,f), ^{243}Am, E_n=4.5 MeV, and ^{243}Cm(n$_{th}$,f).

4. Two experiments for ^{239}Pu(n$_{th}$,f) give diverging results.

5. There are some inconsistencies in different data tables from the same experiment for ^{243}Cm(n$_{th}$,f) . There is very good agreement of the calculated prompt-neutron spectrum with the spectrum, while there are strong deviations to the ratio with respect to ^{252}Cf(sf).

Pre-fission neutron emission: The pre-fission neutrons are registered in coincidence with fission only if the excitation energy of the residual nucleus falls above its fission barrier. This causes a pronounced structure in the prompt-fission-neutron spectrum. The structure of the calculated spectrum reproduces the structure in the measured spectra rather well in most cases. In the calculations, the structure depends on the description of pre-scission neutron emission, pre-equilibrium and statistical, as well as on the excitation-energy-dependent fission probabilities of the different nuclei. In particular, the mean energy of the structure in the calculated spectra depends on the value of

the fission threshold in the GEF code. In particular for even-even fissioning nuclei, the number and the nature of levels at the fission barrier below the pairing gap are subject to strong nuclear-structure effects [126] and difficult to model with a global approach. In the experiment, the width of this structure is very sensitive to the energy spread of the incoming neutrons and the energy resolution in the measurement of the emitted neutrons. The mean energy is very sensitive to the energy definition of the incoming neutrons.

Inverse cross section: Since the evaporation spectrum is calculated with a modified Weisskopf formalism where the angular momentum is explicitly considered, the mass- and energy-dependent transmission coefficients for neutron emission were parametrised by using inverse capture cross-sections according to Dostrowsky et al. [210] in a slightly modified version for fast computing, as already mentioned in Section 3.10.[7]

Since the fast-neutron spectrum in fission is composed of the contributions from many emitting fragments, the use of this global description is probably a satisfactory approximation.

8.5.2.5 Conclusion: The model behind the GEF code is unique in the sense that it provides practically all observables from nuclear fission without any needs for specific experimental information by using a single fully consistent model description for all heavy fissioning systems. The present comparison with measured prompt-neutron spectra shows good agreement in most cases, but also some deviations, mostly in the high-energy tail of the spectrum and in the structures caused by threshold effects in pre-fission neutron emission. These structures are not exactly reproduced by the calculation, although their integral strength and their position in energy deviate only little in most cases. In particular in the fission of the lighter systems at higher energies, the model does not provide enough intensity at very low energies, mostly below 0.5 MeV, in the frame of the fissioning system. Some of this additional intensity is explained by the emission during the acceleration phase, but this contribution does not reach far enough down in energy. There seems to be a source of very low-energetic neutrons with an exponential-like spectrum in the frame of the fissioning system, which is not accounted for in the model. This problem has already been discussed in [209, 199]. A possible origin of these low-energy neutrons could be the pre-acceleration emission from fragments with very large transmission coefficients at low energies, which are not accounted for in the global description used in the present model.

A systematic view on the experimental data suggests that the uncertainties are underestimated in several cases. There are strange fluctuations in the measured spectra for ^{241}Am(n,f), E_n=2.9 MeV, for ^{242}Am(n$_{th}$,f), for ^{243}Am(n,f), E_n=4.5MeV, and for ^{245}Cm(n$_{th}$,f). Contradictory results were obtained from different experiments for ^{239}Pu(n$_{th}$,f). In the energy range up to E_n = 7 MeV, where at least most part of the spectrum is only fed by first-chance fission, the high-energy tail of the measured spectra

[7]The present version of the GEF code is conceived as a very fast code. Whenever possible, fast algorithms were used as long as their approximations do not exceed the estimated general uncertainties of the model. They may easily be replaced by more elaborate descriptions in the freely accessible code.

becomes in general stiffer with increasing energy of the impinging neutron. This trend is weaker in the calculated spectra in some cases. But the variation of the stiffness is not continuous in the data as a function of the incoming-neutron energy. Sometimes, e.g. for ^{238}U(n,f) at $E_n = 7$ MeV, the spectrum becomes softer again with increasing energy of the incoming neutrons. Moreover, the variations from one system to another one are not consistent with the model. After a careful analysis of this problem, the situation appears to be unclear. On the one hand, the mean temperature of the emitting fragments is expected to increase with increasing incoming-neutron energy. Thus, the trend to stiffer prompt-neutron spectra found in the experiment is qualitatively expected. On the other hand, these experiments are certainly very challenging, and some results may suffer from an incompletely suppressed background of scattered neutrons. This might be the reason for some unexpected fluctuations of the logarithmic slope of the spectra from one system to another as a function of incoming-neutron energy or total prompt-neutron yield. More data of high quality would certainly be helpful for a better understanding of this problem.

We would like to point out a slight inconsistency between the good agreement of the ratios of most prompt-neutron spectra to the spectrum of ^{252}Cf(sf) in this section and the deviations found in the previous section between the measured and the calculated spectrum of ^{252}Cf at energies below 5 MeV, while the spectrum of ^{235}U(n_{th},f) was well reproduced. This finding suggests to perform a deeper analysis of the experimental results.

One may conclude that the GEF model provides a global view on the systematic variation of the fission observables as a function of the fissioning system and its excitation energy. It reproduces the measured prompt-neutron spectra in general rather well. A detailed analysis reveals three types of deviations that are found for some of the systems: the description of the structure in the prompt-neutron spectrum due to the contribution of second-chance fission suffers probably from difficulties in modelling the level densities of even-even nuclei below the pairing gap by the global approach used in the code. Furthermore, there seems to be a source for the emission of neutrons with very low energies in some systems before or slightly after scission that is not sufficiently accounted for in the model. Finally, we think that there are indications that the stiffness of the measured prompt-neutron spectra is distorted in several cases by an incompletely suppressed background of scattered neutrons. Predictions for other systems where no experimental data are available are expected to be possible with rather good quality.

8.6 Prompt-gamma emission

In Figure 122, the calculated prompt-gamma spectrum for the system ^{235}U(n$_{th}$,f) is compared with the experimental data of [211]. One can distinguish the signatures of the different contributions. The statistical E1 emission dominates the high-energy part above 2 MeV. E2 emission from rotational bands at the yrast line strongly fills up the spectrum below 2 MeV. The structure in the calculated gamma spectrum in this energy range that is caused by the energies of the rotational and vibrational transitions is not fully visible due to the 100-keV binning of the spectrum. The amount of E2 emission is constrained by the angular-momentum distribution of the fission fragments. The deviation of the calculated from the measured spectrum at very low energy is probably explained by efficiency losses of the gamma detection to a great part. Internal conversion does not seem to play a major role, because the gamma spectrum for ^{252}Cf(sf) shown in Figure 123 is well reproduced in this low-energy range.

Figure 122: Prompt-gamma spectrum for ^{235}U(n$_{th}$,f)

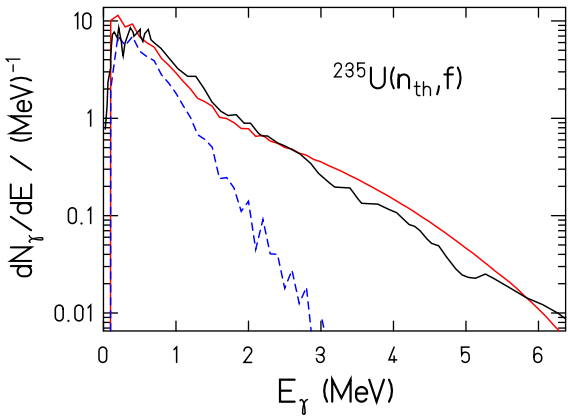

Note: Experimental prompt-gamma spectrum for ^{235}U(n$_{th}$,f) [211] (black line) in comparison with the result of the GEF model (red line). The calculated contribution from E2 radiation is shown separately (blue dashed line).

Detailed experiments with very high counting statistics and large-volume, high-granularity detectors, e.g. with the Darmstadt-Heidelberg Crystal ball, have been performed for spontaneous fission of ^{252}Cf. These experiments cover a γ-energy range up to 80 MeV including the whole GDR and extending to the postulated radiation from nucleus-nucleus coherent bremsstrahlung of the accelerating fission fragments [212], which is not considered in the GEF model. Figure 123 shows an overview on these data in comparison with the result of the GEF code up to 15 MeV. Obviously, the features of this spectrum are fairly well reproduced, in particular the contribution of E2 gammas below 3 MeV and the kink near 8 MeV, approaching the peak energy of the GDR. The measured spectra have not

been unfolded for the detector response. This explains most of the discrepancies between measured and calculated spectra above 9 MeV [215]. In the lower-energy range (below 6 MeV), the data from [216, 217, 218, 219] are very close to the other experimental data shown.

Figure 123: Prompt-gamma spectrum for ^{252}Cf(sf)

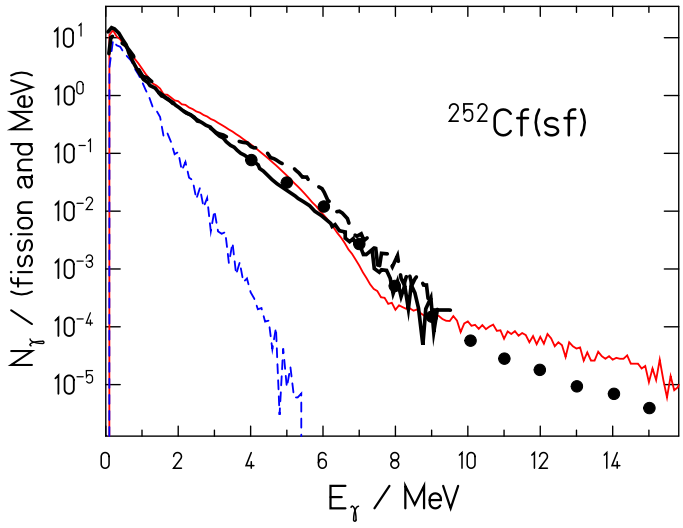

Note: Experimental prompt-gamma spectrum for ^{252}Cf(sf) (data points and black lines) in comparison with the result of the GEF code (thin red line). Black dashed line: Raw spectrum from [213], gate on the mass of the heavy fragment $126 \leq A_H \leq 136$. Black full line: Raw spectrum from [213], gate on $144 \leq A_H \leq 154$. Full symbols: Raw data from [214]. The calculated contribution from E2 radiation is shown separately (dashed blue line).

Several theoretical studies of the many complex features of these data have been performed, mostly with modified versions of the CASCADE code [220], see e.g. refs. [221, 222]. A recent effort to simulate the spectrum of prompt fission gammas [223] exploited detailed empirical knowledge on the spectroscopic properties of the fission fragments. These calculations are complementary to the calculations with the GEF model: the models mentioned are based on measured A-TKE distributions and prompt-neutron multiplicities for determining the yields and the excitation energies of the fission fragments after scission as a starting point of their calculation. In contrast, the GEF model treats the whole fission process in a consistent and global way and does not use any particular empirical information for a specific system.

Comparing the total gamma energies and even more the gamma multiplicities is delicate, because they strongly depend on the lower threshold of the gamma detection [224] and eventually the branching of internal conversion, which is not considered in the GEF model.

8.7 Fragment kinetic energies

Another main fission observable is the kinetic energy of the fragments. The global shape of the kinetic energy as a function of fragment mass is easily reproducible: the kinetic energy can be estimated by the Coulomb repulsion between the deformed fragments. Describing the kinetic energy with high precision is however difficult.

The kinetic energies of pre- and post-neutron fragments are usually measured by the $2v$ technique and the $2E$-technique, respectively. The $2E$-technique is very often used to extract the pre-neutron energies, however, a correction on mass-dependent prompt-neutron yields $\nu(A)$ must be applied. This $\nu(A)$ correction is often based on the Wahl evaluation e.g. [225]. The kinetic-energy data are usually of great quality, and the precision on the mean values is supposed to be around 0.5 MeV. The energy resolution of the detectors, however, is limited, leading to a mass resolution between 2 and 3 units [225]. The kinetic energy is also measured at the Lohengrin spectrograph, where only post-neutron fragments are available.

Figure 124: Mass-dependent mean kinetic energy for ^{233}U(n$_{th}$,f)

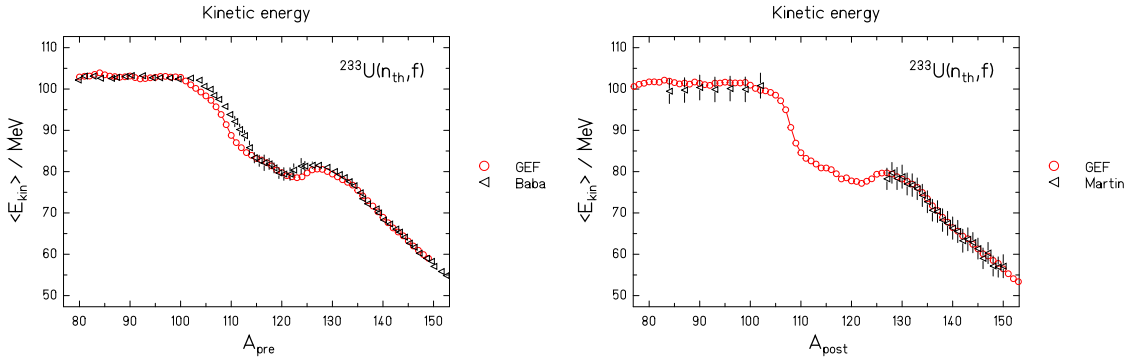

Note: The measured mean kinetic energy before evaporation (left) and after evaporation (right) of prompt neutrons as a function of the mass of the fragment for ^{233}U(n$_{th}$,f) [225, 226] is compared with the result of the GEF model.

Table 13: Mean TKE before prompt-neutron emission for well known systems

Nucleus	^{233}U(n$_{th}$,f)	^{235}U(n$_{th}$,f)	^{239}Pu(n$_{th}$,f)	^{252}Cf(sf)
Recommended value	170.1 ± 0.5	170.5 ± 0.5	177.9 ± 0.5	184.1 ± 1.3
GEF	172.32	172.04	178.85	188.14

Note: Mean TKE in MeV before evaporation of prompt neutrons for well known systems. The recommended values are extracted from ref. [230], page 321.

Figure 125: Mass-dependent mean kinetic energy for ^{235}U(n$_{th}$,f)

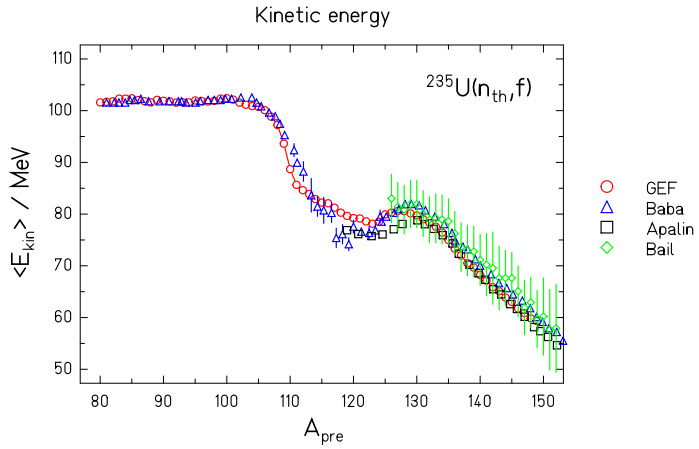

Note: The measured mean kinetic energy before evaporation of prompt neutrons as a function of the mass of the fragment for ^{235}U(n$_{th}$,f) [225, 227, 228] is compared with the result of the GEF model.

Figure 126: Mass-dependent mean kinetic energy for ^{239}Pu(n$_{th}$,f)

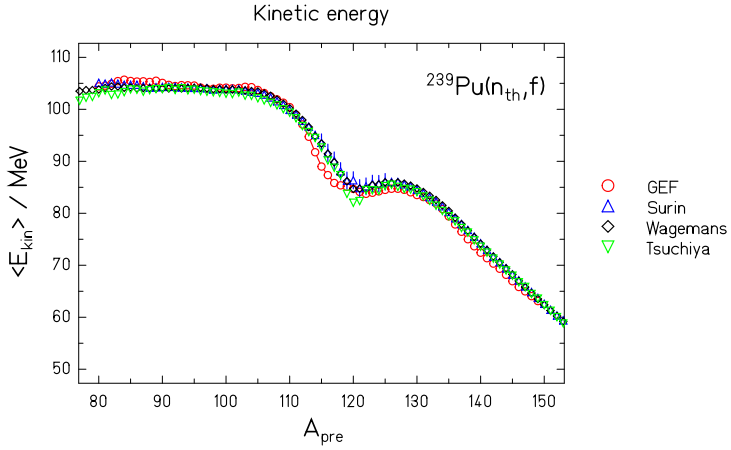

Note: The measured mean kinetic energy before evaporation of prompt neutrons as a function of the mass of the fragment for ^{239}Pu(n$_{th}$,f) [229, 230, 231] is compared with the result of the GEF model.

Figures 124 to 127 show the mean kinetic energy of the fragments for different fissioning nuclei. The agreement between the GEF predictions and the experimental data is very good in the thermal-neutron-induced fission of ^{233}U, ^{235}U and ^{239}Pu (see Figures 124-126). However, the total kinetic energies of ^{252}Cf(sf) from the GEF model are higher by 4 MeV than the measured data (see Figure 127 and Table 13). A wider analysis of this deviation

can be found in Section 10.3.

Important deviations are also seen in the kinetic energy of neutron-induced fission of ^{232}Th (see Figure 128) especially in the A = 120-130 region i.e. in the border region of the SL and the S1 fission channel. This problem will be further investigated in Section 10.2.

Figure 127: Mass-dependent TKE before prompt-neutron emission for ^{252}Cf(sf)

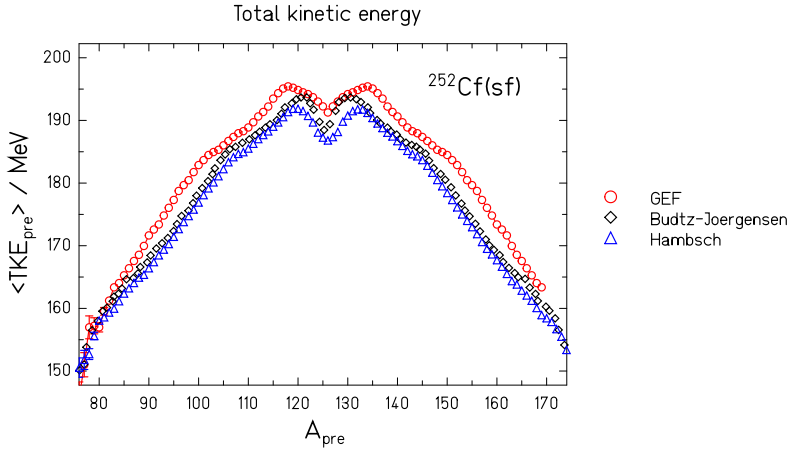

Note: The measured mean total kinetic energy before evaporation of prompt neutrons as a function of the mass of the fragment for ^{252}Cf(sf) [192, 174] is compared with the result of the GEF model.

Figure 128: Mass-dependent pre-neutron TKE for ^{232}Th(n,f)

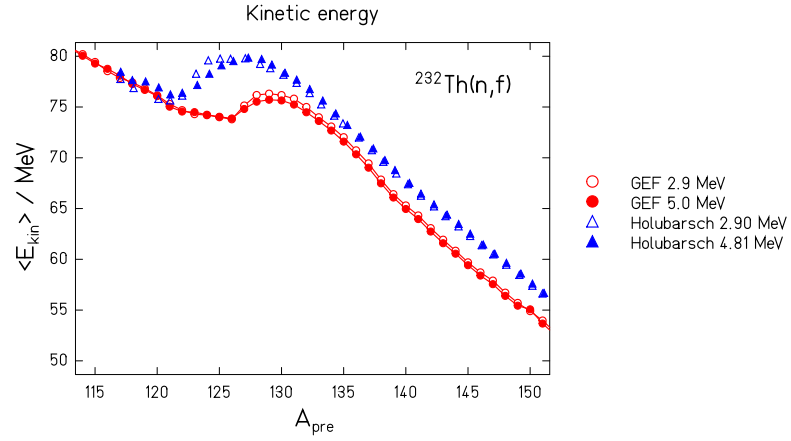

Note: The measured mean total kinetic energy before evaporation as a function of the mass of the fragment for ^{232}Th(n,f) [233] is compared with the result of the GEF model.

Small deviations for ^{232}Th(n,f) can also be observed in the regions of the S1 and the SL modes; they can be due to a wrong correction of prompt-neutron multiplicity ($\nu(A)$ for the experimental data when extracted from $2E$ technique or to an underestimation of the TKE(S1) in the modelling of the S1 mode. The fission of the ^{240}Pu compound nucleus, either in neutron-induced fission or in spontaneous fission, gives some answers about the energy contribution of the S1 mode as its yield contribution is different (see Table 14).

It was observed that nearly all total-kinetic-energy distributions in neutron-induced fission have a shape close to a Gaussian with some skewness, which is well reproduced by the GEF code, see Section 3.7. An example is shown in Figure 129 for the ^{239}Pu+n reaction. For the spontaneous fission of ^{238}Pu, ^{240}Pu and ^{242}Pu a second component appears due to the large weight of the S1 mode. The component is also seen in the GEF calculated distribution as shown in Figure 129. The calculated distributions are slightly shifted and systematically narrower than the measured ones. It has already been noted in [232] that the data of Milton et al. should be increased by 4 MeV to correspond to the recommended value for ^{239}Pu obtained in several measurements with the $2v$ technique.

Figure 129: Pre-neutron TKE distribution for ^{240}Pu(n$_{th}$,f) and ^{240}Pu(sf)

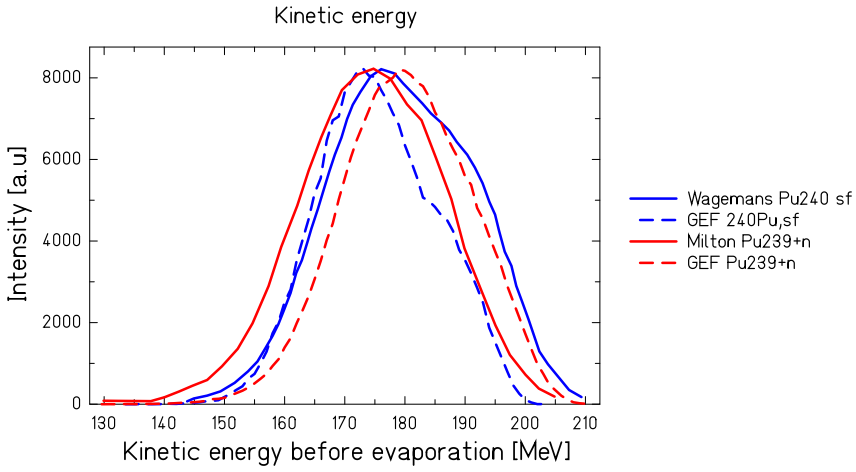

Note: Total-kinetic-energy distribution before prompt-neutron evaporation for ^{240}Pu(n$_{th}$,f) and ^{240}Pu(sf) [236, 230].

Though the mean TKE value is, in a lot of cases, in very good agreement, the dispersion of this value should also be studied. Figure 130 illustrates the variance of the TKE distribution for neutron-induced reactions. The order of magnitude and the Z dependence is well reproduced by the GEF model, however, the variance predicted by the GEF code is always lower than the experimental value. Because of energy conservation, a too small width in TKE also implies a too small width in the neutron multiplicity. The neutron-multiplicity distribution, as detailed in Section 8.4, is also slightly too narrow for ^{235}U(n$_{th}$,f), but the width agrees perfectly for ^{239}Pu(n$_{th}$,f) and ^{252}Cf(sf). In view of the

Table 14: Weights of fission modes for ^{239}Pu(n$_{th}$,f) and ^{240}Pu(sf)

	S1	S2	SA
^{240}Pu(sf)	16,2 %	83.2 %	0.6 %
^{239}Pu + n	7.7 %	88.9 %	2.8 %

Note: Relative contributions of the different modes for ^{239}Pu(n$_{th}$,f) and ^{240}Pu(sf) according to the GEF model.

good agreement of the measured prompt-neutron multiplicity distributions with the GEF results, it may not be excluded that the influence of the experimental energy resolution is underestimated to some extent when this effect is substracted from the width of the measured TKE distribution.

Figure 130: Variance of the TKE distribution for neutron-induced fission

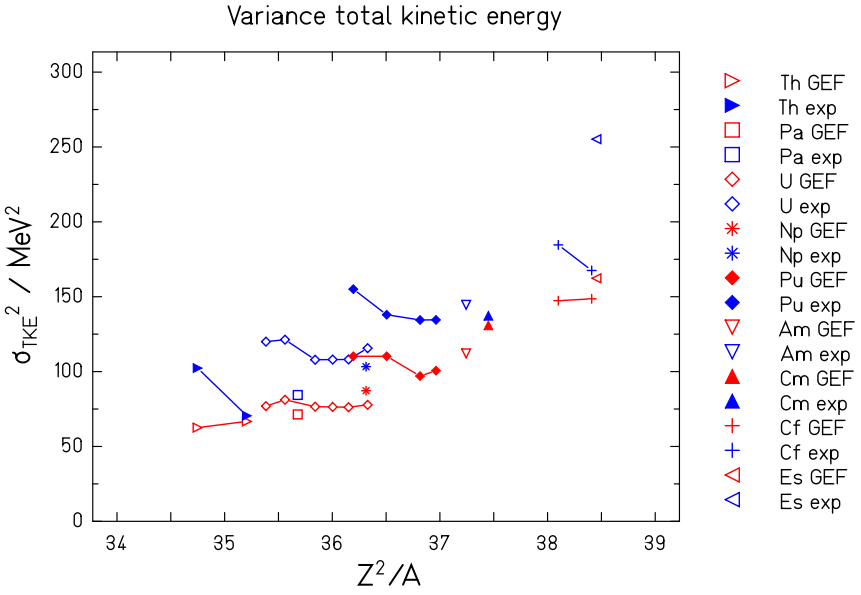

Note: The measured variance of the TKE distribution before prompt-neutron evaporation for neutron-induced reactions [232] is compared with the result of the GEF model.

Moreover, the kinetic-energy distribution for each mass is narrower than the measured ones as shown in Figure 131 for ^{252}Cf(sf).

Figure 132 shows the width of the kinetic energy for ^{233}U(n$_{th}$,f) before and after evaporation of prompt neutrons. In agreement with the previous conclusions, the calculated width before evaporation is always narrower than the measured ones. It has to be noted that the experimental data (e.g Martin and Faust ones on Figure 132) for the width of

Figure 131: Mass-dependent width of the TKE distribution for ^{252}Cf(sf)

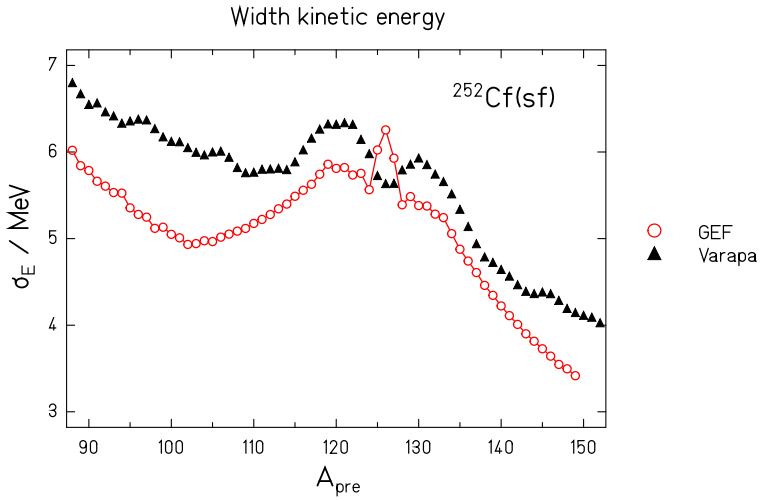

Note: The measured width of the total-kinetic-energy distribution for ^{252}Cf(sf) [234] is compared with the result of the GEF model.

the kinetic energy distribution can show some discrepancies mainly due to the correction of the influence of the target thickness on the width of the energy distribution. The situation is not so clear after evaporation, where the GEF results agree with the data of Faust et al. for the light fragments. The calculated values are, however, smaller than all measured values in the heavy group.

According to a lot of experiments (ref. [232], page 366) it was observed that when increasing the excitation energy of the system the mean TKE does not change a lot. For example for ^{235}U(n,f) TKE(5 MeV) - TKE(th) was observed to be around -1 MeV ±0.5 MeV [237, 238, 100] which represents 0.5% of the TKE(th). This difference is of 2 MeV for the ^{239}Pu(n,f) reaction. However, the influence of the excitation energy of the system on the mean TKE is clearly overestimated by the GEF code as shown in Figure 133. Due to energy conservation, the number of neutrons emitted should also evolve too much with the excitation energy of the system, by about 0.2 neutrons on 5 MeV. But this is not so much seen in Figure 85 in Section 8.4. Possible explanations could be an increased mean kinetic energy of the prompt neutrons or an enhanced gamma emission. This demonstrates, how the interconnection between different fission observables can be studied by the GEF model.

Figure 132: Width of the TKE distribution for ^{233}U(n$_{th}$,f)

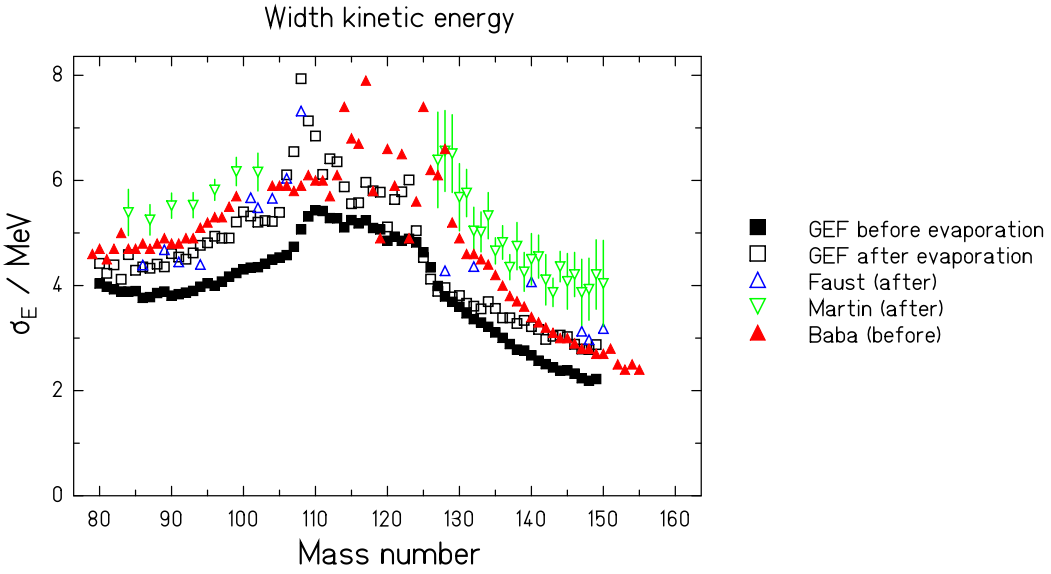

Note: The measured width of the kinetic-energy distribution for ^{233}U(n$_{th}$,f) before evaporation (full symbols) and after evaporation (open symbols) [225, 235, 226] are compared with the result of the GEF model.

Figure 133: TKE as a function of the incident-neutron energy for ^{235}U(n,f)

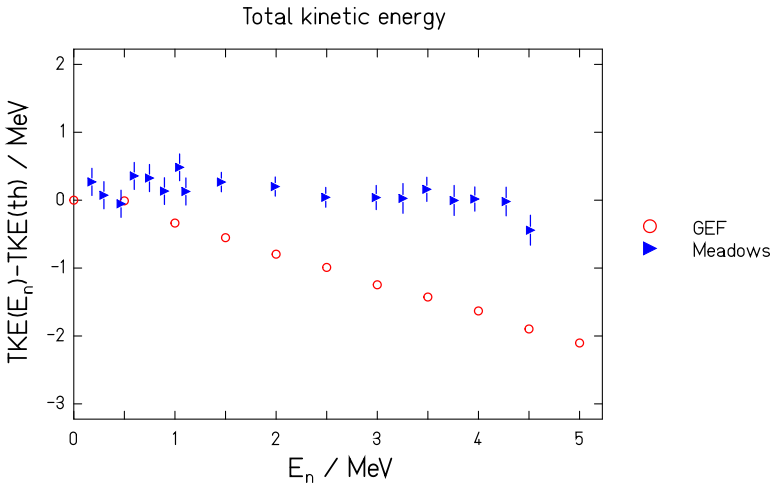

Note: Difference between the total kinetic energy (TKE(E_n)) and the thermal value (TKE(th)) as a function of the neutron energy for ^{235}U(n,f). Measured data [238] are compared with the result of the GEF model.

9 Data for application

Nuclear industry strongly relies on the values of some specific fission yields. A very short overview of some important features of the nuclear-reactor industry, where fission yields are important, is presented below.

9.1 Decay heat

The isotopic fission yields are used in order to evaluate the decay heat. In a lot of cases, the decay data (I_γ, ...) are the main problem of the decay-heat prediction, however, as shown in [239], fission yields are also of importance for the prediction.

The decay-heat calculation was performed for ^{235}U for a fission pulse at thermal energy, see Figure 134. The GEF results as shown in the figure agree quite well with the JEFF ones proving the quality of the GEF prediction. The discrepancies between the experimental data [241] and the calculated decay heat are mainly due to the decay data [242].

Figure 134: Total decay heat for ^{235}U(n$_{th}$,f)

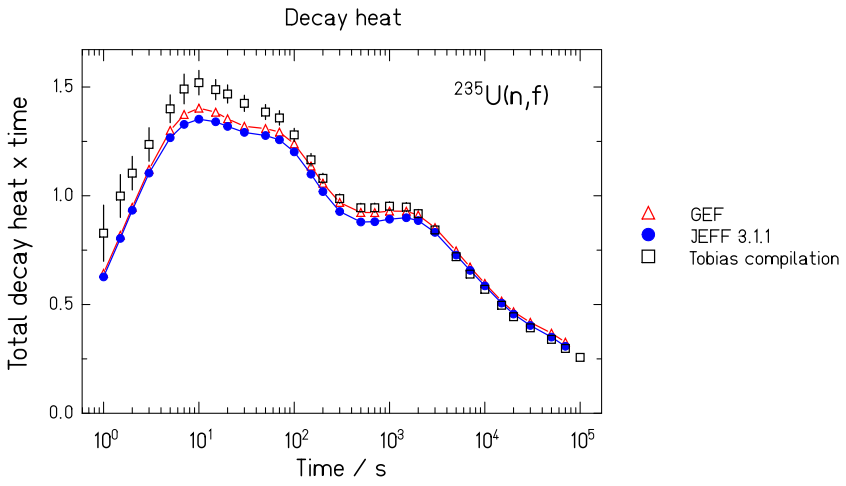

Note: Total decay heat for a fission pulse for ^{235}U(n$_{th}$,f). The calculations were performed with [240] with different fission yields.

9.2 Delayed neutrons

In order to calculate the delayed fission-neutron yield, the code implemented in [243] and the associated delayed-neutron-precursor values were used. This procedure was validated for ^{235}U. When the JEFF 3.1.1 fission yields are used, the calculated value of $100 \cdot \nu_d$ is 1.61; the recommended value is 1.62.

As the number of the main delayed neutron precursors is limited (^{87}Br, ^{137}I, ^{88}Br, ^{138}I, ^{93}Rb, ^{89}Br, ^{94}Rb, ^{139}I, ^{85}As, ^{98m}Y, ^{93}Kr, ^{144}Cs, ^{140}I, ^{91}Br, ^{95}Rb, ^{96}Rb, ^{97}Rb), the delayed-neutron yield allows observing some local discrepancies of the fission yields, which were found to be in good agreement with the empirical data in Section 8.2 at the first order.

Figure 135: Influence of the odd-even effect on the delayed-neutron yield

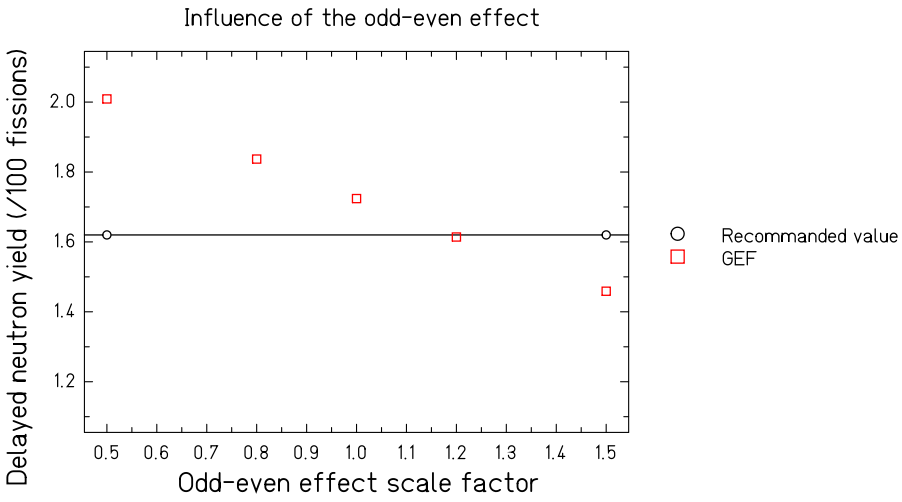

Note: Influence of the odd-even effect on the ^{235}U(n$_{th}$,f) calculated delayed-neutron yield in comparison with the recommended value [244].

Table 15: Delayed-neutron yields

	^{235}U thermal	^{235}U fast	^{238}U fast	^{239}Pu thermal	^{239}Pu fast
NEA	1.62	1.63	4.65	0.65	0.651
GEF	1.72	1.64	4.40	0.71	0.673
(GEF-NEA)/NEA	+6.2 %	+0.6 %	-5.4 %	+9.2 %	+3.4 %

Note: Delayed-neutron yields for well-known system. The NEA recommended values are extracted from [244]. GEF calculations were performed at E_n = 2 MeV for the fast values.

Moreover, the delayed-neutron precursors are usually odd-Z nuclei, the delayed neutrons are consequently a non-direct way to observe the even-odd effect. Figure 135 illustrates the influence of the odd-even effect on the delayed-neutron yields for ^{235}U. When the odd-even effect is modified by multiplying the local odd-even effect obtained by the GEF code by a scale factor larger (smaller) than one, the odd yields decrease (increase) and then, consequently, the delayed-neutron yield decreases (increases), as observed in Figure 135.

The delayed fission-yield values were also compared with the recommended values for well-known fissioning systems in Table 15. The GEF code over-estimates the delayed-fission yield in each case.

The group (as defined by Keepin et al. in ref. [245]) repartition obtained with the GEF fission yield is also compared with the GODIVA and IPPE measurement at 1 MeV. This repartition is in good agreement with the measured ones.

Figure 136: Delayed-neutron yield for ^{235}U(n,f), E_n = 1 MeV

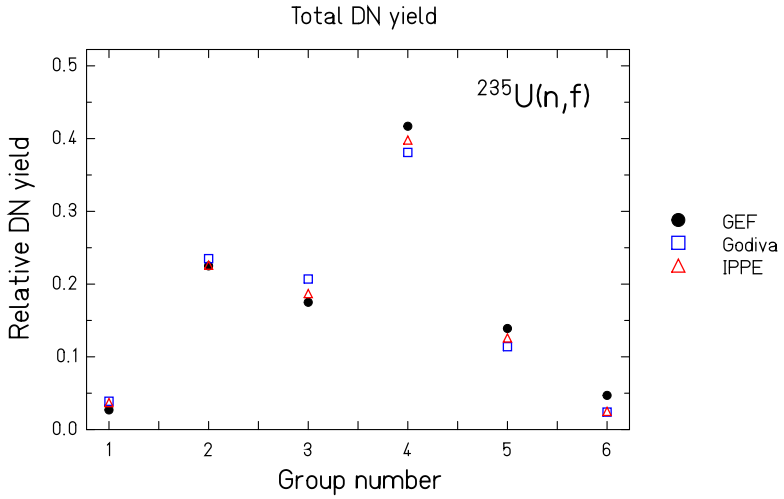

Note: Relative delayed-neutron yield for ^{235}U(n,f) at E_n = 1 MeV as a function of the group number as defined by Keepin et al. [245], Annex 1.

Figure 137: Delayed-neutron yields for ^{237}Np(n,f), ^{235}U(n,f) and ^{238}U(n,f)

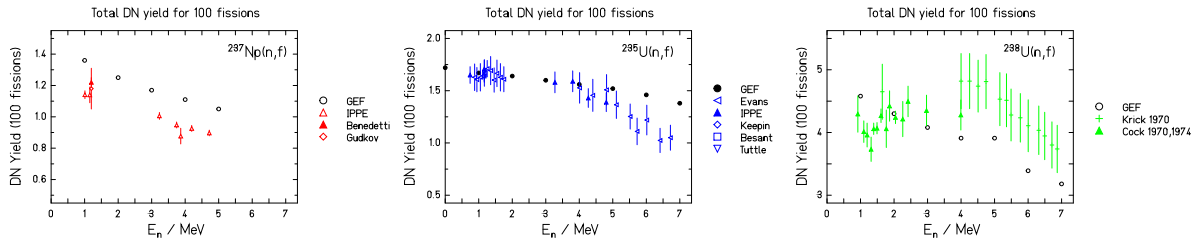

Note: Delayed-neutron yields for ^{237}Np(n,f), ^{235}U(n,f) and ^{238}U(n,f), from [244] and references therein, in comparison with the GEF results.

The energy dependence of the delayed-neutron yield was also studied for ^{237}Np, ^{235}U and ^{238}U, see Figure 137. The experimental data show a constant behaviour up to 4 MeV and then a sharp decreasing slope. However, the GEF results show a decreasing slope whatever the energy domain. The slope is also lower than in the experimental results.

Figure 138: Calculated mass yields for ^{235}U(n,f), E_n = thermal and 5 MeV

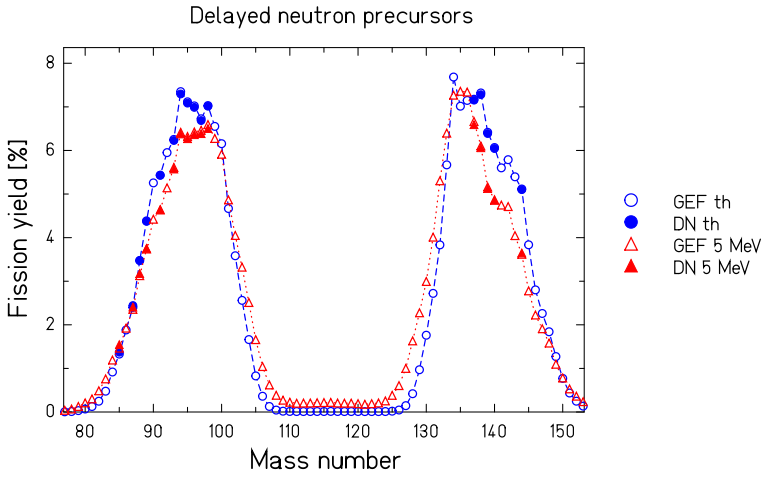

Note: Mass-yield distribution for ^{235}U(n,f) at thermal energy and at $E_n = 5$ MeV calculated with the GEF code. The full points correspond to masses with a main delayed-neutron precursor.

Figure 139: Delayed neutron yield up to E_n = 14 MeV

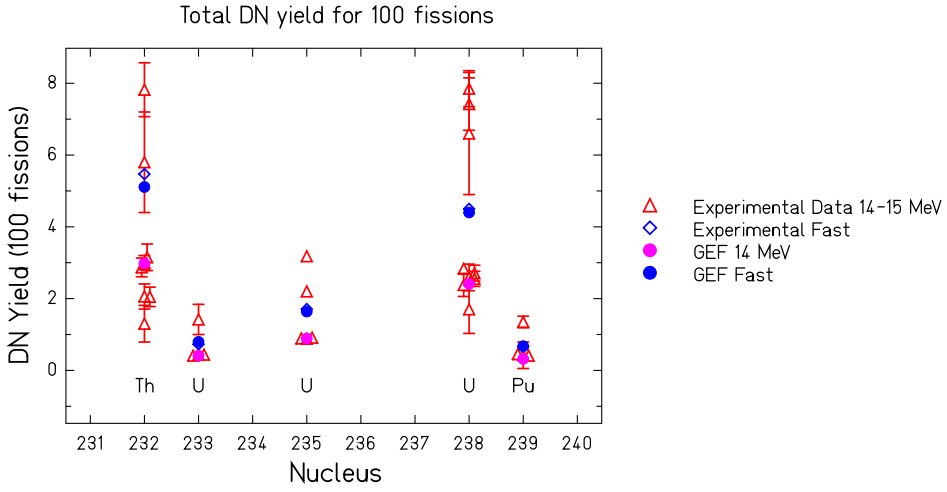

Note: Delayed-neutron yield for different fissioning systems at fast energy and at 14 MeV. Data from [244] are compared with the GEF results.

This slope should not only be associated with the odd-even effect because, when increasing the excitation energy this effect is reduced so the delayed-fission-neutron yields should increase, which is the opposite of the experimental observation. The slope is essentially due to the decrease of the peak-to-valley ratio as a function of the excitation

energy. Figure 138 shows the fission yields of the masses with at least one main delayed-neutron precursor. The fission yields of these masses decrease with the excitation energy. The constant behaviour is due to the competition between the decreasing odd-even effect and the decreasing peak/valley [246].

There is very few data above $E_n \approx 6$ MeV, so the energy dependence when multi-chance fission is involved is difficult to benchmark. However, some data are available at 14 ± 1 MeV. Figure 139 shows that the experimental data are sometimes inconsistent among each other giving an increase or a decrease of the delayed neutron yields with the excitation energy. When considering that the delayed-neutron emission probability (P_n) does not change with excitation energy and that $\nu_d = \Sigma(Y_i \cdot Pn_i)$, the fission yields clearly confirm a decreasing tendency. The GEF results are consistent with the experimental data.

10 Validation and evaluation of nuclear data

The GEF model does not directly make quantitative predictions. It rather provides a rigid theoretical framework that defines a stringent link among a few key properties of the fissioning systems and practically all kind of fission observables. The quantitative predictions of the model depend on the values of a limited number of parameters, which are determined in a comprehensive agree rather well with great part of the large body of various experimental data.

Considering the large number of several hundred systems that is covered by the model (not considering the intricate variation of the fission observables with excitation energy) and the enormous complexity of the fission observables already for one system, the number of about 50 adjustable model parameters (that means far below one parameter per system) is remarkably small. These numbers elucidate that the model establishes strong relations between the different observables of one system and between the same observables of different systems. Thus, the model possesses the following fundamental virtues and constraints:

1. The model allows predicting the behaviour of a specific system without any particular experimental information.

2. The model cannot be adjusted to a peculiar feature of a specific system.

The adjustment of the parameter values is difficult mainly by two reasons. First, the amount and diversity of measured fission observables is so huge that a complete survey is practically impossible. Second, erroneous experimental results should be recognised and excluded from the fit procedure. This is not an easy task. However, the good agreement of the model results with the majority of the data considered in this report proves the excellence of the basic concept of the GEF model and gives confidence in the reliability of the results. Thus, we propose to go a step further by using the GEF model for validating the experimental and evaluated data by verifying their consistency. In this way, the GEF model is employed for improving the quality of nuclear data. Moreover, due to its predictive power, the GEF model is used for extending the amount of nuclear data. The feasibility of this ambitious aim will be demonstrated by a few examples.

10.1 Indications for a target contaminant

The first case to be investigated is the fission-fragment mass distribution of the system ^{237}Np(n$_{th}$,f). Figure 140 demonstrates that the evaluated spectrum can rather well be explained by a 60 % (!) target contaminant of ^{239}Pu. An additional strong argument for the presence of a heavier target contaminant is the mean value of the mass distribution $< A > = 118.03$, which would let room for the prompt emission of 1.94 neutrons, only. This is in contradiction with the measured value of $\bar{\nu} = 2.5218$ [172].

Figure 140: Evidence for a ^{239}Pu contaminant in a ^{237}Np target

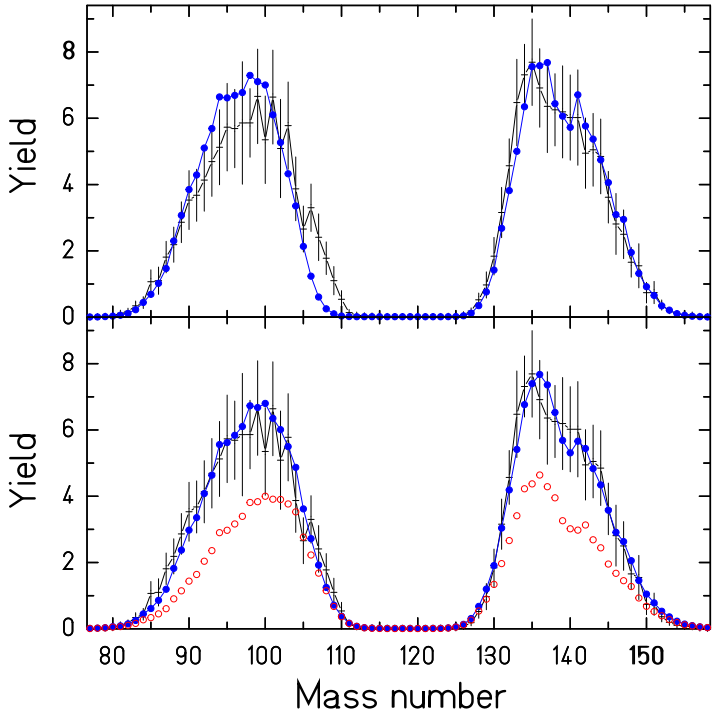

Note: The fission-fragment mass distribution of the system ^{237}Np(n$_{th}$,f) from ENDF/B-VII (black crosses with error bars) in comparison with the result of the GEF code for a pure ^{237}Np target (upper figure, blue full points) and for a composite target (40 % ^{237}Np and 60 % ^{239}Pu) (lower figure, blue full points). In addition, the contribution from the ^{239}Pu contaminant is shown separately in the lower figure (open red symbols).

Thus, we found two convincing arguments for the presence of an important target impurity in the measurement underlying the evaluation of the mass distribution of the system ^{237}Np(n$_{th}$,f).

Similar considerations can be employed to investigate and eventually revise the mass distributions of other systems, for example ^{254}Es(n$_{th}$,f) and ^{255}Fm(n$_{th}$,f), which showed severe deviations from the GEF results (see Section 8.2).

10.2 An inconsistent mass identification

The next problem to be investigated is the discrepancy in the kinetic energy of neutron-induced fission of ^{232}Th between the GEF model and the experimental data found in Section 8.7. Figure 141 reveals that there is most probably a problem in the experimental data. According to our understanding, the kink in the kinetic-energy curve is caused by the transition from the SL to the lumped S1 and S2 fission-channel component with increasing mass asymmetry. This transition can also be observed by a kink in the mass distribution. In Figure 141 this transition occurs at $A = 126$ consistently in the mass distribution and in the kinetic energies from the GEF model. Also, the evaluated mass distribution for fast-neutron-induced fission is found at almost the same place. However, the kink in the measured kinetic energies is shifted by about 5 units to lower masses. This

Figure 141: Inconsistency of mass and TKE for ^{232}Th(n,f), $E_n = 2.9$ MeV

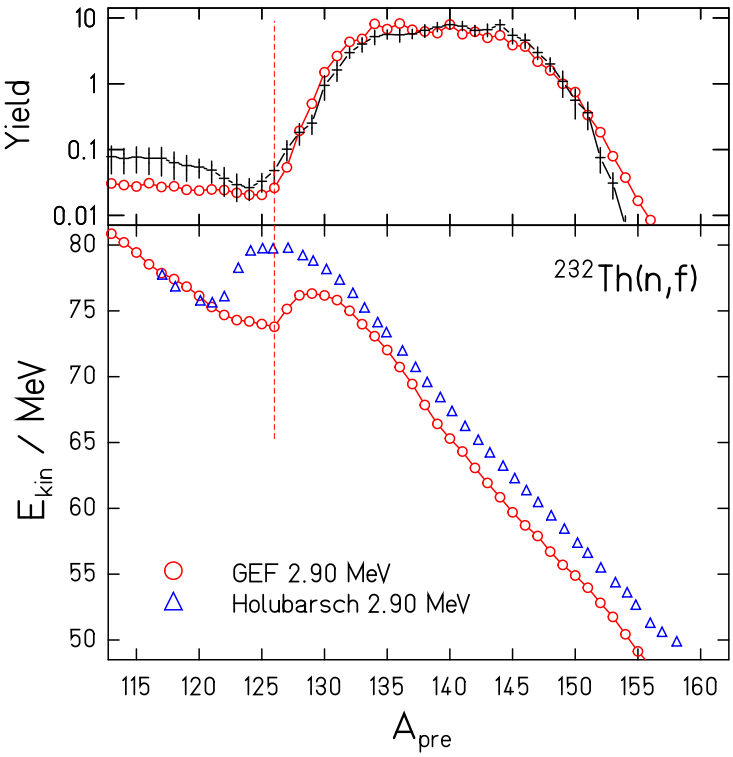

Note: Fission-fragment mass distribution (upper part) and kinetic energies (lower part) of the system ^{232}Th(n,f), $E_n = 2.9$ MeV from the GEF model (red symbols) together with the evaluated mass distribution from ENDF/B-VII from fast-neutron induced fission of ^{232}Th (upper part, black crosses) and with the measured kinetic energies [233] (lower part, blue triangles). The dashed line marks the border of the asymmetric fission component according to the GEF model.

finding evokes severe doubts on the reliability of this measurement. The same problem appears for the measurement at $E_n = 4.81$ MeV of the same authors.

10.3 A problem of energy conservation in ^{252}Cf(sf)

Now we will have a closer look on the discrepancy found in the total kinetic energy for spontaneous fission of ^{252}Cf documented in Section 8.7. Since this is one of the most carefully studied system, the shift of 4 MeV found in the GEF result relative to the experimental data must be considered very seriously.

However, there is a connection of the TKE with the prompt-neutron yield, the prompt-neutron energy spectrum, the prompt-gamma spectrum and the fission-fragment nuclide distribution: the nuclide distribution defines the weights of the different fission Q values, and the data on prompt-gamma and prompt-neutron emission define the total excitation energy of the fragments. Since all these observables are well reproduced by the GEF model, as much as experimental data are available, the observed shift of 4 MeV is surprising.

Since the prompt-neutron yield is most strongly correlated with the TKE, the empirical values from different sources are compared with the GEF result in Table 16. There is good agreement.

Table 16: Prompt-neutron multiplicity of the system ^{252}Cf(sf)

Model	GEF	ref. [172]	ref. [171]	ref. [141]
$\bar{\nu}$	3.75	3.759 ± 0.0048	3.755	3.88

Note: Mean prompt-neutron multiplicity of the system ^{252}Cf(sf) from the GEF code in comparison with the values from different evaluations.

The span between the different values from the different evaluations correspond to a span of about 1 MeV in TXE. Assuming that the ENDF value [141] is correct, this would explain 1/4 of the shift. Thus, there remains a real problem to describe all the interconnected observables in a consistent way, in particular in view of the good agreement of the GEF results with the TKE values of other systems.

10.4 Complex properties of fission channels

It is remarkable that the GEF model is able to describe the fission-fragment distributions and their kinetic energies for all fissioning systems with a unique set of four fission channels. This is in contrast to previous work, where a complex set of channels had to be used in order to reproduce the experimental data. This becomes most evident for spontaneous fission of ^{252}Cf. Table 17 compares different parametrisation on the basis of the Brosa model [56] with the result of the GEF model.

Table 17: Yields of fission channels for the system ^{252}Cf(sf)

Model	GEF	Brosa [247]	Brosa [248]
SL	2.6E-3 %	(3.0 ± 0.2) %	3.1566 %
S1	0.54 %	(13.5 ± 0.5) %	12.6676 %
S2	85.93 %	(48.2 ± 1.1) %	46.9569 %
SA	13.53 %	(0.3 ± 0.1) %	—
S3	—	(35.0 ± 1.2) %	0.9284 %
SX	—	—	36.2905 %

Note: Relative yields of the fission channels for the system ^{252}Cf(sf) according to different parametrisation.

^{252}Cf(sf) is one of the most intensively investigated systems. The mass distribution that has been determined with high precision is reproduced by the GEF model with a reduced Chi-squared of 0.62 with practically only 3 fission channels, the S1, S2 and the super-asymmetric (SA) channel. The super-long channel is so weak that it does not play any role. Also, the kinetic energies are well reproduced, except a general shift, see dedicated sections.

The reason for the smaller number and the strongly different yields of the fission channels obtained with the GEF model lies in the properties of the fission channels themselves. In the Brosa model [56], the shape of the mass distribution of all fission channels is assumed to be Gaussian. The mean total kinetic energy is parametrised as

$$Y(TKE) = (\frac{200}{TKE})^2 \cdot h \cdot \exp(\frac{-(L - l_{max})^2}{(L - l_{min})l_{dec}}) \tag{75}$$

The charge-asymmetry degree of freedom enters via:

$$L = \frac{e_0^2 Z(Z_{CN} - Z)}{TKE} \tag{76}$$

As described in Section 6.2, in the GEF model the shape of the mass distribution of the S2 fission channel is given by a rectangular distribution convoluted with Gaussian distributions with different diffusenesses at the lower and the upper border. Moreover, the variation of the TKE as a function of fragment mass does not only consider the Coulomb factor $Z_1 \cdot Z_2$. The TKE is also influenced by the fact that the deformation of the fragments in the different fission channels is mass dependent. This implies a different behaviour of the mean TKE as a function of fragment mass.

These more complex properties of the fission channels explain the strongly different relative yields of the fission channels in the GEF model and allows describing all systems consistently with the same set of fission channels.

10.5 Data completion and evaluation

In many cases, the experimental data are incomplete, and it is the task of an evaluation process not only to estimate the reliability and consistency of the measured data but also to estimate the missing values with the help of systematics or theoretical models. The GEF model in combination with the dedicated optimisation code MATCH [10] offers an efficient tool for this purpose.

The GEF code provides a complete set of fission-fragment yields for a specific fissioning system with uncertainties and covariances between all individual yields as determined by the model. Also many other observables with their uncertainties and covariances can be obtained, see Section 7. If there are no experimental data, the GEF result may directly be used as a set of estimated values e.g. in order to extend evaluated data tables. In many cases, however, there are some experimental results available, but they are incomplete or rather uncertain. In this case, the result of the GEF code can be used for complementing the partial experimental data set in a consistent way. For this purpose, the GEF results should be adjusted in a suitable way to the experimental data.

10.5.1 Mathematical procedure in two dimensions

In order to illustrate the solution of the problem, a schematic case in two dimensions is presented. The result of the GEF code, fission-fragment yields with their uncertainties and the covariance matrix, defines a multi-variant normal distribution. This is a multi-dimensional probability-density distribution of a Gaussian-shaped cloud. In two dimensions, this distribution is given by:

$$f(x,y) = \frac{1}{2\pi\sigma_x\sigma_y\sqrt{1-\rho_{xy}^2}} \cdot \exp(-\frac{1}{2(1-\rho_{xy}^2)}[\frac{(x-\mu_x)^2}{\sigma_x^2} \tag{77}$$

$$+\frac{(y-\mu_y)^2}{\sigma_y^2} - \frac{2\rho_{xy}(x-\mu_x)(y-\mu_y)}{\sigma_x\sigma_y}])$$

The variables are defined as follows:
– x and y form a two-dimensional space of possible values of two fission-fragment yields.
– μ_x and μ_y are the most probable values of the yields given by the GEF code.
– σ_x and σ_y are the standard deviations of the uncertainty ranges of these two yields given by GEF.
– ρ_{xy} is the correlation coefficient between the variables x and y given by the GEF code.
– $\rho_{xy} \cdot \sigma_x \cdot \sigma_y$ is the covariance between the variables x and y.

From this distribution, one can derive a Log-Likelihood function L that expresses the likelihood of a set of fission-fragment yields x and y to be compatible with the GEF result:

$$L(x,y) = \frac{1}{2(1-\rho_{xy}^2)}[\frac{(x-\mu_x)^2}{\sigma_x^2} + \frac{(y-\mu_y)^2}{\sigma_y^2} - \frac{2\rho_{xy}(x-\mu_x)(y-\mu_y)}{\sigma_x\sigma_y}] \tag{78}$$

Let us assume that there is one experimental value x_m available with the standard deviation of the uncertainty range σ_m. The Log-Likelihood function L_m that expresses the likelihood of a fission-fragment yield x to be compatible with the experiment is given by:

$$L_m(x) = -\frac{(x - x_m)^2}{2\sigma_{xm}^2} \tag{79}$$

A set of variables x and y that is best compatible with both the model and the experiment may be found by constructing a combined Log-Likelihood function L_c, essentially as the sum of L and L_m and by searching the parameter values x_c and y_c that maximise the combined Log-Likelihood function L_c. This way, the information of the model calculation is considered in two ways: First, the absolute values deduced from the general knowledge on the physics derived from the body of available data and, secondly, the covariances that link the different yields by the inner logic of the model. However, this procedure would give more weight to the model result. Therefore, the number of yields provided by the model, in this case 2, and the number of measured yields, in this case 1, should be considered by enhancing L_m accordingly.[8]

Thus, the proposed combined Log-Likelihood function with the appropriate weight is:

$$L_c = L + 2 \cdot L_m \tag{80}$$

The exponential of the combined Log-Likelihood function (properly normalized) defines the resulting multi-variant normal distribution, that is the multi-dimensional probability-density distribution of the fission yields, by which the corresponding covariance matrix is defined

It is expected that the correlations inside the model already assure that the resulting yields respect to a high degree some trivial conditions, e.g. that complementary yields are equal or the sum over the yields is normalised. In the code, the correlations of the model can be enhanced by increasing the last term in the bracket of Equation 78. This way, the behaviour of the code can be tuned.

10.5.2 Two examples

Figures 142 and 143 illustrate the function of the MATCH code for the case of ^{235}U(n$_{th}$,f) and for the case of ^{241}Pu(n,f). The first case stands for a system with an almost completely measured mass distribution. Only a few yields near symmetry need to be completed. The MATCH code was used with its default options. The data for the second system are much

[8] This weighting assumes that all values provided by the model have the same relevance for the complete set of data. In detail this depends on the degree of correlations between the different variables, which should be considered to develop a more adequate description for weighting. Moreover, one may also arbitrarily increase the weight of the experimental data if desired, without loosing the correlations given by the model for the unmeasured yields.

Figure 142: Matching measured ^{235}U(n$_{th}$,f) mass yields with GEF results

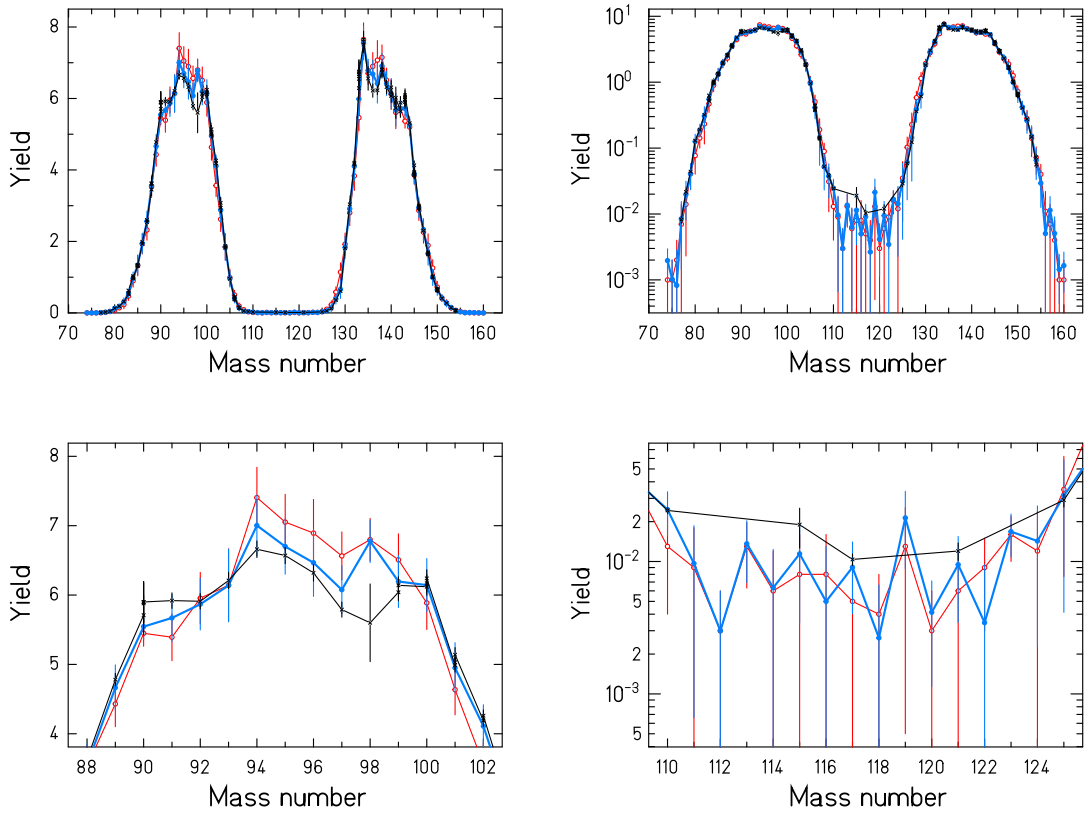

Note: Adjustment of the fission-fragment mass yields from GEF (red symbols) to evaluated data [141] (black symbols) with the MATCH code for the system ^{235}U(n$_{th}$,f). The blue symbols show the set of fission yields that maximizes the combined likelihood function of the evaluated data and the GEF result together with the covariance matrix from GEF. The upper figures show the full mass distribution in linear and logarithmic scale. The lower figures zoom on specific parts of the distribution. See text for details.

more incomplete. For example, there is a large gap around symmetry which is clearly seen by the straight dashed line that connects the available experimental points. In this case, the MATCH code was used with a relative weight of 100 for the experimental data and a relative weight of 10 for the covariances.

Figure 143: Matching measured ^{241}Pu(n$_{fast}$,f) mass yields with GEF results

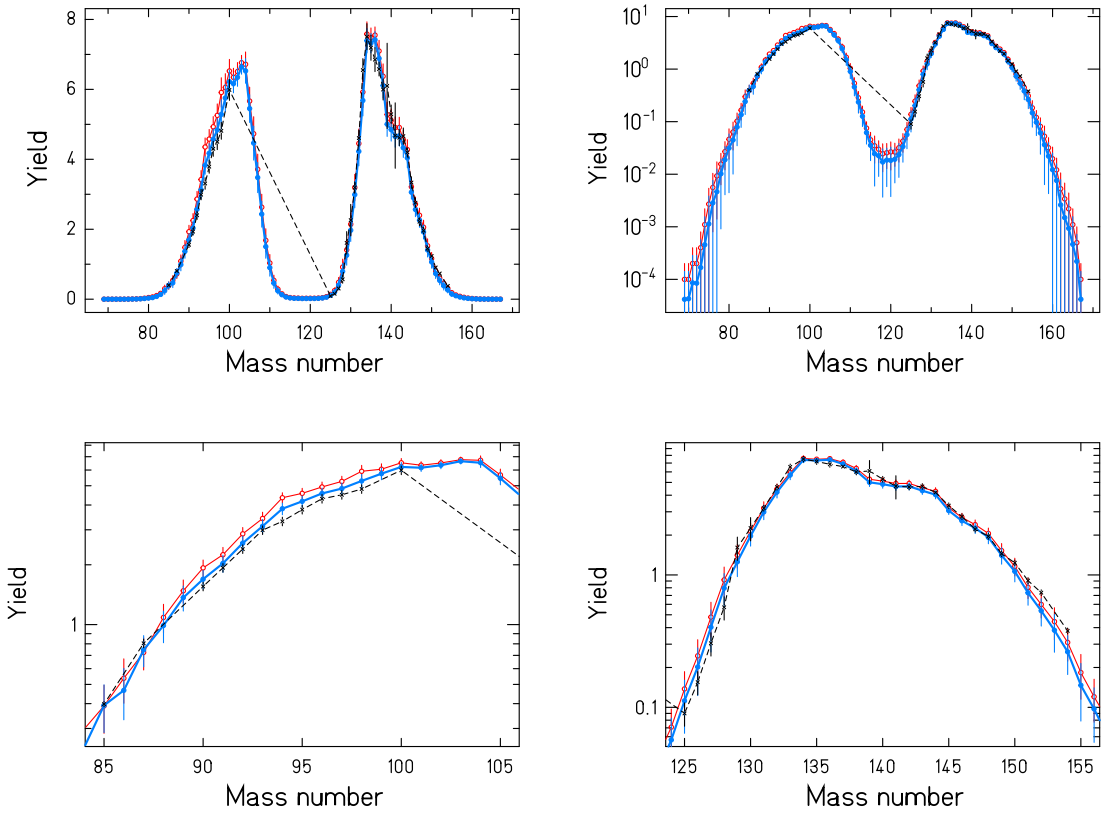

Note: Adjustment of the fission-fragment mass yields from GEF (red symbols) to evaluated data [141] (black symbols) with the MATCH code for the system ^{241}Pu(n,f), E_n = 2.5 MeV. The blue symbols show the set of fission yields that maximises the combined likelihood function of the evaluated data and the GEF result together with the covariance matrix from GEF. The upper figures show the full mass distribution in linear and logarithmic scale. The lower figures zoom on specific parts of the distribution. See text for details.

11 Conclusion

A new general approach for modelling nuclear fission using global theoretical models and considerations on the basis of universal laws of physics and mathematics has been derived. The most prominent features of the GEF model are the evolution of quantum-mechanical wave functions in systems with complex shape, memory effects in the dynamics of stochastic processes, the influence of the Second Law of thermodynamics on the evolution of open systems in terms of statistical mechanics, and the topological properties of a continuous function in multi-dimensional space.

It has been demonstrated that the model reproduces the measured fission barriers and the observed properties of the fission fragments, prompt neutrons and prompt-gamma radiation with a remarkable precision. This success reveals that the fission process possesses a high degree of inherent regularity that is hardly deducible from microscopic models. The suitability of the model for the evaluation of nuclear data is shown.

References

[1] C. Wahl, Atom. Data Nucl. Data Tables 39 (1988) 1.

[2] T. Asano, T. Wada, M. Ohta, T. Ichikawa, S. Yamaji, H. Nakahara , J. Nucl. Radioch. Sc. 5 (2004) 1.

[3] T. Asano, T. Wada, M. Ohta, S. Yamaji, H. Nakahara , J. Nucl. Radioch. Sc. 7 (2006) 7.

[4] J. Randrup, P. Möller, A. J. Sierk, Phys. Rev. C 84 (2011) 034613.

[5] H. Goutte, J. F. Berger, P. Casoli, D. Gogny, Phys. Rev. C 71 (2005) 024316.

[6] A. S. Umar, V. E. Oberacker, J. A. Maruhn, P.-G. Reinhard, J. Phys. G: Nucl. Part. Phys. 37 (2010) 064037.

[7] V. V. Sargsyan, Z. Kanokov, G. G. Adamian, N. V. Antonenko, @ Phys. Part. Nuclei 41 (2010) 175.

[8] https://mcnp.lanl.gov/

[9] http://www.fluka.org/fluka.php

[10] MATCH computer code, available at http://www.khs-erzhausen.de

[11] E. Wigner, Trans. Faraday Sot. 34, part 1 (1938) 29.

[12] U. Mosel, H. W. Schmitt, Nucl. Phys. A 165 (1971) 73.

[13] P. Moeller, A. J. Sierk, T. Ichikawa, A. Iwamoto, R. Bengtsson, H. Uhrenholt, S. Aberg, Phys. Rev. C 79 (2009) 064304.

[14] G. D. Adeev, V. V. Pashkevich, Nucl. Phys. A 502 (1989) 405c.

[15] A. Ya. Rusanov, M. G. Itkis, V. N. Oklovich, Phys. At. Nucl. 60 (1997) 683.

[16] A. V. Karpov, P. N. Nadtochy, D. V. Vanin, G. D. Adeev, Phys. Rev. C 63 (2001) 054610.

[17] W. D. Myers, G. Manzouranis, J. Randrup, Phys. Lett. B 98 (1981) 1.

[18] A. V. Karpov, G. D. Adeev, Eur. Phys. J. A 14 (2002) 169.

[19] A. Al-Adili, F.-J. Hambsch, S. Pomp, S. Oberstedt, Phys. Rev. C 86 (2012) 054601.

[20] W. D. Myers, W. J. Swiatecki, Nucl. Phys. A 601 (1996) 141.

[21] A. Kelic, K.-H. Schmidt, Phys. Lett. B 634 (2006) 362.

[22] G. Royer, C. Bonilla, J. Radioanalytical Nuclear Chemistry 272 (2007) 237.

[23] A. Dobrowolski, K. Pomorski, J. Bartel, Phys. Rev. C 75 (2007) 024613.

[24] M. Kowal, P. Jachimowicz, A. Sobiczewski, Phys. Rev. C 82 (2010) 014303.

[25] M. Mirea, L. Tassan-Got, Centr. Eur. J. Phys. 9 (2011) 116.

[26] P. Jachimowicz, M. Kowal, J. Skalski, Phys. Rev. C 85 (2012) 034305.

[27] M. Kowal, J. Skalski, Phys. Rev. C 85 (2012) 061302(R).

[28] H. Abusara, A. V. Afanasjev, P. Ring, Phys. Rev. C 85 (2012) 024314.

[29] Bing-Nan Lu, En-Guang Zhao, Shan-Gui Zhou, Phys. Rev. C 85 (2012) 011301(R).

[30] J.-P. Delaroche, M. Girod, H. Goutte, J. Libert, Nucl. Phys. A 771 (2006) 103.

[31] S. Goriely, M. Samyn, J. M. Pearson, Phys. Rev. C 75 (2007) 064312.

[32] F. Minato, K. Hagino, Phys. Rev. C 77 (2008) 044308.

[33] S. Goriely, S. Hilaire, A. J. Koning, M. Sin, R. Capote, Phys. Rev. C79 (2009) 024612.

[34] F. A. Ivanyuk, K. Pomorski, Phys. Rev. C 79 (2009) 054327.

[35] A. V. Karpov, A. Kelic, K.-H. Schmidt, J. Phys. G: Nucl. Part. Phys. 35 (2008) 035104.

[36] W. D. Myers, W. J. Swiatecki, Phys. Rev. C 60 (1999) 014606.

[37] M. Baldo, U. Lombardo, E. E. Saperstein, M. V. Zverev Phys. Rep. 391 (2004) 261.

[38] S. Bjoernholm, J. E. Lynn, Rev. Mod. Phys. 52 (1980) 725.

[39] R. Capote, M. Herman, P. Oblozinsky, P. G. Young, S. Goriely, T. Belgya, A. V. Ignatyuk, A. J. Koning, S. Hilaire, V. A. Plujko, M. Avrigeanu, O. Bersillon, M. Chadwick, T. Fukahori, Zhigang Ge, Yinlu Han, S. Kailas, J. Kopecky, V. M. Maslov, G. Reffo, M. Sin, E. Sh. Soukhovitskii, P. Talou, Nucl. Data Sheets 110 (2009) 3107.

[40] M. Dahlinger, D. Vermeulen, K.-H. Schmidt, Nucl. Phys. A 376 (1982) 94.

[41] C. Barbero, J. G. Hirsch, A. E. Mariano, Nucl. Phys. A 874 (2012) 81.

[42] J. Duflo, A. P. Zuker, Nucl. Phys. A 576 (1994) 65.

[43] K.-H. Schmidt, B. Jurado, Phys. Rev. C 86 (2012) 044322.

[44] T. von Egidy, D. Bucurescu, Phys. Rev. C 80 (2009) 054310.

[45] A. V. Ignatyuk, G. N. Smirenkin, A. S. Tishin, Sov. J. Nucl. Phys. 21 (1975) 255.

[46] A. V. Ignatyuk, Hadrons Nuclei Appl. 3 (2001) 287.

[47] K.-H. Schmidt, B. Jurado, EPJ Web of Conferences 62 (2013) 06001.

[48] K.-H. Schmidt, S. Steinhäuser, C. Böckstiegel, A. Grewe, A. Heinz, A. R. Junghans, J. Benlliure, H.-G. Clerc, M. de Jong, J. Müller, M. Pfützner, B. Voss, Nucl. Phys. A 665 (2000) 221.

[49] M. G. Itkis et al., Sov. J. Nucl. Phys. 52 (1990) 601.

[50] A. N. Andreyev et al., Phys. Rev. Lett. 105 (2010) 252502.

[51] S. I. Mulgin, K.-H. Schmidt, A. Grewe, S. V. Zhdanov, Nucl. Phys. A 640 (1998) 375.

[52] J. P. Unik et al., Proc. Symp. Phys. Chem. Fission, Rochester 1973, IAEA Vienna (1974), vol. 2, p. 19.

[53] B. D. Wilkins, E. P. Steinberg, R. R. Chasman, Phys. Rev. C 14 (1976) 1832.

[54] http://www.cenbg.in2p3.fr/GEF, http://www.khs-erzhausen.de

[55] I. Ragnarsson, R. K. Sheline, Phys. Scr. 29 (1984) 385.

[56] U. Brosa, S. Grossmann, A. Müller, Phys. Rep. 197 (1990) 167.

[57] M. G. Itkis, V. N. Okolovich, A. Ya, Rusanov, G. N. Smirenkin, Z. Phys. A 320 (1985) 433.

[58] A. A. Naqvi, F. Käppeler, F. Dickmann, R. Müller, Phys. Rev. C 34 (1986) 21.

[59] W. Lang, H.-G. Clerc, H. Wohlfarth, H. Schrader, K.-H. Schmidt, Nucl. Phys. A 345 (1980) 34.

[60] P. Fong, Statistical Theory of Nuclear Fission (Gordon and Breach, New York, 1969).

[61] G. A. Pik-Pichak, V. M. Strutinsky, Physics of the fission of the atomic nuclei, eds. N. A. Perfilov and V. P. Eismont, (Moscow, Gosatmomizdat, 1962) p. 12.

[62] A. V. Ignatyuk, Yad. Fiz. 9 (1969) 357.

[63] Yu. Ts. Oganessian, Yu. A. Lazarev, Treatise on Heavy Ion Science, Vol. 4, ed. D. A. Bromley, Plenum Press, New York, 1985, p. 1.

[64] J. R. Nix, W. J. Swiatecki, Nucl. Phys. 71 (1965) 1.

[65] M. G. Itkis et al., Phys. At. Nucl. 58 (1995) 2026.

[66] A. Ya. Rusanov, V. V. Pashkevich, M. G. Itkis, Phys. At. Nucl. 62 (1999) 547.

[67] F.-J. Hambsch, F. Vives, P. Siegler, S. Oberstedt, Nucl. Phys. A 679 (2000) 3.

[68] H. Nifenecker, J. Physique Lett. 41 (1980) 47.

[69] M. Asghar, Z. Phys. A 296 (1980) 79.

[70] J. R. Huizenga, R. Vandenbosch, Phys. Rev. 120 (1960) 1305.

[71] R. Vandenbosch, J. R. Huizenga, Phys. Rev. 120 (1960) 1313.

[72] V. M. Strutinski, L. V. Groshev, M. K. Akimova, Nucl. Phys. 16 (1960) 657.

[73] J. O. Rasmussen, W. Nörenberg, H. J. Mang, Nucl. Phys. A 136 (1969) 465.

[74] L. G. Moretto, G. F. Peaslee, G. J. Wozniak, Nucl. Phys. A 502 (1989) 453c.

[75] M. Zielinska-Pfabe, K. Dietrich, Phys. Lett. B 49 (1974) 123.

[76] F. Gönnenwein, I. Tsekhanovich, V. Rubchenya, Intern. J. Mod. Phys. E 16 (2007) 410.

[77] L. Bonneau, P. Quentin, I. N. Mikhailov, Phys. Rev. C 75 (2007) 064313.

[78] M. M. Hoffman, Phys. Rev. 133 (1964) B 174.

[79] S. G. Kadmensky, Phys. Atom. Nuclei 71 (2008) 1193.

[80] Geometrical Relationships of Macroscopic Nuclear Physics, R. W. Hasse, W. D. Myers, Springer, Berlin, 1988.

[81] B. S. Tomar, R. Tripathi, A. Goswami, Pramana 68 (2007) 111.

[82] D. G. Madland, T. R. England, Nucl. Sci. Eng. 64 (1977) 859.

[83] G. Rudstam, Proc. Specialists' Meeting on Fission Product Nuclear Data, Tokai, Japan, May 25-27, 1992, NEA/NSC/DOC(92)9.

[84] K.-H. Schmidt, B. Jurado, Phys. Rev. C 83 (2011) 061601.

[85] M. Mirea, Phys. Lett. B 680 (2009) 316.

[86] M. Asghar and R. W. Hasse, J. Phys. Colloques 45 (1984) C6-455.

[87] H. J. Krappe, Int. J. Mod. Phys. E 16 (2007) 396.

[88] W. D. Myers, W. J. Swiatecki, Nucl. Phys. A 612 (1997) 249.

[89] D. H. Gross, Entropy 6 (2004) 158 / Special Issue Quantum Limits to the Second Law of Thermodynamics.

[90] M. Guttormsen et al. , Phys. Rev. C 68 (2003) 034311.

[91] A. Schiller et al., Phys. Rev. C 63 (2001) 021306.

[92] U. Agvaanluvsan et al., Phys. Rev. C 70 (2004) 054611.

[93] A. Bürger et al., Phys. Rev. C 85 (2012) 064328.

[94] A. C. Larsen et al., Phys. Rev. C 76 (2007) 044303.

[95] N. U. H. Syed et al., Phys. Rev. C 80 (2009) 044309.

[96] M. Guttormsen et al., Phys. Rev. C 83 (2011) 014312.

[97] A. C. Larsen et al., Phys. Rev. C 73 (2006) 064301.

[98] K.-H. Schmidt, B. Jurado, Phys. Rev. Lett. 104 (2010) 21251.

[99] K.-H. Schmidt, B. Jurado, Phys. Rev. C 83, 061601 (2011) 061601.

[100] R. Müller, A. A. Naqvi, F. Käppeler, F. Dickmann, Phys. Rev. C 29 (1984) 885.

[101] J. R. Nix, Ann. Phys. 41 (1967) 52.

[102] N. Dubray, H. Goutte, J.-P. Delaroche, Phys. Rev. C 77 (2008) 014310.

[103] J. R. Nix, J. Sierk, H. Hofmann, F. Scheuter, D. Vautherin, Nucl. Phys. A 424 (1984) 239.

[104] S. V. Zhdanov et al., Phys. At. Nucl. 56 (1993) 175.

[105] M. Caamano, F. Rejmund, K.-H. Schmidt, J. Phys. G: Nucl. Part. Phys. 38 (2011) 035101.

[106] K.-H. Schmidt. B. Jurado, arXiv:1007.0741v1[nucl-th] (2010).

[107] M. V. Ricciardi, A. V. Ignatyuk, A. Kelic, P. Napolitani, F. Rejmund, K.-H. Schmidt, O. Yordanov, Nucl. Phys. A 733 (2004) 299.

[108] M. V. Ricciardi, K.-H. Schmidt, A. Kelic-Heil, arXiv:1007.0386v1 [nucl-ex] (2010).

[109] D. Rochman, H. Faust, I. Tsekhanovich, F. Gönnenwein, F. Storrer, S. Oberstedt, V. Sokolov Nucl. Phys. A 710 (2002) 3.

[110] I. I. Gontchar, P. Fröbrich, N. I. Pischasov, Phys. Rev. C 47 (1993) 2228.

[111] W. J. Swiatecki, Phys. Rev. 100 (1955) 937.

[112] Z. Patyk, A. Sobiczewski, P. Armbruster, K.-H. Schmidt, Nucl. Phys. A 491 (1989) 267.

[113] G. Vladuca, A. Tudora, F.-J. Hambsch, S. Oberstedt, I. Ruskov, Nucl. Phys. A 720 (2003) 274.

[114] Deleplanque et al., Phys. Rev. C 69 (2004) 044309.

[115] I. Dostrovsky, Z. Fraenkel, G. Friedlander, Phys. Rev. 116 (1959) 683.

[116] A. R. Junghans et al., Phys. Lett. B 670 (2008) 200.

[117] J. J. Griffin, Phys. Rev. Lett. 17 (1966) 478.

[118] M. Blann, Ann. Rev. Nucl. Sci. 25 (1975) 123.

[119] M. Blann, M. B. Chadwick, Phys. Rev. C 62 (2000) 034604.

[120] C. Kalbach, Phys. Rev. C 73 (2006) 024614.

[121] A. V. Ignatyuk, V. M. Maslov, A. B. Pashchenko, Sov. J. Nucl. Phys. 47 (1988) 224.

[122] W. D. Myers, W. J. Swiatecki, Nucl. Phys. 81 (1966) 1.

[123] Th. Rubehn et al., Phys. Rev. C 54 (1996) 3062.

[124] V. M. Kupriyanov et al, Sov. J. Nucl. Phys. 32 (1980) 184.

[125] B. Back et al., Phys. Rev. C 9 (1974) 1924.

[126] B. Back et al., Phys. Rev. C 10 (1974) 1948.

[127] A. Gavron et al., Phys. Rev. Lett. 34 (1975) 827.

[128] A. Gavron et al., Phys. Rev. C 13 (1976) 2374.

[129] A. Gavron et al., Phys. Rev. Lett. 38 (1977) 1457.

[130] E. Cheifetz et al., Phys. Rev. C 24 (1981) 519.

[131] K.-H. Schmidt, B. Jurado, JEF/DOC 1423, NEA of OECD, Paris, 2011, available from [54].

[132] K.-H. Schmidt, B. Jurado, Phys. Proc. 31 (2012) 147.

[133] E. A. C. Crough, At. Data Nucl. Data Tables 19 (1977) 419.

[134] W. E. Stein, Phys. Rev. 108 (1957) 94.

[135] J. C. D. Milton and J. S. Fraser, Phys. Rev. 111 (1958) 877.

[136] H. W. Schmitt, W. E. Kiker, C. W. Williams, Phys. Rev. 137 (1965) B837.

[137] E. Moll et al., Nucl. Instrum. Methods 123 (1975) 615.

[138] C. Donzaud et al, Eur. Phys. J. A 1 (1998) 407.

[139] A. Ebran et al., Nucl. Instrum. Methods 728 (2013) 40.

[140] M. Caamano et al., Phys. Rev. C 88 (2013) 024605.

[141] M. B. Chadwick et al., Nucl. Data Sheets 112 (2011) 2887.

[142] P. Schillebeeckx et al., Nucl. Phys. A 545 (1992) 623.

[143] L. Dematte et al., Nucl. Phys. A 617 (1997) 331.

[144] E. K. Hulet et al., Phys. Rev. C 40 (1989) 770.

[145] D. C. Hoffman et al., Phys. Rev. C 41 (1990) 631.

[146] T. M. Hamilton et al., Phys. Rev. C 46 (1992) 1873.

[147] M. R. Lane et al., Phys. Rev. C 53 (1996) 2893.

[148] U. Quade et al., Nucl. Phys. A487 (1988) 1.

[149] C. Schmitt et al. Nucl. Phys. A 430 (1984) 21.

[150] M. Djebara et al., Nucl. Phys. A 496 (1989) 346.

[151] R. Hentzschel et al. Nucl. Phys. A 571 (1994) 427.

[152] C. Budtz-Joergensen, H.-H. Knitter, Nucl. Phys. A 490 (1988) 307.

[153] IAEA Tecdoc 1168, IAEA, Vienna, 2000.

[154] L. E. Glendenin et al., Phys. Rev. C 24 (1981) 2600.

[155] E. Gindler et al., Phys. Rev. C 27 (1983) 2058.

[156] L. E. Glendenin et al., Phys. Rev. C 22 (1980) 152.

[157] S. Nagy et al., Phys. Rev. C 17 (1968) 163.

[158] G. P. Ford et al., Phys. Rev. 37 (1965) 826.

[159] J. Laurec et al., Nucl. Data Sheets 111 (2010) 2965.

[160] M. Mac Innes et al., Nucl. Data Sheets 112 (2011) 3135 and references therein.

[161] T. C. Chapman et al., Phys. Rev. C 17 (1978) 1089.

[162] H. Naik et al., Nucl. Phys A (1995) 273.

[163] H. Naik et al., Phys. Rev. C 71 (2005) 014304.

[164] A. Bail et al., Phys. Rev. C 84 (2011) 034605.

[165] H. Naik et al., Eur. Phys.J A 7 (2000) 377.

[166] A. L. Nichols, IAEA, Workshop on Nuclear Reaction Data and Nuclear Reactors: Physics, Design and Safety, Trieste, 2002.

[167] T. Datta et al., Phys. Rev. C 25 (1982) 235.

[168] G. P. Ford et al., Phys. Rev. C 30 (1984) 195.

[169] H. Thierens et al., Phys. Rev. C 25 (1982) 1547.

[170] E. K. Hulet, J. F. Wild, R. J. Dougan, R. W. Lougheed, J. H. Landrum, A. D. Dougan, M. Schädel, R. L. Hahn, P. A. Baisden, C. M. Henderson, R. J. Dupzyk, K. Sümmerer, G. R. Bethune, Phys. Rev. Lett. 56 (1986) 313.

[171] V. V. Malinovskij, V. G. Vorob'eva, B. D. Kuz'minov, Report INDC(CCP)-239, IAEA, Vienna, 1985.

[172] R. W. Mills, PhD thesis, university of Birmingham, 1995.

[173] F. Manero, V. A. Konshin, Atomic Energy Rev., 10 (1972) 637.

[174] C. Budtz-Jorgensen, H.-H. Knitter, Nucl. Phys. A 490 (1988) 307.

[175] M. S. Zucker, N. E. Holden , Report BNL-38491 (1986).

[176] E. J. Axton, Nucl. Stand. Ref. Data (1985) 214.

[177] N. V. Kornilov et al., Nucl. Science Engin. 165 (2010) 117.

[178] W. Mannhart, INDC(NDS)-220/L (1989) 305, IAEA, Vienna.

[179] V. P. Eismont, Atomn. Ener. 19 (1965) 113.

[180] V. M. Maslov et al., Eur. Phys. J. A 18 (2003) 93.

[181] N. V. Kornilov et al., Nucl. Phys. A 686 (2001) 187.

[182] G. V. Danilyan et al., Phys. Atom. Nucl. 71 (2008) 200.

[183] G. A. Petrov et al., Phys. Atom. Nucl. 71 (2008) 1137.

[184] N. Carjan. M. Rizea, Phys. Rev. C 82 (2010) 01461.

[185] A. A.Bojcov et al., 6th All Union Conf. Kiev (1983) Vol. 2, p. 294.

[186] A. Lajtai et al., Nucl. Data Conf., Santa Fe (1985) Vol. 1, p. 613.

[187] L. V. Drapchinsky et al., communicated by N. Capote, 2012.

[188] A. S. Vorobyev et al., Nucl. Instrum. Methods A 598 (2009) 795.

[189] J. W. Boldeman et al., Aust. J. Phys. 24 (1971) 821.

[190] A. S. Vorobyev, EXFOR 41516.

[191] N. V. Kornilov, private communation, 20. 4. 2012.

[192] F.-J. Hambsch, S. Oberstedt, Nucl. Phys. A 617 (1997) 347.

[193] B. E. Watt, Phys. Rev. 87 (1952) 103.

[194] D. Madland, J. Nix, Nucl. Sci. Eng. 81 (1982) 213.

[195] Madland, D.G., LaBauve, R.J., Nix, J.R., 1989. IAEA-INDC(NDS)-220, 259.

[196] S. Lemaire, P. Talou, T. Kawano, M. B. Chadwick, D. G. Madland, Phys. Rev. C 72 (2005) 024601.

[197] A. Tudora, F.-J. Hambsch, Ann. Nucl. Energy 37 (2010) 771.

[198] R. Vogt, J. Randrup, D. A. Brown, M. A. Descalle, W. E. Ormand, Phys. Rev. C 85 (2012) 024608.

[199] M. I. Svirin, G. N. Lovchikova, A. M. Trufanov, Phys. Atom. Nuclei 60 (1997) 727.

[200] A. M. Trufanov et al., Phys. Atom. Nuclei 64 (2001) 1.

[201] G. N. Lovchikova et al., Phys. Atom. Nuclei 67 (2004) 1246.

[202] V. M. Maslov, At. Energy 103 (2007) 633.

[203] W. Mannhart, IAEA-TECDOC-410 (IAEA, Vienna, 1987), p. 158.

[204] M. V. Kornilov et al., Phys. Atom. Nuclei 62 (1999) 209.

[205] I. Kodeli et al., Nucl. Instrum. Methods A 610 (2009) 540.

[206] V. M. Maslov et al., J. Korean Phys. Soc. 59 (2011) 1337.

[207] V. Manea, A. Tudora, Ann. Nucl. Energy 38 (2011) 72.

[208] R. J. Howerton, Nucl. Science Engineering 62 (1977) 438.

[209] G. S. Boykov et al., Nucl. Energy 21 (1994) 585.

[210] I. Dostrowsky, Z. Fraenkel, G. Friedlander, Phys. Rev. 116 (1959) 683.

[211] R. W. Pelle, F. C. Maienschein, Phys. Rev. C 3 (1971) 373.

[212] S. P. Maydanyuk et al., Phys. Rev. C 82 (2010) 014602.

[213] P. Singer et al., Z. Phys. A 359 (1997) 41.

[214] D. Pandit et al., Phys. Lett. B 690 (2010) 473.

[215] A. Hotzel et al., Z. Phys. A 356 (1996) 299.

[216] F. Pleasonton, R. L. Ferguson, H. W. Schmitt, Phys. Rev. C 6 (1972) 1023.

[217] V. V. Verbinski, H. Weber, R. E. Sund, Phys. Rev. C 7 (1973) 1173.

[218] A. Chyzh, C. Y. Wu, E. Kwan, R. A. Henderson, J. M. Gostic, T. A. Bredeweg, R. C. Haight, A. C. Hayes-Sterbenz, M. Jandel, J. M. ODonnell, and J. L. Ullmann, Phys. Rev. C 85 (2012) 021601.

[219] R. Billnert, F.-J. Hambsch, A. Oberstedt, S. Oberstedt, Phys. Rev. C 87 (2013) 024601.

[220] F. Pühlhofer, Nucl. Phys. 280 (1977) 267.

[221] D. J. Hofman et al., Phys. Rev. C 47 (1993) 1103.

[222] H. van der Ploeg et al., Nucl. Phys. A 569 (1994) 83.

[223] B. Becker, P. Talou, T. Kawano, Y. Danon, I. Stetcu, Phys. Rev. C 87 (2013) 014617.

[224] K. Skarsvag, Phys. Rev. C 22 (1980) 638.

[225] H. Baba et al., J. Nucl. Sci. Techn. 34 (1997) 871.

[226] F. Martin, PhD thesis, University of Grenoble, 2013 (in French).

[227] V. F. Apalin et al., Nucl. Phys. 71 (1965) 546.

[228] A. Bail, PhD thesis, University fo Bordeaux, 2009 (in French).

[229] W. Surin et al., Yader. Fiz. 14 (1971) 935.

[230] C. Wagemans et al., Phys. Rev. C 30 (1984) 218.

[231] C. Tsuchiya et al., Nucl. Science Techn. 37 (2000) 941.

[232] C. Wagemans, The Nuclear Fission Process, 1991, CRC Press, Boca Raton, USA.

[233] W. Holubarsch et al., Nucl. Phys. A 171 (1971) 631.

[234] N. Varapai et al., in Proc. of the Int. Workshop on Nuclear Fission and Fission Product Spectroscopy, Cadarache (France), May 11-14, 2005. Eds. G. Fioni et al., AIP Conf. Proc., vol. 447, p. 369.

[235] H. Faust et al., Nucl. Phys. A 736 (2004) 55.

[236] C. Milton et al., Can. Journ. Phys. 40 (1962) 1626.

[237] Ch. Straede et al., Nucl. Phys. A 462 (1987) 85.

[238] W. Meadows et al, Nucl. Data & Meas. Series, ANL/NDM-64 (1963).

[239] J.-C. Benoit, PhD thesis, Universite Paris Sud, 2012.

[240] R. A. Forrest, FISPACT2007: User manual, March 2007.

[241] A. Tobias, CEGB Report RD/B/6210/R89, May 1989.

[242] The JEFF3.1/3.1.1, Radioactive Decay Data and Fission Yields Sublibrairies, JEFF Report 20, NEA, 2009.

[243] M.-L. Giacri-Mauborgne, PhD thesis, University Caen, 2005 (in French).

[244] G. Rudstam et al., NEA WPEC6 "Delayed neutron data for the major actinies" and references therein.

[245] G. R. Keepin et al., Phys. Rev. 107 (1957) 1044.

[246] D. R. Alexander, M. S. Krick, Nucl. Sci. Eng. 62 (1977) 627.

[247] J. van Aarle, W. Westmeier, R. A. Esterlund, P. Patzelt, Nucl. Phys. A 578 (1994) 77.

[248] F.-J. Hambsch et al., Ann. Nucl. Energy 32 (2005) 1032.